Removing the Spin-Triplet Loss Pathway in Organic Solar Cells: A Strategy to Enhance Radiative Efficiency and Minimise Energy Loss

Alexander James Gillett

Selwyn College

University of Cambridge

This dissertation is submitted for the degree of

Doctor of Philosophy

29th March, 2019

Removing the Spin-Triplet Loss Pathway in Organic Solar Cells: A Strategy to Enhance Radiative Efficiency and Minimise Energy Loss

Alexander J. Gillett

Selwyn College, University of Cambridge

In this dissertation, we describe our work into suppressing the formation of triplet excitons in organic solar cells, created as a result of unavoidable non-geminate charge recombination processes. Triplet excitons represent a major non-radiative loss pathway in organic solar cells and through this work, we demonstrate tactics to reduce the non-radiative decay of photo-generated charges and thereby enhance the radiative efficiency of their decay processes. As the ideal solar cell would have only voltage loss resulting from the radiative recombination of charge carriers, we aim to decrease the magnitude of the non-radiative voltage losses in organic solar cells. In this work, we present two distinct strategies to achieve this:

i. The kinetic suppression of the back electron transfer process from the triplet charge transfer state to the local triplet state, so it is out-competed by re-dissociation of the charge transfer state into free charges.
ii. The use of low-exchange energy materials that allow for the simultaneous creation of a charge transfer state that is close in energy to the lowest singlet state to minimise the energy loss associated with charge generation, but still below the energy of the lowest triplet state, thermodynamically forbidding the formation of any local triplet states.

The first study investigates two closely-related high-performing organic solar cells that show an extremely low total voltage loss. Through detailed investigations of these donor-acceptor blends, we determine that the low voltage loss can be attributed to enhanced levels of radiative recombination. Further, we show that over the timescales of non-geminate recombination there is no observable formation of triplet excitons in the blend. Accrediting

the enhanced radiative recombination to the absence of the non-radiative triplet loss pathway, we explore the factors controlling the rate of the back electron transfer process that leads to triplet formation. From our preliminary calculations, we determine that the factor most likely responsible for a slow back electron transfer rate is the electronic coupling between the triplet charge transfer state and the molecular triplet exciton. If the rate of this process is sufficiently slowed, it will be out-competed by the rate of the re-dissociation of the charge transfer state, leading to the kinetic suppression of triplet exciton formation.

Having determined the efficacy of removing the triplet loss pathway in enhancing the radiative efficiency of recombination, the next two investigations focus on the second strategy discussed: thermodynamically forbidding triplet formation. For this, we utilise two different low exchange energy organic thermally activated delayed fluorescence materials as electron acceptors that are paired with wider band gap, high triplet energy donors. Through spectroscopic studies of the blends, we demonstrate that charge generation can proceed efficiently from both components, a prerequisite for efficient solar cell operation. Furthermore, the excellent radiative efficiencies and low non-radiative voltage losses of the blends confirms that this is indeed an effective route to improve the performance of organic solar cells.

Declaration

I hereby declare that except where specific reference is made to the work of others, the contents of this dissertation are original and have not been submitted in whole or in part for consideration for any other degree or qualification in this, or any other university. This dissertation is my own work and contains nothing which is the outcome of work done in collaboration with others, except as specified in the text and acknowledgements. In the following chapters, the use of first person plural is strictly a matter of style. This dissertation contains fewer than 60,000 words including appendices, bibliography, footnotes, tables and equations and has fewer than 150 figures.

Alexander J. Gillett
29th March, 2019

Acknowledgements

I would first like to thank the most important person in my life, Julie, for letting me have priority use of our desk during the writing process, relegating her to working on the sofa, or worse, banishing her to the library. In return for such a selfless act, I will grant you the occasional use of the superior processing power of my laptop to indulge in Sims 4, as I know this brings you many hours of joy.

Back in the academic world, I would like to thank Professor Sir Richard Friend for his supervision. As the Godfather of organic electronics, his near-encyclopaedic knowledge of the subject area, combined with his knack for knowing the best direction to take projects, has helped me develop immensely as a scientist. Thanks must be given to Dr. Matt Menke, who helped set me up on my first project and became my day-to-day contact for all questions related to organic electronics during his time here. Next to thank is Dr. Emrys Evans, with whom I have had many interesting discussions about TADFs with and always kindly furnished me with samples throughout my PhD (and who also took upon the unenviable task of checking through my probably slightly-too-long background and theory section). I thank Dr. Tudor Thomas for always keeping me up to date on the lab gossip and for making the many evenings spent together measuring TA entertaining. Patrick Conaghan and Qinying Gu are also deserving of thanks for fabricating devices for me to facilitate my crazy ideas of using TADFs in OPV. I would also like to thank the PIs of Optoelectronics, especially Dr. Akshay Rao and Dr. Dan Credgington for their discussions and collaborations during my PhD (and also for checking over my thesis chapters for me). In the Fastlab, where I have spent the majority of my time during my PhD, there are too many people to thank individually. But special mention must go to Dr. David Palek and Pete Budden, for enabling me to fulfil my pipe-dream of bringing the Fastlab into the UV-age. No longer shall any disgruntled nano-crystallers declare: "even green is too blue for the Fastlab". Finally, I do NOT want to thank the nameless person who removed the quartz rod from the TA1 visible NOPA for their own experiment: an afternoon was lost to this that will never be regained.

Table of Contents

List of Figures

List of Tables

List of Abbreviations

ΔE_{ST}: Singlet-Triplet Energy Difference

ΔV_{nr}: Magnitude of the Non-Radiative Voltage Loss

^{1}CT: Singlet Charger Transfer State

^{3}CT: Triplet Charger Transfer State

^{1}ICT: Singlet Intramolecular Charger Transfer State

^{3}ICT: Triplet Intramolecular Charger Transfer State

^{3}LE: Local Excited Triplet State

A: Acceptor

A2: IOTIC-2F

A3: SiOTIC-4F

AM1.5G: Air Mass 1.5 Global Solar Spectrum

AO: Atomic Orbital

B-O: Born-Oppenheimer

CT: Charge Transfer

D: Donor

EQE_{EL}: Electroluminescence External Quantum Efficiency

EQE_{PV}: Photovoltaic External Quantum Efficiency

FF: Fill-Factor

FRET: Förster Resonance Energy Transfer

fs: femtosecond

GA: Genetic Algorithm

GSB: Ground State Bleach

HOMO: Highest Occupied Molecular Orbital

ICT: Intramolecular Charge Transfer

IQE_{PV}: Photovoltaic Internal Quantum Efficiency

ISC: Intersystem Crossing

J_{SC}: Short-Circuit Current Density

J-V: Current density-Voltage

LCAO: Linear Combination of Atomic Orbitals

LUMO: Lowest Occupied Molecular Orbital
MO: Molecular Orbital
meV: milli-electron volt
NFA: Non-Fullerene Acceptor
NIR: Near Infrared
NOPA: Non-Collinear Optical Parametric Amplifier
ns: nanosecond
OLED: Organic Light Emitting Diode
OPV: Organic Photovoltaic
PCE: Power Conversion Efficiency
PES: Potential Energy Surface
PIA: Photo-Induced Absorption
PL: Photoluminescence
PLQE: Photoluminescence Quantum Efficiency
P2: PTB7-Th
ps: picosecond
QE: Quantum Efficiency
rISC: Reverse Intersystem Crossing
S_0: Singlet ground state
S_1: First-excited singlet state
SE: Stimulated Emission
SOC: Spin-Orbit Coupling
S_n: Higher-lying singlet state
T_1: Lowest energy triplet state
TA: Transient Absorption
TADF: Thermally Activated Delayed Fluorescence
T_n: Higher-lying triplet state
trPL: ns – μs Transient Photoluminescence
TTA: Triplet-Triplet Annihilation
V_{OC}: Open-circuit Voltage
μs: microsecond

1 Introduction

Since the first report of electroluminescence from conjugated polymers in the early 1990s,[1] the field of organic electronics has grown at an exponential rate. Organic electronics now have a broad spectrum of applications from photovoltaics[2] to light emitting diodes[3] and transistors.[4] Indeed, the rapid progress made in their performance in recent years has led to the commercialisation of optoelectronic devices based on organic materials. Broadly, organic optoelectronic devices can be divided into two key areas: organic photovoltaics (OPVs) and organic light emitting diodes (OLEDs), both concerned with the interconversion of photons and electrical current. It is on the former of these two subsets of organic optoelectronics that this thesis is primarily based, exploring the properties and applications of novel photovoltaic (PV) systems. However, we shall borrow heavily from the latter in this work, both in terms of materials and ideas. We hope with the knowledge gained from this work, we will be able to design new OPV systems that exceed the performance of their forerunners.

The role of PV devices is to convert incoming solar photons into useful electrical work. For this, photons in the ultraviolet (UV) to near infrared (NIR) region of the solar spectrum, spanning 300 nm – 2000 nm, are typically harvested. As such, semiconducting materials with a suitable band gap (between 2.5 and 0.6 eV) are employed as the light harvesting material. In the case of a single junction PV (a cell with a single light absorbing semiconductor layer), it is the band gap that limits the overall power conversion efficiency (PCE) of the cell as absorbed photons with an energy greater than the band gap of the semiconductor are rapidly thermalized to the band edge, with any excess energy lost as heat. The relationship between band gap and maximum theoretical obtainable PCE was first described by William Shockley and Hans J. Queisser, who found the maximum obtainable PCE for a single junction device to be 33.7%, corresponding to a band gap of 1.34 eV.[5,6] There have been attempts to circumvent this limit through the use of multi-junction cells which employ multiple absorbing layers to minimise thermalization losses,[7] which whilst successful, have so far proved to be too expensive and complicated for large scale production and adoption.

Traditionally, inorganic materials, such as silicon (Si), have been used in the light absorbing role. Monocrystalline Si PV demonstrates good performance, with a maximum PCE of 26.1% for a single junction cell.[8] However, PCEs of commercially available multi-crystalline Si modules are somewhat lower, with efficiencies in the region of 15% more typical. Though Si PV is a mature technology, with substantial infrastructure already in place for its manufacture, it does have a number of drawbacks. For example, Si PV is bulky and fragile and until recently, relatively expensive to produce, meaning the price per unit Watt of power produced was relatively high. Additionally, the creation of the Si wafers on which Si PV is based is a very energy intensive process, requiring temperatures of over 2000°C for thermal reduction and creates toxic by-products, undermining its green credentials.

Consequently, alternatives to Si PV have been investigated in recent years, with one of the more promising candidates involving organic semiconductors. With the adoption of non-fullerene acceptors (NFAs), OPV has recently seen a resurgence, demonstrating impressive maximum PCEs of 15.7% and 17.3% for single junction and tandem cells respectively.[9,10] Additionally, flexible modules can be produced by methods such as inkjet printing, which is a high throughput, low temperature process[11] and thermal evaporation.[12] The direct band gaps of organic materials means low thicknesses of the light absorbing materials (50 – 200 nm) are required for efficient light absorption, minimising the material requirements when compared to indirect band gap materials like Si. These innate properties make OPVs especially attractive and thus much effort in the field has been dedicated to improving their performance and stability.

In this thesis, we present our work on improving the efficiency of OPV devices through the suppression non-radiative loss channels, namely triplet formation. The creation of triplet excitons as a final product of bimolecular recombination is well-known in the OPV field and is suspected to contribute significantly to the high levels of non-radiative voltage loss seen in these devices.[13] As the voltage obtained from OPVs relative to their band gap is the primary metric in which they fall short compared to other PV technologies, any strategies to reduce this deficit are likely to greatly increase the competitiveness of OPVs with their inorganic peers.

To begin, we discuss the background theory that underpins the class of materials that is organic semiconductors in Chapter 2. This discussion is also extended to key concepts and operating principles of OPV and OLED devices of which we must be aware. Chapter 3 presents the experimental methods used in this work. In Chapter 4, we at last begin to explore the experimental results of this thesis. Here, we study model OPV systems based around two different NFAs that produce efficient OPV devices with a very low energy loss. Through spectroscopic measurements, we suggest that kinetically suppressed molecular triplet exciton formation in these systems contributes to this impressive metric. Finally, though calculations based off Marcus theory of electron transfer, we explore the effect the properties of the materials on the rate of triplet exciton formation and use the outcomes to suggest design rules to minimise triplet formation in future NFA OPV blends. Chapter 5 explores the potential for a low exchange energy thermally activated delayed fluorescence (TADF) OLED emitter materials to be used as the electron acceptor in an OPV device. By blending the TADF material TXO-TPA with wider band gap, high triplet energy electron donors, we construct a system where there is now no low energy molecular triplet state to act as a non-radiative trap. As a result of this, we report an OPV device that has significantly enhanced levels of radiative recombination, with a correspondingly low non-radiative voltage loss. Building on the work in Chapter 6, we investigate the properties and photovoltaic applications of a novel class of materials known broadly as curcuminoids. These TADF materials demonstrate efficient operation in both OLED and OPV applications, though there has been little further investigation into their innate photophysical behaviour. Through our spectroscopic studies, we reveal the factors limiting the performance of curcuminoid OLEDs at high current densities. Given their impressive attributes, including the strong absorption of visible light, we next employ them in OPV applications. Here, we investigate their use as both an electron donor and acceptor, the latter scenario being the direct follow on to the TXO-TPA work in Chapter 5. However, we find the OPV device performance of curcuminoids when used as the electron acceptor is poor. In light of this, we suggest possible reasons for their lack of aptitude for this role and propose that they primarily be utilised as the electron donor in following work. Finally, Chapter 7 summarises the findings of the experimental work and highlights interesting avenues for future investigation.

2 Background and Theory

Organic semiconductors are a diverse class of molecules constructed primarily of carbon and hydrogen, with the inclusion of some heteroatoms (including those such as sulphur, nitrogen, oxygen and fluorine) that are crucial to tuning their intrinsic properties. The enormous variety of structures available to the synthetic chemist allows for the creation of materials with finely-tuned properties for many applications. Key to their usefulness is absorption and/or emission of light in the UV, visible or NIR region of the electromagnetic spectrum and electrical conductivity that is suitable for use in classical semiconductor devices, including light emitting diodes, photovoltaics and transistors. But in order to make use of these properties, we must first understand their origins.

2.1 The Electronic Structure of Organic Semiconductors

2.1.1 The Schrödinger Equation and Wavefunctions

Before beginning our journey through the theory that describes organic semiconductors, we must first understand the concept of the wavefunction, Ψ. From quantum mechanics, we know the wavefunction of a molecule is a mathematical function containing all of the measurable information about that system. We can extract the desired information about the energy of the system from the wavefunction by solving the time-independent Schrödinger equation:

$$\hat{H}\Psi = E\Psi \tag{2.1}$$

Where $\hat{H}$ is the Hamiltonian operator, Ψ is the wavefunction of the system and E is the energy of the system. The Hamiltonian operator is device used to perform a mathematical operation on the wavefunction, in order to return the desired information about the system. In this case, when the Hamiltonian operator is multiplied by an allowed wavefunction (the eigenfunction), it returns the energy of the system (the eigenvalue) multiplied by the original wavefunction. However, as only certain wavefunctions are solutions to the Schrödinger equation, it follows that there are only certain, discrete energies that are allowed. This is because there are strict boundary conditions on the acceptable forms of the wavefunction. Therefore, as a consequence of these constraints on the wavefunction, the energies of all molecular states are quantised.[14]

Whilst the Schrödinger equation is solvable for the simplest system of a hydrogen atom, to generate solutions for large organic molecules requires the use of the Born-Oppenheimer (B-O) approximation. Key to this is the decoupling of nuclear and electronic motion, as the motions of the electrons in orbitals are much faster than that of the nuclei. As a point of reference, the timescale for photon absorption is $<10^{-15}$ seconds, whereas nuclear vibrations typically occur over a period of 10^{-12} - 10^{-14} seconds. Therefore in the B-O approximation, electronic motion occurs within a static nuclear arrangement. This allows us write total wavefunction as a product of three independent wavefunctions:

$$\Psi_{Total} \sim \Psi_e(r,R)\Psi_n(R)\Psi_s(\alpha,\beta) \tag{2.2}$$

Where Ψ_{Total} is the total wavefunction. $\Psi_e(r, R)$ is the electronic wavefunction, which contains information about the position and motion of the electrons and is a function of the electronic (r) and nuclear (R) co-ordinates. $\Psi_n(R)$ is the nuclear wavefunction, which only depends on the nuclear co-ordinates (R) and contains information about the nuclear configuration. $\Psi_s(\alpha, \beta)$ is the spin wavefunction, a function of the electrons' individual spin wavefunctions α and β.[15,16] We can simplify this further by considering only the parts of the Ψ_{Total} that contain spatial co-ordinates: $\Psi_e(r, R)$ and $\Psi_n(R)$. This is known as the spatial wavefunction:[16]

$$\Psi_{Spatial} = \Psi_e(r,R)\Psi_n(R) \tag{2.3}$$

The B-O approximation greatly simplifies the solution to the Schrödinger equation, allowing us to solve the electronic wavefunction alone for any set of fixed nuclear co-ordinates. However, it is important to note that the B-O approximation breaks down when there is significant vibronic coupling (interaction between the electrons and nuclear vibrational motion). Through the solving of the Schrödinger equation for the electronic wavefunction at different R, we can build up a potential energy surface (PES) for the molecule. The PES is an important concept and will be re-introduced in subsequent sections.

2.1.2 Atomic Orbitals and Hybridisation

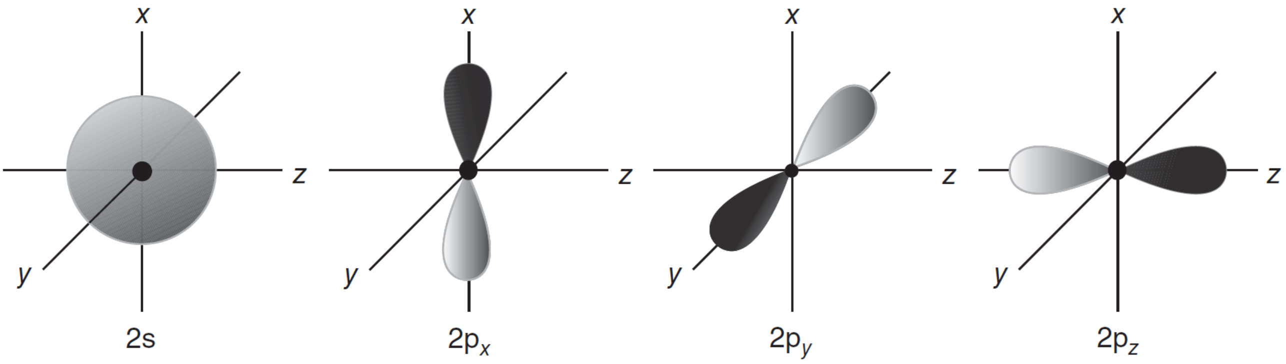

Figure 2.1*: The atomic 2s and 2p orbitals. Figure taken from reference 15.*

In order to truly understand organic semiconductors, we must begin at the building block of all matter: the atom. Specifically, the carbon atom. The carbon atom contains 6 electrons, with the electronic configuration $1s^2 2s^2 2p^2$. The 1s electrons are bound tightly in a deep orbital and thus do not contribute to the bonding of the atom. Rather, the higher energy electrons in the shells with a principle quantum number of n = 2 control this. These electrons are known as the valence electrons and are ultimately responsible for the macroscopically observed properties of all organic materials. Delving deeper into the atomic orbits (AOs) themselves, we notice that the lone 2s orbital is spherical in shape, whilst the 2p orbitals are dumbbell like. There are also 3 different 2p orbitals, resulting from the 3 different possible magnetic quantum numbers of m_l = -1, 0, 1. The lobes of these 2p orbitals all point along distinct axis, giving rise to the naming convention of $2p_x$, $2p_y$, and $2p_z$. These AOs are shown in Figure 2.1, with the phase of the wavefunction represented by the dark and light grey lobes.[16] Using these 4 n = 2

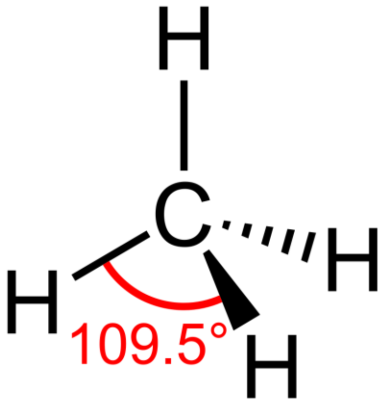

Figure 2.2*: The tetrahedral structure of methane, with all equivalent C-H bonds possessing a bond angle of 109.5º relative to each other.*

AOs, carbon can form up to 4 single bonds to other atoms, known as σ-bonds. These σ-bonds involve the sharing of 2 electrons between the atoms, where (in most cases) each atom contributes one of these electrons. By forming these 4 single bonds, the carbon atom can achieve its ultimate goal: to possess a full stable octet of valence electrons. Starting with perhaps the simplest organic molecule, methane (CH_4), we immediately run into a problem. It is well known that methane consists of a central carbon atom making 4 equivalent bonds to 4 individual hydrogen atoms, with an angle between all bonds of 109.5° (Figure 2.2). This particular arrangement of atoms is known as the tetrahedral structure. However, if we simply considered the scenario of the 4 individual n = 2 AOs on carbon (with one of the 2s electrons promoted to the unfilled 2p orbital to allow for the 4 bonds to be made) bonding with the 4 hydrogen atom 1s orbitals, we would not reproduce the known structure of methane. Thus, we must consider the hybridisation, otherwise known as "mixing", of these basic AOs to form hybrid AOs (HAOs). In the case of methane, we must form 4 equivalent bonds, so the 2s orbital is hybridised with the 3 2p orbitals. This gives rise to 4 $2sp^3$ HAOs, displayed in Figure 2.3, where sp^3 refers to the mixing of 1 s and 3 p orbitals. The bonds that can be formed between these $2sp^3$ HAOs and 4 hydrogen 1s AOs are now all equivalent, with the required bond angle of 109.5°.

The organic molecules used in semiconductor applications however do not simply contain only single σ-bonds between atoms. If this were the case, they would not possess many of the optical or electronic properties that make them of great interest. What ultimately bequeaths them these properties are π-bonds. These particular bonds are formed between p-orbitals. For this, the previously discussed sp^3 hybridisation is not appropriate: there are no un-hybridised p orbitals to take part in π-bonding. Therefore, instead of mixing all 3 p orbitals

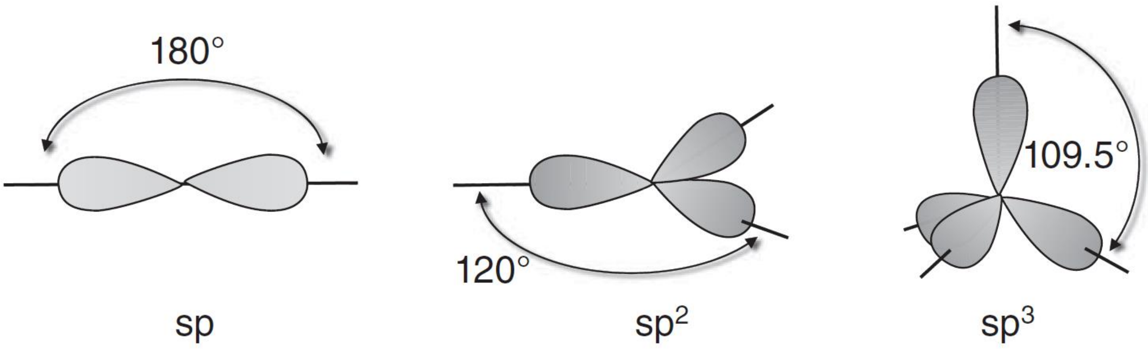

Figure 2.3: *The 3 different types of hybridisation accessible to carbon: sp, sp^2 and sp^3 and the associated bond angles. Figure taken from reference 15.*

with the s, either 2 or 1 p orbitals can be mixed instead, giving either 3 sp^2 or 2 sp HAOs, respectively. Examples of these orbitals are shown in Figure 2.3. This leaves either 2 or 1 un-hybridised p orbitals that can take place in the π-bonding, forming double or triple bonds with suitably hybridised partner atoms. Perhaps the simplest example of the 3 different types of hybridisation accessible to carbon is exemplified by comparing the 3 simplest hydrocarbons containing 2 carbon atoms in Figure 2.4: ethane, ethene and ethyne. Ethane contains 2 sp^3 hybridised carbon atoms and 6 hydrogen atoms, all bonded by a σ-bonding framework. In ethene, the carbons are sp^2 hybridised, with a double bond (1 σ bond and 1 π bond) between them and consequently only has 4 hydrogens attached via the remaining 4 sp^2 HAOs on the 2 carbons. Finally, in ethyne, the carbons are now sp hybridised, allowing for a triple bond (1 σ bond and 2 π bonds) between them, with only 2 remaining sp HAOs for bonding to hydrogen.

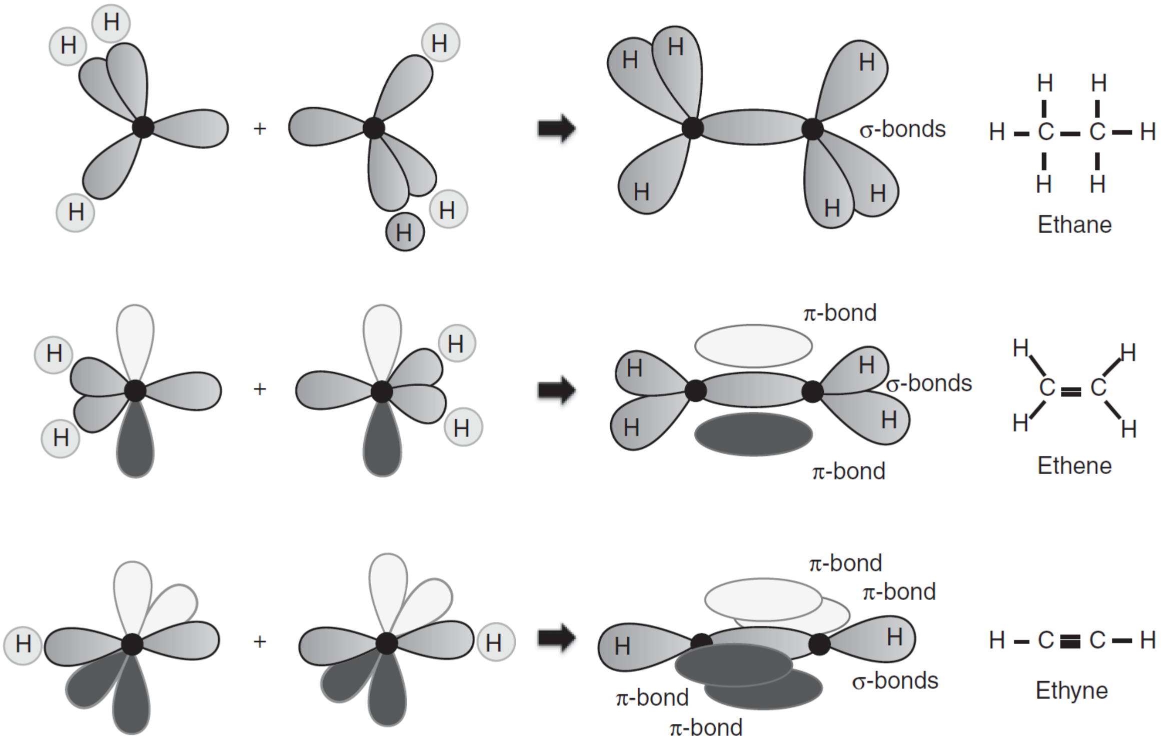

Figure 2.4: *The 3 simplest hydrocarbons containing 2 carbon atoms: ethane, ethene and ethyne, containing 0, 1 and 2 π-bonds, respectively. In ethane, the carbon atoms are* sp^3 *hybridised, in ethene they are* sp^2 *and in ethyne, they are sp. Figure taken from reference 15.*

2.1.3 Molecular Orbitals and π-Conjugation

The next step in our journey to understand organic semiconductors is to move from a simple AO picture to a molecular orbital (MO) picture. In MO theory, electrons do not just belong to individual bonds, but are instead spread out over the whole molecule. However, we know that we cannot solve the Schrödinger equation for all of the electrons in the molecule, as this is made impossible by complex electron-electron interactions. Therefore, the electronic wavefunction is approximated as many overlapping one-electron wavefunctions that are solutions of the Schrödinger equation. This is known as the orbital approximation:

$$\Psi_e \sim \prod_i \varphi_i \tag{2.4}$$

Where Ψ_e is the molecular electronic wavefunction and φ is a one-electron wavefunction, known as an MO. We construct each one-electron MO as a linear combination of atomic orbitals (LCAO):

$$\varphi_i = \sum_i c_i \phi_i \tag{2.5}$$

Here, ϕ is the wavefunction of the AO and c is an orbital weighting coefficient. This LCAO forms an MO, where the number of MOs generated must be equal to the number of AOs used. The weighting coefficient determines what fraction of each AO contributes to the MO and can be varied to gain a better approximation of the actual orbitals in the molecule.

We begin by considering the simplest conjugated organic molecule, ethene, with its single π-bond. Herein, we treat the π-orbitals separately from the σ-orbitals, with the latter providing the rigid framework that gives the shape of the molecule. When calculating the energies of the π-orbitals, we shall use the Hückel approximations. This approach has the benefit of greatly simplifying the calculations involved whilst still giving reasonable results for the energies of the MOs.[14] For ethene, the π-orbital can be expressed as the LCAO of the two carbon 2p orbitals $C_{2p,A}$ and $C_{2p,B}$ (ϕ_A and ϕ_B) that are orientated orthogonal to the molecular plane:

$$\varphi = c_A\phi_A + c_B\phi_B \tag{2.6}$$

Where c_A and c_B are the orbital weighting coefficients. In order to determine the weighting coefficient for each carbon 2p orbital to the MO, we use the variation principle. It states: "if an arbitrary wavefunction is used to calculate the energy, the value calculated is never less than the true energy". From this, we know that we can obtain the coefficients which correspond to the minimum energy MO that can be built from our chosen basis set of AOs by varying the coefficients in our trial wavefunctions until the expectation value of the energy is minimised. We will now outline this process mathematically. Starting with our trial wavefunction φ (equation 2.6) which is a solution to the Schrödinger equation, its energy is given by the expectation value of the energy operator:[14]

$$E = \frac{\int \varphi^* \hat{H} \varphi d\tau}{\int \varphi^* \varphi d\tau} \tag{2.7}$$

First, we express the denominator integral in terms of the orbital weighting coefficients:

$$\begin{aligned} \int \varphi^2 d\tau &= \int (c_A\phi_A + c_B\phi_B)^2 d\tau \\ &= c_A^2 + c_B^2 + 2c_Ac_BS \end{aligned} \tag{2.8}$$

Where S is the overlap integral:

$$S = \int \phi_A^* \phi_B d\tau \tag{2.9}$$

And next the numerator integral:

$$\begin{aligned} \int \varphi \hat{H} \varphi d\tau &= \int (c_A\phi_A + c_B\phi_B)\hat{H}(c_A\phi_A + c_B\phi_B) d\tau \\ &= c_A^2\alpha_A + c_B^2\alpha_B + 2c_Ac_B\beta \end{aligned} \tag{2.10}$$

Where α is the Coulomb integral, which is the energy of the electron when it occupies ϕ_A or ϕ_B and β is the resonance integral:

$$\alpha_i = \int \phi_i \widehat{H} \phi_i d\tau \tag{2.11}$$

$$\beta = \int \phi_A \widehat{H} \phi_B d\tau = \int \phi_B \widehat{H} \phi_A d\tau \tag{2.12}$$

Substituting 2.8 and 2.10 into equation 2.7 gives us an expression for E:

$$E = \frac{c_A^2 \alpha_A + c_B^2 \alpha_B + 2 c_A c_B \beta}{c_A^2 + c_B^2 + 2 c_A c_B S} \tag{2.13}$$

Next, we search for the values of the coefficients in the trial wavefunction that minimise the energy by finding:

$$\frac{\partial E}{\partial c_A} = 0 \qquad \frac{\partial E}{\partial c_B} = 0$$

$$\frac{\partial E}{\partial c_A} = \frac{2(c_A \alpha_A - c_A E + c_B \beta - c_B S E)}{c_A^2 + c_B^2 + 2 c_A c_B S} \tag{2.14}$$

$$\frac{\partial E}{\partial c_A} = \frac{2(c_B \alpha_B - c_B E + c_A \beta - c_A S E)}{c_A^2 + c_B^2 + 2 c_A c_B S} \tag{2.15}$$

Setting the derivatives to zero, we obtain the two secular equations whose solutions give the optimal coefficients for our chosen basis set:

$$c_A \alpha_A - c_A E + c_B \beta - c_B S E = (\alpha_A - E) c_A + (\beta - E S) c_B = 0 \tag{2.16}$$

$$c_B \alpha_B - c_B E + c_A \beta - c_A S E = (\beta - E S) c_A + (\alpha_B - E) c_B = 0 \tag{2.17}$$

These equations have a trivial solution: $c_A = c_B = 0$. However, the condition that there should exist a non-trivial solution is that the secular determinant should equal zero. In the case of ethene $\alpha_A = \alpha_B = \alpha$:

$$\begin{vmatrix} \alpha - E & \beta - ES \\ \beta - ES & \alpha - E \end{vmatrix} = 0 \tag{2.18}$$

In order to calculate an estimate for the MO energies more readily, we can now use the Hückel approximations. The key principle behind the approximations is that it neglects overlap and interactions between atoms that aren't neighbours:[14]

1. All overlap integrals are set to zero.
2. All resonance integrals between non-neighbours are set to zero.
3. All remaining resonance integrals are set equal (to β).

Using the approximations results in the following form of the secular determinant:

1. All diagonal elements = $\alpha - E$.
2. Off-diagonal elements between neighbouring atoms = β.
3. All other elements = 0.

The Hückel approximations result in secular determinant of equation 2.18 taking the following form:

$$\begin{vmatrix} \alpha - E & \beta \\ \beta & \alpha - E \end{vmatrix} = 0 \tag{2.19}$$
$$= (\alpha - E)^2 - \beta^2 = 0$$

Giving the following solutions for the energies of the MOs:

$$E_{\pm} = \alpha \pm \beta \tag{2.20}$$

As α and β are both negative, the + sign gives the energy of the π-bonding orbital and the – sign gives the energy of the π^*-antibonding orbital. The form and approximate energies of the bonding and antibonding π-orbitals of ethene are given in Figure 2.5.

For ethene, the π and π^* orbitals are the frontier molecular orbitals (FMOs), defined as the orbitals at the "frontier" of electron occupancy and alone provide an excellent approximation for the reactivity of the molecule. More precisely, the π-orbital is defined as the highest occupied molecular orbital (HOMO) and the π^*-orbital as the lowest unoccupied

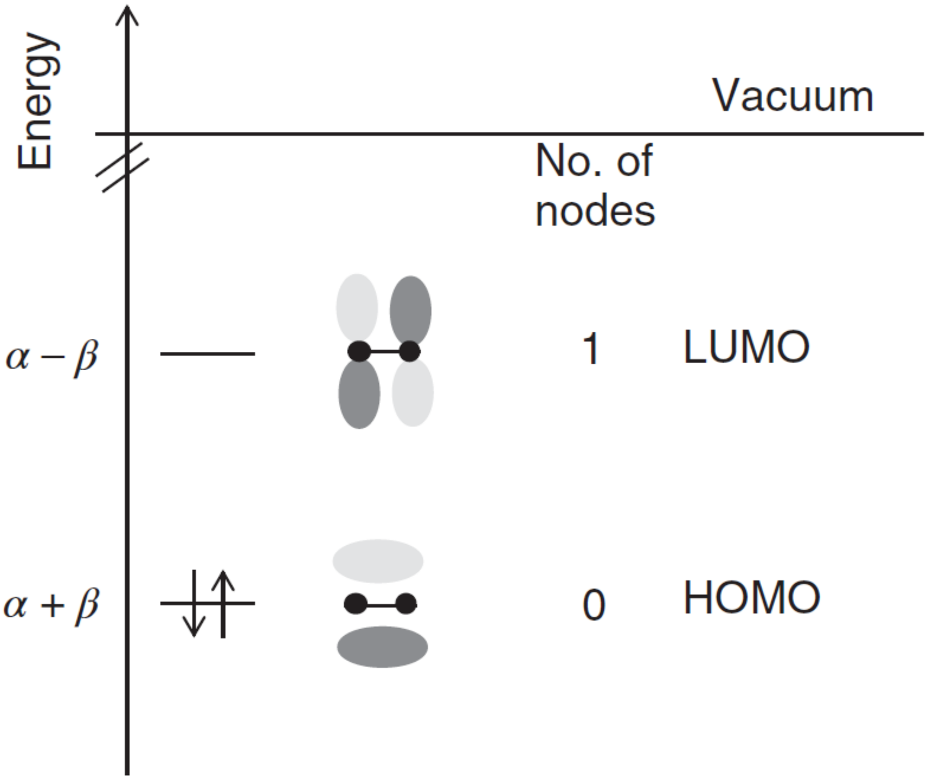

***Figure 2.5**: The form and approximate energies of the ethene π-bonding and π*-antibonding orbitals. Figure adapted from reference 15.*

molecular orbital (LUMO). These MOs are of great importance to the behaviour of organic semiconductors, as the lowest energy electronic transition is almost always from the HOMO to LUMO. It is the energy difference between these states that defines the electronic band gap of the material and its electronic properties. In this case, they can be thought of as being analogous to the valence and conduction bands of classical inorganic semiconductors. It is also important to note that the optical band gap (E_g) differs to the electronic band gap by the exciton binding energy: the stabilising interaction between the electron and hole reduces the energy of the optical transition. As with ethene, this typically corresponds to a $\pi \rightarrow \pi^*$ transition. However, the $\pi \rightarrow \pi^*$ transition in ethene has an energy of around 6.7 eV, meaning it lies deep into the UV and much higher in energy than the visible photons (1.8 – 3.1 eV) with which we want it to interact. The question which prevails is how we bring this $\pi \rightarrow \pi^*$ transition down in energy so that it becomes accessible by photons in the visible region? The answer is through having multiple double bonds interacting with each other through a delocalised network on π-bonds, known as π-conjugation. The next molecule up in the conjugation series from ethene is butadiene. Butadiene consists of a chain of 4 carbon atoms, with 2 double bonds rather than one. Similarly to ethene, we can form four new MOs that are a LCAO of the four carbon 2p AOs:

$$\varphi = c_A\phi_A + c_B\phi_B + c_C\phi_B + c_D\phi_B \tag{2.21}$$

Where, as before, c_x is weighting coefficient, whilst ϕ_X is the AO of the $C_{2p,x}$ for all 4 different carbon atoms. In the interest of conciseness, we shall skip directly to the secular determinant for butadiene, with the Hückel approximations already applied:

$$\begin{vmatrix} \alpha - E & \beta & 0 & 0 \\ \beta & \alpha - E & \beta & 0 \\ 0 & \beta & \alpha - E & \beta \\ 0 & 0 & \beta & \alpha - E \end{vmatrix} = 0 \tag{2.22}$$

We can simplify the form of the secular determinant for butadiene by dividing by β throughout and defining the new variable, x:

$$x = \frac{\alpha - E}{\beta} \tag{2.23}$$

Equation 2.22 then becomes:

$$\begin{vmatrix} x & 1 & 0 & 0 \\ 1 & x & 1 & 0 \\ 0 & 1 & x & 1 \\ 0 & 0 & 1 & x \end{vmatrix} = 0 \tag{2.24}$$

Expansion of equation 2.24 gives the fourth order polynomial equation:

$$x^4 - 3x^2 + 1 = 0 \tag{2.25}$$

Equation 2.25 can be further simplified by recognising that it is a quadratic equation in terms of x^2 and solved to give the roots:

$$x^2 = \frac{3 \pm \sqrt{5}}{2} \tag{2.26}$$

And the solutions:

$$x = \pm 0.618, \pm 1.618 \tag{2.27}$$

From this, we can now calculate the energies of the four π MOs of butadiene, ordered from lowest to highest:

$$\varphi_1 \quad E = \alpha + 1.618\beta \tag{2.28}$$
$$\varphi_2 \quad E = \alpha + 0.618\beta \tag{2.29}$$
$$\varphi_3 \quad E = \alpha - 0.618\beta \tag{2.30}$$
$$\varphi_4 \quad E = \alpha - 1.618\beta \tag{2.31}$$

For reference, the orbital form and energies of the four MOs are shown in Figure 2.6. After filling the MOs from lowest to highest energy with the 4 electrons from the 4 carbon atoms in the π-system, we find that the HOMO is φ_2 and the LUMO is φ_3 and this electronic transition defines the band gap. Important to note is that as the MOs must lie within an energy range of 4β ($\pm 2\beta$ of the original AO energy), the average energy separation must decrease as the number of atoms in the chain increases. This is consistent with what we have calculated: the HOMO and LUMO of butadiene lie within the original band gap of ethene and hence the band gap of butadiene is narrower: 5.8 eV. By further increasing the length of the π-conjugation, the band gap can be bought into the visible region with octatetrane, containing 4 conjugated double bonds (band gap = 3.1 eV). Further increasing the length the conjugation by combining many ethene monomer units (typically 100-200) leads to the conjugated polymer polyacetylene. The band gap of this material is further reduced to around 1.5 eV, meaning that this material can absorb across the entire visible range of photons.[17] It is for this reason why the vast majority of organic molecules used in optoelectronic applications are highly conjugated, often polymeric, containing many π-bonds.

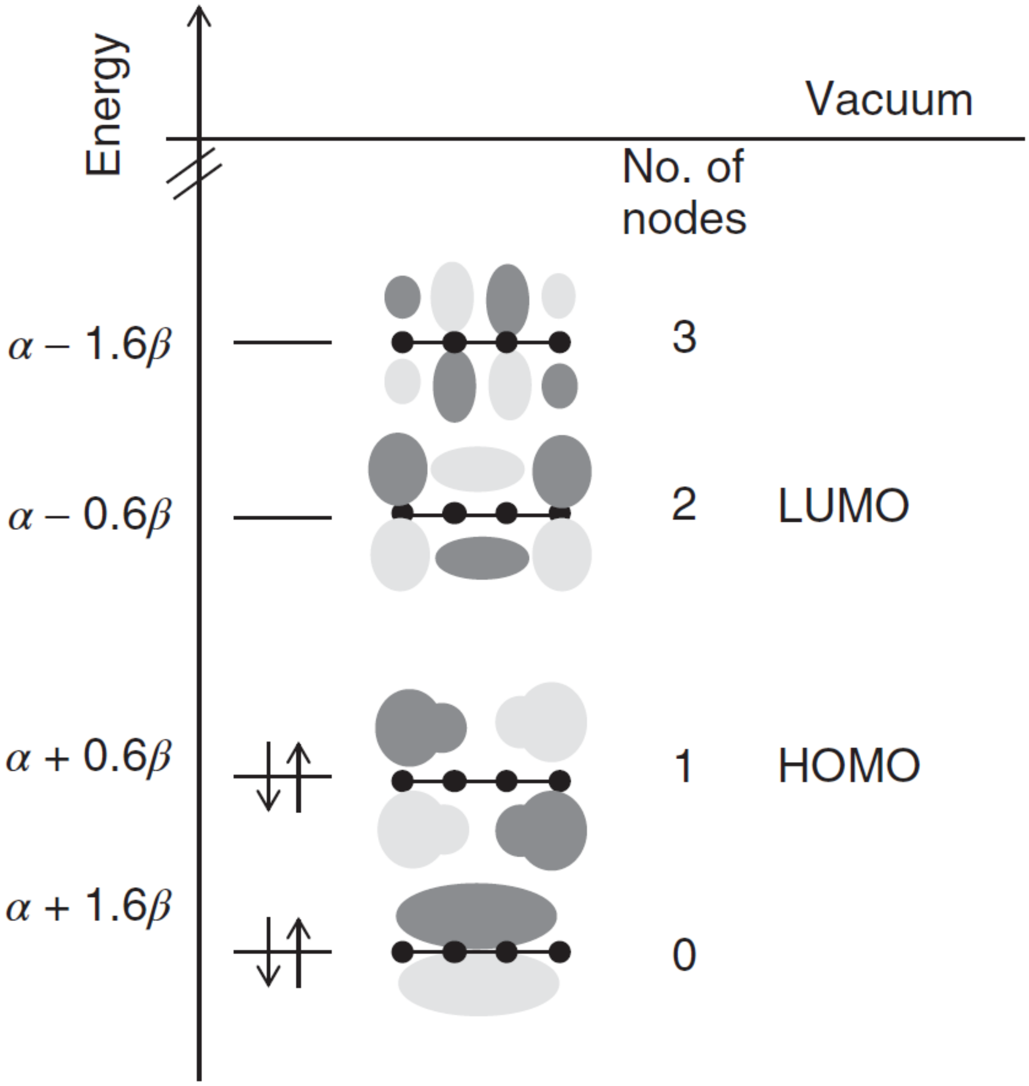

***Figure 2.6**: The form and approximate energies of the four butadiene MOs. Figure adapted from reference 15.*

2.2 The Interaction of Light with Matter

2.2.1 The Photon

Before we consider the interaction of photons with organic semiconductors, we must briefly discuss the photon itself. A photon is the particle representation for light and contains a discrete amount of electromagnetic energy. The energy of the photon is as follows:

$$E = hv \tag{2.32}$$

Where E is the energy of the photon in joules, h is Planck's constant and v is the frequency. The photon, like all quantum objects, also possess wave-particle duality, where it can simultaneously exhibit both particle and wave-like properties. Because of this, it also possesses momentum, p:

$$p = {}^{h}\!/_{\lambda} \tag{2.33}$$

With this knowledge, we can now express the energy of a photon in terms of its wavelength λ:

$$E = {}^{hc}\!/_{\lambda} \tag{2.34}$$

Where c is the speed of light in a vacuum (2.998x10^8 m/s). One can also easily interconvert the wavelength of the photon and its energy in eV through the following convenient relation:

$$E(eV) \sim {}^{1240}\!/_{\lambda} \tag{2.35}$$

As the wavelength of a photon containing 1 eV of energy is 1240 nm. A photon physically consists of electric and magnetic fields that oscillate in a sinusoidal fashion, perpendicular to each other and the direction of propagation, whilst also being in phase with each other. The distance between the peaks of the oscillating waves is defined as the wavelength. This is represented visually in Figure 2.7.

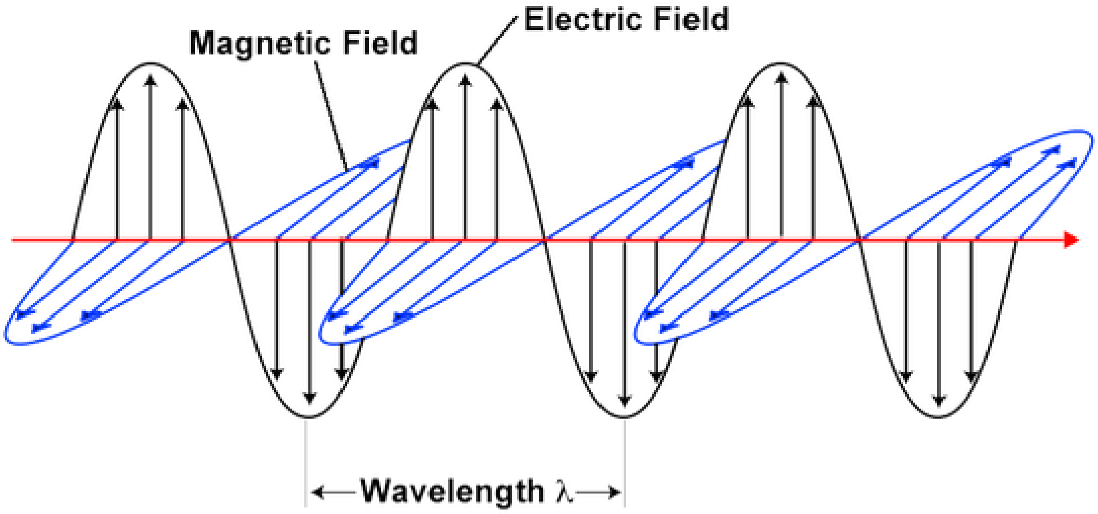

***Figure 2.7**: A visual representation of a photon, showing the perpendicular magnetic and electric fields and the wavelength.*

2.2.2 The Absorption and Emission of Photons

The absorption and emission of photons by organic semiconductors are key to their use in optoelectronic applications. The complete mathematical treatment of photon absorption is beyond the scope of this work. However, the general process is still of interest and thus we will discuss it briefly. We saw previously that a photon is comprised of an electric field, oscillating at a frequency that defines its energy (equation 2.32). It is this electric field that can interact with the electron distribution in a molecule, setting the electrons into harmonic oscillation nearly instantaneously. When the frequency of the electric field is the same as the natural frequency of an electronic transition, the transfer of energy is at a maximum and results in the photon being absorbed and the electronic transition occuring.[16] A critical point is that a photon possesses one unit of angular momentum ($\hbar$). Therefore, as the absorption of the photon by the molecule requires the conservation of angular momentum, there must be a change in the total angular momentum J of the electron to offset it. As the total spin angular momentum S cannot change during photon absorption, the change must occur in the total orbital angular momentum L. This leads us to our first selection rule: $\Delta L = \pm 1$.[15]

One can imagine that the larger the effect of the electric field on the electron distribution, the stronger the electronic transition is. The ability of the electron cloud to distort in response to an electric field $\boldsymbol{E}$ is defines its polarizability α and depends on the magnitude of the change in dipole moment $\boldsymbol{\mu}$ associated with the transition between the two states:

$$\alpha = {}^{\boldsymbol{\mu}}/_{\boldsymbol{E}} \tag{2.36}$$

The dipole moment $\boldsymbol{\mu}$ is defined as:

$$\boldsymbol{\mu} = e\boldsymbol{r} \tag{2.37}$$

Where e is the elementary charge and $\boldsymbol{r}$ is the position vector of the electron. Thus, the larger the transition dipole moment involved in the transition, the stronger it is.[15] This will be briefly revisited in the following section.

Now that we understand how a photon is absorbed, we are in a position to discuss further what determines the intensity of light absorption (and emission). The rate for a transition between an initial and final state, such as between the HOMO and LUMO in photon absorption or emission, is given by Fermi's Golden Rule:

$$k_{if} = \frac{2\pi}{\hbar}\left|\langle\Psi_f|\hat{H}'|\Psi_i\rangle\right|^2 p \tag{2.38}$$

Where k_{if} is the rate of the transition between the initial Ψ_i and final Ψ_i states, $\hbar$ is the reduced Planck's constant, $\hat{H}'$ is the perturbing Hamiltonian and p is the density of final states. For the electronic transitions we are interested in for photon absorption and emission, the perturbing Hamiltonian is the transition dipole moment operator $\hat{M}$ and we can substitute in our approximation for the total wavefunction $\Psi_{Total} \sim \Psi_e\Psi_n\Psi_s$ (equation 2.2):

$$k_{if} = \frac{2\pi}{\hbar}\left|\langle\Psi_{e,f}\Psi_{n,f}\Psi_{s,f}|\hat{M}|\Psi_{e,i}\Psi_{n,i}\Psi_{s,i}\rangle\right|^2 p \tag{2.39}$$

This somewhat complex expression can be simplified by applying the B-O approximation. We know that the electric field of the photon only interacts with the electrons, causing them to oscillate in resonance with it. However, in the B-O approximation, the nuclei are stationary on the timescale of the electron oscillations. The spins are also insensitive to the changing electric field and are only minutely affected by the oscillating magnetic field of the photon. Thus, the nuclear and spin wavefunctions can be treated as constants, giving:

$$k_{if} = \frac{2\pi}{\hbar}\left|\langle \Psi_{e,f}\middle|\widehat{M}\middle|\Psi_{e,i}\rangle\right|^2 \left|\langle \Psi_{n,f}\middle|\Psi_{n,i}\rangle\right|^2 \left|\langle \Psi_{s,f}\middle|\Psi_{s,i}\rangle\right|^2 p \qquad (2.40)$$

From this expression, we can see that the rate of an electronic transition is proportional to the square of the matrix element:

$$\left|\langle \Psi_{e,f}\middle|\widehat{M}\middle|\Psi_{e,i}\rangle\right|^2 \qquad (2.41)$$

From this, we can deduce that the electronic wavefunctions of the initial and final states must overlap for the transition to occur, as if the integral is zero, the rate of the transition will be zero. This means that the absorption and emission intensity will be highest for transitions where the MOs are strongly overlapping. As well as this, the integral will also scale with the transition dipole moment due to the presence of the dipole moment operator, which is the same as the classical quantity $\boldsymbol{\mu}$ (equation 2.37). Consequently, the involvement of larger, more extended orbitals will lead to increased absorption and emission intensity as they are more polarisable.

2.2.3 Oscillator Strength and the Molar Extinction Coefficient

After the previous theoretical discussions of Fermi's Golden Rule, it is useful to define a more "real world" parameter that we can use to discuss the strength of electronic transitions. The one we will use is the oscillator strength, *f*. In classical physics, the oscillator strength is defined as the probability of an electronic transition induced by the interaction between the electric field of light and the electrons in a molecule occurring. When $f = 1$, every photon that interacts with an electron will be absorbed. The theoretical oscillator strength can be related empirically to the experimentally measured molar extinction coefficient ε (L mol^{-1} cm^{-1}):[15]

$$f \equiv 4.3 \times 10^{-9} \int \varepsilon \, d\bar{v} \qquad (2.42)$$

Where $\bar{\nu}$ is the energy of the absorbed photons in inverse centimetres (cm^{-1}). This integral essentially corresponds to the area under the absorption transition in question of a plot of ε vs $\bar{\nu}$. As a rough guide, Table 2.1 lists typical oscillator strengths for a range of commonly encountered electronic transitions.[16] Importantly, the notion of oscillator strength also applies to the emission of a photon, so a high oscillator strength corresponds to both a large absorption coefficient and a strong luminescence for a given electronic transition.

Type of transition	Oscillator Strength (relative strength)	Extinction coefficient ($\text{L mol}^{-1}\text{ cm}^{-1}$)
Singlet $\pi \rightarrow \pi^*$	$10^{-2} - 1$	$10^{3} - 10^{5}$
Singlet charge transfer (CT)	$10^{-3} - 10^{-5}$	$10^{0} - 10^{2}$
Triplet (organometallic)	$\sim 10^{-4}$	$\sim 10^{1}$
Triplet (organic)	$\sim 10^{-9}$	$\sim 10^{-4}$

***Table 2.1**: A rough guide to the approximate oscillator strengths and extinction coefficients for a range of different electronic transitions.*

For reference, ε is a measure of how strongly a species attenuates a given wavelength of light and is defined as:

$$\varepsilon = {}^{A}\!/_{cl} \tag{2.43}$$

Where A is the absorbance of light of a particular wavelength, c is the molar concentration of the species and l is the path length the light travels through. Thus, ε is reported with the units of $\text{L mol}^{-1}\text{ cm}^{-1}$. For completeness, we will define the absorbance A:

$$A = -\log_{10} T \tag{2.44}$$

Where T is the percentage of incident photons transmitted through the sample.

2.2.4 The Role of Vibrations in Light Absorption and Emission

In our previous discussions of Fermi's Golden Rule (equation 2.38), we considered only the electronic portion of the total wavefunction. Here, we saw that this controlled the strength of the transition through the overlap of the initial and final electronic wavefunctions and the magnitude of the transition dipole moment. We will now consider the role of the nuclear part of the wavefunction, which contains information about the positions and motions of the nuclei, including their vibrational and rotational motion. The vibrational factor is of far greater importance to us in this work than the rotational factor, so we will consider this alone. Therefore, for the purposes of clarity in this discussion, we can replace the nuclear wavefunction with the vibrational wavefunction: $\Psi_n \equiv \Psi_{vib}$.

Referring back to section 2.1.1 where we discussed the concept of the PES, we can construct an energy diagram where the PES of the singlet ground (S_0) and first excited (S_1) states are represented by an anharmonic oscillator (Figure 2.8a and b).[16] Note that there is a

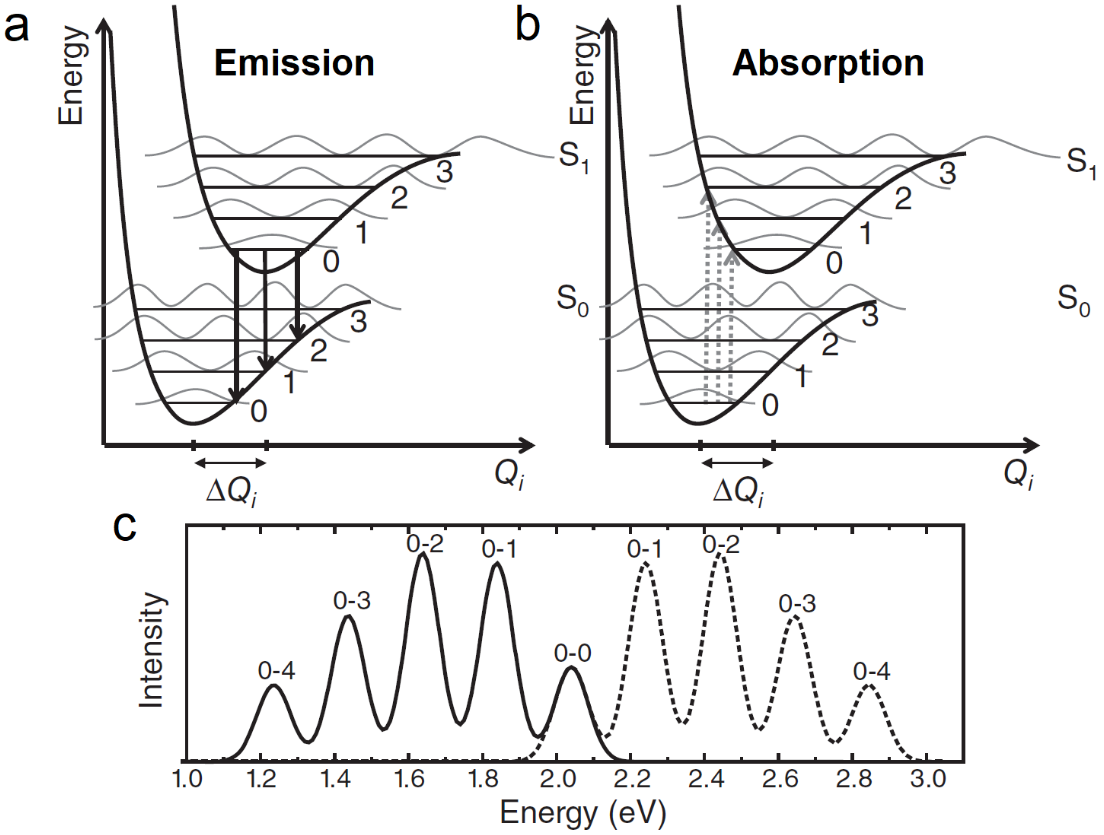

***Figure 2.8**: (a) The 1D PES of the singlet ground and first excited states, with the individual vibrational levels and their corresponding wavefunctions included. The arrows indicate emissive transitions from the zeroth vibrational level of the excited state. (b) The same diagram as for (a), except here absorptive transitions from the zeroth vibrational level of the ground state are shown. (c) The absorption (dashed) and emission (solid) spectrum of an imaginary molecule represented by the PES in (a) and (b). Figure adapted from reference 15.*

change in equilibrium nuclear co-ordinate (ΔQ) between these states, indicating a re-arrangement of the atoms in the molecule induced by this electronic transition: for rigid molecules, ΔQ will be small. Important to note is the Franck-Condon (F-C) principle, an extension of the previously discussed B-O approximation. The F-C principle states that electronic transitions occur with no change in the nuclear position. Therefore, transitions must occur vertically in our energy diagram. Into the PESs, we can insert the different discrete vibrational energy levels (shown in Figure 2.8a and b are arbitrary wavefunctions for these different vibrational states). These occur naturally from solving the Schrödinger equation, where as a result of the restrictions on the acceptable form of the vibrational wavefunction, the energies of the different vibrational states of the molecule are quantised into discrete levels. These vibrational levels are separated by energies on the order of ~100 meV. Thus, at room temperature where the thermal energy available is ~25 meV (given by k_BT where k_B is the Boltzmann constant and T = 298 K), all molecules can be considered to be in zeroth vibrational level of the singlet ground state.

Referring back to equation 2.22, we recall that the rate of a transition depends on the square of the overlap integral of the initial and final vibrational wavefunctions. This is known as the Franck-Condon factor F:[16]

$$F = \left|\langle \Psi_{vib,f} \middle| \Psi_{vib,i} \rangle\right|^2 \tag{2.45}$$

Therefore, the F-C factor determines the likelihood of a transition from the zeroth vibrational level of the ground state to the n^{th} vibrational level of the excited state. This concept is represented pictorially in Figure 2.8, where vibrational states with the largest wavefunction overlap in a vertical transition (0-1, 0-2) correspond to the transitions with the highest intensity. Because of this, the vibrational part of the wavefunction can be considered to control the shape of the absorption.

In the case of emission, this will almost always occur from the zeroth vibrational level of the lowest excited state due to very rapid (sub-picosecond) vibrational relaxation. As for photon absorption, the intensity of the emission vibrational bands is again determined by the F-C factor. Typically, absorption and emission are mirror images of each other as the vibrational level spacing is similar for the ground and excited states. Therefore, the same transitions are often most favourable for both absorption and emission. The emission of a molecule is also red-shifted from that absorption, a phenomena known as the Stokes Shift. The explanation for this is simple: emission occurs from the lowest vibrational level of the excited state and often occurs to higher vibrational levels of the ground state, leading to a reduction in the energy of the emitted photon when compared to the absorption.

Whilst in theory we should always see well defined vibrational structure in the absorption and emission spectra, the reality is that this is not that case. Often, the absorption and emission consist of broad, featureless bands. This is due to disorder, as a wide variety of slightly different nuclear configurations are present in the ensemble of molecules being probed. As a result of this, the energy gap for absorption and emission is slightly different for all the molecules and a featureless band is seen, resulting from the overlap of all these different spectra.

2.2.5 The Role of Spin in Light Absorption and Emission

Having now evaluated the electronic and vibrational elements and their role in light absorption, we finally address the role of spin. We note in Fermi's Golden Rule (equation 2.38), there is a term involving the square of the value of the overlap integral of the initial and final spin wavefunctions:

$$\left|\langle \Psi_{s,f} | \Psi_{s,i} \rangle\right|^2 \tag{2.46}$$

The value of this integral can be either 1 or 0 in the case that the initial and final spin states are the same or different. Therefore, transitions between states with the same spin can be considered "spin-allowed" and "spin-forbidden" if they are different. This gives us the selection rule $\Delta S = 0$ for electronic transitions. We will explore the role of spin in more detail in later sections, however it suffices to say that transitions between states with different spins are far from being completely forbidden.

2.3 Excitons and Spin

2.3.1 The Exciton

In semiconducting materials, an exciton is formed upon the absorption of a photon, which promotes an electron across the band gap and to a higher lying state. In the case of organic semiconductors, this is most often involves the promotion of an electron from the HOMO to the LUMO of a molecule, leaving behind a vacancy in the HOMO. A similar picture is present in inorganic semiconductors, except the HOMO and LUMO are represented by the valence and conduction bands instead. The vacancy resulting from the promotion of the electron is treated as positively charged quasiparticle, known as a hole. Together with the electron, it forms an electrically neutral quasiparticle called an exciton, of which there are two distinct types: Wannier-Mott and Frenkel excitons. Key to the unique behaviours of organic semiconductors when compared to their inorganic counterparts is the properties of their Frenkel excitons, defined as an electron and hole pair electrostatically bound through the coulomb interaction. The strength of this interaction is defined by Coulomb's Law:

$$F = k_e \frac{q_1 q_2}{r^2} \tag{2.47}$$

Here, F is the force of the interaction (negative if the charges have the opposite sign), k_e is Coulomb's constant, q_1 and q_2 are the signed magnitude of the charges and r is the separation of the charges. However the Coulomb interaction between the electron and hole is screened by other electrons in semiconducting materials. Therefore, the dielectric constant of the material ε_R must be taken into account when considering the strength of the interaction between the electron and hole, known as the exciton binding energy (E_b). Typically in inorganic semiconductors, E_b is determined from the Wannier-Mott hydrogenic model[18] and is defined as:[19]

$$E_b = \frac{m^* e^4}{2\hbar^2 \varepsilon_R^2} \tag{2.48}$$

Where m^* is the reduced effective mass of the exciton (given by $1/_{m^*} = 1/_{m_e^*} + 1/_{m_h^*}$, m_e^* and m_h^* are the effective masses of the electron and hole), e is the elementary charge and ħ is the reduced Planck's constant. Taking silicon as an example, the dielectric constant is quite large

($\varepsilon_R = 11.7$), whilst the effective masses of the electron and hole are relatively low, reducing the exciton binding energy to around 15 meV.[20] This leads to an exciton with a very large radius (~10 nm) and is termed a Wannier-Mott exciton. As the thermal energy at room temperature is equal to 25 meV, excitons created in these systems will essentially behave as free charge carriers in these conditions. In contrast, organic semiconducting materials typically have a much lower ε_R of ~2-4, which significantly affects the columbic binding energy (E_c) of the electron-hole interaction, given by:[21]

$$E_c = \frac{e^2}{4\pi\varepsilon_0\varepsilon_R r} \tag{2.49}$$

Where e is the elementary charge and ε_0 is the permittivity of free space. In organic semiconductors, the reduced ε_R results in an increased exciton binding energy on the order of 0.1 – 1 eV. This leads to a small exciton radius (~1 nm) and often the localisation of the exciton on a single molecule. Such an exciton is named a Frenkel exciton.[22] An important property derived from this expression is the coulomb capture radius r_c, defined as the distance at which E_c equals the thermal energy available at room temperature, k_BT (25 meV):

$$r_c = \frac{q^2}{4\pi\varepsilon_0\varepsilon_R k_B T} \tag{2.50}$$

When free electrons and holes come within the coulomb capture radius, they will no longer be free charge carriers, but constitute a bound exciton again. In photovoltaics for example, the exciton binding energy must be overcome in order to separate the exciton into free electrons and holes that can be extracted as electrical current.

2.3.2 Singlet and Triplet States

As discussed in the previous section, an exciton in an organic molecule consists of a promoted electron in the LUMO, with the remaining electron (and hole) in the HOMO. Before the creation of the exciton, the molecule will be in the ground state. Here, the HOMO is doubly occupied, with 2 electrons in the same orbital. As per the Pauli Exclusion Principle, these electrons must have opposite spin quantum numbers ($m_s = \pm½$),[14] giving an overall spin of $S = 0$. This arrangement of antiparallel spins is known as a singlet state, with the state described

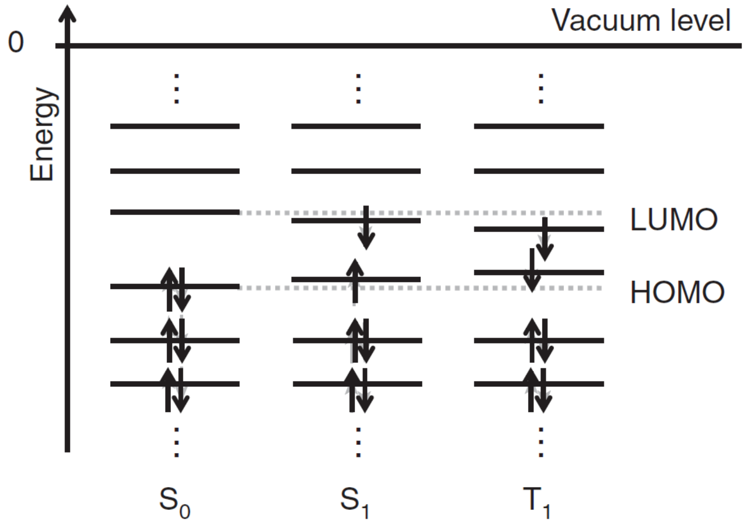

***Figure 2.9:** The orbital configuration of the ground (S_0) and first (S_1) excited singlet states and the first excited triplet state (T_0). The S_0 state has a doubly occupied HOMO where the electrons have antiparallel spins. The S_1 results from the promotion of an electron to the LUMO, again with spins antiparallel. The T_1 state again has an electron in the LUMO, but this time the spins are parallel. Figure adapted from reference 15.*

previously as having both electrons in the HOMO known as the singlet ground state (S_0). Optical excitation of an electron to the LUMO by a photon, which possesses zero spin angular momentum, results in the formation of a singlet excited state (S_n) with the electrons retaining their original spins. However, when an uncorrelated electron and hole collide, they will each possess a random spin and thus can have either parallel or antiparallel spins. In the case that they have parallel spins, a triplet excited state is formed (T_n) with an overall spin of $S = 1$. A schematic showing the orbital configuration of the S_0 and first excited singlet (S_1) and triplet (T_1) states is included in Figure 2.9.[16]

For completeness, we will now discuss the origin of singlet and triplet states. From the B-O approximation, we know that that total wavefunction can be approximated as a product of the electronic, nuclear and spin wavefunctions: $\Psi_{Total} \sim \Psi_e \Psi_n \Psi_s$ (equation 2.2). Considering a 2 particle system, there are 3 ways the spins of the $s = ½$ electron can be arranged to give an overall spin of $S = 1$ (T+, T_0 and T-: hence the origin of the term “triplet”), and 1 way they can be arranged to give an overall spin of S = 0. The spin wavefunctions for these 4 states can be defined in terms of the spin wavefunctions of the one electron states, α and β. Here, α refers an electron with $m_s = +½$ and β to an electron with $m_s = -½$:[16]

$$\Psi_{s,T+} = \alpha_1\alpha_2 \qquad S = 1, \qquad M_s = 1 \tag{2.51}$$

$$\Psi_{s,T0} = \frac{1}{\sqrt{2}}(\alpha_1\beta_2 + \beta_1\alpha_2) \qquad S = 1, \qquad M_s = 0 \tag{2.52}$$

$$\Psi_{s,T-} = \beta_1\beta_2 \qquad S = 1, \qquad M_s = -1 \tag{2.53}$$

$$\Psi_{s,S} = \frac{1}{\sqrt{2}}(\alpha_1\beta_2 - \beta_1\alpha_2) \qquad S = 0, \qquad M_s = 0 \tag{2.54}$$

In this case, the subscript of 1 and 2 on α and β relate to the individual electrons that make up the pair that defines the total spin state. The total spin S and spin quantum number M_s are also given for each of the spin wavefunctions. Important to note is that the 3 triplet states are not degenerate: they have an energy offset of order 10 μeV under zero magnetic field, known as the zero-field splitting. A schematic illustrating the relative orientations of the electron spins for the singlet and triplet states is shown in Figure 2.10.[16]

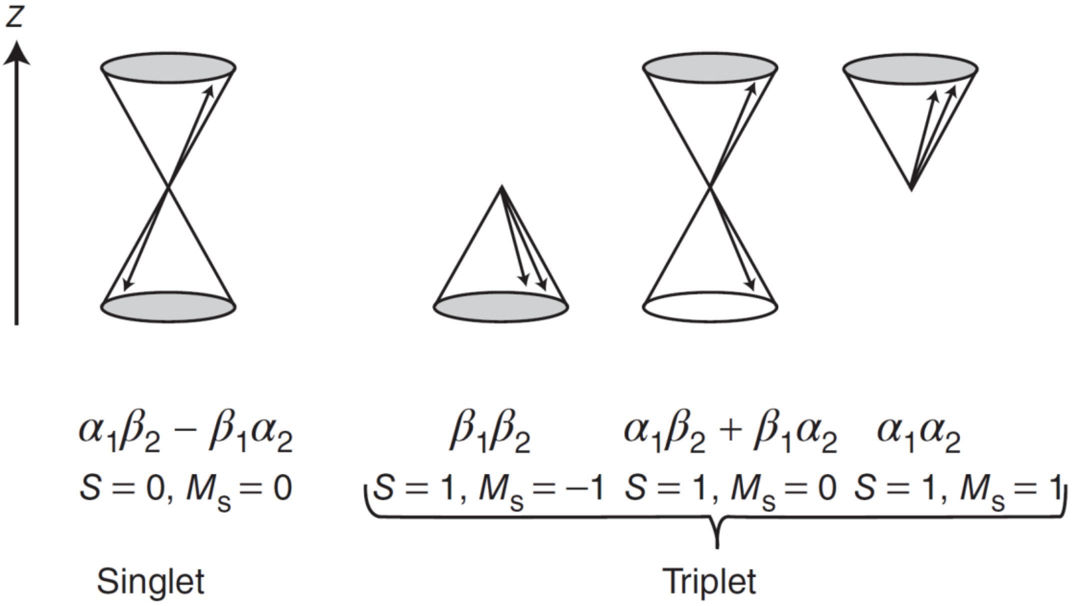

Figure 2.10: *Vector representation of the singlet and triplet states. The singlet state is composed of 2 electrons whose spins are anti-parallel and 180^o out of phase with each other, giving an overall spin of S = 0. In the case of the triplets, all of the electron spins are in phase and do not cancel, giving an overall spin of S = 1. Figure taken from reference 15.*

An important consideration is that the singlet and triplet states are not degenerate in energy due to the differences in their electron-electron repulsion. This comes about as a result of the Pauli Exclusion Principle, which states that 2 identical fermions may not occupy the same quantum state in a quantum system simultaneously, forbidding electrons with parallel spins to occupy the same space at the same time.[15] This Pauli repulsion force causes the spin parallel electrons in the triplet state to avoid each other. Conversely, the spin antiparallel electrons have an enhanced probability of approaching each other. Therefore, the electrons in the triplet state are able to minimise their electron-electron repulsions and this state has a lower energy.[15] The magnitude of this stabilisation (ΔE_{ST}) is given by twice the electron exchange energy J:[23]

$$\Delta E_{ST} = E_{S1} - E_{T1} = 2J \tag{2.55}$$

Where J is defined as the matrix element:[24]

$$J = \iint \varphi_H(r_1)\varphi_L(r_2)\left(\frac{e^2}{4\pi\varepsilon_0(r_1 - r_2)}\right)\varphi_H(r_2)\varphi_L(r_1)\, dr_1 dr_2 \tag{2.56}$$

Where φ_H is the HOMO wavefunction, φ_L is the LUMO wavefunction, e is the elementary charge, ε_0 is the permittivity of free space and $(r_1 - r_2)$ is spatial separation of the electrons. The triplet state is stabilised by J, whilst the singlet is destabilised by J, giving the relation $\Delta E_{ST} = 2J$. From this, it is apparent that the exchange energy depends strongly on the electron-electron interaction potential and the overlap integral of the HOMO and LUMO. This can be easily rationalised as a larger orbital overlap increases the probability of the electron being found in the same position on the molecule. Therefore, molecules with decoupled HOMO and LUMOs and thus a strong charge transfer (CT) character in their excited state will have a small ΔE_{ST}, an important point that will be revisited later.

2.3.3 The Interconversion of Singlet and Triplet States

As previously seen in equation 2.46, the interconversion of singlet and triplet states, broadly termed intersystem crossing (ISC) processes, is formally forbidden due to the matrix element $\langle \Psi_{s,f} | \Psi_{s,i} \rangle$. However, such spin-forbidden transitions can occur in organic (and more pervasively in organometallic) semiconductors. The dominant mechanism for inducing a spin change in a transition is spin-orbit coupling (SOC), arising from the interaction of the spin magnetic moment with the magnetic field generated by the orbital angular momentum.[14] The basis behind this is that a change in the electron's spin angular momentum S can be compensated for by an equal and opposite change in the orbital angular momentum L. As a result of this, the total angular momentum J is unchanged during the transition:

$$J = L + S \tag{2.57}$$

One can think of SOC as slightly mixing the singlet and triplet states, meaning that they no longer have "pure" singlet or triplet character. As a result of this, the matrix element for the singlet-triplet transition $\langle \Psi_{s,t} | \Psi_{s,s} \rangle$ is non-zero and therefore the transition is slightly allowed. The mixing of the pure triplet state wavefunction $\left| {}^3\Psi_1^0 \right\rangle$ with a small amount of the wavefunction of other singlet states can be expressed mathematically through perturbation theory as:[16]

$$\left| {}^3\Psi_1' \right\rangle = \left| {}^3\Psi_1^0 \right\rangle + \sum_k \frac{\left\langle {}^1\Psi_k^0 \middle| \hat{H}_{SO} \middle| {}^3\Psi_1^0 \right\rangle}{E(T_1) - E(S_k)} \left| {}^1\Psi_k^0 \right\rangle \tag{2.58}$$

Where $\left| {}^3\Psi_1' \right\rangle$ is the resulting wavefunction of triplet-singlet admixture, $\left| {}^1\Psi_k^0 \right\rangle$ is the wavefunction of the k$^{\text{th}}$ singlet state, $\hat{H}_{SO}$ is the perturbing SOC Hamiltonian, $E(T_1)$ is the energy of the first excited triplet state and $E(S_k)$ is the energy of the k$^{\text{th}}$ singlet state. An equivalent expression can also be written for the mixing of the pure singlet ground state wavefunction $\left| {}^1\Psi_0^0 \right\rangle$ with a small amount of higher lying triplet states:[16]

$$\left| {}^1\Psi_0' \right\rangle = \left| {}^1\Psi_0^0 \right\rangle + \sum_k \frac{\left\langle {}^3\Psi_k^0 \middle| \hat{H}_{SO} \middle| {}^1\Psi_0^0 \right\rangle}{E(S_0) - E(T_k)} \left| {}^3\Psi_k^0 \right\rangle \tag{2.59}$$

Importantly, for atoms, the perturbing Hamiltonian $\hat{H}_{SO}$ for the spin-orbital interaction proportional to the fourth power of the atomic charge Z:

$$\hat{H}_{SO} \propto \frac{Z^4}{n^3(l+1)(l+0.5)l} \tag{2.60}$$

Where n is the principle quantum number and l is the orbital angular momentum quantum number. A similar result is obtained for molecules.[16] As a result, the mixing of singlet and triplet states is much more significant when atoms of high mass (e.g. Pt or Ir) are incorporated into the molecule, termed the "heavy atom effect". In order to determine the rate of the transition between the no longer pure singlet and triplet states (in this case between T_1 and S_0), we can substitute equations 2.58 and 2.59 into Fermi's Golden Rule (equation 2.38), yielding:[16]

$$k_{if} = \frac{2\pi}{\hbar}\left|\langle {}^3\Psi_1' | \widehat{M} | {}^1\Psi_0' \rangle\right|^2 p = \frac{2\pi}{\hbar}(A + B + C + D)^2 p \tag{2.61}$$

Where:

$$A = \langle {}^3\Psi_1^0 | \widehat{M} | {}^1\Psi_0^0 \rangle \tag{2.62}$$

$$B = \sum_k \frac{\langle {}^1\Psi_k^0 | \widehat{H}_{SO} | {}^3\Psi_1^0 \rangle}{E(T_1) - E(S_k)} \langle {}^1\Psi_k^0 | \widehat{M} | {}^1\Psi_0^0 \rangle \tag{2.63}$$

$$C = \sum_k \frac{\langle {}^3\Psi_k^0 | \widehat{H}_{SO} | {}^1\Psi_0^0 \rangle}{E(S_0) - E(T_k)} \langle {}^3\Psi_1^0 | \widehat{M} | {}^3\Psi_k^0 \rangle \tag{2.64}$$

$$D = \sum_k \frac{\langle {}^1\Psi_k^0 | \widehat{H}_{SO} | {}^3\Psi_1^0 \rangle}{E(T_1) - E(S_k)} \sum_j \frac{\langle {}^3\Psi_j^0 | \widehat{H}_{SO} | {}^1\Psi_0^0 \rangle}{E(S_0) - E(T_j)} \langle {}^1\Psi_k^0 | \widehat{M} | {}^3\Psi_j^0 \rangle \tag{2.65}$$

This expression can be simplified by reminding that ourselves that the total wavefunction can be written as a product of the spatial parts of the wavefunction ($\Psi_{Spatial} = \Psi_e\Psi_n$) and the spin wavefunction (Ψ_s): $\Psi_{Total} \sim \Psi_e\Psi_n\Psi_s$. Therefore, the matrix element of the terms containing wavefunctions being operated on by $\widehat{M}$ with opposite spins will equal zero. Because of this, terms A and D in equation 2.43 will go to zero and we can write the rate of the transition between T_1 and S_0 (known as phosphorescence) as:

$$k_{T_1 \to S_0} = \frac{2\pi}{\hbar} p \left(\left(\sum_k \frac{\left\langle {}^1\Psi_k^0 \middle| \hat{H}_{SO} \middle| {}^3\Psi_1^0 \right\rangle}{E(T_1) - E(S_k)} \langle {}^1\Psi_k^0 | \hat{M} | {}^1\Psi_0^0 \rangle \right) + \left(\sum_j \frac{\left\langle {}^3\Psi_k^0 \middle| \hat{H}_{SO} \middle| {}^1\Psi_0^0 \right\rangle}{E(S_0) - E(T_j)} \langle {}^3\Psi_1^0 | \hat{M} | {}^3\Psi_j^0 \rangle \right) \right)^2 \quad (2.66)$$

In this expression, the B term will provide a much larger contribution to the overall rate than C as there is a much smaller energy difference between T_1 and excited single states S_k than S_0 and higher lying triplet states T_k. Whilst we have defined the rate for the transition of T_1 → S_0, the same principles can be applied to other spin-forbidden transitions.

We can now understand the previous comment that spin-forbidden transitions are more pervasive in organometallic compounds, as they may happen rapidly enough to out-compete other competing pathways due to the large magnitude of $\hat{H}_{SO}$. This also rationalises the differences in oscillator strength for transitions involving the interconversion of singlet and triplet states for organometallic and organic compounds in Table 2.1. However, in purely organic compounds containing no heavy atoms, the spin-orbital coupling is small and often another mechanism must provide the prerequisite coupling interaction for the spin-flip to occur. This is achieved by the vibronic coupling of orbitals with different orbital angular momentum and will be discussed when it becomes relevant in a later section.

2.4 Radiative and Non-Radiative Transitions

From the previous theoretical discussions, we have now reached a point where we can begin to explore the different types of transitions that interconvert electronic states. These can be well-represented in a Jablonski diagram, as seen in Figure 2.11.[18,25] Here, we can see that there are numerous possible transitions between states that can be broadly divided into 2 categories: those that involve the emission of a photon (radiative transitions) and those that do not (non-radiative transitions). We will now explore these 2 sub-categories in turn.

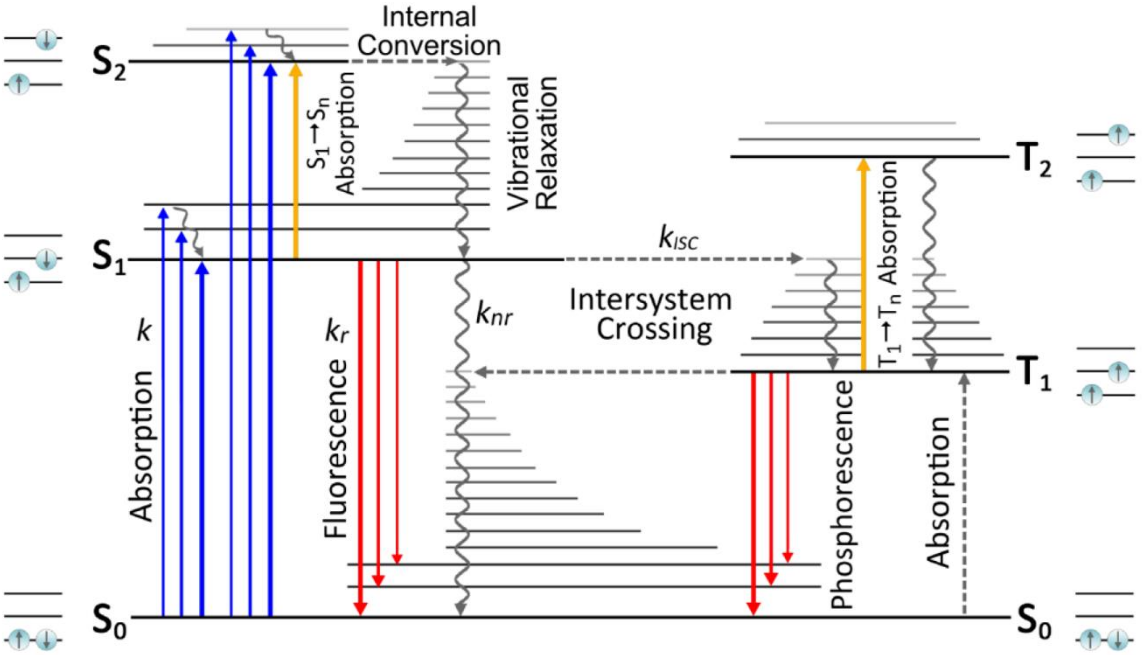

Figure 2.11: *A Jablonski diagram describing the transitions that can take place between the different electronic states. Figure adapted from reference 17.*

2.4.1 Radiative Transitions

In this scheme, there are 2 types of radiative transitions possible: fluorescence and phosphorescence. Fluorescence occurs when an electron in an excited state orbital relaxes back to the ground state via the emission of a photon. It is a spin-allowed process, occurring between a spin-singlet exited state and the singlet ground state. The discussions involving the factors affecting the intensity of the fluorescence (and photon absorption) can be found in Section 2.2 Phosphorescence also involves the relaxation of an electron in an excited state orbital via the emission of a photon, but in this case the excited state orbital involved is a triplet. Therefore, this transition is formally spin-forbidden, but can be enabled by sufficient spin-orbit coupling, as described in the previous section.

An important parameter to consider when discussing radiative transitions is their quantum efficiency Φ, known as the photoluminescence quantum efficiency (PLQE), Φ_{PL}:

$$\Phi_{PL} = \frac{Number\ of\ photons\ emitted}{Number\ of\ photons\ absorbed} \tag{2.67}$$

For fluorescent emission, the quantum efficiency $\Phi_f$can be written in terms of the various rate constants for fluorescence (k_f) and the competing processes:

$$\Phi_f = \frac{k_f}{\sum_i k_i} \tag{2.68}$$

Where:

$$\sum_i k_i \tag{2.69}$$

Is the sum of all the different rate constants for excited state decay. For the case of fluorescence, this includes fluorescence itself, ISC and internal conversion (IC).

2.4.2 Non-Radiative Transitions

Turning our attention now to the non-radiative transitions, we note that there are 2 possible types: IC (those taking place between states on the same spin) and ISC (those occurring between states with different spins). For IC, the transition occurs isoenergetically from the 0th vibrational level of the initial electronic state to a high vibrational level of final electronic state. This is then followed by rapid vibrational relaxation to the 0th vibrational level of the final state. Important to note is that ISC may also occur from higher vibrational levels of the initial electronic state if these are closer in energy to the final state than the 0th level.

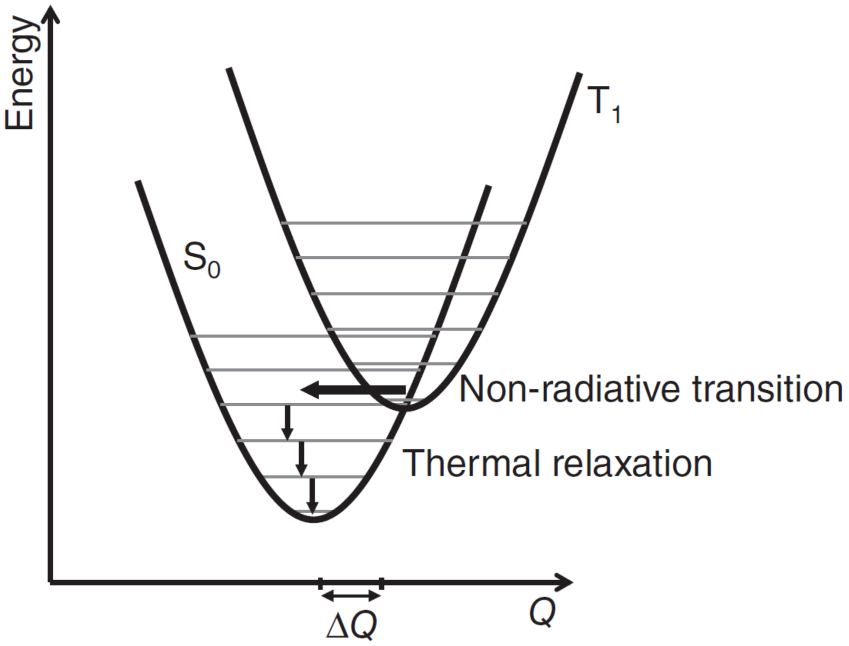

Figure 2.12: *The PESs of the initial and final states involved in in a non-radiative transition, in this case ISC from* T_1 *to* S_0*. The first step is the horizontal isoenergetic transition from a vibrational level of the triplet state to a high vibrational level of the singlet ground state, with the change in nuclear geometry ΔQ. This is then followed by rapid vibrational relaxation to the 0th vibrational level of* S_0*. Figure taken from reference 15.*

Considering the PES of the states, this can be pictured as a 2-step transition: the first involves a horizontal step from the equilibrium geometry of the initial state, to a higher vibronic level of the final state, followed by a vertical transition comprising of the vibrational relaxation to the 0th vibrational state (Figure 2.12).[16] Mathematically, the rate of the non-radiative transition can be determined from Fermi's Golden Rule, where the perturbing Hamiltonian is the nuclear kinetic energy operator ($^{\delta}/_{\delta Q}$), where Q is the normal mode displacement:

$$k_{if} = \frac{2\pi}{\hbar}\left|\langle \Psi_{e,f}\Psi_{n,f}\Psi_{s,f}\left|{}^{\delta}/_{\delta Q}\right|\Psi_{e,i}\Psi_{n,i}\Psi_{s,i}\rangle\right|^{2} p \qquad (2.70)$$

In the case on non-radiative transitions, due to the change in both nuclear and electronic coordinate during the transition (i.e. it is non-adiabatic), the B-O approximation is no longer valid. Siebrand was able to define an expression for the non-radiative decay rate (k_{nr}) outside of the B-O approximation:[26]

$$k_{nr} = \frac{2\pi}{\hbar} p J^2 F \tag{2.71}$$

Where J is the electronic coupling between the initial and final states (containing the electronic and spin wavefunctions) and F is the previously discussed F-C factor (equation 2.45). Through evaluation of the energy dependence of the F-C factor, one finds an exponential dependence of the non-radiative decay rate with respect to the energy gap between the initial and final electronic states:[16]

$$k_{nr} \propto e^{\left(\frac{-\gamma \Delta E}{\hbar \omega_0}\right)} \tag{2.72}$$

Where γ is a constant depending on the molecular properties and ω_0 is the frequency of the highest energy vibrational mode involved in the transition. One can think of the expression as saying that the smaller the energy gap, the fewer phonon modes are required to couple the states in order to dissipate the energy through vibrations. The consequence of the energy gap law is that when the energy difference between states is small, or the transition is formally spin-forbidden, non-radiative recombination will likely out-compete radiative recombination. It is for this reason why phosphorescence is seldom observed in purely organic molecules at room temperature, due to their minimal SOC and relatively small $T_1 \rightarrow S_0$ energy gaps and that the PLQE of molecules generally decreases with decreasing band gap.

2.5 Energy and Electron Transfer

We have seen that once an exciton is created on a molecule, there are a multitude of processes that can occur intramolecularly. However, a key factor enabling the application of organic materials in optoelectronic devices is the interactions of the exciton with nearby molecules. Such intermolecular interactions can include energy transfer, where a donor (D) molecule in its excited state may transfer energy to an acceptor (A) molecule, or electron transfer, where an electron is transferred from an electron D to an electron A. For energy transfer, there are 2 distinct types which we will now explore: Förster resonance energy transfer (FRET) and Dexter energy transfer.

2.5.1 Förster Resonance Energy Transfer

FRET is a dipole-dipole interaction between chromophores where energy is transferred by the emission and absorption of a virtual photon by the D and A, respectively. The rate of FRET (k_{FRET}) is defined as:[27]

$$k_{FRET} = \frac{1}{\tau}\left(\frac{R_0}{r}\right)^6 \tag{2.73}$$

Where τ is the donor exciton lifetime, r is the intermolecular separation and R_0 is the intermolecular separation at which the rate of FRET is equal to the sum of all the other rates for the decay of the donor exciton, that is the distance at which $\Phi_{FRET} = 50\%$. R_0 can be further defined as:

$$R_0^6 = \frac{9\Phi_{PL}\kappa^2}{128\pi^5 n^4} J \tag{2.74}$$

Where Φ_{PL} is the PLQE of the donor, κ is the dipole orientation factor, J is the overlap of the D emission and A absorption spectra and n is the refractive index at the wavelength where J is maximised. J is given by:

$$J = \int_0^\infty \lambda^4 F_d(\lambda)\varepsilon_A(\lambda)d\lambda \tag{2.75}$$

Here, λ is the wavelength, F_D is the normalised emission spectrum of the donor and ε_A is the extinction coefficient of the acceptor. As it does not rely on the direct exchange of electrons, no D-A wavefunction overlap is required. Therefore, FRET can occur over ranges of up to 10 nm, compared to <1 nm for Dexter energy transfer. A critical point is that FRET is dependent on the oscillator strengths of the donor emission and acceptor absorption transitions and so, FRET is not a suitable mechanism for energy transfer involving triplet excitons.

2.5.2 Dexter Energy Transfer

As previously mentioned, Dexter energy transfer involves the direct exchange of electrons between the D and A, requiring D-A wavefunction overlap. As a consequence, Dexter energy transfer is efficient at distances of 1 nm or less. The rate of Dexter energy transfer (k_D) is defined as:[28]

$$k_D = KJe^{\left(\frac{-2r}{L}\right)} \tag{2.76}$$

Where K is a factor related to the orbital interaction, J is the normalised spectral overlap integral, r is the intermolecular separation and L is the van der Waals radius of the molecule. Importantly, the rate of Dexter energy transfer does not depend on the extinction coefficient of the A. Therefore, it can mediate energy transfer between states with very low oscillator strength, such as triplets.

2.5.3 Electron Transfer

The transfer of electrons between organic molecules is an extremely important process that underpins the functionality of these materials in many optoelectronic applications. Marcus theory for electron transfer was originally developed for interacting ions in solution,[29] but can also be used to describe charge transfer in organic D-A blends.[30,31] The Marcus equation for the rate of an electron transfer process (k_{et}) is defined as:

$$k_{et} = \frac{2\pi}{\hbar}|H_{DA}|^2 \frac{1}{\sqrt{4\pi\lambda k_B T}} e^{\left(-\frac{(\lambda+\Delta G^o)^2}{4\lambda k_B T}\right)} \tag{2.77}$$

Where H_{DA} is the electronic coupling matrix element between the donor and acceptor, ΔG^o is the Gibbs free energy of the electron transfer (the driving force), λ is the reorganisation energy and T is the temperature. The reorganisation energy can be thought of as the energy required to reorganise the "reactant" donor and acceptor nuclear geometries for the electron transfer, as well as accounting for the polarization changes to the surrounding medium to stabilise the "products".[21] This can perhaps be more simply visualised on a PES in Figure 2.13, where the reactants are given by the neutral D + A, and the products by the charged D^+ + A^-. The interplay between ΔG^o and λ is of great importance in determining the overall rate for the electron transfer. This can be shown mathematically in the following equation for the activation energy ($\Delta G^\ddagger$) of the electron transfer step:

$$\Delta G^\ddagger = \frac{(\lambda + \Delta G^o)^2}{4\lambda} \tag{2.78}$$

When $\Delta G^o < -\lambda$, this is the Marcus normal region, where increasing ΔG^o towards λ increases the rate of the electron transfer by decreasing the activation energy. When $\Delta G^o = -\lambda$, the reaction becomes barrierless, and the rate of electron transfer is at a maximum. However, when $\Delta G^o > -\lambda$, the rate of reaction begins to slow again. This phenomena is known as the Marcus inverted region for electron transfer. Meaning, perhaps counter-intuitively, when the driving energy for the electron transfer becomes very large, its rate actually decreases.

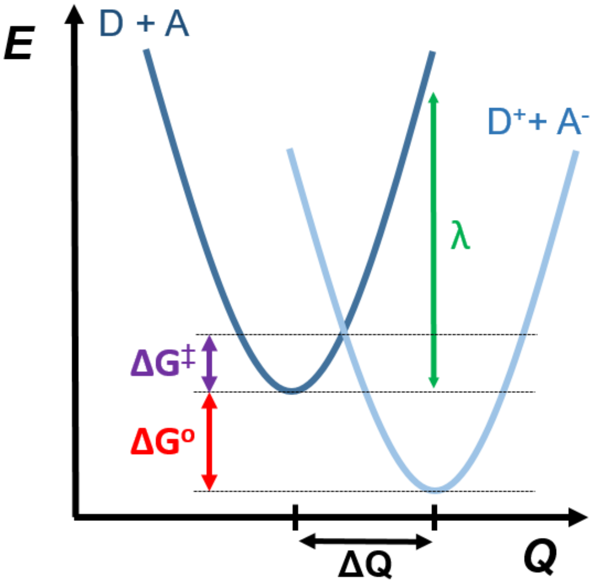

Figure 2.13: *The PESs of the reactant (D + A) and product (D^+ + A^-) states of the electron transfer process. The reorganisation energy (λ) is shown as the energy required to re-arrange the reactant nuclear co-ordinates to match that of the products (ΔQ). The free energy of the reaction (ΔG^o) is defined as the energy difference between the equilibrium conformations of the reactant and product states.*

2.6 Organic Photovoltaics

2.6.1 Operating Principles

OPV devices are solar cells constructed from organic semiconductor materials. The light absorbing later is typically comprised of a nanostructured blend of electron donating and electron accepting materials. Traditionally, a polymer is used as the electron donor and a fullerene derivative as the electron acceptor,[2] though there has been significant recent success through the use of non-fullerene acceptors (NFAs).[32] As previously discussed, organic materials inherently possess a large excitonic binding energy, often on the order of hundreds of meV.[33] In the absence of a D/A interface to enable exciton separation, the absorption of a photon by an organic semiconductor will almost always result in the rapid (sub-ns) recombination of an electron and hole pair generated on one molecule. Consequently, 2 (or more) organic semiconductors are used together, with an energetic offset between the LUMOs for D → A electron transfer, as well as the HOMOs for A → D hole transfer used to drive exciton separation into free electron and holes.[34] These free charges can then be transported through the thin film and then collected at the metallic contacts as electrical current.[35] By breaking down the photovoltaic external quantum efficiency (EQE_{PV}), an important performance metric of an OPV device, we can gain a deeper understanding about how they operate. The EQE_{PV} of an OPV device at a particular wavelength is defined as:

$$EQE_{PV}(\lambda) = \frac{Number\ of\ charge\ carrier\ pairs\ extracted}{Number\ of\ incident\ photons} \tag{2.79}$$

The EQE_{PV} can therefore be defined as the product of 4 efficiencies:[36]

$$EQE_{PV}(\lambda) = \eta_A(\lambda)\,\eta_{ED}(\lambda)\,\eta_{CS}(\lambda)\,\eta_{CC} \tag{2.80}$$

Where η_A is the quantum efficiency (QE) of photon absorption, η_{ED} is the QE of exciton diffusion, η_{CS} is the QE of charge separation and η_{CC} is the QE of charge collection. These processes are represented pictorially in Figure 2.14 for clarity. It is important to remember that this diagram is merely a schematic and may not provide the most accurate picture of the nuanced processes occurring during device operation. For example, it doesn't consider that the acceptor may also contribute to photocurrent generation, nor the effect of morphology, such as the presence of pure and mixed domains,[37] on η_{ED}, η_{CS} and η_{CC}. These metrics can be further defined:

$$\eta_A = \frac{Number\ of\ photogenerated\ excitons}{Number\ of\ incident\ photons} \tag{2.81}$$

$$\eta_{ED} = \frac{Number\ of\ excitons\ reaching\ D/A\ interface}{Number\ of\ photogenerated\ excitons} \tag{2.82}$$

$$\eta_{CS} = \frac{Number\ of\ free\ charges\ generated}{Number\ of\ excitons\ reaching\ D/A\ interface} \tag{2.83}$$

$$\eta_{CC} = \frac{Number\ of\ charge\ carrier\ pairs\ extracted}{Number\ of\ free\ charges\ generated} \tag{2.84}$$

Now that we have defined the key processes occurring in an OPV device for photocurrent extraction, we will discuss each of these parameters in more depth.

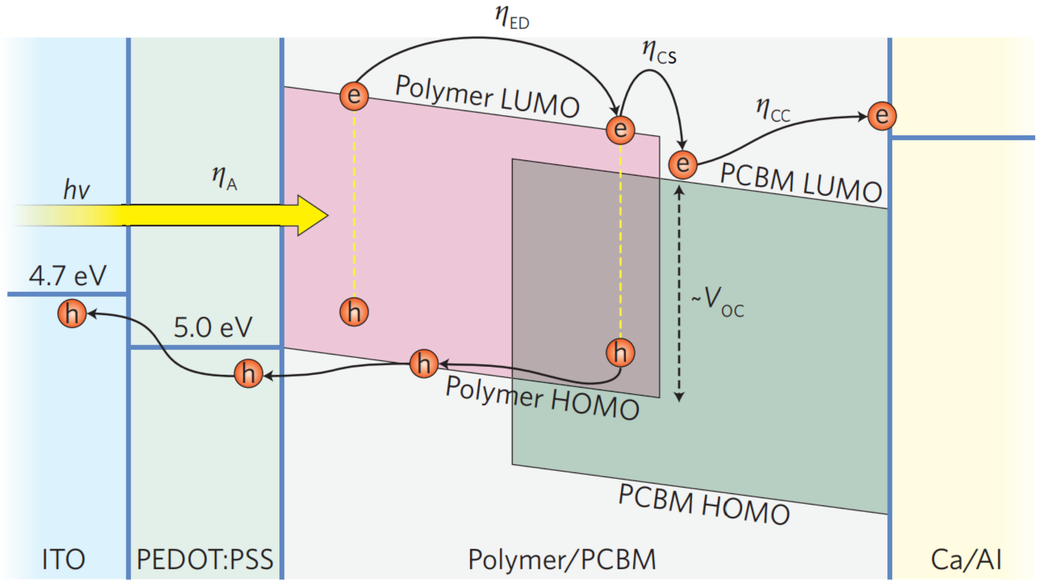

Figure 2.14: *The processes leading to the successful conversion of a photon into an electron in an OPV device. This includes photon absorption (η_A) to generate an exciton, exciton diffusion (η_{ED}) to a charge separating interface, charge separation (η_{CS}) of the exciton into free electron and holes and finally collection (η_{CC}) of the free charge carriers as photocurrent. Figure taken from reference 35.*

The QE of light absorption depends on 2 critical parameters: the oscillator strength of the material and the thickness of the light-absorbing layer. The organic materials used in OPV applications are typically selected for their high oscillator strengths and consequently large absorption coefficients (~10^5 cm^{-1}), meaning only a relatively thin layer (~100 – 300 nm) of an organic material is required for good light absorption. Also important to consider is the band gap of the light absorbing material. To generate the maximum amount of photocurrent, we want to be able to absorb as many photons as possible. The solar radiation available at the Earth's surface is visualised in Figure 2.15, where the standard solar radiation spectrum for an absolute air mass of 1.5 at a global 37^o south-facing tilt (AM1.5G) is shown. Therefore, one might naively assume that by making the band gap of the materials as small as possible, that the maximum power conversion efficiency (PCE) would be achieved. However, this is not the case as hot carriers generated from photons above the band gap will quickly thermalize to the band edge, with the excess energy being lost as heat. Therefore, the band gap of the material essentially limits the maximum voltage obtainable from the device, reducing the maximum PCE obtainable. From the work of William Shockley and Hans J. Queisser, the maximum

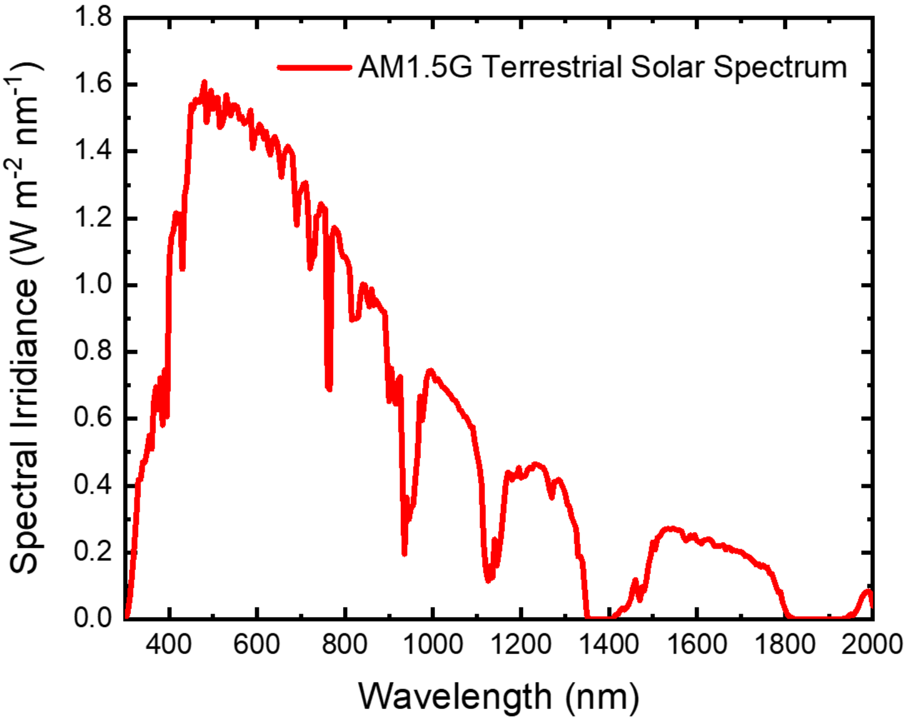

***Figure 2.15**: The AM1.5G standard solar radiation spectrum for an absolute air mass of 1.5 at a global 37^o south-facing tilt.*

obtainable PCE for a single junction device was found to be 33.7%, corresponding to a band gap of 1.34 eV.[5,6]

For the QE of exciton diffusion, we must consider how far a photo-generated exciton can travel to a charge separating interface before it ultimately recombines. Upon the absorption of a photon, a singlet exciton is initially generated. Singlet exciton transport typically occurs by FRET between neighbouring molecules: excitons travel from higher energy sites to local energy minima, where they trap. This leads to an exciton diffusion length of the order ~5 – 15 nm, controlled by local energetic disorder.[38] Therefore, to maximise the QE of this process, all excitons should be generated within roughly ~10 nm of an interface. In the case of a simple D/A bilayer structure, this would imply that a total thickness for the light absorbing layer of 20 nm would be required for optimal exciton transport to the D/A interface. This however is not enough for effective light absorption and would severely limit η_A. Therefore, in order to allow for light absorbing layers of >100 nm with a high η_{ED}, a bulk heterojunction (BHJ) structure is employed instead.[39] A BHJ consists of a layer of randomly mixed D and A, where through careful optimisation, the D and A domain size is on the order of the exciton diffusion length. Careful control of the morphology of the active layer is therefore crucial to maximising the ability of excitons to reach the heterojunction interface.

When considering the QE of charge separation, we must discuss first the initial charge transfer process. Here, for electron transfer, an electron hops from the LUMO of the D to the lower energy LUMO of the A, creating an intermolecular charge transfer (CT) state that is coulombically bound at the D/A interface. Note that the same following theory applies for the hole transfer process from the A HOMO to the higher energy D HOMO. In order for this CT state to separate into free charge carriers, it must overcome its binding energy and achieve an electron-hole separation greater than the coulomb capture radius (equation 2.32). Otherwise the CT will eventually decay without separating, known as geminate recombination. The process through which the bound CT dissociates into free charge carriers is described through Onsager-Braun theory.[40] Here, the CT may undergo multiple separation attempts during its lifetime, with only successful attempts resulting in complete charge separation. A key parameter in determining the mechanism by which the CT dissociates is the driving energy for the charge separation, defined as the different in energy between the singlet exciton of the donor and the energy of the CT state ($E_{CT} \sim E_{D,HOMO} - E_{A,LUMO}$). When considering efficient polymer-fullerene systems with a large driving energy (>300 meV), it has been demonstrated that charge separation occurs rapidly (<100 fs) through delocalised band-like states in fullerene aggregates.[41] However, it is desirable to perform charge separation with the minimum energy loss possible so as to reduce the voltage loss of the device. Subsequently there have been reports of efficient charge separation with a very small (<100 meV) driving energy in both polymer-fullerene[42,43] and polymer-NFA systems.[44] In this case, charge separation proceeds more slowly (>1 ps) and likely relies on the entropy gain from the increasing number of ways for the charge carriers to be arranged at larger separations to overcome the coulombic binding energy.[45,46] It has also been suggested that ordering at the interface is critical, as this reduces the probability of the CT state localising in a low energy trap state before charge separation can occur.[42]

Finally, the QE of carrier collection depends on the ability of the now-separated charge carriers to diffuse to the respective collecting electrodes. For this, the morphology of the BHJ is critical, as needs to provide continuous charge percolation pathways to the electrodes, otherwise the charge carriers will not be able to escape the active layer and will ultimately recombine.[47] Even if the prerequisite charge percolation pathways are present, charge recombination between separated charge carriers, termed non-geminate recombination, may still take place if the charges come within their coulomb capture radius. In this case, reformation of the CT will occur, with 3:1 ratio of spin-triplet CTs (^{3}CT) to spin-singlet CTs (^{1}CT) being formed due to spin statistics.[13] The thermalized CT states can either re-dissociate, or recombine back to the ground state in a mostly non-radiative fashion, reducing η_{CC}. A critical point that will be revisited later in this thesis is that if there is a local triplet state present on either the D or A that is lower in energy than the ^{3}CT, this may be formed by back electron transfer from $^3CT \rightarrow T_1$. This low energy T_1 acts as a terminal non-radiative recombination pathway, as ^{3}CTs that transfer to it are energetically trapped and cannot escape.[13]

2.6.2 OPV Device Characterisation

The power conversion efficiency (PCE) of a solar cell is the primary performance metric by which it is judged. The PCE is defined in terms of the open-circuit voltage (V_{OC}), the short circuit current density (J_{SC}) and fill-factor (FF):

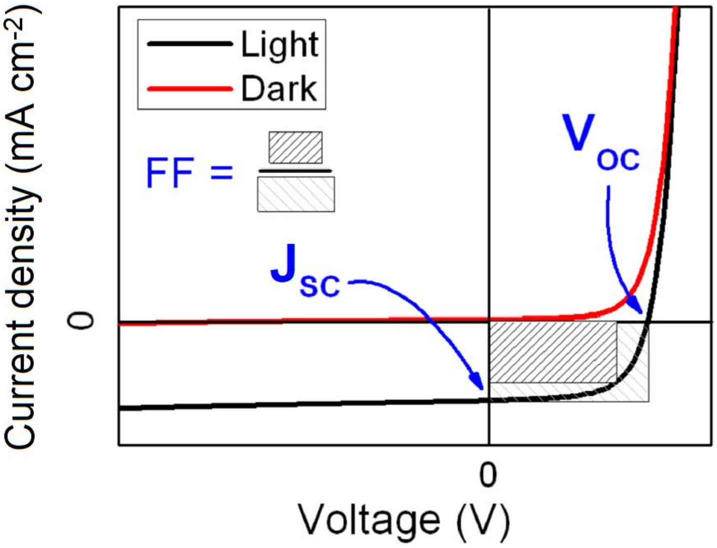

***Figure 2.16**: An example J-V curve for a solar cell device. Shown are the V_{OC} (the voltage at which the curve crosses J=0), the J_{SC} (the current density at which the curve intersects V=0) and the FF (the "square-ness" of the J-V curve). Figure credit: Dr Alex Marsh.*

$$PCE = \frac{V_{OC} J_{SC}\ FF}{P_{in}} \tag{2.85}$$

Where $P_{in} = 100$ mW/cm^2 under AM1.5G solar illumination. The FF can be further defined as the ratio of the product of the voltage (V_{max}) and current density (J_{max}) at the maximum power point of the solar cell divided by the product of the V_{OC} and J_{SC}:

$$FF = \frac{V_{max} J_{max}}{V_{OC} J_{SC}} \tag{2.86}$$

All of the above information is often represented visually in the form of the current density-voltage curve (J-V curve) of the solar cell, shown in Figure 2.16. From this, it is clear that a useful alternative way to think of the FF is as the "square-ness" of the J-V curve.

The EQE_{PV} of a solar cell (equation 2.79) is also an important performance metric and is often given alongside the J-V curve of an OPV device. It can be related to the J_{SC} by integrating under the curve of an absolute EQE_{PV}-wavelength plot:

$$J_{SC} = -q\int_{\lambda_1}^{\lambda_2} EQE_{PV}(\lambda)SS_{AM.15G}(\lambda)d\lambda \tag{2.87}$$

Where q is the elementary charge and $SS_{AM15.G}$ is flux of the AM1.5G solar spectrum. Finally, it is useful to define the internal quantum efficiency ($\mathrm{IQE_{PV}}$):

$$IQE_{PV} = \frac{EQE_{PV}}{1-R} \tag{2.88}$$

Where R is the fraction of light reflected off the device. Therefore, the $\mathrm{IQE_{PV}}$ is a measure of the efficiency of the conversion of absorbed photons only into photocurrent and is perhaps a more useful metric for the performance of solar cells that do not absorb light strongly.

2.6.3 Energy Loss in OPV

A significant focus of this thesis will be on strategies to minimise the energy loss in OPV devices, so it is prudent to take some time to discuss its origins. The total energy loss of a solar cell (ΔV_{total}) is defined as the difference between the band-gap of the lowest energy absorber (E_g) and the energy of the extracted charges (eV_{OC}):

$$\Delta V_{total} = E_g - eV_{OC} \tag{2.89}$$

For OPV devices, the total energy loss is typically 0.7 – 1.0 V,[48] though there are some recent reports of systems with $\Delta V_{total} \approx 0.5$ V.[49,50] This is much larger than other competing photovoltaic technologies, such as perovskites, where $\Delta V_{total} \approx 0.4$ V or less.[51] The total energy loss can be further broken down into energy loss incurred from charge generation ($\Delta V_{generation}$) and charge recombination ($\Delta V_{recombination}$):

$$\Delta V_{total} = \Delta V_{generation} + \Delta V_{recombination} \tag{2.90}$$

$$\Delta V_{generation} = E_g - E_{CT} \tag{2.91}$$

$$\Delta V_{recombination} = E_{CT} - eV_{OC} \tag{2.92}$$

Where (E_{CT}) is the energy of the CT state. It has been demonstrated that it is possible to fabricate efficient OPV devices with a very low $\Delta V_{generation}$ of <100 meV,[42,44] so we turn our attention to recombination voltage losses. $\Delta V_{recombination}$ can be further separated into radiative (ΔV_r) and non-radiative (ΔV_{nr}) recombination contributions:

$$\Delta V_{recombination} = \Delta V_r - \Delta V_{nr} \tag{2.93}$$

All solar cells must lose some voltage to radiative recombination,[48,52] which is typically on the order of ~200 – 300 meV.[5] However, all energy loss due to non-radiative recombination is superfluous and should be avoided. The amount of non-radiative voltage loss in a solar cell can be conveniently be related to the electroluminescence external quantum efficiency ($\mathrm{EQE_{EL}}$) of the device run at forward bias:[48]

$$\Delta V_{nr} = -\frac{k_B T}{q}\ln(EQE_{EL}) \tag{2.94}$$

Non-radiative recombination can take many forms. It can be either geminate or non-geminate recombination and can be mediated through the formation of local triplet states,[13] by low-energy traps (consisting of structural defects) and Auger recombination.[48] The previously discussed energy gap law may also increase the rate of non-radiative recombination for lower band gap systems with a correspondingly lower $\mathrm{E_{CT}}$,[53] frustrating efforts to fabricate OPV devices that harvest more of the solar spectrum into the NIR region.

Given the pertinence of local triplet formation and its effect on energy loss to this thesis, we shall now discuss this process in more detail. After the dissociation of the CT states formed between the D and A that is a prerequisite for charge generation in OPVs, the free change carriers now percolate throughout the film. If these now spin-uncorrelated carriers come within their respective coulomb capture radii, they will reform the bound CT state. Due to spin statistics, the ratio of spin-triplet CT (^{3}CT) to spin-singlet (^{1}CT) states formed will be roughly 3:1.[13] If there is a molecular triplet state on either the donor or the acceptor that is lower in energy than the ^{3}CT, then the transfer of the ^{3}CT to the local triplet via a back electron transfer is spin-allowed and may occur. This will form a low energy triplet state that cannot re-dissociate and will ultimately decay non-radiatively, often via triplet-charge annihilation processes that can significantly reduce the device performance and introduce superfluous energy loss into the system.[13,54,55] This process is summarised in Figure 2.17. In addition to the formation of ^{3}CT states through non-geminate recombination, work by Dimitrov *et al.* has suggested that triplet excitons may also be formed through the rapid ~1 ns spin-mixing of ^{1}CT states formed by the initial charge transfer process that do not fully dissociate into free charges, known as bound polaron pairs.[56] However, Benduhn *et al.* have recently proposed that triplet exciton formation may not substantially affect non-radiative voltage losses.[57] In this work, they examine the non-radiative voltage loss of a selection of OPV devices where the energy of the donor triplet and CT states are known. Through this analysis, they find that the magnitude of the non-radiative voltage loss is similar for some devices with a comparable CT state energy, irrespective of whether the donor triplet state is lower in energy than the CT or not. Whilst an interesting observation, they only take into account fullerene acceptors and the vast majority of systems analysed have PCEs <3%, with the highest being 7.3%. As a result, their findings may not be representative of state-of-the-art NFA OPVs, which now routinely achieve PCEs well in excess of 14%.[9,32,58–60] Indeed, previous investigations have suggested that it is actually the relative positioning of the CT to the fullerene triplet, not the donor triplet, which controls whether triplet excitons are formed.[61]

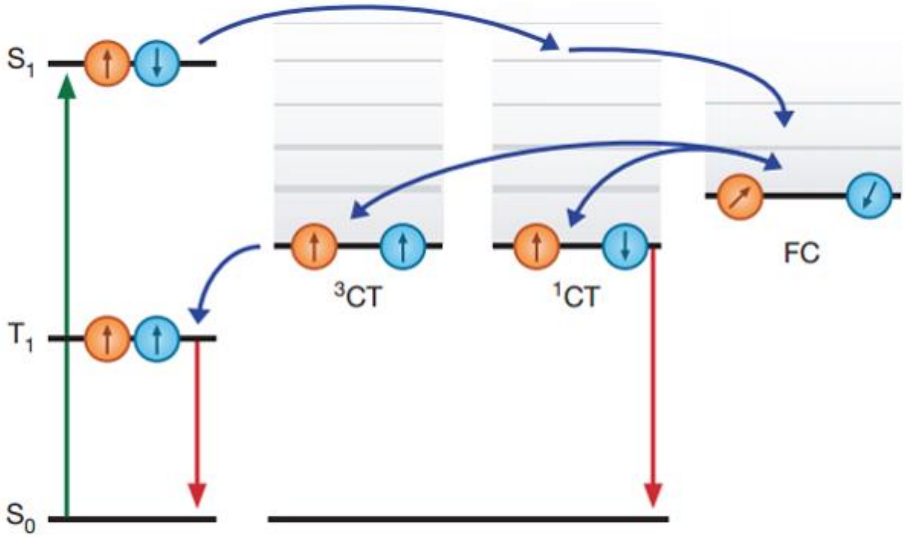

Figure 2.17*: A schematic demonstrating the pathway to the formation of low energy local triplet states. First, the singlet excited state is separated into free charges via the ^{1}CT intermediate. If these spin-uncorrelated free charge carriers come within their coulomb capture radius, they will interact and become bound CT states again. By spin-statistics, the ratio of ^{3}CT to ^{1}CT formed will be 3:1. These ^{3}CT states may then transfer to a lower energy molecular triplet state on either the donor or the acceptor, where they become energetically trapped. Once the triplet state has been formed, it cannot re-separate as it is too low in energy and will ultimately decay back to the ground state non-radiatively, increasing the energy loss of the system. Figure adapted from reference 12.*

2.7 Organic Light Emitting Diodes

2.7.1 Operating Principles

The role of OLEDs is to turn injected charge carriers into photons, and thus can be considered to be performing to opposite function of the previously discussed OPV devices. A typical OLED device stack consists of many components layered on top of each other, including hole (HIL) and electron (EIL) injection layers, hole (HTL) and electron (ETL) transport layers and the emissive layer (EML).[62] The HIL, HTL, EIL and ETL are present to ensure the efficient injection and transport of holes and electrons from the electrodes, as well as the blocking of the opposite charge carrier to ensure all charges are trapped inside of the EML. The EML itself typically consists of a highly emissive material (guest) doped into a wide band-gap material (host) at low weight percentages (typically <10 wt %). This doping ensures the guest molecules are well dispersed from each other, minimising any self-quenching effects that could reduce their emissive efficiency.[63] In the EML, the electrons and holes come within their coulomb capture radius and form an exciton, in this case aided by the small dielectric constants of organic materials. Once this exciton is formed on the guest material, it will then recombine, and if this recombination is radiative, emit a photon. This process, as well as a typical device stack, is imaged in Figure 2.18.[62]

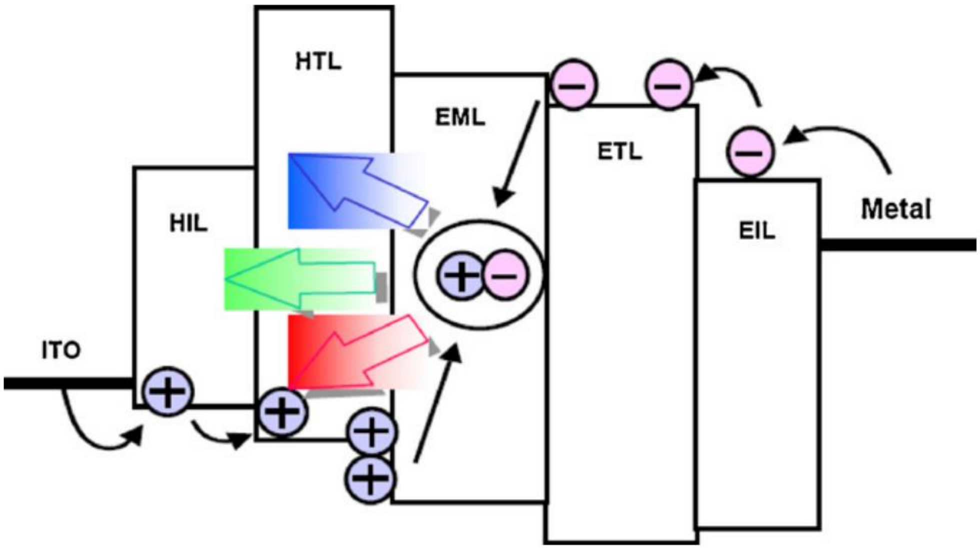

***Figure 2.18**: A typical OLED device stack. The HIL, HTL, EIL and ETL ensure efficient charge carrier injection and transport though the device from the electrodes. Upon reaching the EML, the charge carriers are trapped inside of this layer by high LUMO and deep HOMO of the HTL and ETL respectively, ultimately forming an exciton and recombining. Figure taken from reference 59.*

To enhance our understanding, we can define the EQE_{EL} (and IQE_{EL}) of an OLED device and further break it down into the individual processes:

$$EQE_{EL} = \frac{Number\ of\ photons\ emitted\ from\ device}{Number\ of\ charge\ carrier\ pairs\ injected} \tag{2.95}$$

$$EQE_{EL} = \gamma\ \Phi_{PL}\ \chi\ \eta_{out} \tag{2.96}$$

$$IQE_{EL} = \gamma\ \Phi_{PL}\ \chi \tag{2.97}$$

Where γ is the charge balance factor (the ratio of electrons to holes in the device), Φ_{PL} is the PLQE of the guest, χ is the fraction of excitons formed that can result in radiative transitions and η_{out} is the photon out-coupling efficiency.[64] γ is typically almost equal to 1 and requires a good balance between the electron and hole injection efficiency into the organic layers to maximise this metric. As expected, a high PLQE is a prerequisite for a guest material in an OLED device in order to ensure a large fraction of generated excitons decay radiatively. For materials that cannot utilise triplet excitons and can only decay radiatively by fluorescence from singlet excitons, $\chi = 0.25$ as a 1:3 ratio of singlets to triplets are formed by the recombination of spin-uncorrelated electrons and holes.[13] Finally, η_{out} is limited by wave guiding in the device layers and the substrate and is given by:[65]

$$\eta_{out} \approx \frac{1}{2n^2} \tag{2.98}$$

For a glass substrate with a refractive index of $n \sim 1.5$, η_{out} is typical equal to ~ 0.2. Taking $\gamma = 1$, $\Phi_{PL} = 1$, $\chi = 0.25$ and $\eta_{out} = 0.2$, we can see that the maximum obtainable IQE_{EL} and EQE_{EL} for a fluorescent OLED device that can only make use of singlet excitons is 25% and 5% respectively.[66] Therefore, in order to improve the efficiency of OLED devices, we require tactics to make use of the previously non-emissive triplet excitons to increase χ.

Currently, 3 major tactics exist to utilise triplet excitons in OLED devices: phosphorescence, triplet-triplet annihilation (TTA) and thermally activated delayed fluorescence (TADF). Phosphorescent OLEDs make use of emitters that contain a heavy metal atom with a large Z, such as iridium. This massively enhances the magnitude of the SOC in the molecule (equation 2.42) and allows for very efficient phosphorescence from the triplet excitons formed by charge recombination. Consequently $\chi = 1$ as now all excitons formed have the potential to decay radiatively and values for $\mathrm{IQE_{EL}}$ can approach 100%.[67] TTA involves the conversion of 2 triplet states located on nearby molecules into one excited singlet and one ground state singlet: $T_1 + T_1 \rightarrow S_1 + S_0$.[68] This can allow for values up to $\chi = 0.625$ in ideal cases: 0.25 contribution from the singlets + 0.75 x 0.5 from triplets.[69] TADF is the most recently discovered mechanism for utilising triplet excitons of the 3 and will now be discussed in greater detail due to its relevance to this thesis.

2.7.2 Thermally Activated Delayed Fluorescence

The breakthrough for TADF came with the seminal 2012 work of Adachi and co-workers, who reported efficient OLED devices based off their prototype TADF emitters.[70] In this class of molecules, χ is maximised through their ability to convert the 75% of otherwise non-emissive triplet excitons back into emissive singlet excitons through a process called reverse intersystem crossing (rISC). Archetypal TADF materials have a very small ΔE_{ST} (typically <100 meV), which is achieved primarily by designing D/A-type molecules that possess excited states with strong intramolecular charge transfer (ICT) character, induced by the decoupling of the FMOs through torsion around the D-A bridge. This D-A torsion effectively modulates the FMO overlap, with overlaps decreasing as the D-A torsional angle approaches 90°, i.e. the D and A are orthogonal, corresponding to a pure ICT state. It is at this point that ΔE_{ST} approaches 0. The rational for this can be seen in equation 2.38, where J is reduced through minimising the overlap integral of the HOMO and LUMO. However, care must be taken to balance the minimisation of J with the need for a non-zero matrix element for the FMO electronic wavefunctions as per Fermi's Golden Rule, otherwise the emission rate will be vanishingly low. Originally, it was thought that the small ΔE_{ST} both allowed for the efficient thermal up-conversion of triplet excitons to singlets, as well as for sufficient mixing between the singlet and triplet states for efficient spin-interconversion (equation 2.58).[70]

However, it has recently been proposed that due to the similarities in the spatial orbital occupation between the singlet ICT (^{1}ICT) and triplet ICT (^{3}ICT) wavefunctions ($^1\Psi_{ICT}^0$ and

${}^3\Psi^0_{ICT}$ respectively), SOC between them is formally forbidden according to El-Sayed's rule, which forbids (r)ISC between electronic states of a similar nature:[71,72]

$$\langle {}^1\Psi^0_{ICT} | \hat{H}_{SO} | {}^3\Psi^0_{ICT} \rangle = 0 \tag{2.99}$$

This is because any change in the spin angular momentum of the electron cannot be compensated for by a change in the orbital angular momentum (equation 2.39).[73] In light of the large rISC rates (k_{rISC}) reported of $k_{rISC} \approx 10^7$ s^{-1},[74] it is unlikely that direct rISC from the pure ^{3}ICT to ^{1}ICT occurs, driven by the SOC between these states. Therefore, it has since been proposed that local triplet excited states (^{3}LE) located on either the D or A may be involved, due to its different spatial orbital distribution to the ICT states. Perhaps the most compelling explanation for the large k_{rISC} reported in TADF materials is the spin-vibronic coupling mechanism, where the ^{3}ICT is mixed with the ^{3}LE through non-adiabatic coupling outside of the B-O approximation.[75] This mixing can be described, like SOC before it, through perturbation theory:

$$|{}^3\Psi'_{ICT}\rangle = |{}^3\Psi^0_{ICT}\rangle + \frac{\langle {}^3\Psi^0_{LE} | \hat{H}_{vib} | {}^3\Psi^0_{ICT} \rangle}{E({}^3ICT) - E({}^3LE)} |{}^3\Psi^0_{LE}\rangle \tag{2.100}$$

Where $|{}^3\Psi'_{ICT}\rangle$ is the wavefunction of the ^{3}ICT-^{3}LE admixture, $|{}^3\Psi^0_{LE}\rangle$ is the wavefunction of the ^{3}LE state, $\hat{H}_{vib}$ is the perturbing spin-vibronic coupling Hamiltonian, $E({}^3ICT)$ is the energy of the ^{3}ICT state and $E({}^3LE)$ is the energy of the ^{3}LE state. Taking an expression for the rate of rISC between the ^{3}ICT-^{3}LE admixture and ^{1}ICT based upon Fermi's Golden Rule, we obtain:

$$k_{rISC} = \frac{2\pi}{\hbar} \langle {}^1\Psi^0_{ICT} | \hat{H}_{SO} | {}^3\Psi'_{ICT} \rangle^2 p \tag{2.101}$$

Which without vibronic coupling, would have a rate of 0 due to the forbidden SOC between the ^{1}ICT and ^{3}ICT. Substituting in our expression for the ^{3}ICT-^{3}LE admixture, $|{}^3\Psi'_{ICT}\rangle$ (equation 2.100), we now obtain:

$$k_{rISC} = \frac{2\pi}{\hbar}\left|\langle {}^{1}\Psi^{0}_{ICT}\middle|\hat{H}_{SO}\middle|{}^{3}\Psi^{0}_{ICT}\rangle + \frac{\langle {}^{1}\Psi^{0}_{ICT}\middle|\hat{H}_{SO}\middle|{}^{3}\Psi^{0}_{LE}\rangle\langle {}^{3}\Psi^{0}_{LE}\middle|\hat{H}_{vib}\middle|{}^{3}\Psi^{0}_{ICT}\rangle}{E({}^{3}ICT) - E({}^{3}LE)}\right|^{2} p \qquad (2.102)$$

Given that $\langle {}^{1}\Psi^{0}_{ICT}\middle|\hat{H}_{SO}\middle|{}^{3}\Psi^{0}_{ICT}\rangle = 0$ from equation 2.99, this term can be removed, leaving us with our final expression:[72]

$$k_{rISC} = \frac{2\pi}{\hbar}\left|\frac{\langle {}^{1}\Psi^{0}_{ICT}\middle|\hat{H}_{SO}\middle|{}^{3}\Psi^{0}_{LE}\rangle\langle {}^{3}\Psi^{0}_{LE}\middle|\hat{H}_{vib}\middle|{}^{3}\Psi^{0}_{ICT}\rangle}{E({}^{3}ICT) - E({}^{3}LE)}\right|^{2} p \qquad (2.103)$$

Therefore, the effect of mixing the ^{3}ICT and ^{3}LE through vibronic coupling is to give an appreciable SOC matrix element for the rISC transition, which is able to account for the relatively rapid rISC seen in TADFs.

Given the finding that vibronic coupling plays a significant part in allowing TADFs to achieve efficient rISC, much effort has been dedicated to exploring the nature of the vibrations that couple the states involved. The vibrational modes that can be reasonably thermally activated at room temperature are low frequency modes (<500 cm^{-1}),[75] largely consisting of torsion around the D/A bridge. By exploring the conformational space around the molecules equilibrium structure through these vibrations, one can access conformations with differing amounts of ^{3}LE admixture into the ^{3}ICT wavefunction (and of singlet local excitons (^{1}LE) admixtures into ^{1}ICT, but this mixing is significantly smaller).[76] We also note that the maximum mixing and therefore largest SOC will correspond to the crossing points in the adiabatic PES for the ^{3}ICT and ^{3}LE where these states are degenerate, as per equation 2.102.[75] Important to note is that the magnitude of the ^{3}ICT-^{3}LE mixing scales with decreasing D-A torsional angles, corresponding to a less ICT-like excited state.[76] However, as previously discussed, ΔE_{ST} also varies with conformation, with the minimum case of $\Delta E_{ST} = 0$ occurring when the FMOs are completely decoupled (i.e. increased D-A torsional angles). Therefore, these effects oppose each other: ΔE_{ST} is minimised when the ^{1}ICT and ^{3}ICT have mostly ICT character (large dihedral angles), but the SOC is maximised with increased LE contributions to the wavefunctions (small dihedral angles). Thus, a dynamic picture with the magnitude of the SOC and ΔE_{ST} fluctuating over the timescales of the coupling vibrations is expected, leading to a vibrationally-gated rISC process.

3 Experimental Methods

3.1 Sample Preparation

In this work, materials were either purchased from suppliers where commercially available, or provided by external collaborators when not. All materials were stored under an inert N_2 atmosphere inside of a glovebox to minimise the risk of degradation. Specifics will be discussed where appropriate in this work, but film sample preparation typically involved the spin coating or drop casting of films from organic solvents onto cleaned fused quartz substrates. The samples were then encapsulated under an N_2 atmosphere using epoxy glue as the sealant and only removed from the inert atmosphere for experimental measurements. For solution measurements, the materials were typically dissolved in toluene before being deposited into 1mm path length quartz cuvettes (Hellma Analystics 110-QS) ready for measurements. When oxygen-free measurements were required, the cuvette was sealed using a suba-seal rubber stopper inside of the N_2 glovebox, which was further wrapped with parafilm and measured as quickly as possible to minimise the risk of oxygen ingression. For measurements which required the oxygen-free environment to be maintained for longer times, a balloon filled with argon that was connected to the cuvette via a syringe. This allowed for a constant positive pressure of an inert gas to replace any N_2 that may have been lost to small leaks.

3.2 Steady-State Absorption

Two techniques were used to measure the steady-state absorption of samples. For measurements on solutions and for those which many orders of magnitude of sensitivity was not required, a HP 8453 spectrometer was used (the detection range spanned 4.3 – 1.1 eV). For these measurements, the absorption spectra was corrected by subtracting a blank background from the measured signal, which either consisted of a cuvette filled with the same neat solvent as the sample for solutions, or an uncoated substrate for films. For measurements that required extreme sensitivity in order to measure band tail states, photothermal deflection spectroscopy (PDS) was employed instead. For PDS measurements, a monochromatic pump light beam is shone on the sample, which upon absorption creates a thermal gradient near the sample surface via non-radiative relaxation induced heating. This results in a refractive index gradient in the area surrounding the sample surface. This refractive index gradient is further enhanced by immersing the sample in an inert liquid FC-72 Fluorinert® (3M Company), which has a high refractive index change per unit change in temperature. A fixed wavelength continuous wave laser probe beam is then passed through this refractive index gradient producing a deflection proportional to the absorbed light at that particular wavelength, which is detected by a photo-diode and lock-in amplifier combination. Scanning through different wavelengths gives the absorption spectra.[77] PDS measurements were performed by Dr Mojtaba Abdi Jalebi and will be accredited where applicable.

3.3 Steady-State Photoluminescence and Photoluminescence Quantum Efficiency

The PLQE was determined using method previously described by De Mello *et al.*.[78] Briefly, samples were placed in an integrating sphere and were photoexcited using a continuous-wave (CW) laser of various wavelengths. The inside of the sphere was coated was a diffusely reflective material, ensuring all light inside of the sphere (both from the laser and PL) are collected by the optical fibre that takes it to the detector. In order to accurately determine the PLQE, 3 measurements are taken: the first directly exciting the sample, the second not hitting the sample directly to account for any PL produced by the indirect absorption of reflections inside sphere and the third on a blank substrate. By comparing the number of photons absorbed by the sample to the number of photons emitted, with the indirect PL subtracted, the PLQE of the sample can be determined with a good degree of accuracy. This measurement also conveniently allows for the measurement of the PL spectrum simultaneously. Depending on the wavelength of the excitation source and PL, the laser and the emission signals were measured and quantified using a calibrated Andor iDus DU420A-BVF Si detector for 400 – 1000 nm and an Andor iDus DU490A-1.7 InGaAs detector for 500 – 1600 nm.

3.4 Transient Photoluminescence

The transient PL (trPL) (2 ns – 1 ms) was measured using an electrically-gated intensified CCD camera (iCCD, Andor iStar DH740 CCI-010) connected to a calibrated grating spectrometer (Andor SR303i). This setup allows for measurement of weak, long-lived PL signals over several orders of magnitude, ideal for monitoring the PL decay of TADF materials. The iCCD consists of a photocathode, a microchannel plate (MCP) and a phosphor screen. In this layout, photons emitted from the sample strikes the photocathode and leads to photoelectron emission. A pulsed electric field, of which the duration and arrival time can be altered by the user to select different temporal regions of the PL, draws this photoelectron towards the MCP. The high potential of the MCP accelerates the electron, leading to the dislodging of secondary electrons from the channel walls and amplification of the signal. These electrons are then converted back into photons by a phosphor layer, where they are read by the CCD. Sample excitation with a 400 nm pump pulse was provided by frequency doubling a small portion of the Ti:sapphire 800 nm output in a BBO crystal. The residual 800 nm was removed from the pulse using a BG39 coloured glass filter. Temporal evolution of the photoluminescence emission was obtained by stepping the iCCD gate delay with respect to the excitation pulse.

3.5 OPV Device Fabrication and Characterisation

Indium tin oxide (ITO) substrates were cleaned by sonicating in acetone and isopropanol for 10 minutes each. These substrates were then cleaned by oxygen plasma treatment before being transferred into an N_2-filled glovebox. Both conventional and inverted architecture devices were fabricated. For the conventional architecture device, the hole transport layer (HTL) consisting 40 nm of poly(3,4-ethylenedioxythiophene) polystyrene sulfonate (PEDOT:PSS, Heraeus Clevios AI 4083) was deposited onto the ITO substrate by spin coating at 3000 rpm, before being thermally annealed on a hotplate for 15 minutes at 120^{o}C. Next, the active layer was fabricated either by spin coating or by thermal evaporation, the specifics of which will be discussed where appropriate. Finally, a thin layer of Ca (5 nm) and the top contact of 100 nm Al was then evaporated through a shadow mask to give a pixel area of 4.5 mm^2. For the inverted architecture device, the same ITO substrates were used. An ETL of zinc oxide (ZnO) was then deposited by first spin coating a solution of zinc acetate dihydrate and ethanolamine dissolved in 2-methoxyethanol (a concentration of 5×10^{-5} moles per mL of each in 2-methoxyethanol) at 3000 rpm. This layer was then heated at 130 ^{o}C for 1 hour to form a ZnO layer of 30 nm thickness. The active layer was then deposited on top of the ZnO layer. Finally, the HTL of MoO_3 (10 nm) was evaporated, before 100 nm of Ag was evaporated through the same shadow mask to give a pixel area of 4.5 mm^2.

An Abet Technology solar simulator was used for J–V characterisation under simulated 100 mW cm^{-2} AM 1.5G illumination, with the lamp power corrected for spectral mismatch. A Keithley 2635 SMU was used to measure the light and dark J-V curves. A 100 W Oriel tungsten lamp with a monochromator (riel Cornerstone 260) was used as the light source for EQE_{PV} measurements. For calibration, a Si photodiode (Thorlabs SM05PD1A) was used. All measurements were carried out under an inert environment. Current density-voltage-luminance characteristics were measured using a Minolta CS-200 luminance meter and a Keithley 2400 source-meter. The EQE_{EL} of the devices were calculated based on the Lambertian emission profile measured. OPV devices were fabricated by Dr Seo-Jin Ko, Patrick Conaghan or Qinying Gu and will be credited where applicable.

3.6 Cyclic Voltammetry

Solution state cyclic voltammetry (CV) was performed using a BioLogic SP-150 potentiostat with ferrocene (Fc) as an internal reference. Measurements were conducted under an Ar atmosphere using a conventional three-electrode cell: a glassy carbon working electrode, a Pt wire auxiliary electrode, and an Ag/Ag^+ quasi-reference electrode. A 0.1 M nBu_4NPF_6 tetrahydrofuran electrolyte was used, with scan rates in the range 25-200 mV s^{-1}. Measurements were performed by Jake Greenfield.

3.7 Transient Absorption Spectroscopy

3.7.1 Principles

Transient absorption (TA) spectroscopy is one of the primary techniques used throughout this work and will therefore be discussed in more depth. TA is an extremely powerful technique that allows the direct probing of all the populated states in a material after photoexcitation, no matter if they are bright or dark (i.e. non-emissive). In TA, an initial pump pulse is used to create short-lived excited state populations with their own unique absorption signatures in the material under study. The evolution of these states is then tracked by a separate probe pulse that is delayed by different time intervals after the pump. By monitoring the change in transmission of the probe between "pump on" and the baseline "pump off" measurements with time, a detailed map of the changes in absorption of the sample with time can be generated and related back to the photophysical processes occurring. Therefore, the signal measured in TA ($\frac{\Delta T}{T}$) is the difference in the transmission of the probe with and without the pump pulse, normalised by transmittance with the pump off to allow for comparison between different experimental conditions:

$$\frac{\Delta T}{T} = \frac{T_{pump\ on} - T_{pump\ off}}{T_{pump\ off}} \tag{3.1}$$

From this, one can naturally see that there will be two distinct categories of signal: those which lead to an increase in the transmittance of the sample, and those which decrease it. Additionally, the magnitude of the signal will be dependent on the absorption cross section σ, given by:

$$\sigma = {}^{\alpha}\!/_{N} \tag{3.2}$$

Where α is the absorption coefficient and N is the atomic number density.

There are three possible origins for signals, which are displayed in Figure 3.1. The first type of signal we will focus on is perhaps the most intuitive: by creating an excited state population with the pump, we have removed molecules from the ground state and therefore the total absorption by the ground state will be decreased. This leads to an increase in transmittance in the sample and a positive signal in the TA, termed a ground state bleach (GSB). The GSB is usually easily identified as it will occupy a similar spectral region to the steady-state absorption spectrum of the molecule and if there are no overlapping bands, a similar spectral shape too. Again assuming there are no overlapping bands, the GSB can be used to track the total excited state population remaining in the sample after excitation by the pump. Additionally, the transmittance of the sample may appear to increase if additional photons appear in the probe after it passes through the sample. This can happen if there is an excited state in the system that is able to radiatively couple to the ground state, typically the initially generated singlet excited state. When this state interacts with a probe photon with the same energy as the transition, it may emit an additional photon through a process known as stimulated emission (SE). Therefore, decay of the SE without a corresponding decay of the GSB is an indication that the emissive state is converting into a new, dark state. The final possible signal is a new absorption feature originating from an excited state, which results in a decrease in the transmittance of the sample. Such a feature is named a photo-induced absorption (PIA) and each excited state will possess a unique set of PIAs, dependent on the absorption cross section of all the possible transitions from the excited state into higher lying states. Through the assignment and tracking of these signals with time, one is able to build up a detailed picture of the photophysics that is not possible through other techniques.

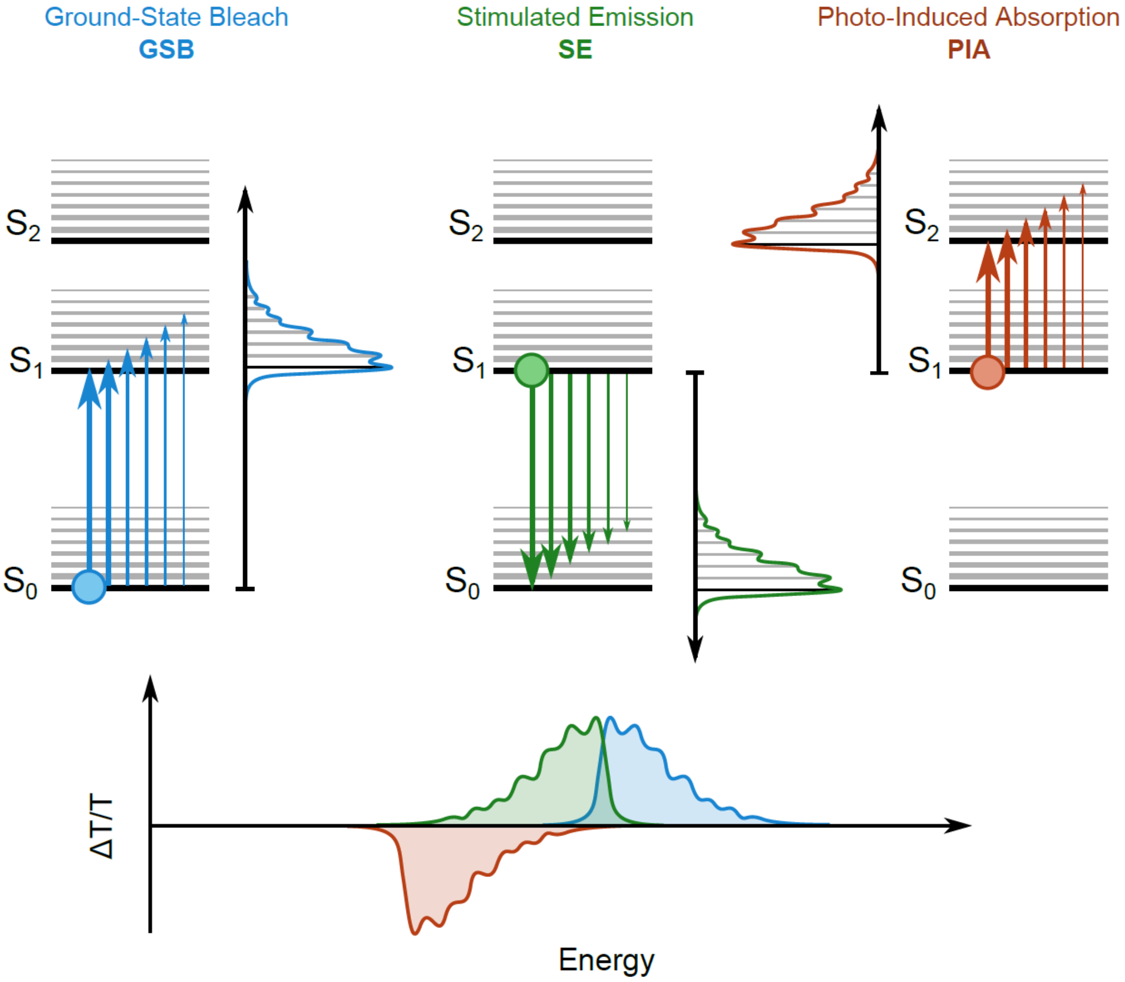

__Figure 3.1__: A diagram illustrating the three possible signals in TA and the optical transitions that create them in Jablonski diagram form: the GSB (blue), SE (green) and PIA (red). The GSB originates from the depletion the number of molecules in the ground state by absorption of the pump, SE is caused by the interaction of a state that can radiatively couple to the ground state with a probe photon and PIAs is as a result of an allowed optical transition into a higher-lying state from an excited state. Figure credit: Dr Simon Gelinas.

3.7.2 Experimental Setups

In this work, all TA data was measured on one of three setups, all with many similarities but some important differences. All of the setups rely on one of four pump sources: a non-collinear parametric amplifier (NOPA), an optical parametric amplifier (TOPAS, Light Conversion) or the the fundamental (or frequency doubled) output of the laser itself for short-time measurements (<100 fs – 2 ns) and an electronically triggered Q-switched Nd:YVO$_4$ laser (Advanced Optical Technologies Ltd AOT-YVO-25QSPX) for long-time (1 ns – 1 ms) measurements. The 1064 nm output of the Nd:YVO$_4$ laser can be frequency doubled or tripled to 532 nm or 355 nm respectively, to give access to visible and UV ns-pulsed pump sources. The probe pulse is provided by either a broadband NOPA or a white light (WL) supercontinuum, generated by focussing a small portion of the laser fundamental into a CaF$_2$ (350 – 750nm) or yttrium aluminium garnet (YAG, 500 – 1400 nm) crystal, depending on the spectral range required.

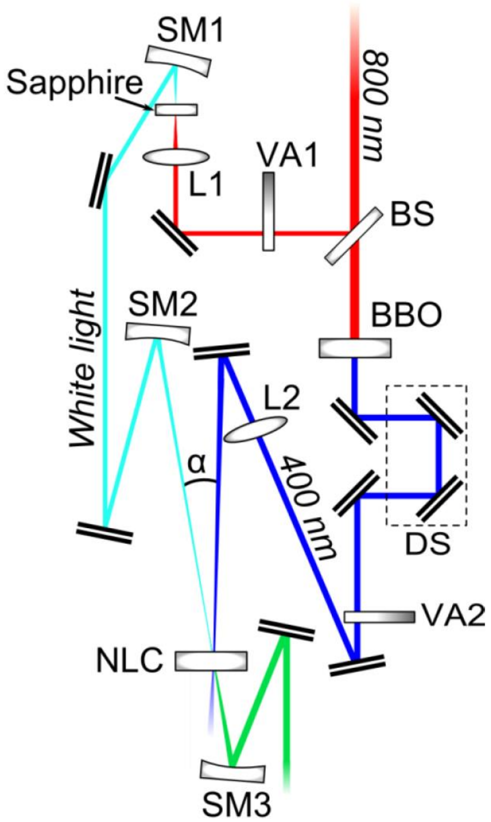

Figure 3.2*: A schematic describing the layout of a NOPA. A portion of the 800 nm laser fundamental is split into two beams by a beam splitter. One of the resulting beams is used for WL seed generation in a sapphire crystal and the rest is used to pump the NOPA (also frequency doubled to 400 nm by a BBO for visible and NIR NOPAs). The WL seed and pump beams are spatially and temporally overlapped in a NLC, where DFG amplifies the WL seed. Figure credit: Dr Andrew Musser.*

Before discussing the specifics of each setup, it is worth briefly covering the basics of NOPA operation. A schematic of a typical NOPA, running off a Ti:sapphire amplifier is shown in Figure 3.2. Depending on the configuration, the NOPA can provide tuneable broadband pulses in the visible (480 – 830 nm),[79] NIR (750 – 1150 nm)[79] and IR (1200 – 1650 nm).[80] Each NOPA is powered by roughly 300 – 400 μW of the 800 nm laser fundamental. This output is split into two separate beams by a 90:10 beam splitter (BS), with the greater power pump beam frequency doubled to 400 nm in a β-barium borate (BBO crystal) for the visible and NIR NOPAs. The lower power beam is used for WL seed generation in a sapphire crystal. The residual fundamental is removed from the WL by a suitable colour filter: BG38 for the visible NOPA and an RG830 for the NIR and IR NOPAs. The WL seed and pump pulses are then focussed into another non-linear crystal (NLC): BBO for the visible and NIR NOPAs and periodically poled stoichiometric lithium tantalite (PPSLT) for the IR NOPA. When the pump and seed pulses are overlapped spatially and temporally in the NLC, with the correct pump-seed angle and cut and orientation of the NLC, the seed is amplified by a process called difference frequency generation (DFG).[79] Here, a higher energy pump photon is split into two new photons: the signal (with the same energy as the seed photon) and the idler, in such a way that energy and momentum are conserved.[79] Through this process, the 800 nm laser fundamental can be converted into a wide range of wavelengths and bandwidths that can be tuned to the users requirements. Additionally, the resulting amplified beam can be temporally compressed to transform-limited durations (<10 fs, dependent on pulse bandwidth) with a pair of chirped-mirrors (CM),[79] if extreme time resolution is required. Otherwise, the pulse duration will be limited by the duration of the pump beam used for amplification, typically ~100 fs.

Two of the setups were powered using a commercially available Ti:sapphire amplifier (Spectra Physics Solstice Ace). The amplifier operates at 1 kHz and generates 100 fs pulses centered at 800 nm with an output of 7 W. One setup has the option of a narrowband NOPA for generation of ~100 fs pump pulses, tuneable between 480 – 780 nm, or the use of the 2nd harmonic of the laser fundamental (400 nm, 100 fs). The probe is provided by a visible or NIR NOPA, as well as WL generated in a CaF_2 crystal, allowing for probing from the UV to NIR (350 – 1100 nm). To complement the probe wavelengths available, the probe pulses are collected with a silicon dual-line array detector (Hamamatsu S8381-1024Q), driven and read out by a custom-built board from Stresing Entwicklungsbüro. The second setup utilises a

TOPAS OPA as the primary pump source. This generates NIR pulses (~1100 – 2000 nm) that can be frequency doubled, quadrupled or summed with the 800 nm fundamental to generate narrowband pump pulses spanning 290 – 2000 nm, allowing for excitation of any desired system. The probes are provided by separate visible, NIR and IR NOPAs, allowing for probing from the visible to IR (500 – 1650 nm). To complement the probe wavelengths available, the probe pulses are collected with an InGaAs dual-line array detector (Hamamatsu G11608-512DA), driven and read out by a custom-built board from Stresing Entwicklungsbüro. When an amplified NOPA probe was used, the probe beam was split into two identical beams by a 50/50 beamsplitter. This allowed for the use of a second reference beam which also passes through the sample, but does not interact with the pump. The role of the reference was to correct for any shot-to-shot fluctuations in the probe that would otherwise greatly increase the structured noise in our experiments. Through this arrangement, very small signals with a $\frac{\Delta T}{T} \sim 10^{-5}$ could be measured. Finally, the electronically triggered Q-switched Nd:YVO$_4$ laser is interchangeable between these two setups, allowing for the measuring of long-time (ns – ms) TA on either, depending on the probe ranges required.

The third setup was powered by a Yb amplifier (PHAROS, Light Conversion), operating at 38 kHz and generating 200 fs pulses centred at 1030 nm with an output of 14.5 W. As with the Ti:sapphire powered setups, there is the option of using either NOPAs (with CM compression) pumped by the 2nd and 3rd harmonics of the 1030 nm fundamental, or a TOPAS as the pump source. The probe is provided by a WL supercontinuum generated in a YAG crystal. After passing through the sample, the probe is split into visible (500 – 950 nm) and NIR (950 – 1400 nm) portions by a dichroic mirror, with the visible part imaged using a Si photodiode array (Stresing S11490) and the NIR by an InGaAs photodiode array (Sensors Unlimited LDH2). This setup provided additional flexibility by allowing for broadband spectrum acquisition in one measurement for improved consistency between visible and IR spectral regions, as well good signal to noise (s/n) in the 750 – 850 nm region, which is difficult to obtain on the other setups due to large fluctuations in the WL seed around the 800 nm fundamental. Whilst the noise-floor of a WL probe is not as low as a well-referenced NOPA probe, the extremely high repetition rate of 38 kHz allows for the acquisition of many more data points in the same amount of time and thus, similarly small $\frac{\Delta T}{T}$ signals could be measured.

In all setups for short-time measurements, the pump beam was passed through an optical chopper (Thorlabs MC2000B-EC), set to a frequency of half or a quarter of that of the laser output (500 Hz for the Ti:sapphire setups and 9.5 kHz for the Yb amplifier). This allowed for the sequential capture of probe beams with and without the pump for calculation of the differential transmission spectra, in the order of "pump-on pump-off" and "pump-on pump-on pump-off pump-off" for the 1 kHz Ti-sapphire and 38 kHz Yb powered setups, respectively. For the long-time measurements where the pump source was the electronically triggered Nd:YVO_4 laser, the trigger output from the Ti:sapphire laser was passed through a custom-built frequency halving box, which removed every other signal and sent a 500 Hz trigger signal to the Nd:YVO_4 laser. To provide the probe delay for the short-time measurements, a mechanical delay stage with 30 cm (Thorlabs DDS300-E/M) of travel was used. Through the extra probe path length added by the forward and return bounce onto a retroreflector mounted on the stage, time delays of up to 2 ns could be obtained. For delays longer than this, mechanical delay becomes impractical due to the extremely long distances required. Therefore, an external delay generator was used to time the pulse of the electronically triggered Nd:YVO_4 laser. This allows us to vary how long before the probe the pump pulse arrives and access the time points that would otherwise be impossible mechanically.

3.8 The Genetic Algorithm

Given its frequent use during this thesis, it is sensible to take some time to discuss the Genetic Algorithm (GA). GA allows us to separate the convoluted data containing multiple species into its fundamental components by reconstructing it using linear combinations of the spectral species that give the smallest residual error. To begin, the software makes a series of initial spectral guesses for the number of species specified by the user. It then selects the spectra that best fit the data, makes small changes to their form, called "mutations", and "breeds" these new species together to generate more guesses. This processes is then repeated iteratively until there is minimal change between generations, indicating that the GA has converged on a solution that can best reconstruct the dataset. Obviously, care must be taken to ensure the absolute minima, and not a local minima, is found. Confidence in the solution can be gained when repeated runs with different starting conditions converge on the same solution. For the interested reader, more detailed information can be found in the work of Deb.[81]

4 Efficient Non-Fullerene Acceptor Organic Solar Cells with a Low Non-Radiative Voltage Loss

4.1 Motivation

The efficiency of OPV devices has increased dramatically in recent years, with record PCEs of 15.7% and 17.3% reported for single junction and tandem cells respectively.[9,10] However, they still lag behind their direct competitors, including perovskite and Si technologies, where PCEs of over 20% and 26% have been respectively reported.[82] Compared to their main competitor amongst emerging photovoltaic technologies, perovskites, single junction OPVs possess comparable J_{SC}'s of over 20 mA/cm^2 and FFs of around 0.7.[9,32,58–60,83–85] However, the metric in which OPV is most lacking is in V_{OC}, relative to the band gap of the material. In Si and perovskite PV, the total voltage loss is typically <0.5 V,[86] whereas in OPVs it is often on the order of 0.7 V, or higher.[48] Therefore, in order for OPV to be competitive with its perovskite counterparts, the total voltage loss should be reduced to 0.5 V or lower, with a simultaneously high J_{SC} and FF. As discussed previously in section 2.6.3, the key tactic that has emerged for reducing the voltage loss in OPV is to target the EQE_{EL} of the cell (equation 2.76). By maximising the radiative efficiency of the inevitable recombination events occurring, one can minimise the non-radiative voltage loss of the cell. For perovskites, an EQE_{EL} of 1.2% can be achieved for well-optimise devices, giving a $\Delta V_{nr} = 113$ mV.[87] By comparison, typical EQE_{EL}'s for OPV lie in the range of $10^{-4} – 10^{-7}$%, resulting in a $\Delta V_{nr} = 350 – 530$ mV.[88]

Recent reports of OPV devices have included two NFA-based systems that show very low total voltage losses of 0.49 V and 0.52 V, with impressive PCEs of up to 12.1% and 9% for champion devices, respectively.[49,50] Such low voltage losses are very exciting as they are approaching those required to increase the competitiveness of OPV with perovskites. Therefore, the focus of this section will be to explore the properties of these OPV blends in an attempt to understand the origin of the low voltage loss in these systems. The ultimate hope is that the lessons learned will be more widely applicable to the OPV field as a whole, leading design rules that will aid in the creation of more OPV blends that exhibit a similarly low voltage loss.

4.2 Materials

The materials used in this study are the OPV donor polymer PTB7-Th, which is paired with the acceptors IOTIC-2F and SiOTIC-4F to create efficient OPV devices. For brevity, PTB7-Th, IOTIC-2F and SiOTIC-4F will be referred to as P2, A2 and A3 respectively. The structures of the materials are displayed below in Figure 4.1.

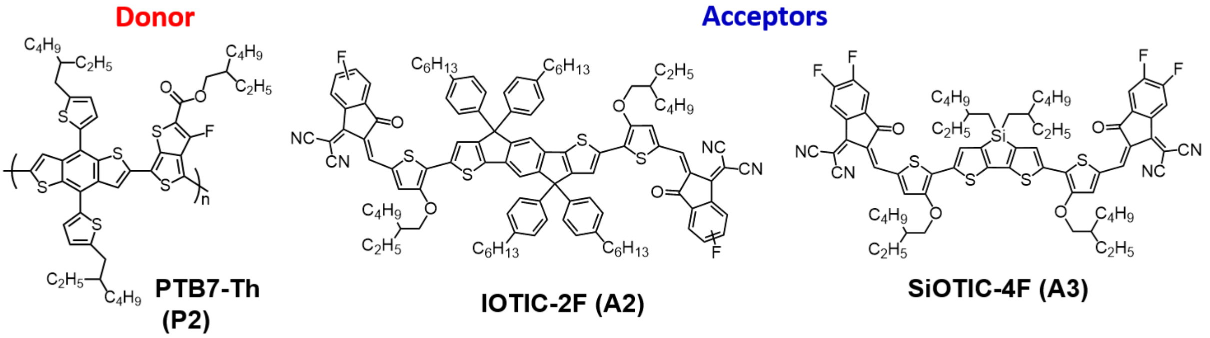

***Figure 4.1**: The chemical structures of the materials used in this study: the donor polymer PTB7-Th (P2) and the acceptors IOTIC-2F (A2) and SiOTIC-4F (A3).*

P2 was purchased from Sigma Aldrich, whilst A2 and A3 were synthesised by Dr Jaewon Lee. The HOMOs of the materials were measured using cyclic voltammetry (CV) by Dr Jaewon Lee, with the LUMO approximated from this using the optical band gap (summarised in Table 4.1). We note that there is an inherent error in using this method to determine the LUMO: it will be higher than stated due to the contribution of the exciton binding energy to the optical band gap. However, this methodology will be applied consistently across all systems. In both blends, the HOMO-HOMO offset is very small: around 100 meV or less. This is an important point, as it ultimately aids in minimising the energy loss incurred from charge separation and therefore is at least partly responsible for the overall total low voltage loss in these systems.

Material	HOMO (eV)	E_g (eV)	HOMO + Eg (eV)	HOMO-HOMO offset (eV)	"LUMO-LUMO" offset (eV)
P2	-5.20	1.59	-3.61	-	-
A2	-5.34	1.37	-3.97	0.14	0.36
A3	-5.28	1.22	-4.06	0.08	0.45

***Table 4.1**: The energetics and optical properties of the three materials under study in this section. Important to note is the small HOMO-HOMO offset between A2 and A3 with P2. This is an important contributory factor to the low overall voltage loss in these OPV systems.*

4.3 Absorption and Photoluminescence

4.3.1 Steady-State Absorption and Photoluminescence

To begin, we investigated the steady-state absorption and PL of the neat materials and the blends. For these measurements, the neat films were fabricated through spin coating a solution of 20 mg/mL in chlorobenzene onto a substrate at 3000 rpm. For the blends, identical conditions to those used for the optimised devices were used. For the P2:A2 blend, a 1:1.5 weight ratio was dissolved to give a 20 mg/mL solution in a 98:2 volume ratio of chlorobenzene (CB) to 1,8-diiodooctance (DIO), before being deposited by spin coating at 900 rpm, yielding a film of 90 nm thickness. For P2:A3, a 1:1.5 weight ratio was dissolved to give a 18.8 mg/mL solution in a 98:2 volume ratio of chloroform (CF) to 1-chloronapthalene (CN), before being deposited by spin coating at 2500 rpm to give a film with an 80 nm thickness. The normalised steady-state absorption of the neat materials are shown first in Figure 4.2. The absorption spectra of P2 is well-matched to those of A2 and A3, providing a complementary absorption profile that covers a different part of the solar spectrum. P2 is a red-absorbing donor polymer,

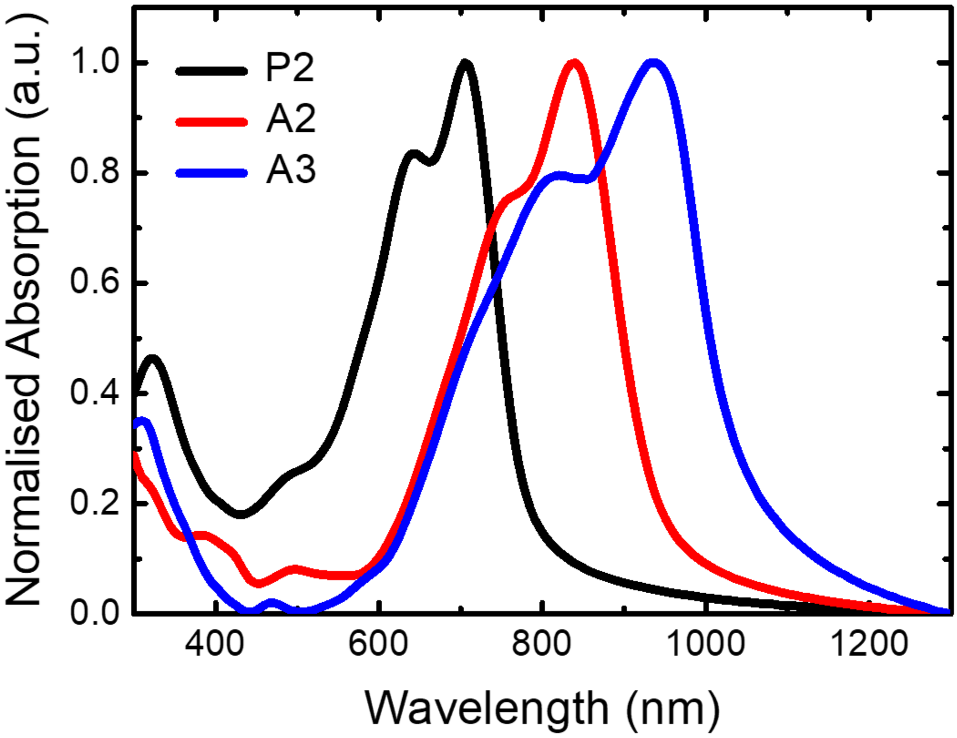

***Figure 4.2**: The normalised absorption spectra of neat films of the materials used in this study.*

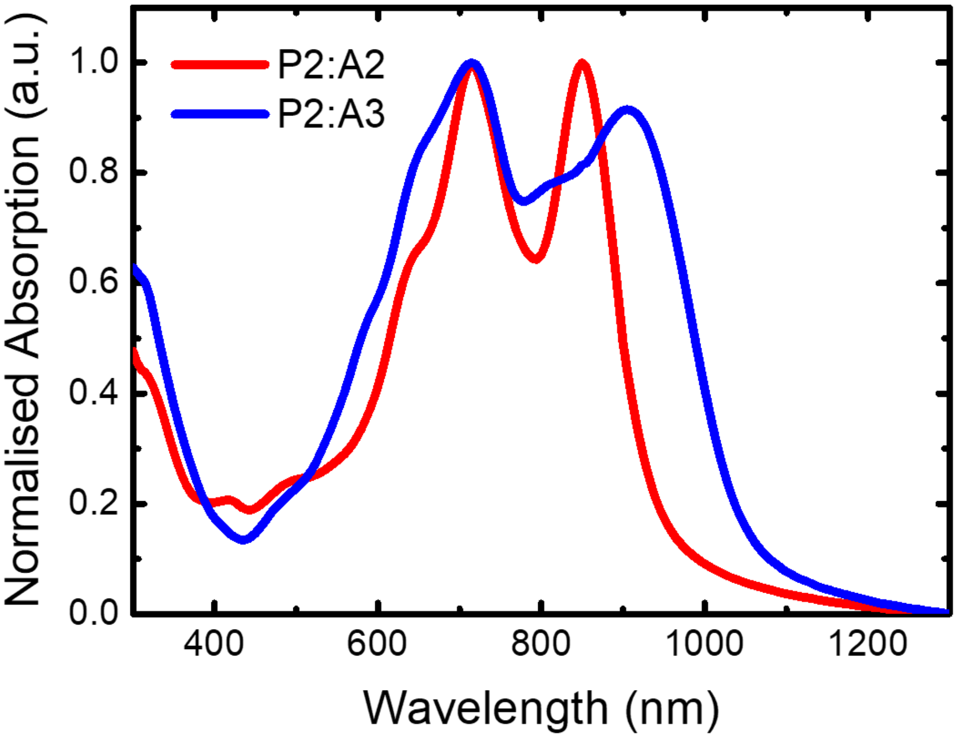

Figure 4.3: *The normalised absorption spectra of the blend films of the materials used in this study. The films were fabricated under identical conditions to those that gave the optimal device performance.*

with strong absorption between 575 – 775 nm, whilst the narrow band gap acceptors cover the NIR region below the band gap of P2, extending up to 950 nm for A2 and 1100 nm for A3. The absorption spectra of the blends are displayed in Figure 4.3 and are, as expected are a clear mixture of the two constituent components.

Turning next to the PL, the steady-state PL spectrum of the neat materials are shown in Figure 4.4. For these measurements, the samples were excited with a 647 nm CW laser. For the blends (Figure 4.5), the same excitation source was used. A clear red-shift between the PL of the neat films and blends is observed, which can be attributed to the fact that the primary source of emission in the blends is from the CT state formed between P2 and A2 or A3. Fitting a straight line to the PL reveals an onset of 841 nm for A2 and 930 nm for A3. Fitting the PL spectrum of the blends in the same way gives us an onset of 928 nm for the P2:A2 blend and 965 nm for P2:A3. Converting to eV, the difference in PL onset between neat A2 and the P2:A2 blend is 138 meV and for neat A3 and P2:A3, it is 48 meV. This energy difference is quite consistent with the HOMO-HOMO offsets listed in Table 4.1, confirming that the PL seen is direct emission of the CT states formed between P2:A2 and P2:A3.

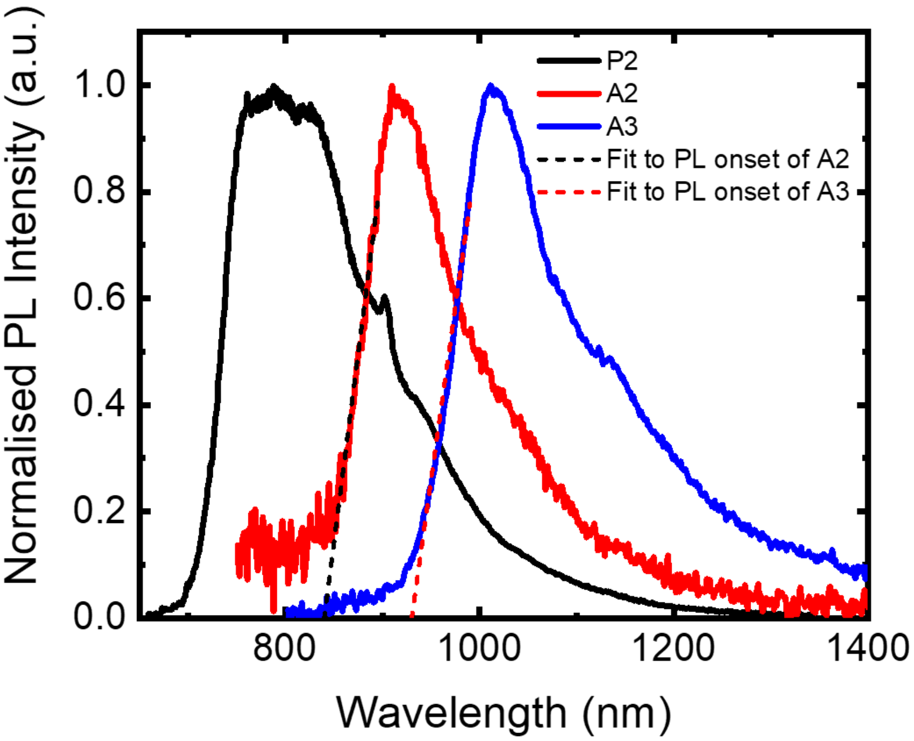

Figure 4.4: The normalised PL spectra of the neat films of the materials used in this study. The PL onset was calculated by taking a linear fit to the rise of the PL peak.

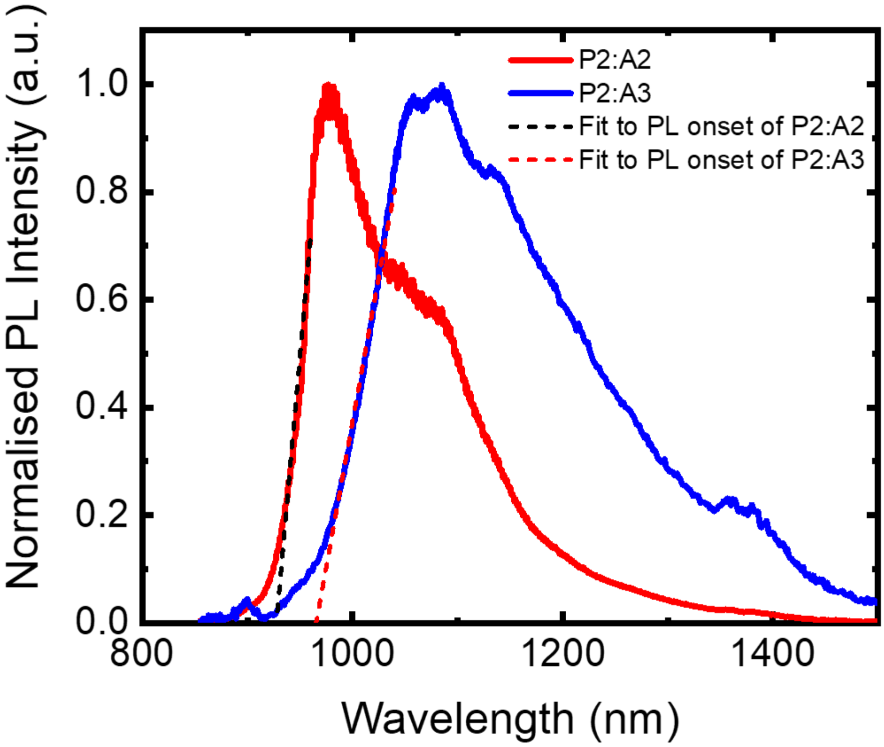

Figure 4.5: The normalised PL spectra of the blend films used in this study. The PL onset was calculated by taking a linear fit to the rise of the PL peak.

4.3.2 Photothermal Deflection Spectroscopy

To further investigate the blend films, PDS was performed by Dr Mojtaba Abdi Jalebi (Figure 4.6). From this measurement, the Urbach Energy could be extracted, through a plot of the natural logarithm of the blend attenuation coefficient α against the photon energy $h\nu$. In this case, the Urbach energy E_u can be obtained by fitting a straight line to the absorption tail of the following form:

$$\ln(\alpha) = \ln(\alpha_0) + \left(\frac{h\nu}{E_u}\right) \qquad (4.1)$$

Where α_0 is a constant. This fit yielded Urbach energies of 26.2 meV and 34.0 meV for the P2:A2 and P2:A3 blends, respectively. The Urbach energy can be considered a measure of the disorder of a material that is manifested through states with sub band gap absorptions.[89] These values, especially for P2:A2 are particularly low amongst OPV blends, where Urbach energies of >50 meV are typically reported,[90,91] suggesting substantial order at the interfaces. Recent

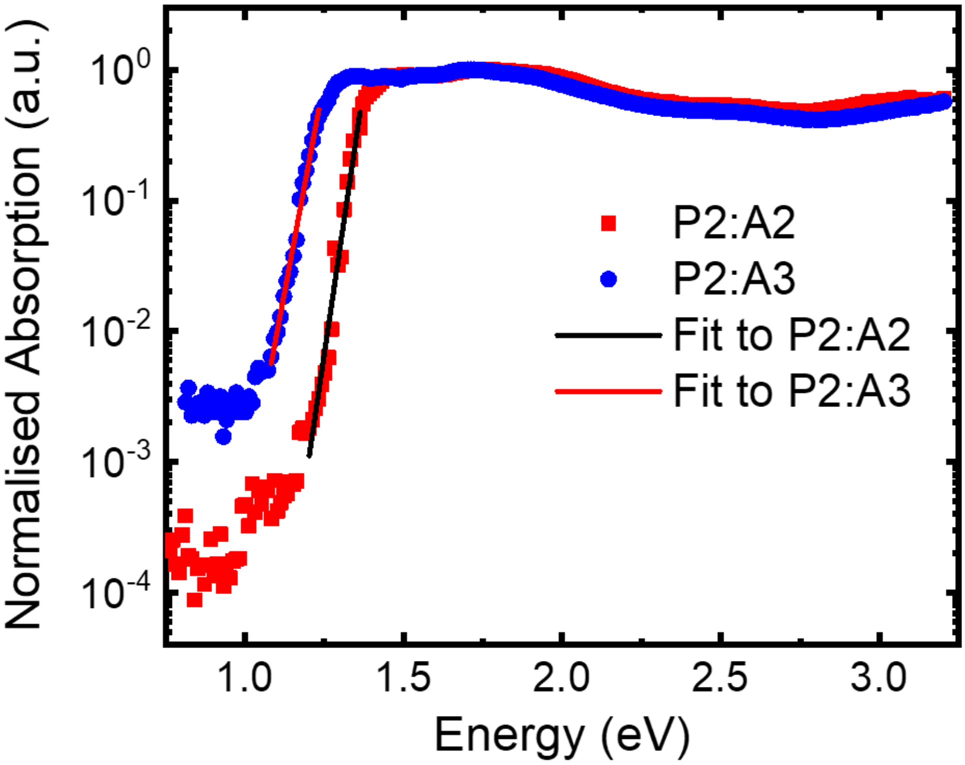

***Figure 4.6**: The normalised absorption spectra of the blend films of the materials used in this study, measured by PDS. The fit of the band tails is shown by the solid lines, from which the Urbach energy was extracted. An E_u of 26.2 eV and 34.0 eV are reported for the P2:A2 and P2:A3 blends, respectively. Measurements performed by Dr Mojtaba Abdi Jalebi.*

work by Menke *et al.* has suggested that a low Urbach energy and consequently reduced energetic disorder may be key for efficient CT dissociation in low-offset OPV blends.[48] This is because there is very little excess energy to aid in overcoming the coulombic binding energy of the electron and hole in the CT state, leading them to remain bound for longer timescales. During this time, the CT state can migrate on the order of 5 – 10 nm, as has previously been observed in organic D/A blends with long CT state lifetimes.[92] Therefore, the low disorder reduces the possibility of the CT states encountering a low-energy trap site before CT dissociation can occur, where they would ultimately decay geminately. Such properties likely allow the P2:A2 and P2:A3 blends to efficiently generate photocurrent, despite their low energetic offsets.

4.4 OPV Device Characterisation

For this work, inverted OPV devices were fabricated and characterised by Dr Seo-Jin Ko to both confirm the previously observed performance and for further testing. The J-V characteristics and $\mathrm{EQE_{PV}}$ response curves are shown in Figures 4.7 and 4.8, with a summary of the results in Table 4.2. The maximum PCE obtained for the P2:A2 device was 11.6% and for P2:A3, 8.9%, which is in good agreement with earlier reports.[49,50]

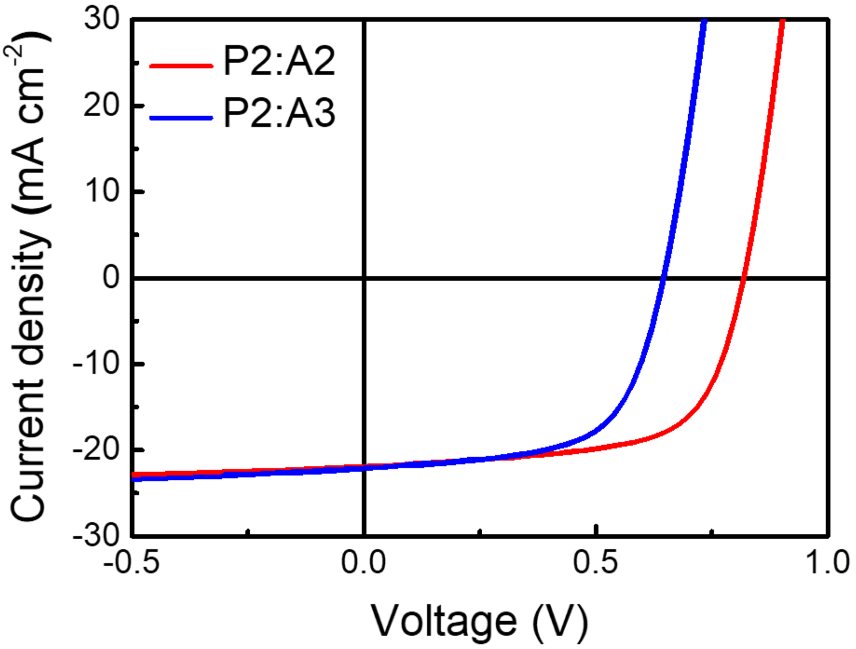

Figure 4.7: *The current density-voltage curves of champion P2:A2 1:1.5 and P2:A3 1:1.5 devices measured under an AM1.5G solar spectrum, giving PCEs of 11.6% and 8.9%. Devices fabricated and tested by Dr Seo-Jin Ko.*

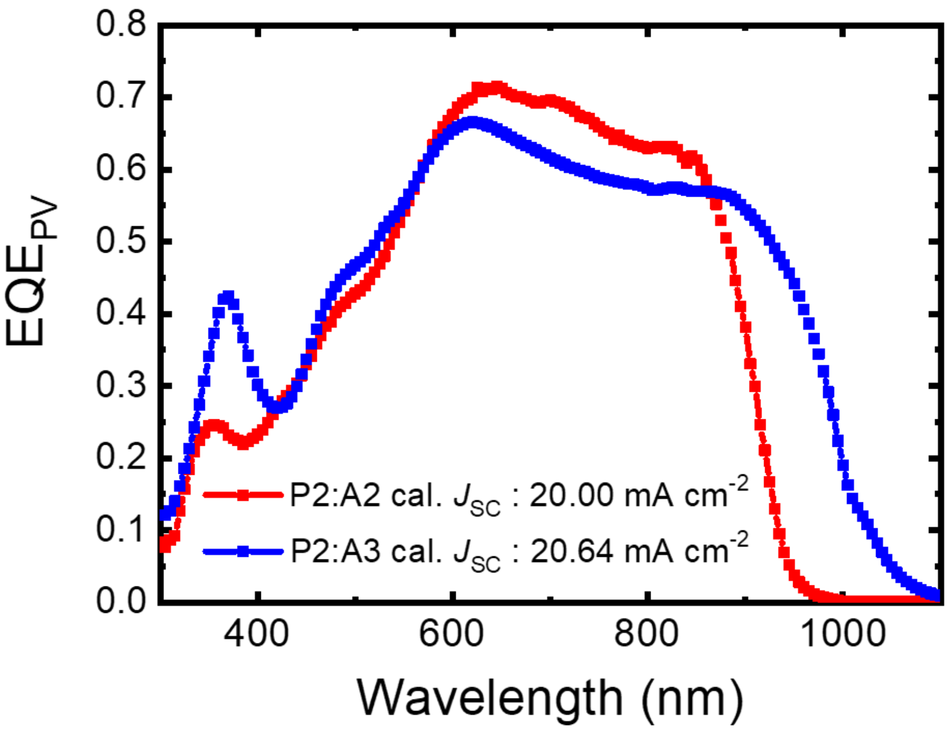

***Figure 4.8**: The EQE_{PV} response curves of champion P2:A2 1:1.5 and P2:A3 1:1.5 devices, with integrated J_{SC}'s of 20.64 and 20.00 mA cm^{-2}. Devices fabricated and tested by Dr Seo-Jin Ko.*

Blend	V_{OC} (V)	J_{SC} (mA cm^{-2})	FF	PCE
P2:A2	0.82	–21.9	0.65	11.6
P2:A3	0.62	–22.2	0.62	8.9

***Table 4.2**: The key performance metrics of the P2:A2 and P2:A3 devices, measured under an AM1.5G solar spectrum.*

After characterisation of the photovoltaic properties of the P2:A2 and P2:A3 devices, we next examine the luminescent properties to gain a deeper understanding of the magnitude of the non-radiative voltage loss. For this, the OPV devices were run at forward bias and any electroluminescence (EL) emitted was detected. These measurements were performed by Akchheta Karki and the current-EQE_{EL} plots for P2:A2 and P2:A3 are shown in Figures 4.9 and 4.10. Immediately apparent is the high EQE_{EL} of the P2:A2 blend, suggesting a very low level of non-radiative voltage loss. A value of 1.2 x10^{-3} % was obtained at a current density equivalent to $-J_{SC}$ of 22 mA cm^{-2}, chosen to be representative of charge carrier densities under realistic operating conditions.[93] The value of P2:A3 at a current density of 22 mA cm^{-2} is somewhat lower, but still relatively impressive amongst previously reported OPV devices.[88,94]

Blend	EQE_{EL} (%)	ΔV_{nr} (meV)	$E_g - eV_{OC}$ (meV)	Radiative Limit of V_{oc} (V)
P2:A2	1.20×10^{-3}	283	490	1.07
P2:A3	1.54×10^{-4}	334	550	0.97
P2:$PC_{70}BM$	8.60×10^{-6}	418	800	-

***Table 4.3**: The maximum EQE_{EL} of the blends under study, as well as that of the analogous P2:$PC_{70}BM$ blend for comparison (data taken from reference 78). From this, the total non-radiative voltage loss is calculated and compared to the overall energy loss of the device.*

One reason for the lower EQE_{EL} of the P2:A3 blend may be due to the energy gap law increasing the rate of non-radiative decay from the CT state. With these values, we can now calculate the magnitude of the non-radiative voltage loss in the devices from equation 2.93. The results are tabulated in table 4.3. For comparison, data from the analogous fullerene blend, P2:[6,6]-phenyl-C_{71}-butyric acid methyl ester ($PC_{70}BM$), is included.[94]

The total non-radiative voltage loss in the P2:A2 blend is calculated to be 283 meV, with a value of 334 meV for P2:A3. The difference of this metric between the two blends is

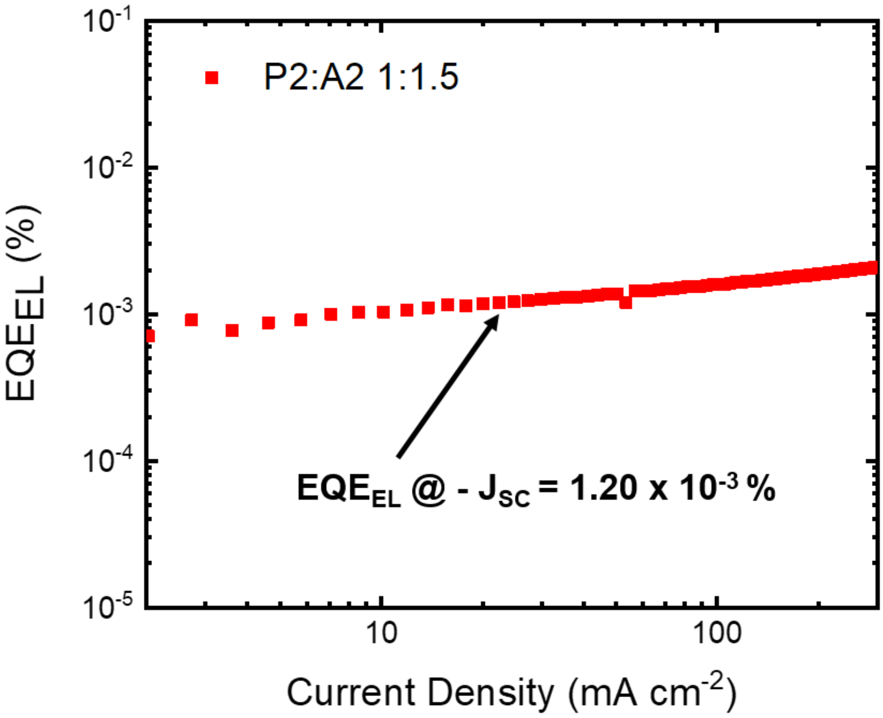

***Figure 4.9**: The plot of current vs EQE_{EL} of the champion P2:A2 device. The maximum EQE_{EL} of 1.20×10^{-3} % is reached at a current density of 22 mA cm^{-2} and a driving voltage of 1.0 V. Measurement performed by Akchheta Karki.*

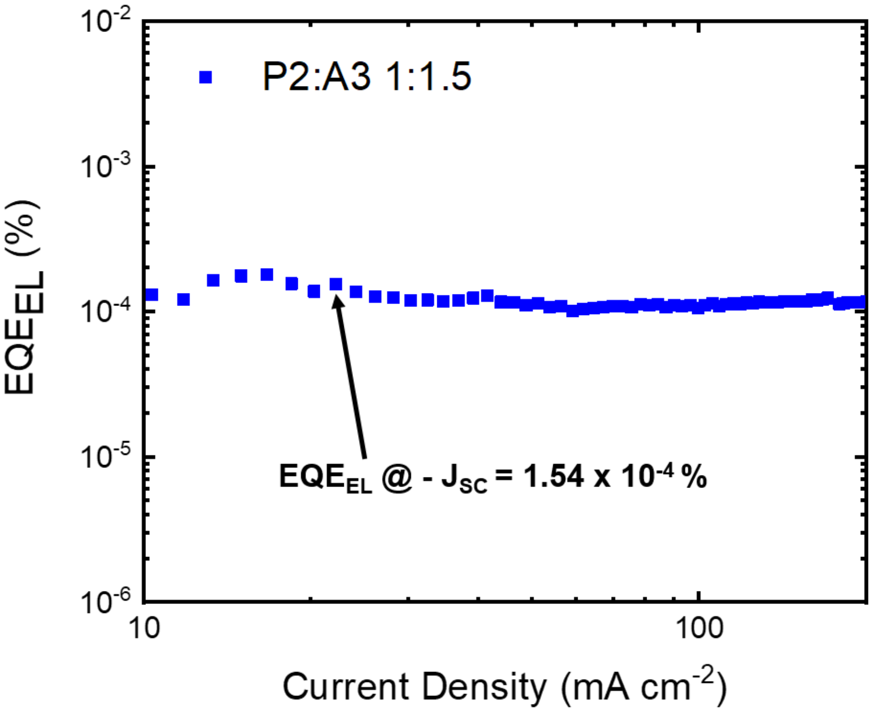

***Figure 4.10**: The plot of current vs EQE$_{EL}$ of the champion P2:A3 device. The maximum EQE$_{EL}$ of 1.54 x 10^{-4} % is reached at a current density of 22 mA cm^{-2} and a driving voltage of 0.87 V. Measurement performed by Akchheta Karki.*

likely related to the lower E$_{CT}$ of P2:A3, which would lead to increased non-radiative decay rates, as predicted by the energy gap law and consistently observed experimentally in a wide range of OPVs.[95] These values compare favourably to that of the fullerene acceptor equivalent, where the total non-radiative voltage loss is 418 meV. This, combined with the large energetic offset for charge transfer, results in the substantial total energy loss of 800 meV for the fullerene system. Therefore, through a combination of a low energy offset for charge transfer and supressed non-radiative recombination, both NFA devices substantially outperform their fullerene counterpart in this metric. Impressively, the total voltage loss of P2:A2 is also approaching that of those reported for inorganic technologies, such as perovskites.[86] We will now turn to other techniques to try and reveal the cause of this low non-radiative voltage loss.

4.5 Transient Absorption of the Pure Materials

TA is the technique of choice to elucidate the complex photophysics of OPV blends on ultrafast timescales relevant to the charge generation processes. As such, we shall utilise it with an aim to determine the cause of the non-radiative voltage loss in our NFA blends. To begin, we first study the neat films alone in order to determine the spectral features and decay timescales involved with the singlet excitons created initially after optical excitation and through which all further processes will progress. Figure 4.11 displays the short-time TA spectra of P2, with the corresponding kinetics shown in Figure 4.12. The excitation wavelength used was 620 nm, with a fluence of 2.1 μJ cm^{-2}. Two key features are visible: the first is the GSB, which closely resembles the steady-state absorption spectrum of P2, including the vibronic progression of the absorption spectrum. This occupies the region between 600 – 800 nm. Secondly, the primary singlet exciton absorption is visible as a broad band between 900 – 1650 nm, peaking into the IR at 1550 nm. The kinetic traces reveal that these 2 species decay in-step, with the majority of excited states having decayed after 1 ns.

We next turn to the neat A2 film, with the TA spectrum and corresponding kinetics shown in Figures 4.13 and 4.14. The film was excited with a pump pulse at 850 nm, with a fluence of 2.1 μJ cm^{-2}. As with neat P2, assignment of the features present is facile: the GSB closely matches that of the steady-state absorption and covers the region from 650 – 900 nm. The strong and narrow PIA band at around 1150 nm is also assigned the absorption of the singlet state. Both the GSB and singlet PIA decay in tandem, but this time more rapidly than that of neat P2, which we attribute to the increased rates of non-radiative decay as predicted by the energy gap law. Decay of the excited states present is largely complete after a few hundred ps.

Finally, to complete our analysis of the neat materials, we performed TA on the neat A3 film. The film was excited with a pump of 975 nm and a fluence of 3.8 μJ cm^{-2} and the TA spectra and kinetics are displayed in Figures 4.15 and 4.16. The GSB spans the range of 800 – 1050 nm, in good agreement with the steady-state absorption. Additionally, there is a very sharp PIA band at 1100 nm, with a weak and broad band out towards 1600 nm, which both decay with very similar kinetics. Therefore, they are assigned as belonging to different absorptions into higher lying states of the singlet exciton formed after photoexcitation. Decay of the GSB and singlet features is even more rapid than for A2, owing to the energy gap law: excited state decay in this system is fully complete after 100 ps.

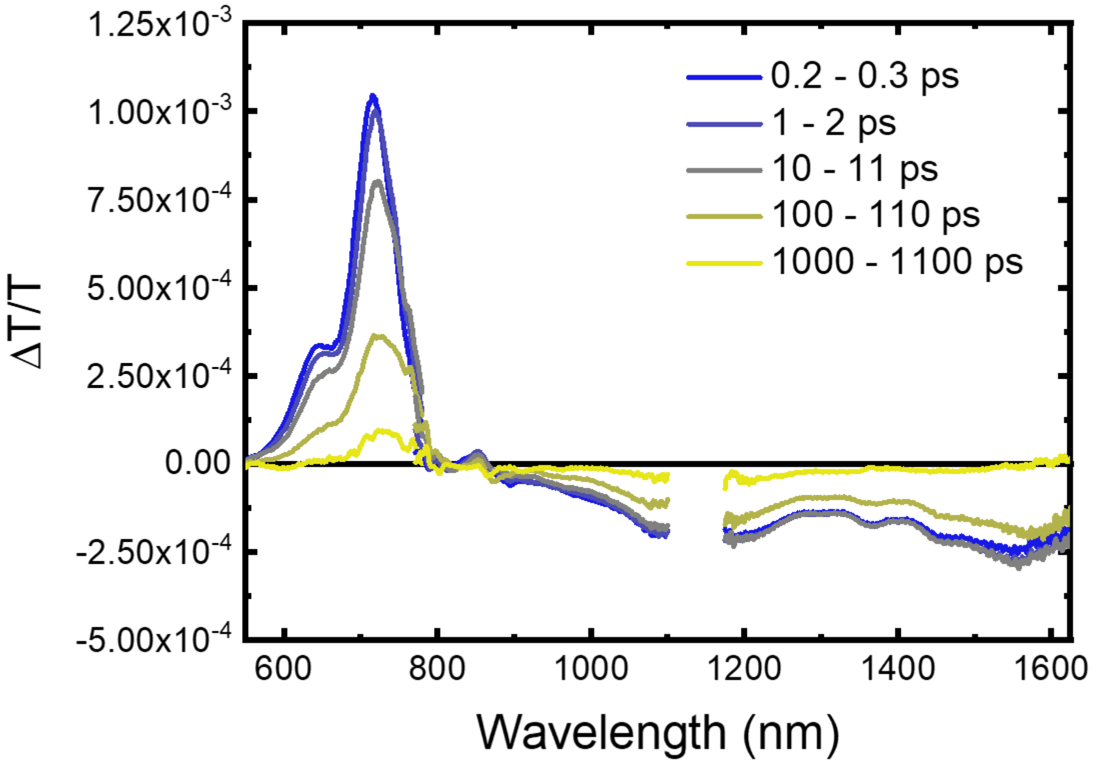

***Figure 4.11**: The short-time TA spectra of a film of neat P2: λ_{ex} = 620 nm, fluence = 2.1 μJ cm^{-2}. The GSB is clearly visible between 600 – 800 nm, with the broad PIA band between 900 – 1650 nm resulting from the singlet exciton.*

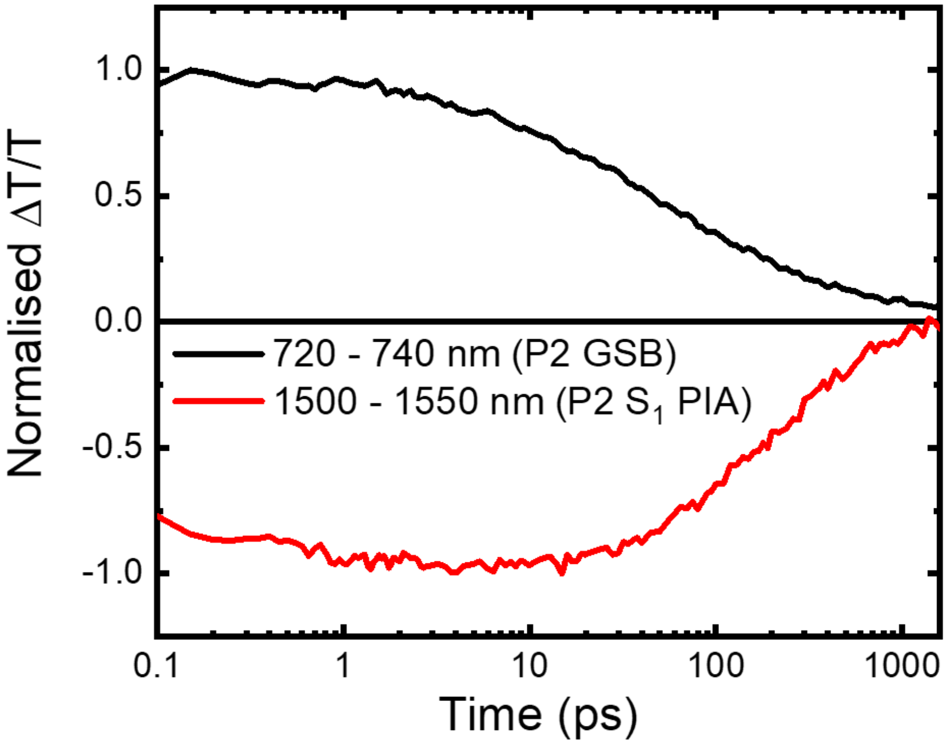

***Figure 4.12**: The short-time TA kinetics of a film of neat P2: λ_{ex} = 620 nm, fluence = 2.1 μJ cm^{-2}. The kinetics for the GSB (720 – 740 nm) and singlet exciton (1500 – 1550 nm) are shown. They both decay with similar profiles, indicating that the two states are linked.*

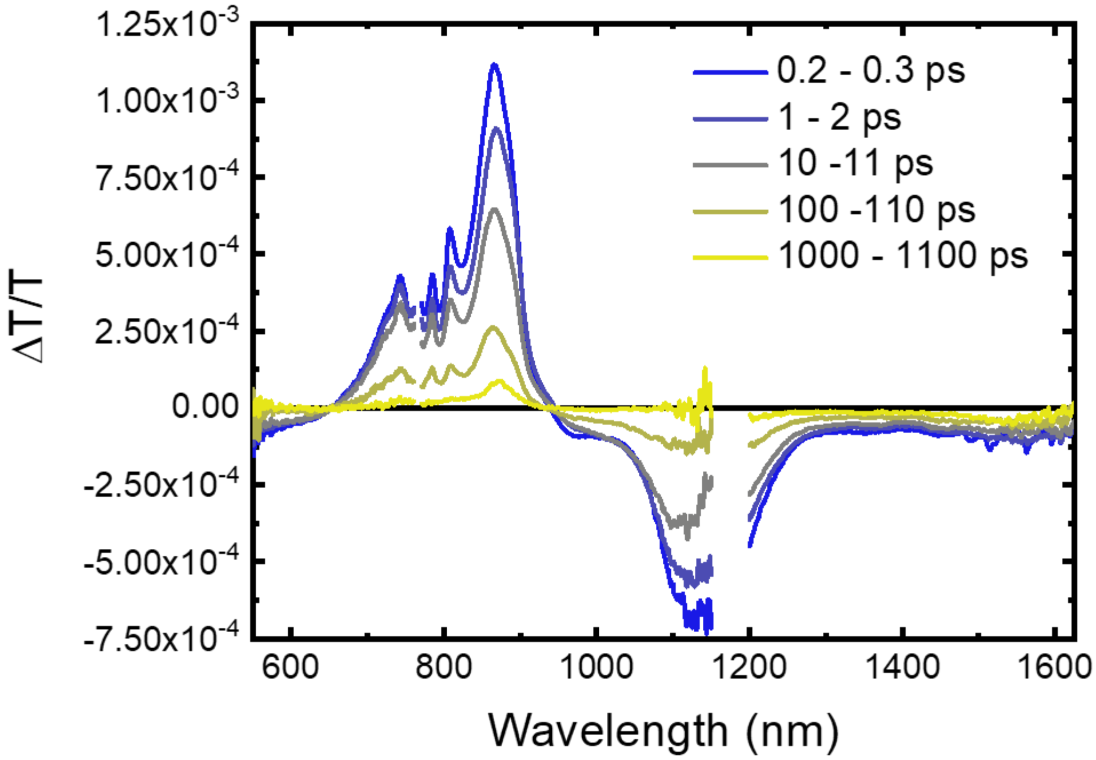

Figure 4.13: *The short-time TA spectra of a film of neat A2:* λ_{ex} *= 850 nm, fluence = 2.1 μJ cm*$^{-2}$*. The GSB is clearly visible between 650 – 900 nm, with the sharp PIA band at 1150 nm resulting from the singlet exciton.*

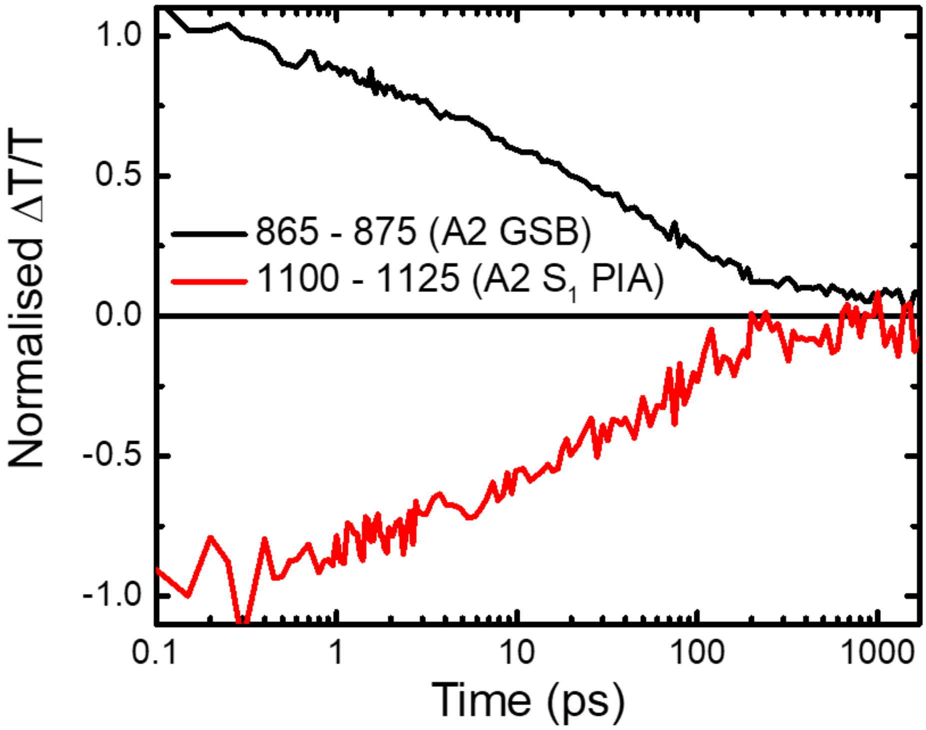

Figure 4.14: *The short-time TA kinetics of a film of neat A2:* λ_{ex} *= 850 nm, fluence = 2.1 μJ cm*$^{-2}$*. The kinetics for the GSB (865 – 875 nm) and singlet exciton (1100 – 1125 nm) are shown. They both decay with similar profiles, indicating that the two states are linked.*

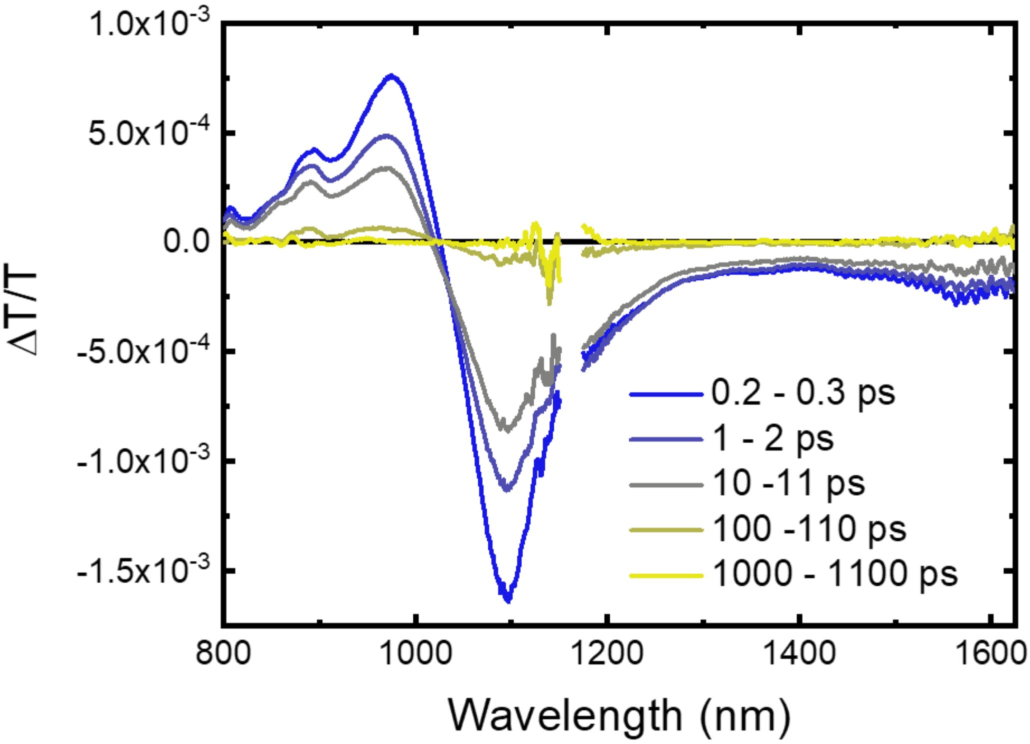

Figure 4.15: *The short-time TA spectra of a film of neat A3: λ_{ex} = 975 nm, fluence = 3.9 μJ cm^{-2}. The GSB is clearly visible between 800 – 1050 nm, with the sharp PIA band at 1100 nm and a weaker one at 1600 nm, resulting from the singlet exciton.*

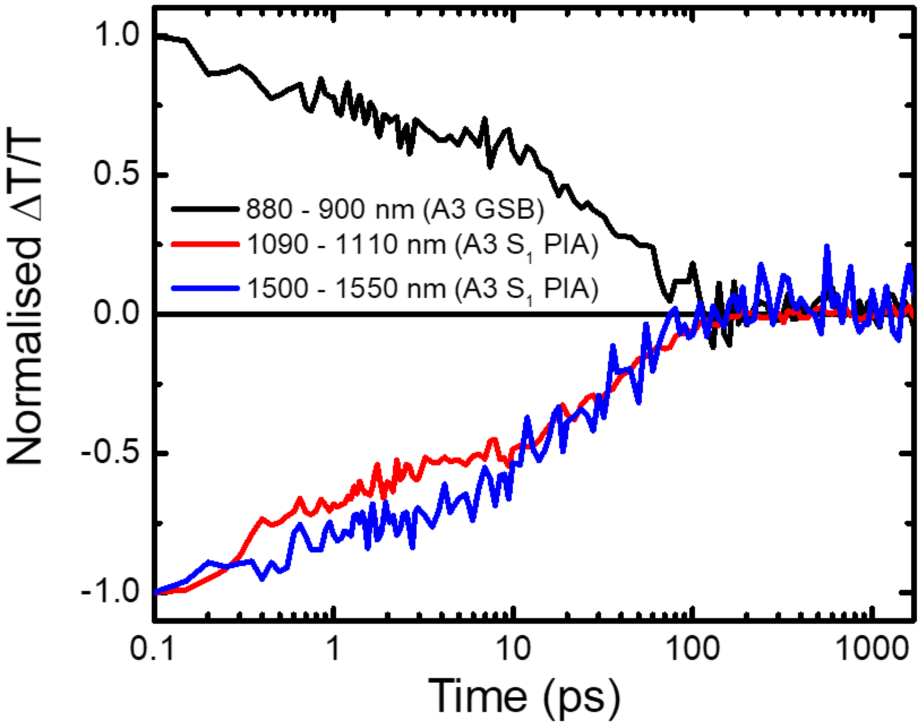

Figure 4.16: *The short-time TA kinetics of a film of neat A2: λ_{ex} = 975 nm, fluence = 3.9 μJ cm^{-2}. The kinetics for the GSB (880 – 900 nm) and singlet exciton (1090 – 1110 nm and 1500 – 1550 nm) are shown. They all decay with similar profiles, indicating that the three states are linked.*

4.6 Short-Time Transient Absorption of the Blends

4.6.1 Selective Excitation of A2 in the P2:A2 Blend

We begin our investigation of the blend films by first examining the blend of P2:A2 using TA. When selecting pump excitation wavelength, we note there are two possible regions: those that are below the band gap of P2 and excite only A2 (>780 nm) and those that excite both components (<780 nm). We will explore both pump regions to compare and contrast the photophysical processes occurring after generation of excitons on either of the D or A components. Whilst it is not possible to completely selectively excite P2, by pumping in the region of 570 – 630 nm where there is substantial P2 absorption with little A2 absorption, we can create an exciton population that mostly resides on the former. Additionally, as the signal-to-noise (s/n) in the 750 – 850 nm region of our setups pumped by the 800 nm fundamental Ti:sapphire is relatively poor, we will supplement this data with TA performed on the 1030 nm pumped Nd:YAG setup, as this probe wavelength region contains the important GSBs for both components.

For the simplest picture, we begin by examining the TA of the P2:A2 blend, pumped at 850 nm with a fluence of 2.1 μJ cm^{-2}. This excitation wavelength is chosen to allow for completely selective pumping of A2 only. The TA spectra are shown in Figure 4.17, with the corresponding kinetics in Figure 4.18. Immediately following excitation at 200 – 300 fs is the formation of a spectrum that broadly resembles neat A2, with the GSB clearly visible and a strong singlet PIA feature at 1150 nm. As we are exciting solely A2, this is entirely as expected. By 10 ps, the primary A2 GSB peak at 850 nm and the singlet PIA at 1150 nm have fallen, and a higher energy GSB with the characteristic vibronic progression of the P2 GSB at 650 nm and 720 nm is beginning to form. Interestingly, the fall of the A2 GSB continues to occur past 10 ps, with little increase in the intensity of the P2 GSB. This is somewhat surprising, as if A2 singlet excitons are being separated via hole transfer to P2, one would expect the A2 GSB to remain a similar intensity as the ground state absorption would still be bleached. There are also no signs in the NIR or IR of any new PIAs forming concurrently with the formation of the GSB on P2. The lack of new PIAs raises the question: where are the excited state absorptions of the hole on P2 and electron on A2? By examining the literature, we find numerous reports of TA on P2:acceptor blends confirming that the PIA of the hole on P2 is

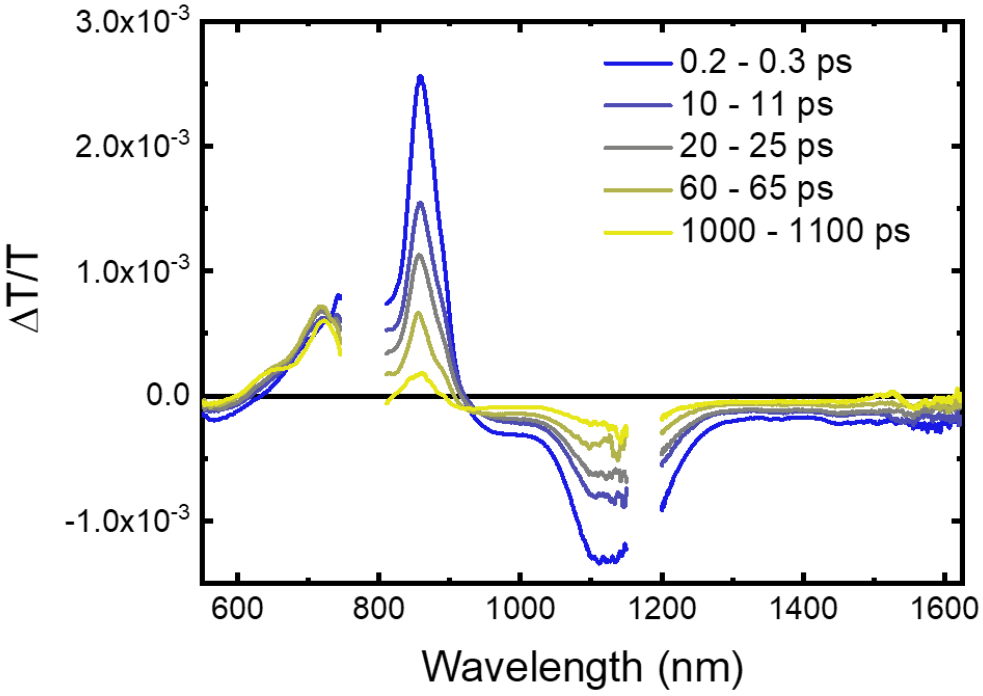

***Figure 4.17**: The short-time TA spectra of a blend film of P2:A2: λ_{ex} = 850 nm, fluence = 2.1 μJ cm^{-2}. The A2 GSB is clearly visible initially between 650 – 900 nm, with the sharp PIA band at 1150 nm, resulting from the singlet exciton. By 10 ps, the formation of the P2 GSB around 650 – 750 nm is occurring. The P2 hole absorption feature lies under the A2 exciton feature at 1150 nm, making it hard to discern. The continued loss of the A2 GSB and lack of growth of the P2 GSB as CT progresses implies the presence of a new PIA under these features, likely associated with the A2 electron.*

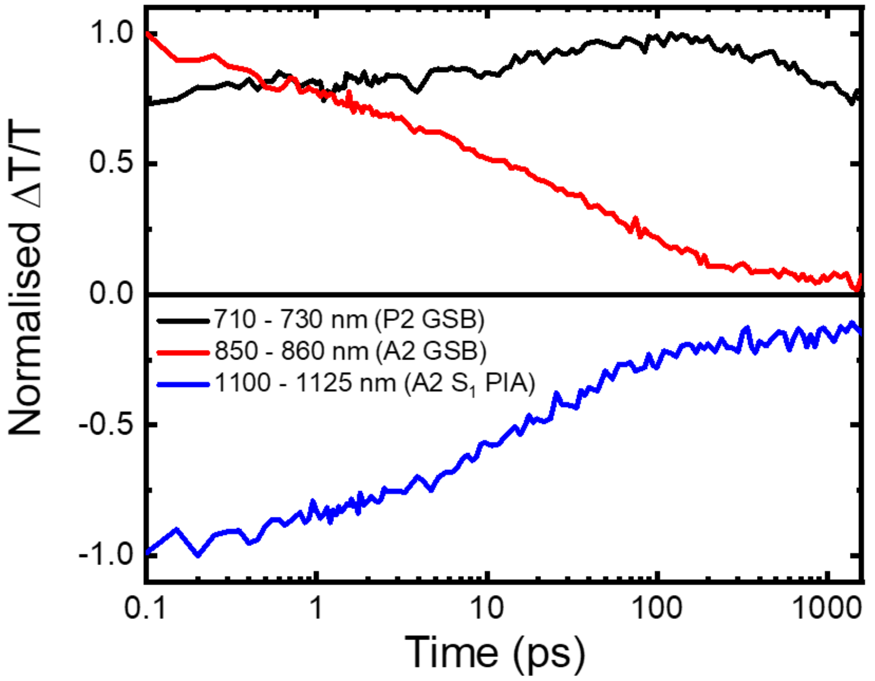

***Figure 4.18**: The short-time TA kinetics of a film of a blend film of P2:A2: λ_{ex} = 850 nm, fluence = 2.1 μJ cm^{-2}. The kinetics for the regions associated with the P2 GSB (710 – 730 nm), A2 GSB (850 – 860 nm) and A2 singlet exciton (1100 – 1125 nm) are shown.*

centred around 1150 nm,[96,97] the same wavelength as the A2 exciton. However, in the kinetic trace of this feature, the intensity of this region falls off continuously until about 100 ps. Whilst somewhat confusing at first, this can be rationalised by considering that the absorption cross section of the P2 hole may be significantly lower than that of the A2 exciton, leading to a fall in the intensity of the PIA as CT progresses. The plateauing of this feature at 100 ps gives an indication of the timescale by which the majority of the CT has occurred. However, observing this region is unlikely to give any more information than this of the dynamics of CT, due to the negligible differences between the A2 singlet exciton and P2 hole PIA spectra. Additionally, the rapid loss of the A2 GSB over the timescales of CT (>10 ps) coupled with the muted increase in P2 GSB intensity implies one of two scenarios: either the majority of A2 singlet excited states decay before CT, or the formation of a new PIA under the GSB, likely associated with the electron on A2, is dragging down both features. Given the high EQE_{PV} (>0.6) of the spectral region associated with the A2 absorption, it is unlikely that significant decay of A2 excitons occurs before CT, otherwise this would manifest itself as a low EQE_{PV}, so we may rule out the former. Additionally, this high EQE_{PV} suggests that the morphology of the active layer must consist of intimately mixed D and A domains. This is a consequence of the short exciton lifetime, which would significantly limit the exciton diffusion length of A2 in particular. Thus, a morphology consisting of large domains would result in a significant amount of exciton recombination prior to CT and a low EQE_{PV}. This is consistent with the previous reports of this system where the addition of the additive DIO resulted in a significantly more intermixed morphology, improving device performance from 9% without DIO to 11.6% with 2% by volume of the additive.[49]

In order to obtain a clearer picture of the CT dynamics of the system, we turn to the TA performed on the alternate Yb amplifier setup to analyse further the interplay of the GSB features. The blend was excited at 840 nm with a fluence of 0.64 μJ cm^{-2} and the resulting TA spectra can be seen in Figure 4.19, with the spectra normalised to the peak of the A2 GSB in Figure 4.20. The A2 GSB is solely visible initially at 200 fs and decays a little up to 10 ps, likely as the result of non-radiative singlet decay. At 10 ps, the P2 GSB begins to be visible, consistent with previous measurement and indicating the start of the CT process. As before, the A2 GSB begins to fall more rapidly at this point, with little increase in the intensity of the P2 GSB. The normalised TA spectra give a much clearer image of the formation of the P2

GSB after selective A2 excitation, however care must be taken when viewing this graph as the continued reduction of the A2 GSB up to 1.5 ns may give the impression that the P2 GSB is continuing to grow in. Of interest is the narrow negative bands that form during CT at the red edge of both the P2 and A2 GSBs. These are likely as a result of the local electric fields formed between the separating charges causing a red-shift in the ground state absorptions of molecules surrounding them. Such a feature is termed an "electro-absorption" (EA) and is often seen in OPV blends.[98]

To extract information about the timescale of CT in the P2:A2 blend, we have run the previously discussed GA on the TA data. Using this technique, we extract the two main contributory spectra and their associated kinetics (Figure 4.21 and 4.22). The first species, represented by the black curve, perfectly resembles the A2 GSB. Whilst the second species (the red curve) gives the final shape of the spectrum after CT has occurred, which includes both the P2 and A2 GSBs. The kinetics of these extracted species provide an unambiguous picture of the timescales involved. Initially, the A2 GSB feature (black) decays away with no rise in the spectrum associated with the completion of CT (red), indicating the recombination of A2 excitons. By the time the CT spectrum begins to rise, approximately 20% of excitons on A2 have decayed. The rise of the CT spectrum from 3 ps can be well fitted with a mono-exponential growth function, shown by the blue line. This yields a time constant of 30 ps, providing a rough idea of the timescales involved. Such a slow hole transfer process is certainly unusual, though not unheard of. Recent work on an ITIC-based acceptor similar to A2 also found CT was not completed until around 100 ps, attributed to the low driving energy for the hole transfer process.[99] Therefore, it is likely that is also the reason for the slow hole transfer in the P2:A2 system, which features a similarly small driving energy.

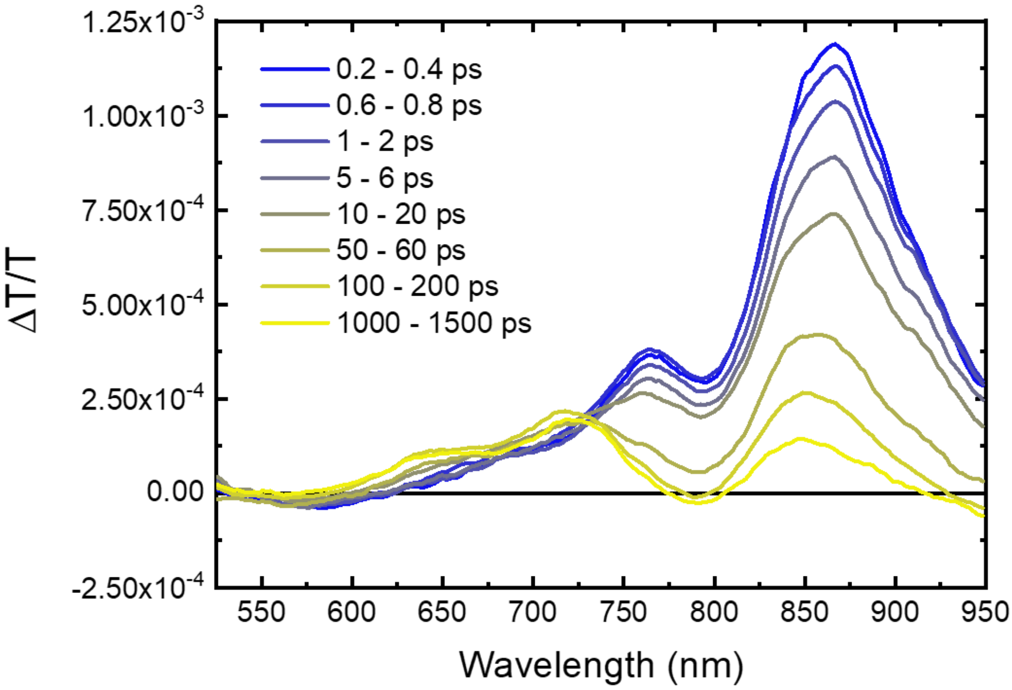

Figure 4.19: *The short-time TA spectra of a blend film of P2:A2, taken in the GSB region: λ_{ex} = 840 nm, fluence = 0.64 μJ cm^{-2}. The A2 GSB is clearly visible initially between 650 – 950 nm and decays slowly at first up to 10 ps. At this point, the decay appears to speed up and the P2 GSB between 600 – 750 nm begins to form. The continued loss of the A2 GSB and lack of growth of the P2 GSB, despite efficient CT occurring again suggests the presence of a new PIA growing in under the GSBs as CT occurs: likely the A2 anion.*

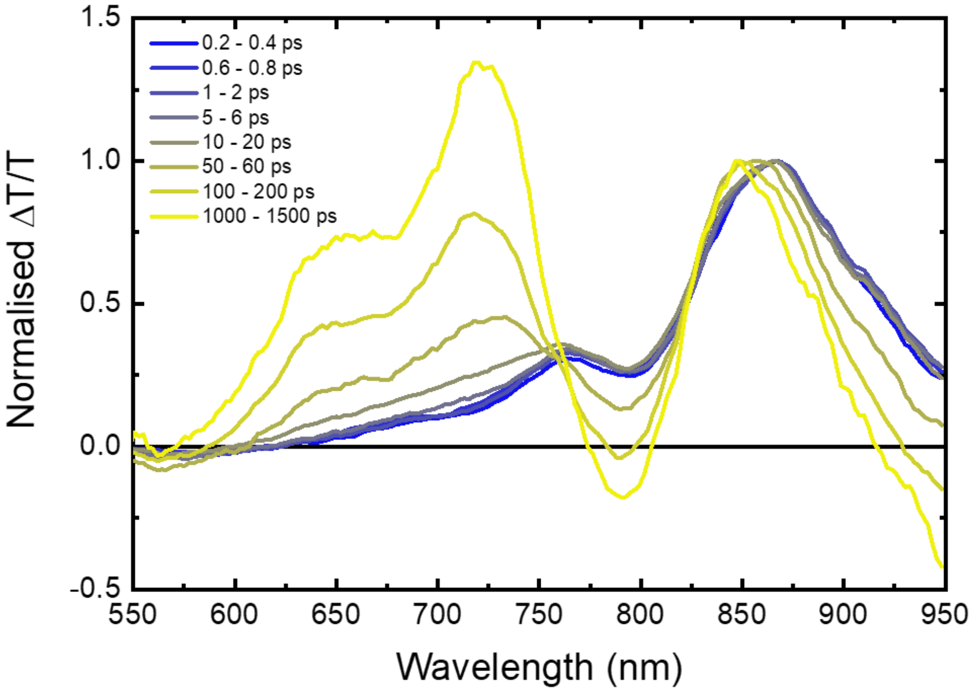

Figure 4.20: *The short-time TA spectra of a blend film of P2:A2, normlaised to the intensity of the A2 GSB peak: λ_{ex} = 840 nm, fluence = 0.64 μJ cm^{-2}. The normalisation allows the formation of the P2 GSB to be more clearly seen.*

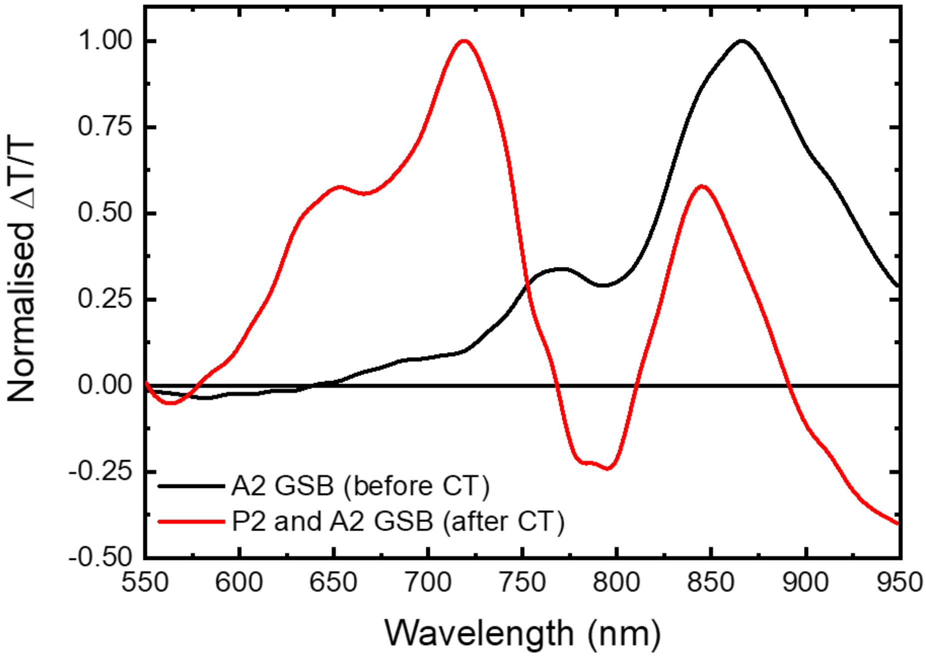

***Figure 4.21**: The GA extracted spectral features of the TA on the P2:A2 blend, taken from Figure 4.19. The black spectrum is present initially and belongs to the A2 GSB. As time progresses, the contribution from the A2 GSB decreases and a new species, representing the absorption of the blend after CT forms.*

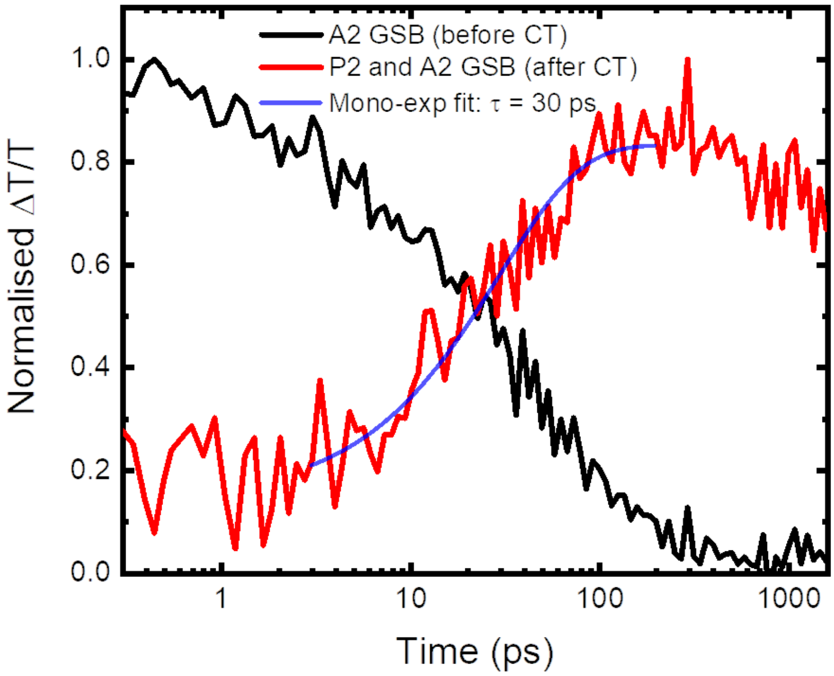

***Figure 4.22**: The kinetics of the GA extracted spectral features from the TA on the P2:A2 blend, taken from Figure 4.19. The black curve tracks the contribution of the A2 GSB to the total spectrum, whilst the red curve tracks the contribution of the spectrum associated with CT completion. The black curve initially decays by 20% in the first 3 ps, before the red curve rises, indicating the loss of A2 excitons. After CT begins at 3 ps, the red curve is fitted with a mono-exponential growth function to track the timescales of CT, yielding a time constant of 30 ps for this process.*

4.6.2 Excitation of mainly P2 in the P2:A2 Blend

Now that we have understood the hole transfer process from A2 to P2, we shall now address the photophysics occurring upon excitation of P2 in the blend. Whilst completely selective P2 excitation is impossible as its band gap is wider than that of A2, we shall excite in a region where A2 absorption in relatively low. With this in mind, we begin by exciting the P2:A2 blend at 620 nm with a fluence of 1.3 μJ cm^{-2}. By comparing the absorption strength at 620 nm, we note that this allows for an approximately 5:1 ratio of donor to acceptor excitation. The TA spectrum and kinetics from this measurement are shown in Figures 4.23 and 4.24.

By the first 200 – 300 fs, there is both a strong GSB signal from P2 and A2, as well as PIA features of the A2 singlet exciton at 1150 nm and the P2 singlet exciton as the broad absorption peaking towards 1600 nm. The presence of the strong A2 GSB at these early times indicates that some direct A2 excitation has also occurred. Of great curiosity though is how the spectral features evolve from this time point onwards. As we have already determined that within the first 10 ps there is minimal CT from A2 to P2, we can by a good approximation attribute any change in the spectral features primarily to excitons that originated on P2. Inside this timescale, there is a rapid loss of the P2 GSB with a parallel decrease in the P2 singlet exciton PIA. With this, there is also a slight increase in the intensity of the A2 GSB and small decrease in the spectral region associated with the A2 singlet and P2 hole PIAs. The interpretation of this evolution is not clear, as there are two possible processes that may be occurring. The first process is the most obvious: electron transfer from P2 to A2. This would result in the loss of the P2 singlet, as well as the growth in the A2 GSB. The rapid loss of the P2 GSB and only modest increase of the A2 GSB could be attributed to the PIA of the electron on A2 forming underneath them, which would drag down both of these features. The second process that could conceivably occur is FRET from P2 to A2, which may be rather efficient due to the excellent overlap of the P2 PL and A2 absorption spectra. Indeed, ultrafast FRET on ps-timescales has previously been observed in organic D/A blends.[100] FRET could also explain the rapid loss of both the P2 GSB and singlet exciton as the population was transferred to A2, as well as the growth of the A2 GSB. Though if the population transfer was as substantial as the loss of the intensity of the P2 singlet PIA was to suggest (around 50% in the first 10 ps), one may arguably expect a larger corresponding increase in the intensity of the A2 GSB. The most likely explanation therefore is that both electron transfer from P2 to

A2 and FRET from P2 to A2 are occurring in the blend within the first 10 ps, leading to the complex spectral evolution seen in the TA. However, due to the intimate convolution of these processes, it is difficult to estimate what fraction of excitons generated on P2 undergo FRET.

Over timescales longer than the first 10 ps, the spectral evolution is clearer. There is a rapid decrease in the intensity of the A2 GSB, with a matching drop in the PIA intensity around 1150 nm. The P2 GSB also stays relatively constant over these timescales, with perhaps a very slight increase in intensity if we observe the kinetics of the vibronic shoulder at 630 – 650 nm, furthest away from the A2 electron PIA under the two GSBs. The timescales and spectral evolutions are consistent with those seen when probing the processes that occur when exciting A2 selectively. Therefore, we attribute the majority of the spectral evolution over longer (>10 ps) timescales to the hole transfer from A2 to P2, regardless of if the origin of the A2 excitons was from direct excitation by the pump or FRET from P2.

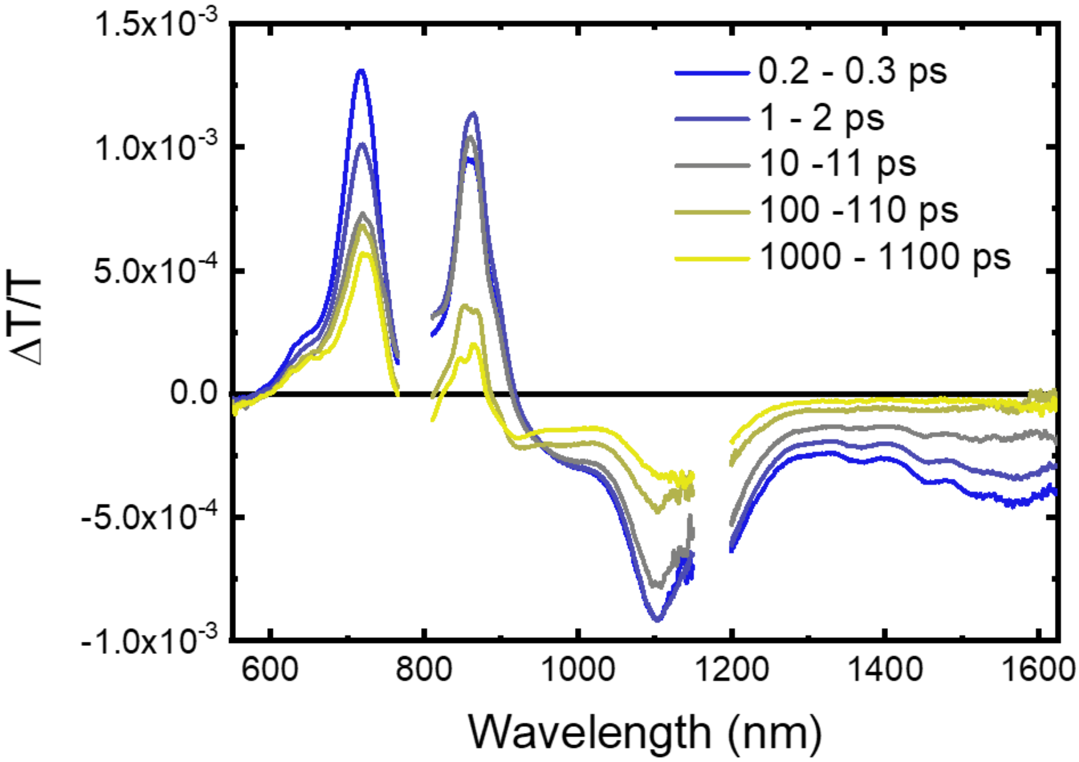

Figure 4.23*: The short-time TA spectra of a blend film of P2:A2: λ_{ex} = 620 nm, fluence = 1.3 μJ cm^{-2}. Both the P2 and A2 GSBs and their corresponding singlet PIAs are strongly visible at 200 fs, suggesting that direct excitation of both P2 and A2 has occurred. Within the first 10 ps where we expect minimal CT from the A2 excitons, there is a decrease in the P2 GSB and singlet PIAs, as well as a small increase in the A2 GSB. This is attributed to a mixture of electron transfer, as well as FRET, from P2 to A2. After 10 ps, the spectral evolution closely matches that of the same blend with selective A2 excitation and is therefore attributed to the hole transfer from excitons located on A2.*

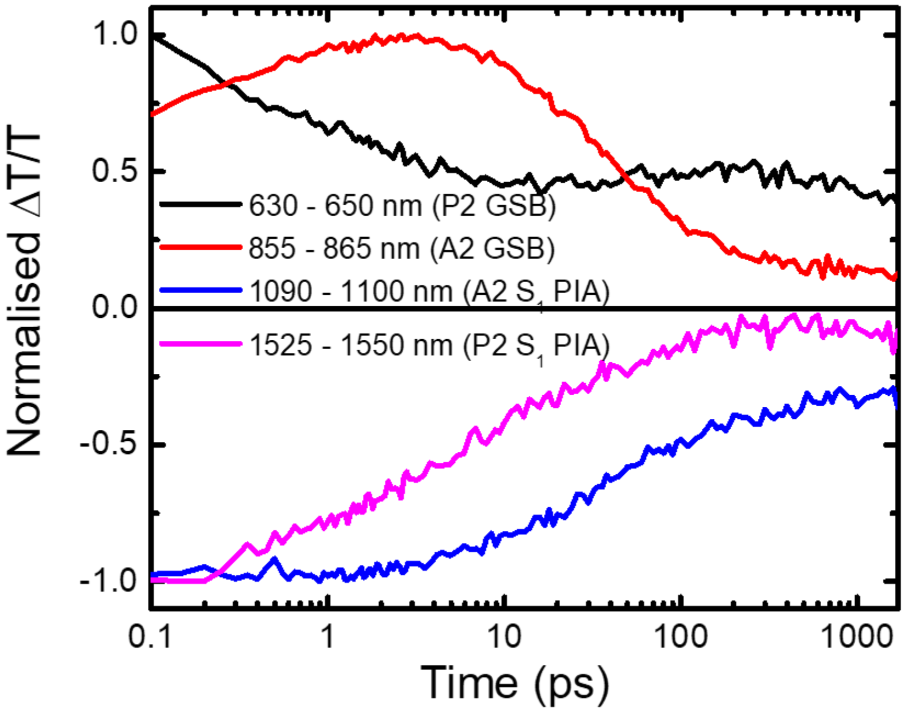

***Figure 4.24**: The short-time TA kinetics of a film of a blend film of P2:A2: λ_{ex} = 620 nm, fluence = 1.3 μJ cm^{-2}. The kinetics for the regions associated with the P2 GSB (710 – 730 nm), A2 GSB (850 – 860 nm), A2 singlet exciton (1100 – 1125 nm) and P2 singlet exciton (1525 – 1550 nm) are shown.*

4.6.3 Selective Excitation of A3 in the P2:A3 Blend

Having now completed our analysis of the early-time photophysics of the P2:A2 blend, we now shift our attention to P2:A3. As with the P2:A2 blend before, we begin our analysis by first exciting A3 selectively with a pump of 975 nm and a fluence of 1.6 μJ cm^{-2}. The associated TA spectrum and kinetics are shown in Figures 4.25 and 4.26. Despite exciting well below the band gap of P2, there is already a clearly visible P2 GSB formed by 200 fs. This suggests that at least some of the hole transfer from acceptor to donor in this blend proceeds on a timescale far faster than that of the P2:A2 blend. At this very early time point, the A3 GSB is also clearly visible, as well as the strong A3 singlet PIA at 1100 nm and the weak A3 singlet PIA band out towards 1600 nm. As time after excitation progresses, the P2 GSB continues to grow in, whilst the A3 GSB and singlet PIAs at 1100 nm and 1600 nm fall in step. In this blend, due the slight offset of the A3 singlet PIA at 1100 nm and the P2 hole PIA at 1150 nm, the hole PIA of P2 is now visible at around 100 ps, as a slightly red-shifted and broader feature under the A3 singlet. By 100 ps, there seems to be no further evolution of the spectral shape, and only a slight decay in the overall spectral intensity is seen. This is consistent with CT being completed by around this time. Indeed, this is confirmed by the kinetic traces of the features, which do not significantly change after 100 ps, bar a slight decrease consistent between them all. The slight decrease observed likely results from the beginning of charge recombination. As with A2, the A3 GSB also seems to rapidly decrease in intensity in tandem with the CT process, which we again attribute to the formation of a new PIA under the A3 GSB, most likely the PIA of the electron located on A3.

The similarity in spectral location of the electron PIA in both A2 and A3 can be readily rationalised by considering the structures of both. These molecules have an A-D-A form, with a central electron-rich core and electron-poor flanks. This A-D-A form means that the first singlet excited state will likely have some intramolecular CT character (ICT), with the hole

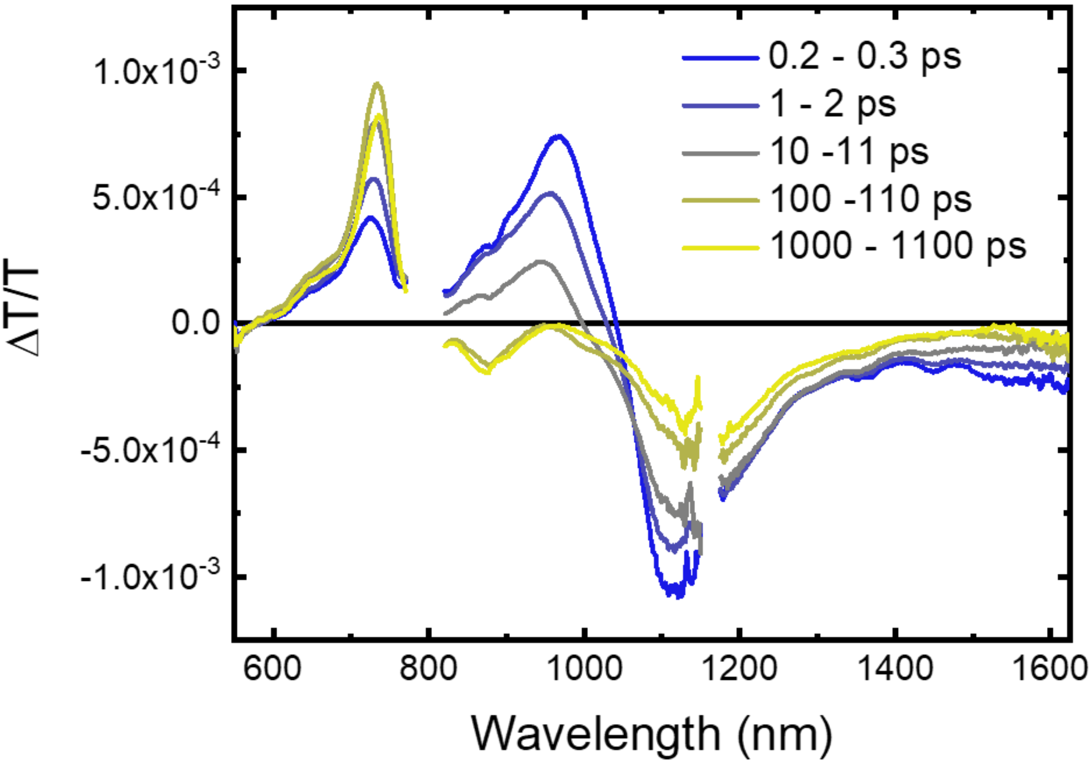

***Figure 4.25**: The short-time TA spectra of a blend film of P2:A3: λ_{ex} = 975 nm, fluence = 1.6 μJ cm^{-2}. The both the P2 and A3 GSBs are visible initially between 600 – 1050 nm, with the sharp PIA band at 1100 nm from the A3 singlet exciton. The P2 GSB continues to grow in, with the reduction of the A3 GSB and singlet features until spectral evolution is completed by 100 ps. Due to the slight offset between the A3 singlet PIA at 1100 nm and the P2 hole PIA at 1150 nm, the CT process can be viewed through the slight redshift and broadening of the band in this region with time.*

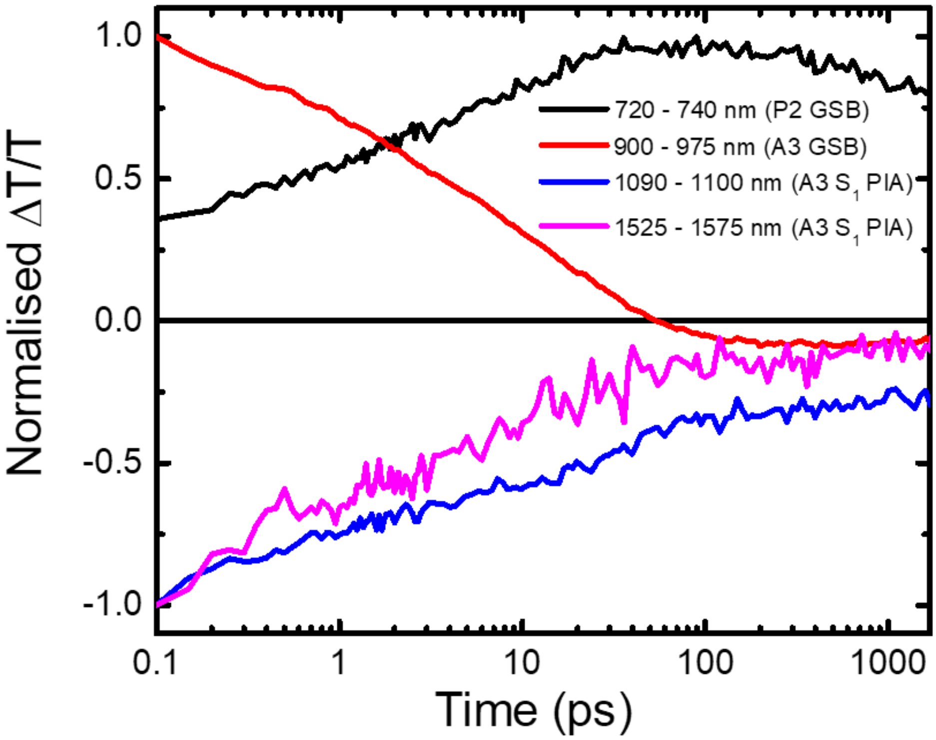

***Figure 4.26**: The short-time TA kinetics of a film of a blend film of P2:A3: λ_{ex} = 975 nm, fluence = 1.3 µJ cm^{-2}. The kinetics for the regions associated with the P2 GSB (720 – 740 nm), A3 GSB (900 –975 nm), and A3 singlet excitons (1090 – 1100 nm and 1525 – 1575 nm) are shown. Little change in the kinetics occurs after 100 ps, except a small decrease in all, likely due to recombination, indicating that the CT is completed by this time.*

wavefunction located on the D and the electron wavefunctions on the A. After the hole transfer process, one might expect the remaining electron wavefunction to remain located primarily on the A moieties of the molecules. Whilst the D core differs between A2 and A3, the A is almost identical, with just an additional fluorine atom on each of the two A moieties in A3. Therefore, this can explain the similarities between the TA of the blends, where the A2 and A3 GSBs are rapidly dragged down over the timescales that CT is occurring.

4.6.4 Excitation of mainly P2 in the P2:A3 Blend

To complete the short-time TA work, we finally look at the P2:A3 blend, excited at 620 nm with a fluence of 2.1 µJ cm^{-2}. With this pump wavelength we will excite mainly P2, with some A3 excitation also. We estimate the ratio of donor to acceptor excitation to be 6:1 at this excitation wavelength. The corresponding TA spectrum and kinetics are displayed in Figures 4.27 and 4.28. At 200 fs after excitation, we see both the P2 and A3 GSBs visible, with a sharp peak belonging to the A3 singlet at 1100 nm seemingly superimposed over a broader band that extends further into the IR past 1200 nm. Additionally, there is also very little evidence of the P2 singlet exciton band at around 1600 nm. The lack of P2 exciton PIA coupled with the broader band of the P2 hole underneath the A3 singlet PIA suggests that a significant portion of the electron transfer from P2 to A3 happens sub-200 fs. Such a rapid electron transfer is certainly possible in some OPV systems.[98,101] After this point, the system seems to evolve in a very similar manner to the measurements performed with selective A3 excitation, further confirming the hypothesis that the electron transfer from P2 is extremely rapid, largely occurring sub-200 fs.

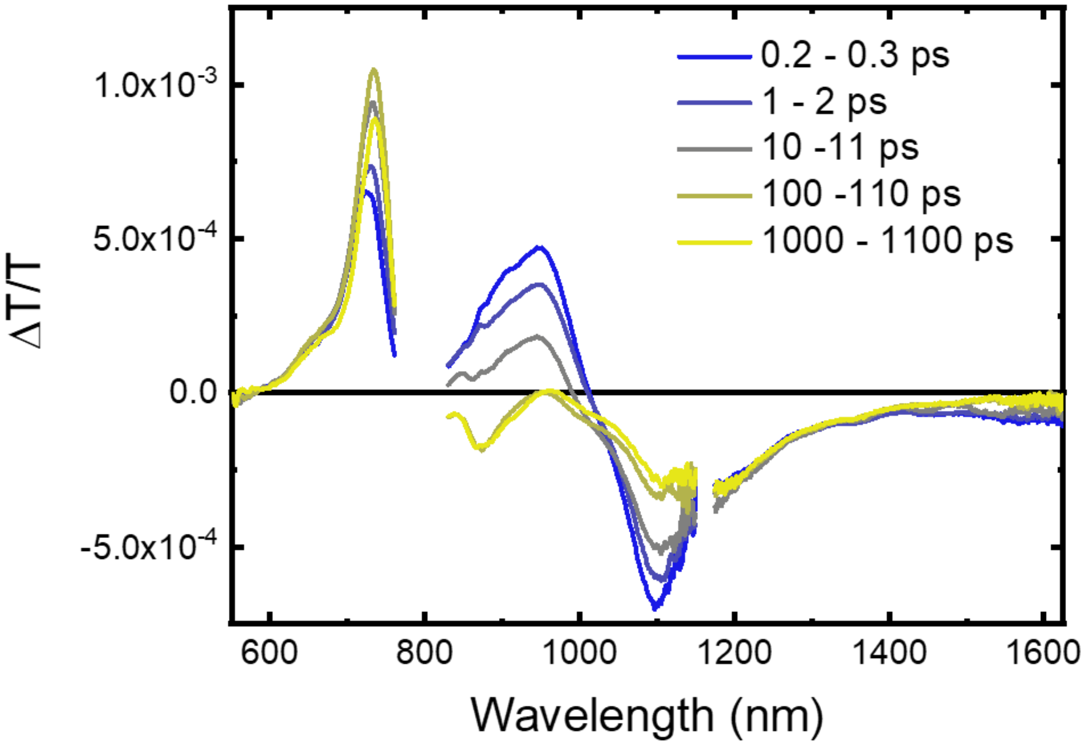

Figure 4.27*: The short-time TA spectra of a blend film of P2:A3: λ_{ex} = 620 nm, fluence = 2.1 μJ cm^{-2}. Both the P2 and A3 GSBs are visible initially between 600 – 1050 nm, with the sharp PIA band at 1100 nm from the A3 singlet exciton and a broader, slightly red-shifted band underneath. This redder band is likely the P2 hole PIA. There is very little evidence of the P2 singlet exciton at 1600 nm, despite the direct excitation of P2. The lack of P2 singlet PIA and what appears to be the presence of the P2 hole PIA suggests electron transfer occurs extremely rapidly, sub-200 fs. From this time onwards, the system seems to evolve as it did before, when A3 was selectively excited at 975 nm.*

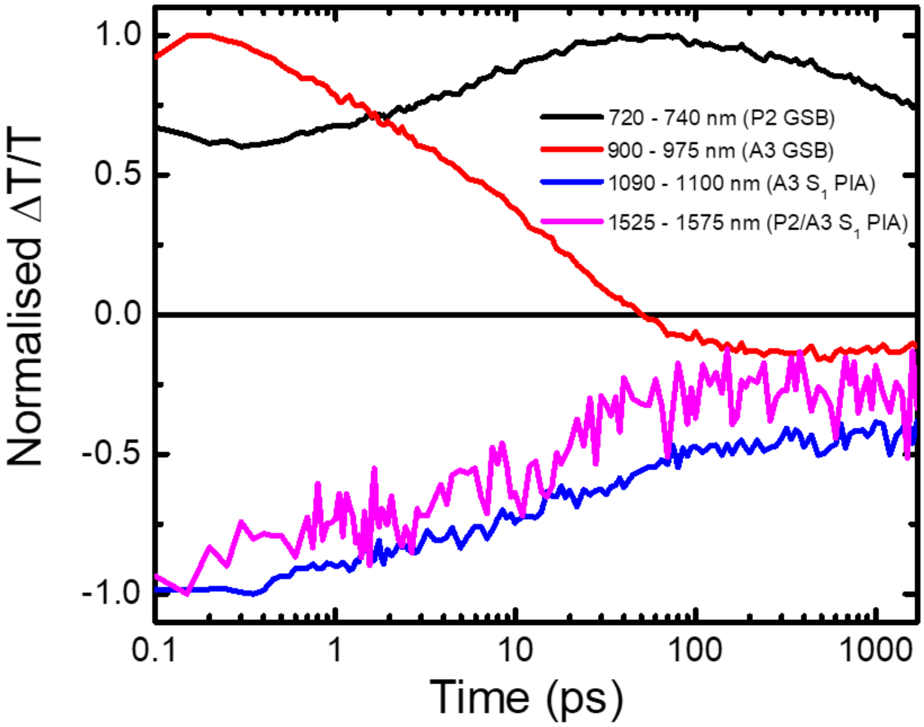

***Figure 4.28**: The short-time TA kinetics of a film of a blend film of P2:A3: λ_{ex} = 620 nm, fluence = 2.1 μJ cm^{-2}. The kinetics for the regions associated with the P2 GSB (720 – 740 nm), A3 GSB (900 –975 nm), and A3 singlet excitons (1090 – 1100 nm and 1525 – 1575 nm) are shown. Note the similarity to the kinetics of the same blend film excited at 975 nm, despite the significant amount of P2 excitation. This provides further proof that the electron transfer process from P2 to A3 occurs extremely rapidly.*

4.7 Long-Time Transient Absorption of the Blends

4.7.1 Long-Time Transient Absorption of P2:A2

Having completed our understanding of the short time photophysics of the blends, we now explore the long-time (ns – μs) behaviour and recombination using ns time resolved TA. For all measurements, a 532 nm excitation source was used. Though not at the absorption maxima of either the donor or acceptor components, it does excite both with a slight preference for P2. Thus, it may be considered somewhat of an extension of the 620 nm excited short-time TA seen previously.

First, we address the long-time TA of the P2:A2 blend, excited at 532 nm with a fluence of 3.7 μJ cm^{-2}. The TA kinetics and spectra are shown in Figures 4.29 and 4.30. As expected, the spectrum closely resembles that of the 1 ns time point spectra from the 620 nm excited short-time TA. The P2 GSB and hole PIA are both clearly visible, with a small hump around 850 nm belonging to the A2 GSB. As time progresses, both the P2 GSB and hole PIA decay in-step, clearly demonstrated by the kinetic traces of these features. Additionally, there appears to be no formation of additional PIAs over the timescale of the recombination processes. This is extremely interesting, as it informs us that no additional species are created as a result of recombination. This includes triplet excitons that are generated from triplet CT states formed via the bimolecular recombination of free charges, that are a well-known non-radiative recombination loss pathway in OPV devices.[13] To further demonstrate this, Figure 4.31 contains the normalised spectrum in the NIR region (950 – 1600 nm) where the PIAs of triplet excitons are typically found in organic materials.[13,54,55,61,102–104] Aside from the loss of a band between 1300 – 1550 nm on the 10s of ns timescale, there is no obvious change in the spectral shape in the NIR, implying that recombination occurs solely via CT states to the ground state directly. The significance of the lack of triplet exciton formation will be further expanded on in a subsequent section.

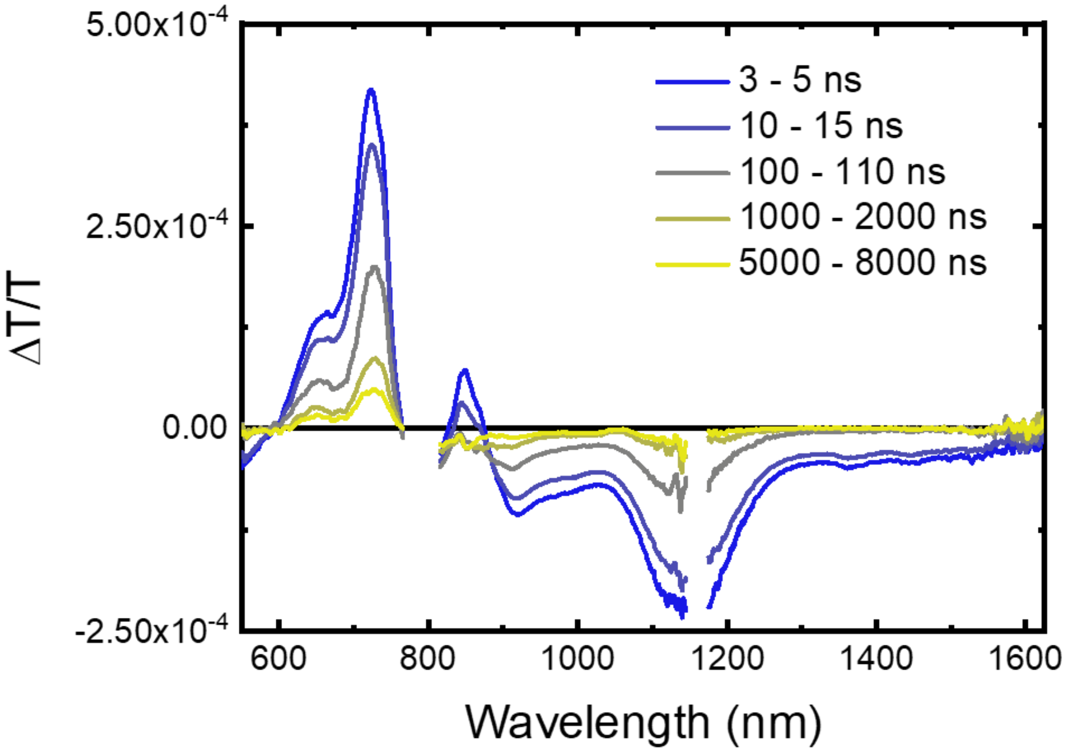

Figure 4.29*: The long-time TA spectra of a blend film of P2:A2: λ_{ex} = 532 nm, fluence = 3.7 μJ cm^{-2}. Both the P2 GSB and hole PIAs are clearly visible and decay in-step up to 10 μs. No additional PIA features are formed over the recombination timescales, indicating the absence of any triplet states formed via bimolecular recombination.*

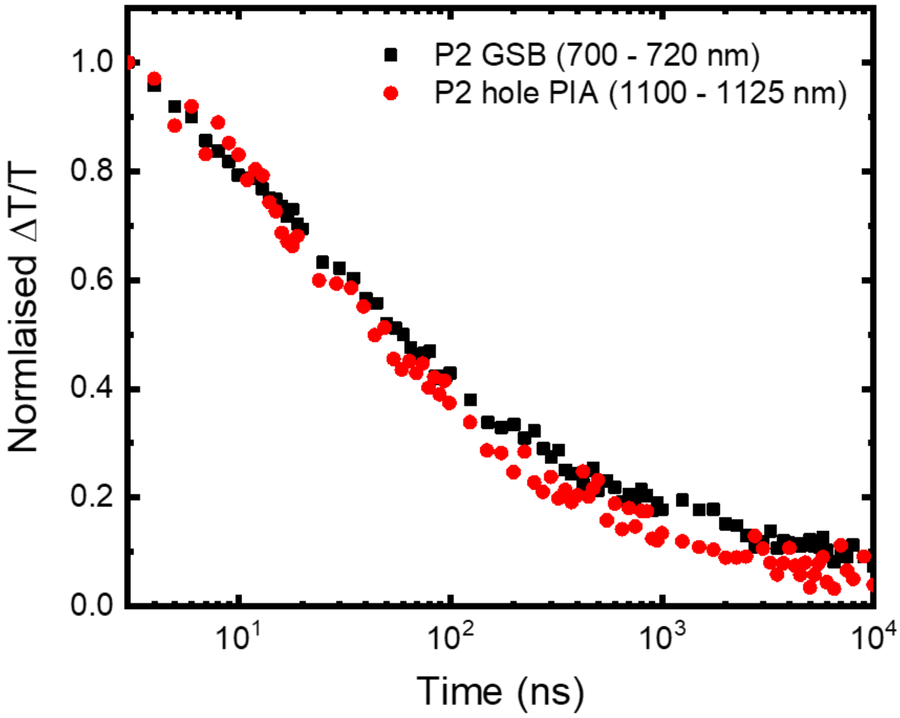

***Figure 4.30**: The normalised long-time TA kinetics of a blend film of P2:A2: λ_{ex} = 532 nm, fluence = 3.7 μJ cm^{-2}. Traces taken from the P2 GSB (700 – 720 nm) and the P2 hole PIA (1100 – 1125 nm) decay in-step up to 10 μs, implying the direct recombination of CT states to the ground state is the only decay pathway.*

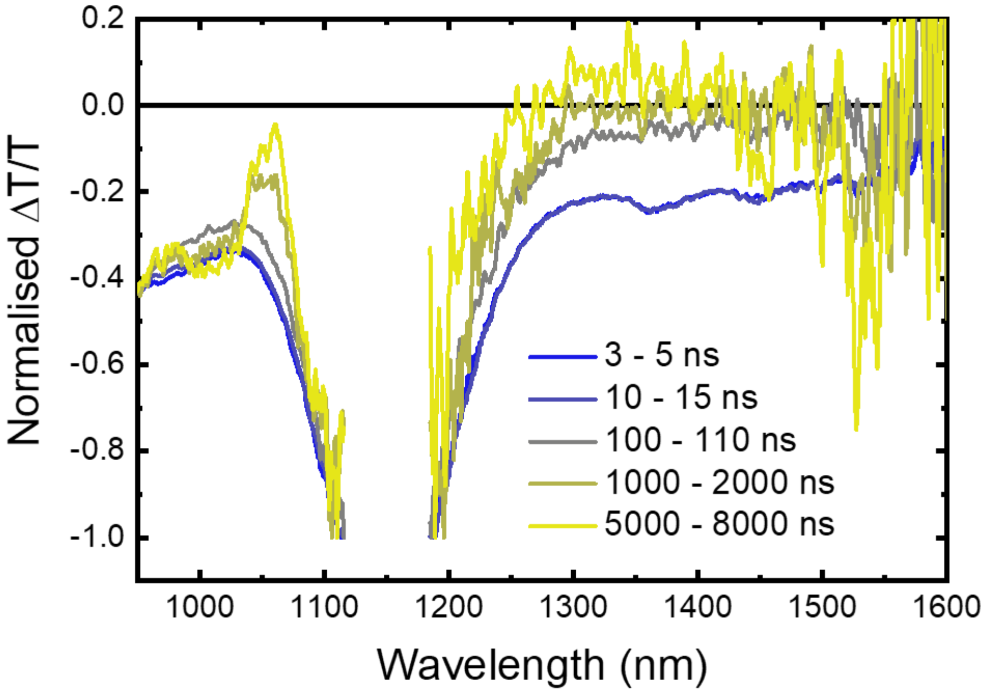

***Figure 4.31**: The long-time normalised TA spectra of a blend film of P2:A2: λ_{ex} = 532 nm, fluence = 3.7 μJ cm^{-2} in the NIR region. There is a decrease in the absorption between 1300 – 1550 nm on the 10s of ns timescales, but no growth in of any new PIA features that could be attributed to triplet excitons. Therefore, it is apparent that triplet exciton formation through bimolecular recombination is suppressed in this blend.*

4.7.2 Long-Time Transient Absorption of P2:A3

Next, we examine the long-time TA of the P2:A3 blend, again excited at 532 nm with a fluence of 9.7 μJ cm^{-2}. The resulting TA spectra and kinetics are shown in Figures 4.31 and 4.32. Very similarly to P2:A2, we see the clear presence of the P2 GSB and hole PIA, with a very small positive bump around 975 nm from the A3 GSB. The spectrum in this blend also appears to decay without evolution, as can be seen by the decays of the P2 GSB and hole PIA closely tracking each other. As with the P2:A2 blend before, we have normalised the NIR region where triplet exciton PIAs are typically found to further demonstrate that new PIA features are formed over the timescales of charge recombination (Figure 4.34). This again implies that no new states are formed through the recombination process, also ruling out the formation of triplets in this blend. The significance of the lack of triplets will now be discussed in more detail in the following section.

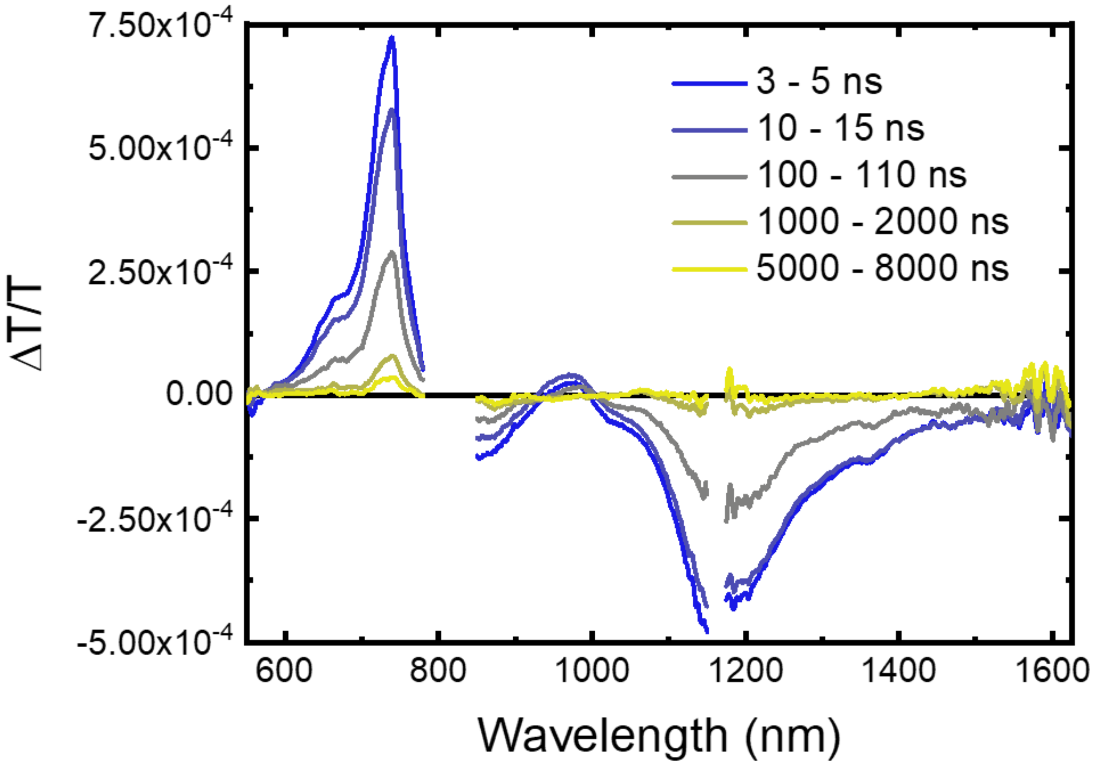

***Figure 4.32**: The long-time TA spectra of a blend film of P2:A3: λ_{ex} = 532 nm, fluence = 9.7 μJ cm^{-2}. Both the P2 GSB and hole PIAs are clearly visible and decay in-step up to 10 μs. No additional PIA features are formed over the recombination timescales, indicating the absence of any triplet states formed via bimolecular recombination.*

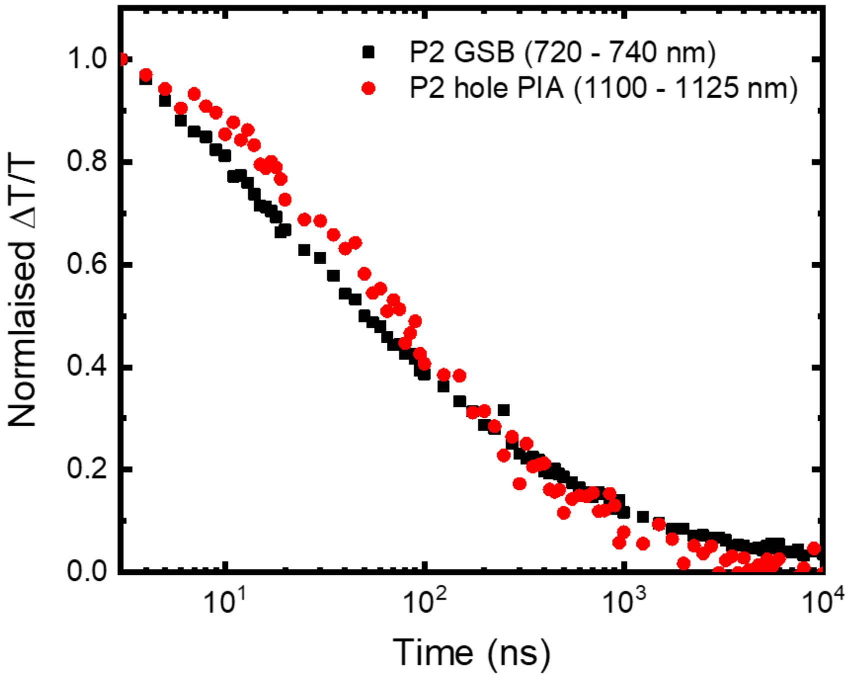

Figure 4.33: *The normalised long-time TA kinetics of a blend film of P2:A3: λ_{ex} = 532 nm, fluence = 9.7 μJ cm^{-2}. Traces taken from the P2 GSB (720 – 740 nm) and the P2 hole PIA (1100 – 1125 nm) are clearly visible and decay in-step up to 10 μs, implying the direct recombination of CT states to the ground state is the only decay pathway.*

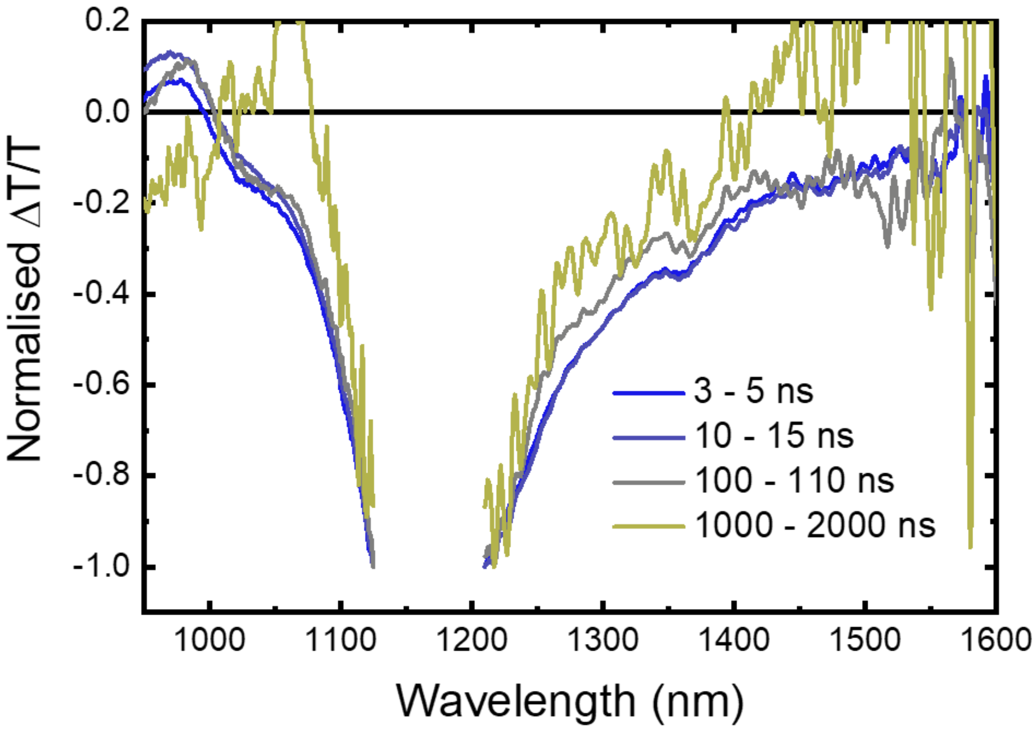

Figure 4.34: *The long-time normalized TA spectra of a blend film of P2:A3: λ_{ex} = 532 nm, fluence = 9.7 μJ cm^{-2} in the NIR region. This plot emphasises that there is no growth in of any new PIA features that could be attributed to triplet excitons over the timescales of recombination. Therefore, it is apparent that triplet exciton formation through bimolecular recombination is suppressed in this blend.*

4.8 Supressed Triplet Formation in the Blends

Having completed our understanding of the photophysics of the blends, we now reflect upon our findings. Of most interest is the discovery that no triplet excitons are visibly formed during the recombination processes, which are considered detrimental to OPV performance as they act as a non-radiative decay pathway, leading to a loss of carriers and the reduction of the open-circuit voltage.[105] Local triplet formation is a pervasive problem in fullerene acceptor OPVs and has been reported in numerous systems, including the analogous fullerene system of our donor polymer P2,[102,104,105] where local triplet formation was also found to be supressed when a perylene-diimide (PDI) based NFA was employed instead.[97] Therefore, the finding that triplet formation is not only supressed in our NFA systems, but is also linked to a much reduced non-radiative voltage loss, is particularly exciting. However, before we attempt to understand the reasoning for this in our blends, we must first deepen our understanding of the processes leading to local triplet formation. Previous work by Schlenker *et al.* provides a valuable insight into the process of local triplet formation.[61] In their work, they investigated a blend of the donor material PIDT-PhanQ with a variety of fullerene derivatives with different band gaps where the fullerene triplet level also remained constant at around 1.4 – 1.5 eV. Through this, they were able to vary the energy of the ^{3}CT state with respect to the constant triplet energy of the fullerene. They found that when the fullerene local triplet was higher in energy than the ^{3}CT and therefore inaccessible, no formation of triplets on PIDT-PhanQ was observed. This was despite it possessing a local triplet energy of 1 eV, well below that of the ^{3}CT state that should make triplet formation thermodynamically favourable. However, when the ^{3}CT energy was raised and became equal to or above that of the fullerene triplet, the formation of triplets on PIDT-PhanQ was observed. This suggested that the fullerene local triplet acted as an intermediate for triplet formation on the donor, with population of the donor triplet occurring via dexter energy transfer from the fullerene triplet. However, a detailed explanation was not given, with only the claim that the fullerene triplet was more kinetically accessible provided.

In recent work by Kraus *et al.* on the blend of PTB7:PC$_{70}$BM, including a very similar donor material to P2, they proposed that if the rate of the electron transfer that forms the local triplet state is sufficiently slow, then it may be out-competed by re-dissociation of the ^{3}CT into free charges, leading to negligible triplet formation.[106] Indeed, previous work by Smith *et al.* has suggested that the dissociation of cool CT states, the type formed by the back electron transfer process, is likely to be possible.[107] However, in order to build on the kinetic argument put forward, we will now consider the energetics of our P2:A2 and P2:A3 systems where triplet formation is not observed. As previously discussed, the formation of a local triplet state from the ^{3}CT requires a relatively slow electron transfer step and as such can be described by Marcus theory. The equation governing the rate of electron transfer (k_{et}) was given previously (equation 2.77), but will be repeated here for clarity:

$$k_{et} = \frac{2\pi}{\hbar}|H_{DA}|^2 \frac{1}{\sqrt{4\pi\lambda k_B T}} e^{\left(-\frac{(\lambda+\Delta G^o)^2}{4\lambda k_B T}\right)} \tag{4.2}$$

From this, there are three variables that control the rate of the electron transfer: the electronic coupling between the electron D and A (H_{DA}), the re-organisation energy (λ) and the driving force for the electron transfer (ΔG^o).

In P2:A2 and P2:A3, the triplet on P2 has previously been reported to lie at about 1 eV.[97,106] Given the narrow band gaps of A2 and A3 of 1.37 eV and 1.22 eV, it is probable that the highest lying triplet state is the one on P2. Therefore, it is likely this state will be involved in the initial back electron transfer, regardless of whether the triplet ultimately ends up on the acceptor. For P2:A2, the CT lies at 1.29 eV and for P2:A3, at 1.19 eV. Therefore, the driving energy for the back electron transfer is around ~0.08 eV in the P2:A2 blend and ~0.03 eV in P2:A3. In organic π-conjugated molecules, the reorganisation energy is typically on the order of 0.1 – 0.3 eV,[107] whilst H_{DA} and ΔG^o are likely to vary significantly between blends. Taking a middle value of $\lambda = 0.2$ eV, calculations performed by Dr Anton Pershin have produced a 2D contour plot of the rate of back electron transfer as a function of H_{DA} and ΔG^o (Figure 4.35). As expected from Marcus theory, when $\Delta G^o = \lambda$, the rate of the electron transfer is maximised. Therefore, in our systems that have a driving energy of only a little lower than the reorganisation energy, this leads to the rate for the electron transfer falling upon a line that would pass near the maxima of the plot. However, we also note that even when the driving energy is increased past 0.2 eV so that the electron transfer falls into the Marcus inverted region, the rate constant still remains extremely high ($k_{et} > 10^{11}$ s^{-1}) up to a driving energy of around 0.8 eV. Such a large energy difference between the CT state and the triplet is far in excess of those likely to be present in high-performance OPV blends, as it would require a high energy CT state (>1.8 eV) that is not compatible with the relatively small band gaps required for significant absorption across the solar spectrum (<1.5 eV). Therefore, we propose that the factor responsible for the kinetically supressed local triplet formation in both our blends and other NFA OPV systems is likely the electronic coupling between the donor and the acceptor. However, the calculation of electronic coupling strengths is complex and depends on the

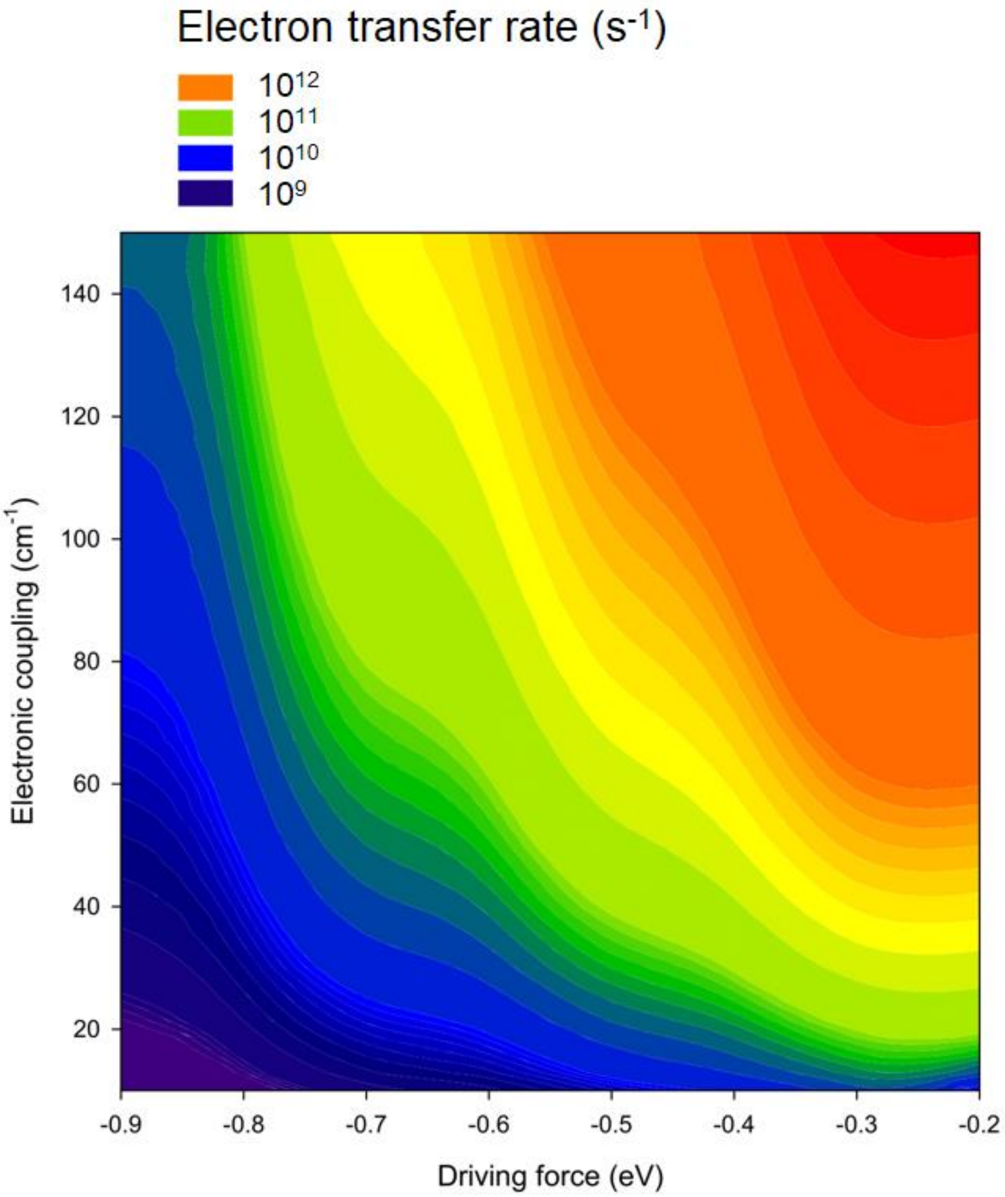

Figure 4.35*: A 2D contour plot of the rate of the back electron transfer process from the ^{3}CT to the local triplet state for a reorganization energy of 0.2 eV. The rate is very fast even into the Marcus inverted regime, with rate constants of >10^{11} s^{-1} up until a driving force of 0.8 eV. Both P2:A2 and P2:A3 have driving forces that would lead the rate to fall on a line that crosses near the maxima of the plot. Therefore, the electronic coupling between D and A is the factor that is most likely to make this process slow enough that it is out-competed by CT re-dissociation. Calculations performed and plot produced by Dr Anton Pershin.*

relative molecular orientations and intermolecular distances.[103] Therefore, future work should focus on further exploring this parameter.

4.9 Conclusions

In this work, we have investigated two efficient polymer-NFA OPV blends that possess a low overall voltage loss. Through EL measurements on the devices, we have shown they benefit from an exceptionally low non-radiative voltage loss, in particular for the blend of P2:A2. In fact, the magnitude of the non-radiative voltage loss in P2:A2 approaching those measured in efficient inorganic photovoltaic technologies, such as perovskites.[87] Through a detailed study of the photophysics of the blends using ultrafast TA (summarised in Figure 4.36), we have shown that the hole transfer process from the NFAs to P2 proceeds exceptionally slowly, likely as a result of the very low driving energy of around 100 meV or less in both systems. Nevertheless, this process is efficient and largely out-competes decay of the singlet state, as evidenced by the high EQE_{PV} of both devices. Additionally, there is evidence for ultrafast FRET from P2 to A2, competing with the electron transfer process. FRET is not observed from P2 to A3, likely as the electron transfer in this blend is extremely rapid (<200 fs).

We further performed long-time TA on the blends to investigate their recombination pathways and dynamics. From these measurements, we saw no evidence of any formation of new PIAs in the NIR region, suggesting that recombination was occurring solely from CT states directly to the ground state with no intermediates. This provides good evidence that both blends have a supressed formation of triplet states, formed via a back electron transfer from the ^{3}CT. As the formation of low-energy triplet excitons is considered a major non-radiative loss pathway in OPV devices, we attribute the extremely low non-radiative voltage loss of the blends to this suppression of triplet exciton formation.

To understand why this back electron transfer process was supressed in our blends, we turned to Marcus theory to describe the electron transfer occurring. By taking a reasonable approximation of the reorganisation energy for this process in our blends from other organic D/A systems, we explored the effect that the other variables have on the rate of this process. We find that the driving force for the electron transfer from ^{3}CT to T_1 is unlikely to significantly retard the rate, unless the offset between these states is very large (>0.8 eV). Such a large offset is not compatible with the low band gaps of typical OPV materials (~1.5 eV), which often render the CT state energy on the order of 1 – 1.3 eV. Therefore, we conclude that the primary factor for the suppression of this process is the weak electronic coupling between the states. An exciting avenue for future exploration is therefore to further investigate the factors affecting the electronic coupling between molecules at the interface of the BHJ. If detailed information about this parameter can be gleaned, it may then be intelligently applied to the design rational of future OPV donor and acceptor materials, in an attempt to help kinetically control the rate of the back electron transfer process that forms the triplets.

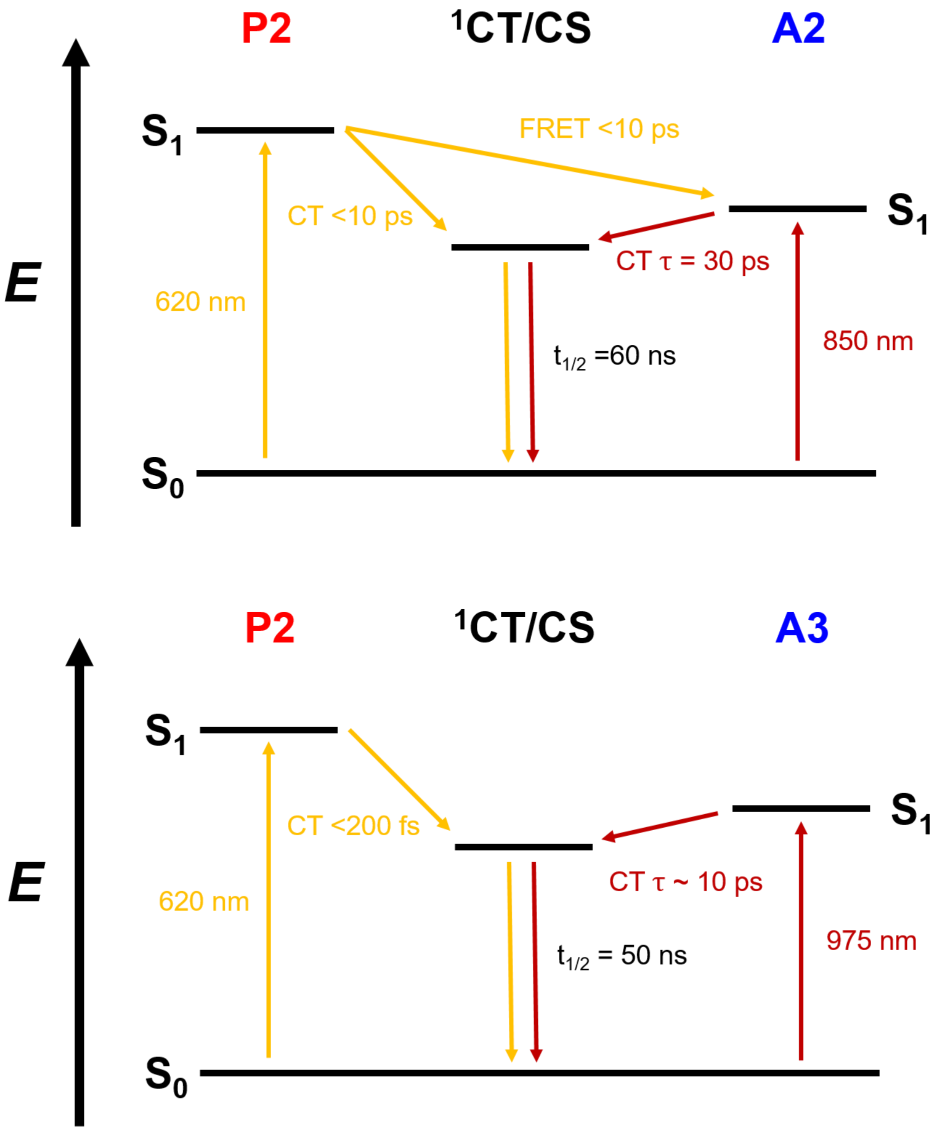

Figure 4.36: *Schematics summarizing the processes occurring on ultrafast timescales in the P2:A2 and P2:A3 blends, as determined from the short-time TA experiments.*

5 Utilising a Low Exchange Energy Acceptor to Turn Off Triplet Exciton Formation in OPV Devices

5.1 Motivation

As we have seen in the previous chapter, the suppression of triplet formation in OPV blends is key to reducing the non-radiative voltage loss in these systems, a prerequisite to making them more competitive with inorganic technologies. However, whilst their suppression was achieved by relying solely on kinetics to turn off triplet formation, as the triplet levels were still below the ^{3}CT and therefore energetically accessible, this is a factor that is unpredictable and difficult to control. Thus, perhaps a more effective way to achieve this would be to thermodynamically forbid triplet formation instead, guaranteeing that this loss pathway is removed.

In order to investigate the effectiveness of thermodynamically forbidding molecular triplet formation, we decided to construct OPV blends where the lowest local triplet state lies higher in energy than the ^{3}CT formed between the D and A components. This however is not a trivial task, as the size of the ΔE_{ST} in most conjugated organic materials is typically 0.6 – 1 eV.[108] Therefore, if we used materials with this magnitude of ΔE_{ST}, we would require an extremely large energy difference between the lowest energy singlet and the CT to achieve this, resulting in a very large overall energy loss that would negate any voltage gained from removing the triplet loss pathway. With this in mind, we need to identify a class of materials that possess a sufficiently small ΔE_{ST} that the triplet energy can be above the CT energy without incurring exorbitant energetic penalties.

One way to achieve this condition is to consider molecules whose lowest energy exciton has strong ICT character. In fact, organic small molecules that exhibit TADF, which have recently garnered much attention for use as emissive dopants in OLEDs, are potential candidates. In these molecules, the strong ICT character of the lowest energy excited state, with minimal spatial overlap between the HOMO and LUMO results in S_1 and T_1 states that are very close in energy (ΔE_{ST} ~25 meV).[109] TADF occurs via successive cycles of ISC and rISC, enabling typically non-emissive triplet excitons to be converted into emissive singlet excitons.[70] In fact, dopants based on TADFs can exhibit PLQEs approaching unity and an EQE_{EL} as high as 37%.[110]

Figure 5.1 shows how these molecules might be used within the context of an OPV device. As previously discussed, conventional polymeric donor materials have a low energy molecular T_1 state to which ^3CTs can transfer and become trapped, increasing non-radiative losses. A donor with strong ICT states would raise the energy of this local T_1 state to be almost isoenergetic with the S_1.[111] This would allow for the creation of a high-energy intermolecular CT state to maximise the V_{OC}, without incurring the energy loss pathway via the ^3CT to the donor T_1.[112] Furthermore, if the formation of ^3CT states no longer leads to terminal non-radiative pathways, their creation could indeed be beneficial to OPV device performance by acting as a barrier to charge recombination, as direct recombination to the singlet ground state from the ^3CT is spin-forbidden.[113] These spin-protected ^3CT states could then either rISC to the ^1CT or re-dissociate into free charges, recovering charge carriers that would have otherwise been lost.

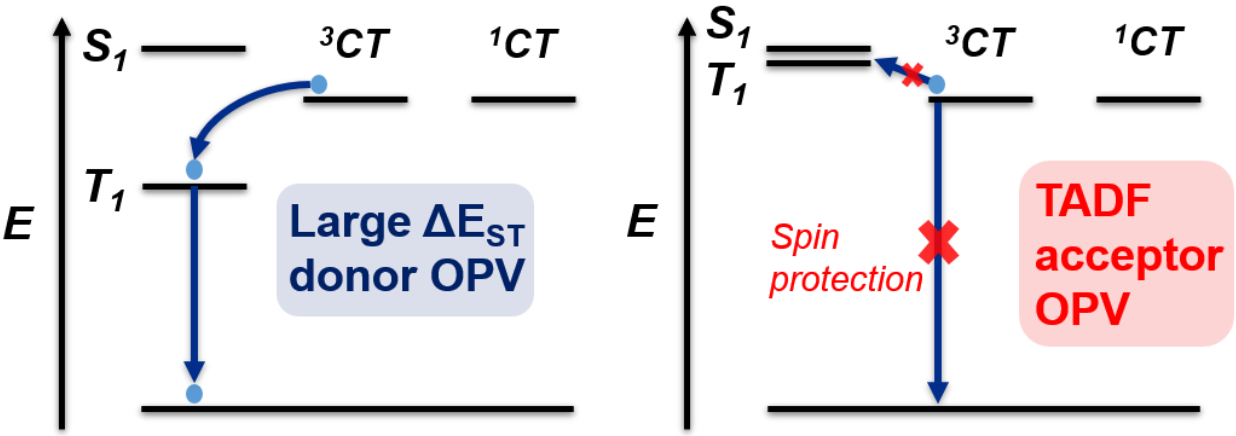

Figure 5.1: *A schematic displaying the energetics of a typical polymeric donor OPV with a large ΔE_{ST} and those of a TADF acceptor OPV with a small ΔE_{ST}. Systems with a large ΔE_{ST} donor possess a low-lying T_1 state to which ^3CT states, formed by the bimolecular recombination of free charges, can transfer to. The exciton is then energetically trapped on this T_1 state, where it ultimately decays non-radiatively. In contrast, a system with a low ΔE_{ST} would remove this low energy T_1, eliminating this loss pathway for ^3CT states. Additionally, now that there are no major non-radiative loss pathways for the ^3CT, their formation could be beneficial for device performance. As they cannot directly recombine to the spin singlet ground state (S_0), their lifetime is increased, allowing for additional time for charge separation to reoccur from the ^3CT. This would enable an OPV device based off a small ΔE_{ST} acceptor to recycle charges that would otherwise be lost, improving photocurrent and reducing non-radiative losses.*

5.2 Materials

The materials used in this study are the TADF dopant material 2-(4-(diphenylamino) phenyl)-10,10-dioxide-9H-thioxanthen-9-one (TXO-TPA), which is employed as the electron acceptor material and N,N′-Di(1-naphthyl)-N,N′-diphenyl-(1,1′-biphenyl)-4,4′-diamine (NPD) and poly[(9,9-dioctylfluorenyl-2,7-diyl)-co-(4,4′-(N-(4-sec-butylphenyl)diphenylamine)] (TFB), which are the electron donors. TXO-TPA and NPD were purchased from Lumtec, whilst TFB was acquired from Sigma Aldrich. The structures of the materials are shown in Figure 5.2. For consistency, the HOMOs of the materials were measured using CV at the same time under identical conditions by Jake Greenfield, with the LUMO calculated from this using the optical band gap calculated from the onset of absorption. The optical properties and energetics of the materials are summarised in Table 5.1. Included in this table is the energy of the lowest triplet state in the molecules as it is extremely relevant to this work. Whilst the LUMO-LUMO offset from D to A is large, on the order of 700 meV, the HOMO-HOMO offset is much smaller: lower than 100 meV. This is an important point to note, as it ultimately aids in minimising the energy loss incurred from charge separation and therefore will contributes to the overall total low voltage loss in these systems. As desired, the lowest energy triplet is located on TXO-TPA at 0.04 eV below its singlet,[114] with an energy of 2.14 eV. The triplets of the donors NPD and TFB are higher at 2.3 eV.[115,116] All triplet energies were estimated from the highest energy peak of the previously-reported low temperature phosphorescence spectra. Though there is some inherent uncertainty in the values calculated from the HOMO that was obtained by CV,[117] the triplet level of TXO-TPA likely lies just above or equal in energy to the ^{3}CT. An important point to note is that even if the triplet of TXO-TPA is accessible by the ^{3}CT, this should not significantly increase the non-radiative recombination in the blend, as the TADF-active TXO-TPA can efficiently convert the triplets back into singlets.[114]

Material	HOMO (eV)	E_g (eV)	HOMO + E_g (eV)	HOMO-HOMO offset (eV)	"LUMO-LUMO" offset (eV)	T_1 energy (eV)
TXO-TPA	-5.24	2.18	-2.95	-	-	2.14
NPD	-5.19	3.00	-2.19	0.05	0.76	2.30
TFB	-5.16	2.90	-2.26	0.08	0.69	2.30

***Table 5.1**: The energetics and optical properties of the three materials under study in this section. Important to note is the small ΔE_{ST} of TXO-TPA, which should allow the triplet state to be equal to or higher in energy than the ^{3}CT formed between it and the donors.*

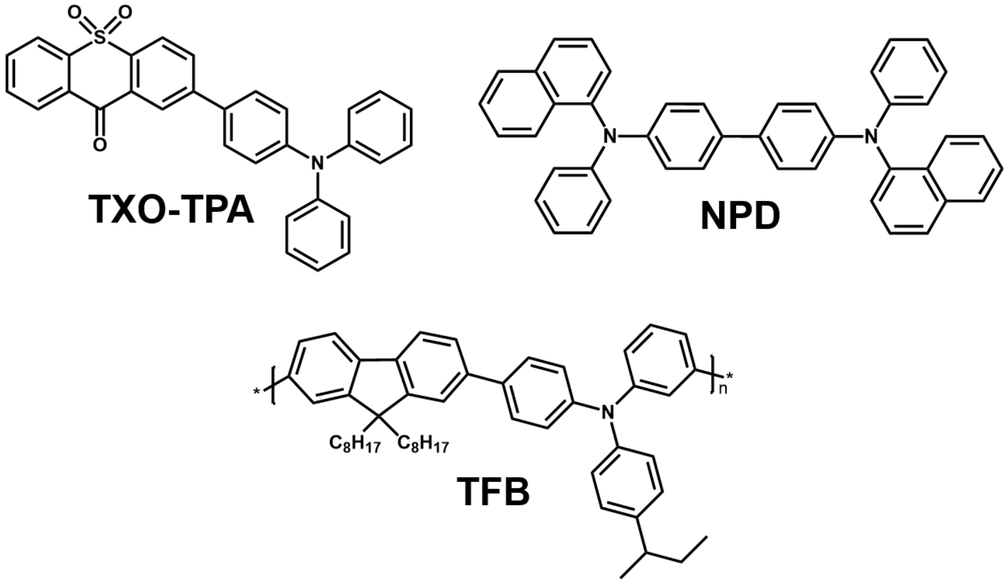

Figure 5.2*: The chemical structures of the materials used in this study: the TADF material TXO-TPA that acts as the electron acceptor and the electron donors NPD and TFB.*

5.3 Steady-State Absorption

We first examine the steady state absorption of films of the neat materials, shown in Figure 5.3. Neat TXO-TPA and NPD films were prepared by thermal evaporation, whilst neat TFB films were spun from a 20 mg/mL chlorobenzene solution at 1000 rpm. It is immediately apparent that the absorption of these materials is primarily located in the blue and UV, not ideal for efficient OPV performance. Whilst this is true, we envisage this work as a model study to investigate the effect of removing the triplet loss pathway, so a high device PCE is not our main priority. Usefully, TXO-TPA possess an ICT absorption band that extends out towards 550 nm, below the absorption onsets of NPD and TFB. This will allow us to selectively excite TXO-TPA so that we can track any potential hole transfer that occurs to the electron donors. Next, we turn to the absorption spectrum of the blend films in Figure 5.4. For these measurements, the NPD:TXO-TPA blend with a 1:1 weight ratio was prepared by thermal evaporation, whilst the 1:1 weight ratio film of TFB:TXO-TPA was spun from a 20 mg/mL solution in chlorobenzene at 2000 rpm. As expected, the absorption spectrum is an admixture of the neat components, with strong absorptions in the UV and a weak ICT band stretching out into the visible region that belongs to TXO-TPA.

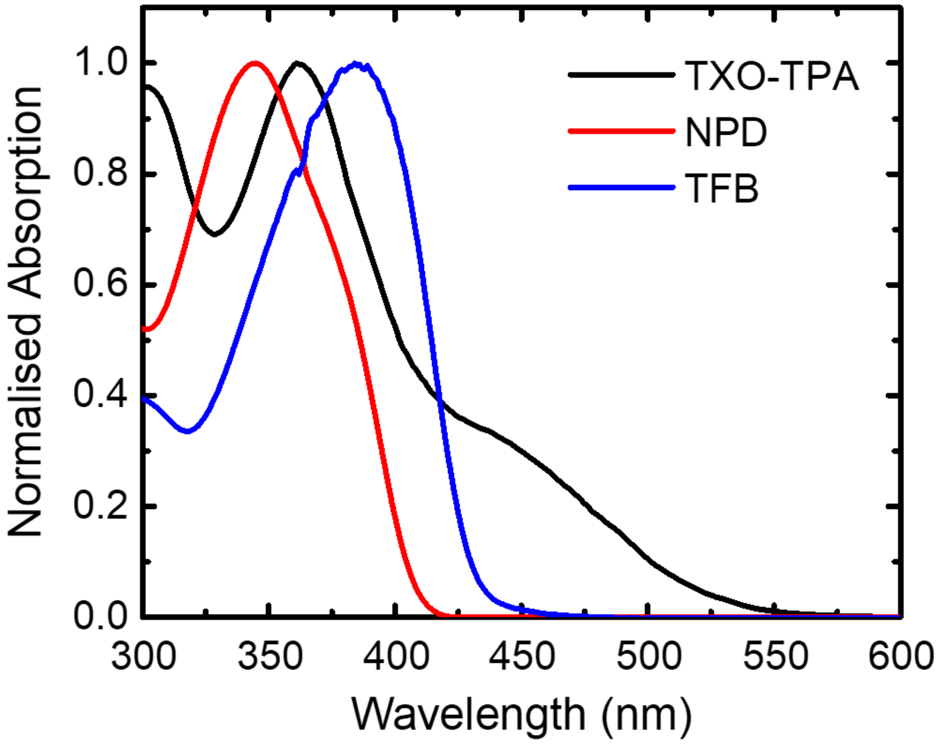

Figure 5.3*: The normalised absorption spectra of neat films of the materials used in this study.*

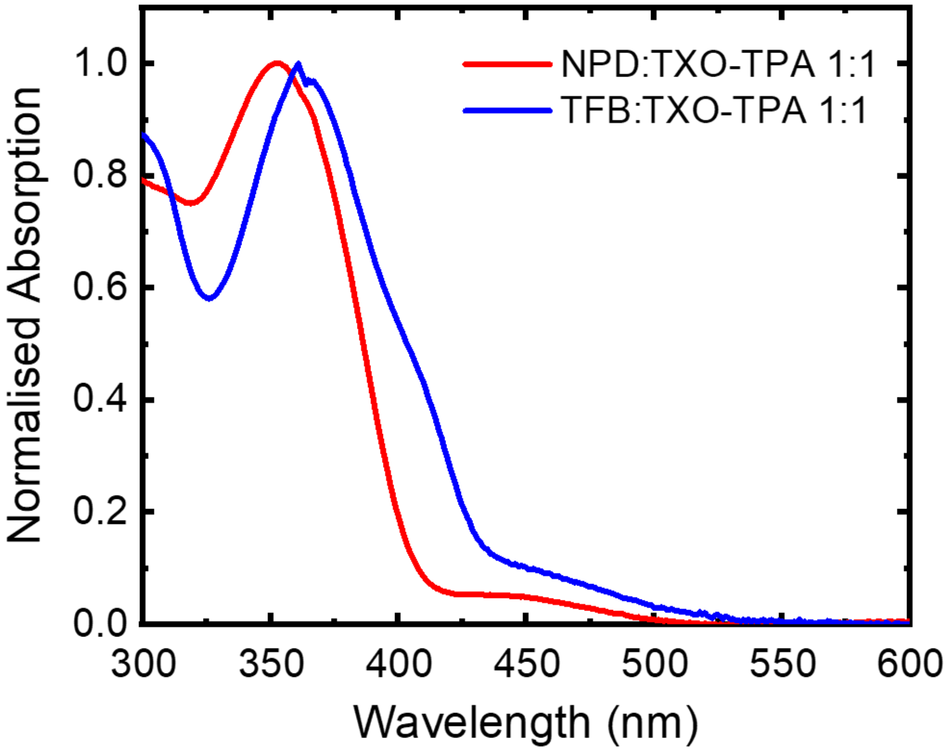

Figure 5.4*: The normalised absorption spectra of the 1:1 blend films of the materials used in this study.*

5.4 Steady-State Photoluminescence and PLQE

The final steady-state measurement we performed is PL and PLQE on the neat TXO-TPA and the blends, excited at 355 nm (Figure 5.5). This wavelength excites both components of the blend strongly, leading to the generation of excitons on both TXO-TPA and the electron donor, with the potential for subsequent charge transfer processes. The PL of neat TXO-TPA is a broad, red emission peaked at 650 nm. When exciting the blends, the first thing we notice is weak emission band in the region between 410 – 500 nm. This come from unquenched excitons generated on NPD and TFB and is consistent with their emission spectra.[118,119] Also present in both is a strong, broad red emission band peaked at around 660 nm, slightly red-shifted from the neat TXO-TPA PL. Interestingly, the PL maxima is slightly more red in the NPD:TXO-TPA blend, despite the smaller HOMO-HOMO offset: perhaps an indication of the limitations of using CV to determine the HOMO.[117] The slight red-shift in the PL maxima for both blends, consistent with the likely small difference in energy between the TXO-TPA singlet and the CT state, as well as the strongly quenched donor emission is very interesting. This suggests that charge transfer does indeed happen in the blends from at least NPD and TFB to TXO-TPA, as would be expected given the large driving energy for this process. For now however, it is not clear whether excitons generated on TXO-TPA can undergo hole transfer back to the electron donor, but this will be investigated by other means in subsequent sections.

Additionally, we have also measured the PLQE of the films, excited at 405 nm. The neat TXO-TPA film has a PLQE of 4.5%, which is low by TADF standards. However, the PLQE is reported to be 83% when dispersed in the wide band gap host mCP,[114] so it is likely that intermolecular interactions quench the PL (a phenomena known as concentration quenching).[120] Interestingly, the PL maxima of TXO-TPA diluted into the wide gap host mCP at a 5 wt % was significantly bluer than the neat film, with a peak at 580 nm.[114] This suggests that the intermolecular interactions not only result in a significant decrease in PLQE, but also red-shift of the PL. Rather excitingly, the PLQE of the blend films is comparable to that of neat TXO-TPA, with PLQEs of 2.2% for NPD:TXO-TPA 1:1 and 1.4% for TFB:TXO-TPA 1:1. This suggests that despite charge transfer seemingly occurring, the recombination of these states still has significant radiative character. This is in stark contrast to typical polymer:fullerene blends, where complete quenching of the PL of the blend was previously seen as advantageous as it suggested complete exciton dissociation on the donor.[121] However, as we know, it is actually essential to have a significant proportion of the recombination be radiative in order to minimise the non-radiative voltage loss of the blend.[48] This therefore bodes well for supressing the non-radiative losses in the OPV devices fabricated from these blends and suggests that removing the triplet loss pathway has had the desired effect of reducing non-radiative decay of the CT states.

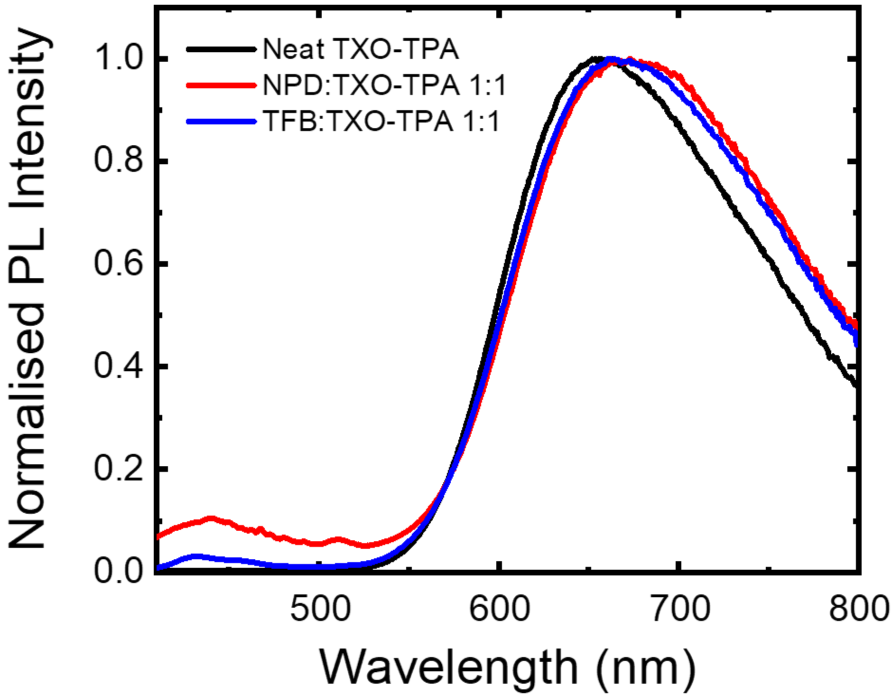

***Figure 5.5**: The normalised PL spectra of neat TXO-TPA and the blend films of the materials used in this study, pumped at a wavelength of λ_{ex} = 355 nm which excites both the donor and TXO-TPA. Of interest is the very weak residual donor emission in both blends, between 410 – 500 nm. This suggests that electron transfer from the donor to TXO-TPA occurs, quenching the donor emission. Additionally, the main PL band in the blends is slightly red-shifted from that of neat TXO-TPA, consistent with it being CT emission given the predicted very small difference in energy between the CT and the TXO-TPA singlet.*

5.5 Transient Absorption of the Pure Materials

In order to determine whether charge transfer does indeed occur in our TADF acceptor systems, as suggested by the steady state PL measurements, we turn to TA. However, before we can investigate the blends, we must develop our understanding of the spectral features present in the neat materials. To begin, we performed TA on a neat film of TXO-TPA, which is shown in Figure 5.6. An excitation wavelength of 400 nm with a fluence of 123 µJ cm^{-2}. We observe the formation of two overlapping PIA peaks and are able to isolate these spectral features and their associated kinetics using GA (Figure 5.7 and 5.8). The first, centred at 570 nm, is formed within the instrument response of our experimental setup (100 fs), whilst the second, peaked at the edge of our probe range at 750 nm, grows in on a picosecond timescale. We consider that there are two possible explanations for this spectral evolution. Firstly, for TADF materials in the solid-state, many different conformers with different D-A dihedral angles can exist in-tandem, locked in by the high energetic barrier to rotation.[122] Each of the stable conformers present can also possess its own distinct band gap and,[123] presumably, its own PIA spectral signatures as the allowed electronic transitions to high-lying excited states will differ between conformers. Therefore, the spectral evolution may be attributed to the energy transfer from the higher energy conformers to their lower band gap neighbours in the film. The second explanation for the PIA shift revolves around a rotationally-mediated molecular relaxation from "hot" singlet excited states to "cool" conformation, impeded by the constrained environment of the film, similar to previous observations in other organic small molecules.[124] Additionally, a small amount of GSB overlapping with the PIAs is present at 460 nm, though tracking the kinetics of this as a measure of the total excited state population is probably unwise due to its convoluted nature.

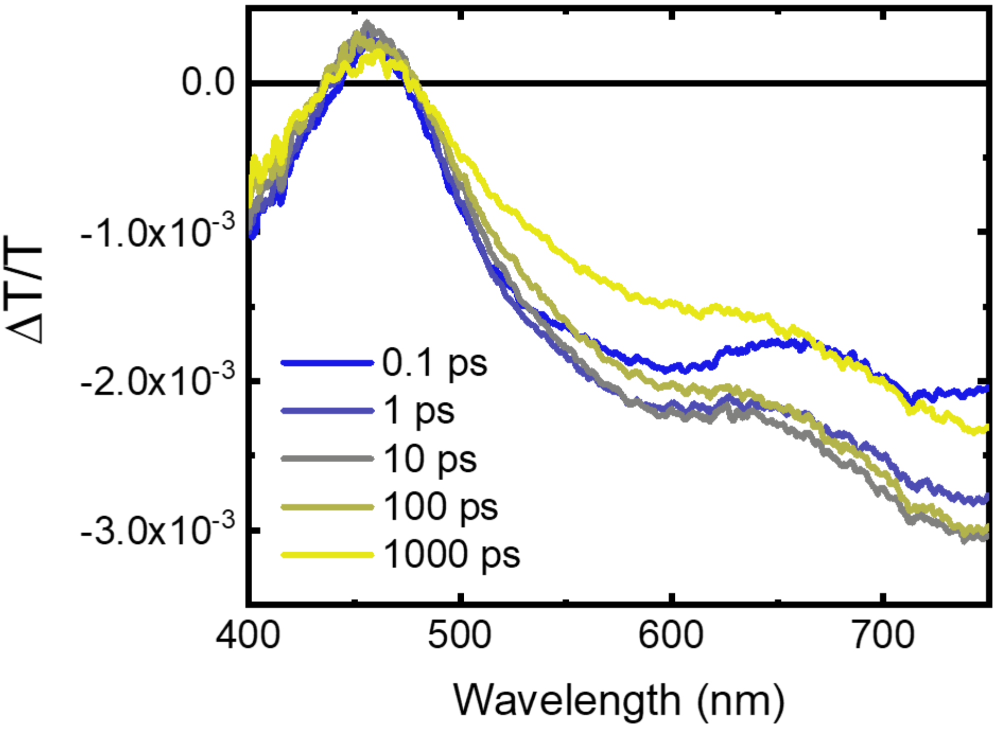

***Figure 5.6**: The short-time TA spectra of a film of neat TXO-TPA: λ_{ex} = 400 nm, fluence = 123 μJ cm^{-2}. The PIA formed initially at 570 nm quickly evolves to form a broad band with a peak towards the edge of our probe range at 750 nm. A small portion of GSB is also visible at 460 nm, convoluted with the PIA features.*

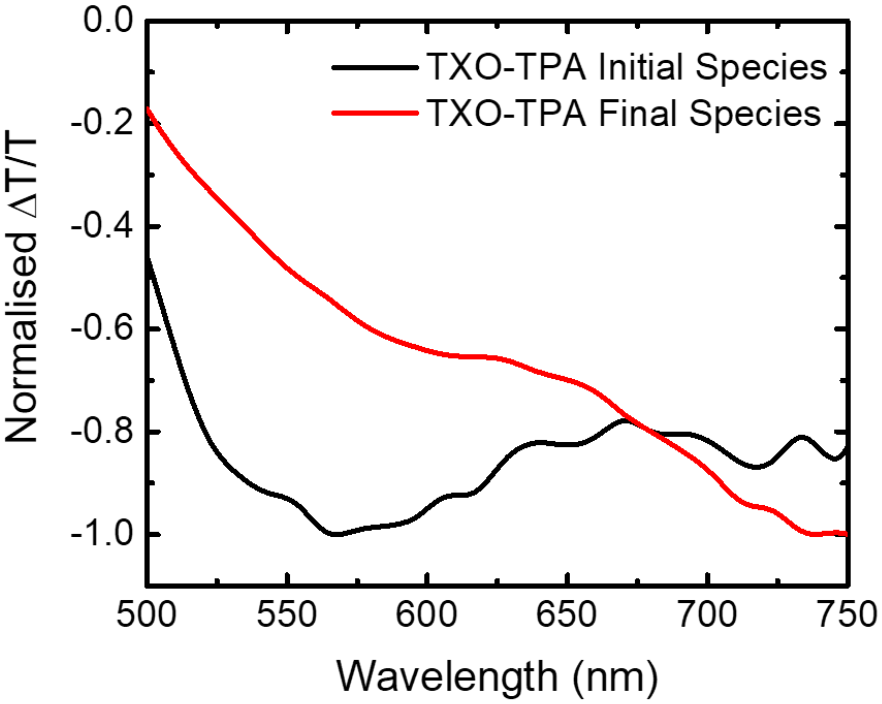

Figure 5.7*: The GA extracted spectral features of the TA on the neat TXO-TPA film, taken from Figure 5.6. The black spectrum is present initially and likely belongs to a rotationally hot conformer created immediately after excitation. As time progresses, the contribution from this conformer decreases and a new species, representing the relaxed form of the excited state, is formed.*

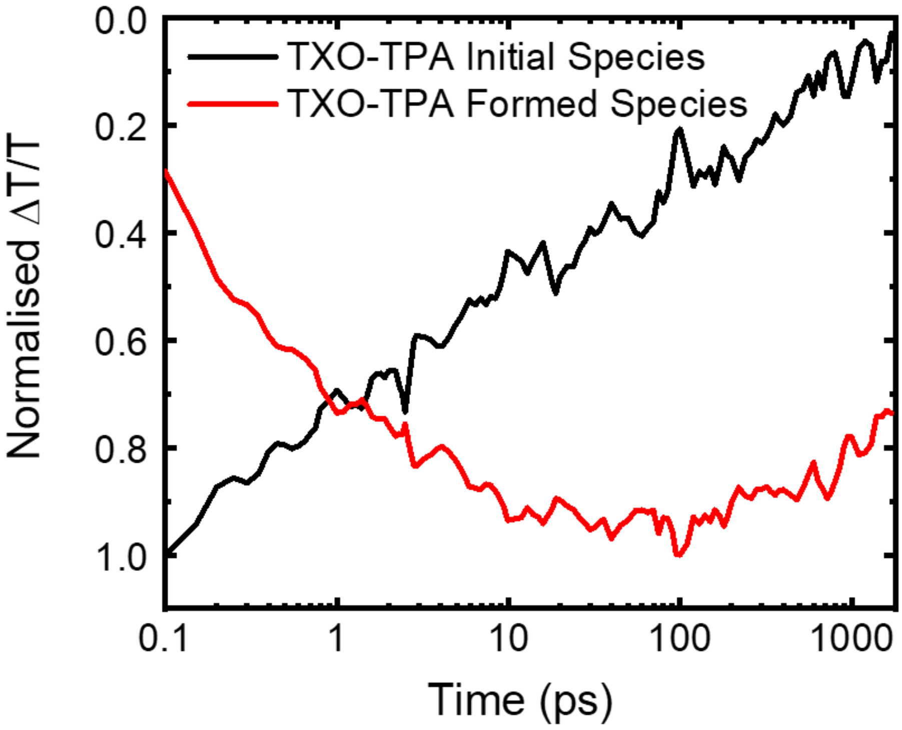

Figure 5.8*: The corresponding kinetics of the GA extracted spectral of the TA on the neat TXO-TPA film, taken from Figure 5.6. The timescale for the relaxation appears to be on the order of ps, as the spectral evolution is largely completed by 10 ps.*

We next examine the normalised TA spectrum of neat NPD and TFB, excited at 400 nm with fluences of 80 and 5 μJ cm^{-2}, respectively (Figure 5.9). For conciseness, only the initial spectrum of NPD and TFB at 1 ps are shown, as no spectral evolution occurs over the timescales of their decays. The PIA peaks present in the donor TA is that of the singlet excited state, formed immediately after optical excitation. For NPD, the PIA is peaked at 580 nm, whilst for TFB the peak is a little broader and is centred at 625 nm. The kinetic traces for both samples (Figure 5.10), averaged around the maxima of the PIAs, indicates that the singlets in both materials decay at a similar rate, with excited state decay largely completed by 1 ns. Additionally, there are positive features present in both blends at shorter wavelengths. In TFB, two bands are seemingly present, one with a peak at 460 nm and the other extending into the UV past the edge of our probe range. The 460 nm band is assigned to the SE of TFB, as this matches closely the wavelengths associated with TFB PL.[103] The higher energy band is assigned to the GSB of TFB, as would be expected from the TFB absorption spectrum. For NPD, the positive signal is very weak and is consists of a small peak at 450 nm, likely overlapping with the redder PIA band. Given there is no ground state absorption at this wavelength, it is assigned to SE.

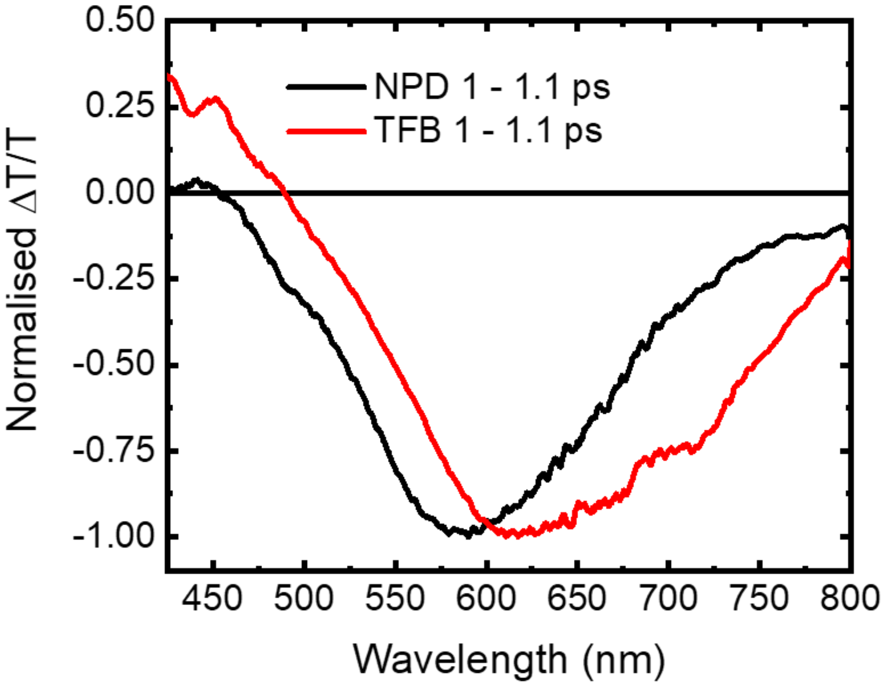

***Figure 5.9**: The normalized 1 ps TA spectra of films of neat NPD and TFB: λ_{ex} = 400 nm, fluence = 80 and 5 μJ cm^{-2}. Both materials show clear PIAs at 580 nm for NPD and 625 nm for TFB, associated with the singlet exciton created immediately following excitation. Additionally, positive bands are visible at wavelengths shorter than 500 nm for both. The peak at 460 nm in TFB is assigned to the SE, with the band extending deeper into the UV originating from the GSB. The weak feature in NPD at 425 nm is assigned to the SE.*

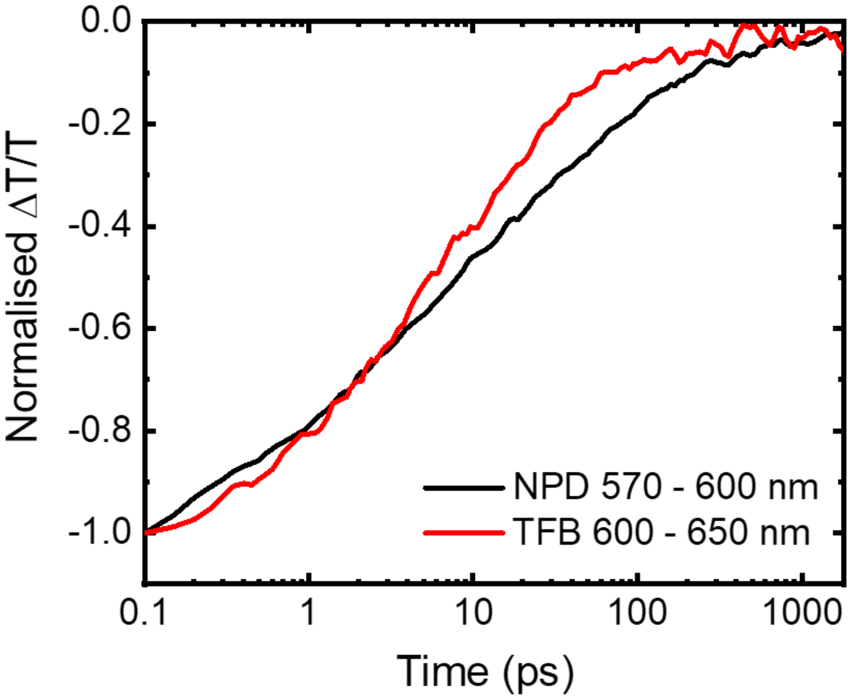

Figure 5.10*: The short-time TA kinetics for the neat films of NPD and TFB: λ_{ex} = 400 nm, fluence = 80 and 5 μJ cm^{-2}, respectively. The kinetics are taken from the regions associated with the NPD (570 – 600 nm) and TFB (600 – 650 nm) singlet exciton PIAs. Singlet exciton decay appears to be largely complete by 1 ns in both materials, possibly as a result of the relatively high excitation fluence used in the measurements.*

5.6 Short-Time Transient Absorption of the Blends

5.6.1 Excitation of mainly NPD in the NPD:TXO-TPA Blend

We begin our investigation of the blend films by first examining the blend of NPD:TXO-TPA using TA. In this instance, we want to determine whether electron transfer from NPD to TXO-TPA is occurring. However, the absorption spectra of NPD and TXO-TPA overlap significantly, so purely selective excitation of NPD is not possible. To counteract this, we have created a 4:1 blend film of NPD:TXO-TPA, where the excess of NPD should allow us to achieve more selective excitation than in the 1:1 blend. Excitation was provided by a 400 nm pump source with a fluence of 170 μJ cm^{-2}, yielding TA spectra and corresponding kinetics shown in Figures 5.11 and 5.12 (the spectral region around 400 nm has been removed due to pump-scatter). It should be noted that high fluences were required to excite this blend due to the weak absorption of light at 400 nm by both NPD and TXO-TPA, owing to their primarily UV absorption. In the TA spectra (Figure 5.11) of the blend, we initially observe a spectrum that resembles that of the NPD singlet exciton, with a PIA peaked at 580 nm. There also appears to be some TXO-TPA contribution to the spectrum, as evidenced by the apparent presence of a broad PIA band underneath the NPD singlet PIA. The NPD singlet appears to decay rapidly and is almost gone by 1 ps, whilst a new PIA peaked at around 515 nm is formed. If charge transfer has occurred, the loss of the NPD singlet PIA and the formation of a new band associated with an absorption of a charge located on either the donor or acceptor would be expected. We attribute this new PIA band at 515 nm to the absorption of a hole located on NPD, an assignment we will confirm with further experiments in subsequent sections. After 5 ps, there appears to be no further spectral evolution and the new PIA decays in step with the NPD GSB at 375 nm from approximately 100 ps onwards, indicating the start of recombination to the ground state. The relatively rapid nature of the NPD hole decay can be attributed to the high excitation fluence used in this measurement, significantly higher than solar fluences. Thus, in this system, the electron transfer appears to occur rapidly, with a time constant of <1 ps.

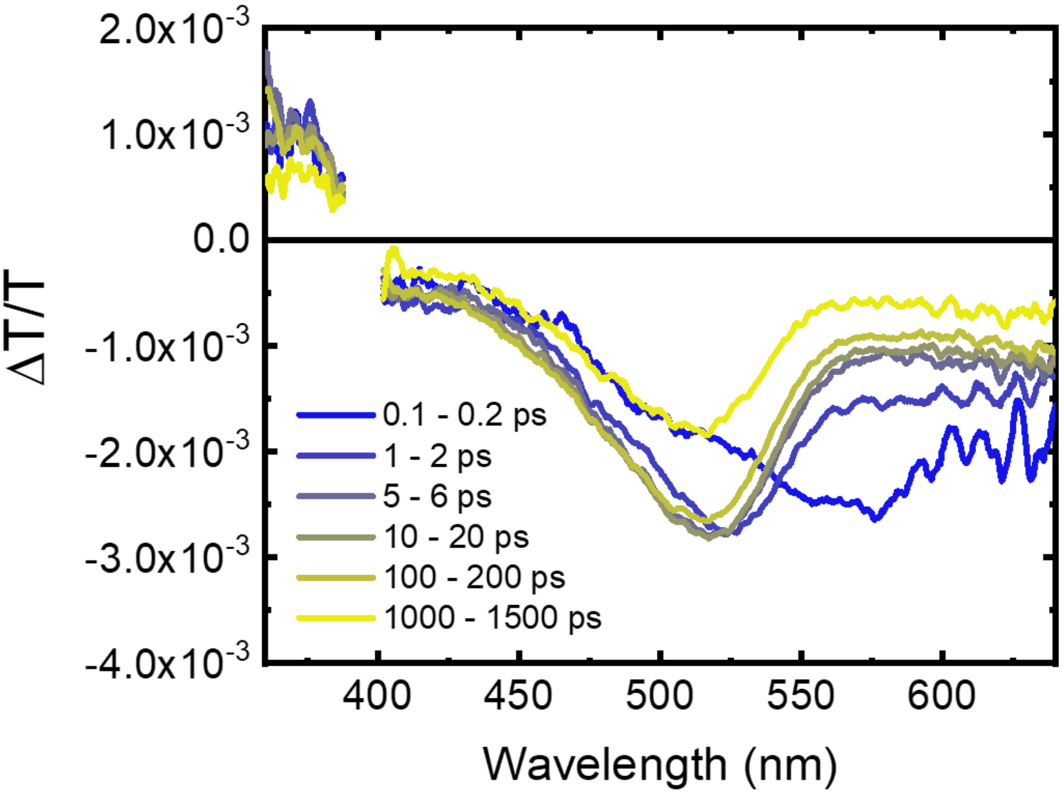

***Figure 5.11**: The short-time TA spectra of the 4:1 NPD:TXO-TPA blend film: λ_{ex} = 400 nm, fluence = 170 μJ cm^{-2}. Initially, a peak at about 580 nm, superimposed over a broad background PIA is present. The 580 nm peak is attributed to the NPD singlet exciton, as previously measured. The background is assigned to the broad PIA in the visible region of the TXO-TPA exciton, also excited by the 400 nm pump. The peak at 580 nm mostly disappears within 1 ps and a new PIA at 515 nm is formed. We attribute this to the electron transfer from NPD to TXO-TPA, with the peak at 515 nm assigned to the hole remaining on NPD after the transfer. After 5 ps, there no more spectral evolution, indicating that the electron transfer is complete.*

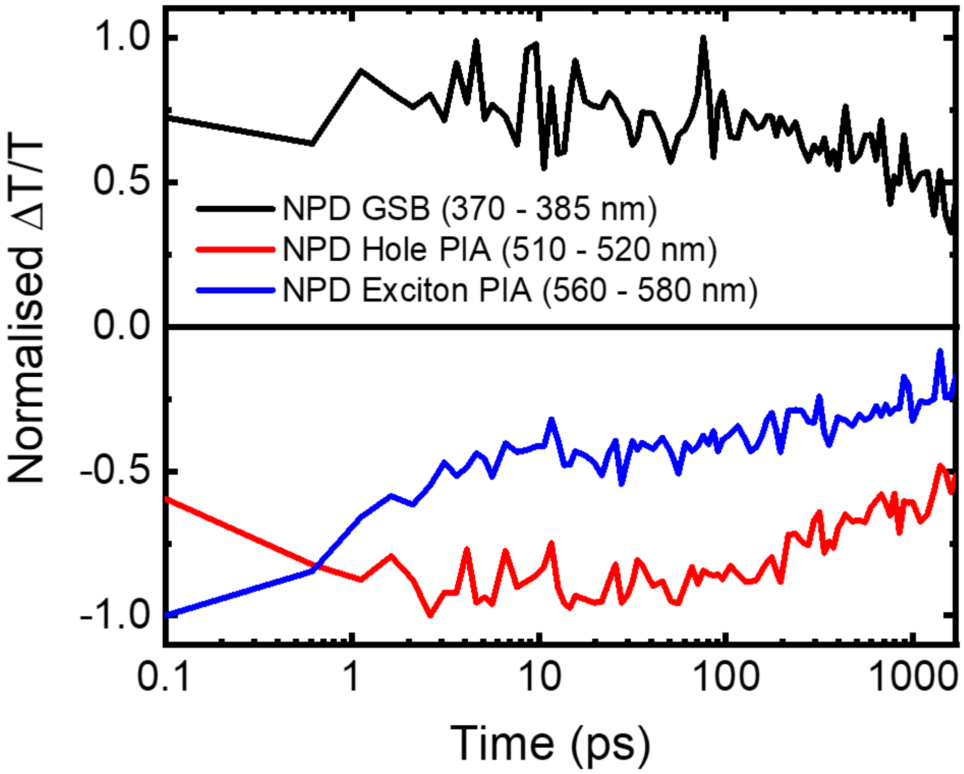

***Figure 5.12**: The short-time TA kinetics of the 4:1 NPD:TXO-TPA blend film: λ_{ex} = 400 nm, fluence = 170 μJ cm^{-2}. The region associated with the NPD singlet exciton PIA falls rapidly in the first ps, with a corresponding increase in the absorption in the region of the NPD hole PIA. During this time, the NPD GSB is constant, reflecting that no population is lost. After 5 ps, there is no further evolution of the kinetic traces until 100 ps, when the NPD hole PIA and GSB decay together in-step, indicating the start of recombination to the ground state.*

5.6.2 Selective Excitation of TXO-TPA in the NPD:TXO-TPA Blend

After confirming that the electron transfer process from NPD to TXO-TPA occurs, we now seek to probe the hole transfer process from TXO-TPA to NPD. We can now make use of the broad, weak ICT band of TXO-TPA that extends out past the absorption onset of NPD to selectively excite TXO-TPA in the 1:1 blend. For this a pump wavelength of 490 nm was chosen and the sample was excited with a fluence of 90 μJ cm^{-2}. The resulting TA spectra and kinetics are displayed in Figures 5.13 and 5.14. In the NPD:TXO-TPA 1:1 film, there is no obvious PIA signature belonging to the TXO-TPA singlet exciton present. Rather, there is a new PIA feature that appears to blue-shift on the 100 ps timescale from 535 nm to the edge of our probe range at 520 nm. Looking at the kinetics, this new feature is at approximately 65% of peak intensity within the time resolution of our setup (100 fs) and continues to grow in, reaching a maximum at ~40 ps. Therefore, we assign the initial PIA feature at 535 nm in the NPD:TXO-TPA film to be a mixture of the NPD hole PIA (515 nm) and the redder PIA of excitons located on TXO-TPA (570 nm) which have not yet been separated. As a higher proportion of the excitons on TXO-TPA separate, the contribution to the PIA from the TXO-TPA exciton decreases and the signal begins to blue-shift, resembling more the PIA seen in the blend when exciting NPD in the 4:1 NPD:TXO-TPA blend at 400 nm. This confirms that hole transfer from TXO-TPA to NPD is occurring in the blend film, with a significant proportion happening on ultrafast (<100 fs) timescales.

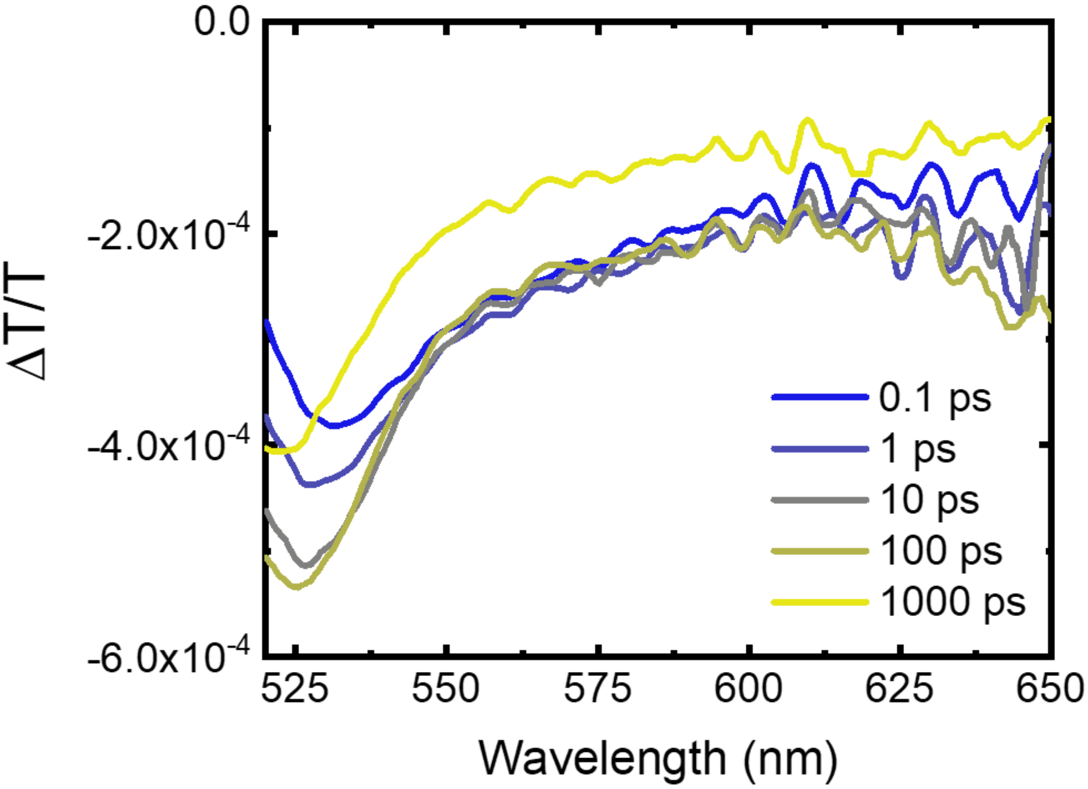

Figure 5.13: *The short-time TA spectra of the 1:1 NPD:TXO-TPA blend film: λ_{ex} = 490 nm, fluence = 90 μJ cm^{-2}. At the earliest times, there is no obvious PIA belonging to the TXO-TPA singlet exciton present, suggesting that a significant proportion of the hole transfer occurs over ultrafast timescales. Rather, there is a broad band with a peak at 535 nm. As time progresses, the peak at 535 nm increases in intensity and blue-shifts to the edge of our probe range at 520 nm. This peak is therefore assigned to a mixture of the NPD hole at 515 nm and the TXO-TPA singlet exciton at 570 nm. As more excitons transfer, the peak increases in intensity and blue-shifts towards 520 nm, indicating an increase in the number of holes on NPD.*

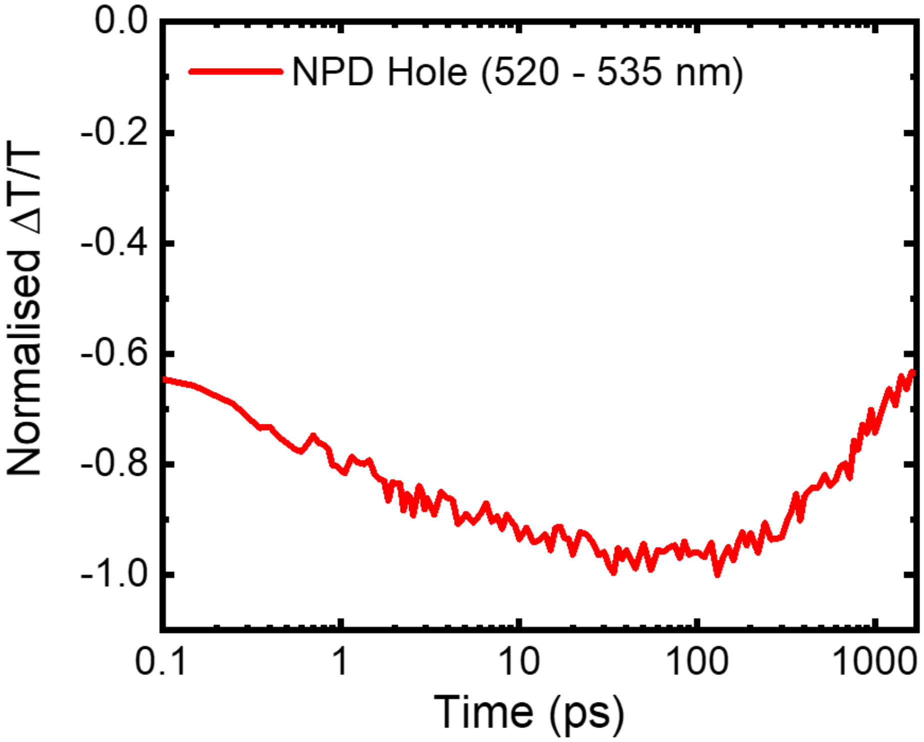

Figure 5.14*: The short-time TA kinetics of the 1:1 NPD:TXO-TPA blend film: λ_{ex} = 490 nm, fluence = 90 μJ cm^{-2}. The wavelength region associated with the NPD hole rises, reaching a maxima after approximately 40 ps. This provides evidence for the timescales of the hole transfer process from TXO-TPA to NPD. Consistent with the blend excited at 400 nm, the intensity of the peaks begins to fall after 100 ps, indicating the timescales at recombination begins to occur.*

5.6.3 Assignment of the NPD Hole Absorption

As alluded to in previous sections, we assigned the new PIA formed in the blend to be that of the hole located on NPD after the charge transfer processes. In order to confirm this assignment, we fabricated blends of NPD and C_{60} fullerene in a 1:1 weight % ratio. C_{60} is an excellent electron acceptor with a deep LUMO of -4.50 eV.[125] Therefore, electron transfer from NPD to C_{60} would be expected in this blend, leaving behind a hole on NPD. TA was performed on this blend with an excitation wavelength of 400 nm and a fluence of 205 μJ cm^{-2}. The TA spectra associated with this blend are plotted in Figure 5.15. Important to note is that the rapid decay of the excited states formed is due to the very large fluence used. However, as we are only interested in the spectral features present, this does not affect our analysis. We observe a strong PIA, peaked at 515 nm in the NPD:C_{60} blend, presumably formed as a result of the expected electron transfer from NPD to C_{60}. This PIA matches very closely the PIA seen in the NPD:TXO-TPA blends after charge transfer, confirming its origin as the hole located on NPD.

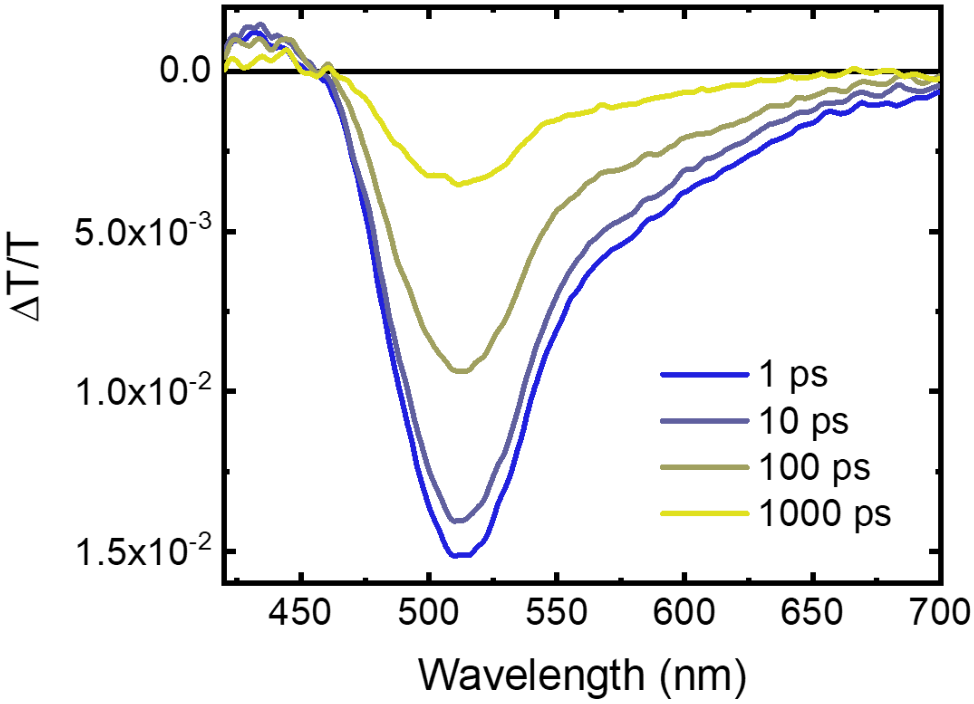

***Figure 5.15**: The short-time TA spectra of the 1:1 NPD:C_{60} blend film: λ_{ex} = 400 nm, fluence = 205 μJ cm^{-2}. After the expected electron transfer from NPD to C_{60} due to the large LUMO-LUMO offset, a new PIA is formed that does not resemble the NPD exciton. The PIA has a sharp peak at 515 nm and closely resembles that seen in the NPD:TXO-TPA blend after charge transfer occurs. Thus, it is assigned to the absorption of the hole located on NPD.*

5.6.4 Excitation of mainly TFB in the TFB:TXO-TPA Blend

After completing our analysis of the short-time TA on the NPD:TXO-TPA blend, we now examine the TFB:TXO-TPA blend in a similar fashion. As before, we begin by exciting the 4:1 TFB:TXO-TPA blend at 400 nm, with a fluence of 44.2 μJ cm^{-2}. The higher weighting of TFB was chosen to ensure selective TFB excitation in the blend, so we can primarily track the electron transfer process. The corresponding spectrum and kinetics are shown in Figures 5.16 and 5.17. Initially at 0.2 ps after excitation, we see a spectrum that very closely resembles that of neat TFB, with a PIA peaked at 620 nm, a SE band at around 450 nm and the GSB between 350 – 430 nm. Very rapidly, the PIA at 620 nm is lost, with a corresponding decrease in the SE band, clearly visible in the kinetics. During this spectral evolution over the first ps, the intensity of the TFB GSB stays constant. By 1 ps, a new PIA band peaked at 535 nm has formed, which remains relatively constant over the timescales of the experiment, with only a decay in-step with the TFB GSB feature. This band is likely formed as a result of the expected electron transfer process from TFB to TXO-TPA and is such assigned to an absorption of the hole on TFB, which we confirm in later sections.

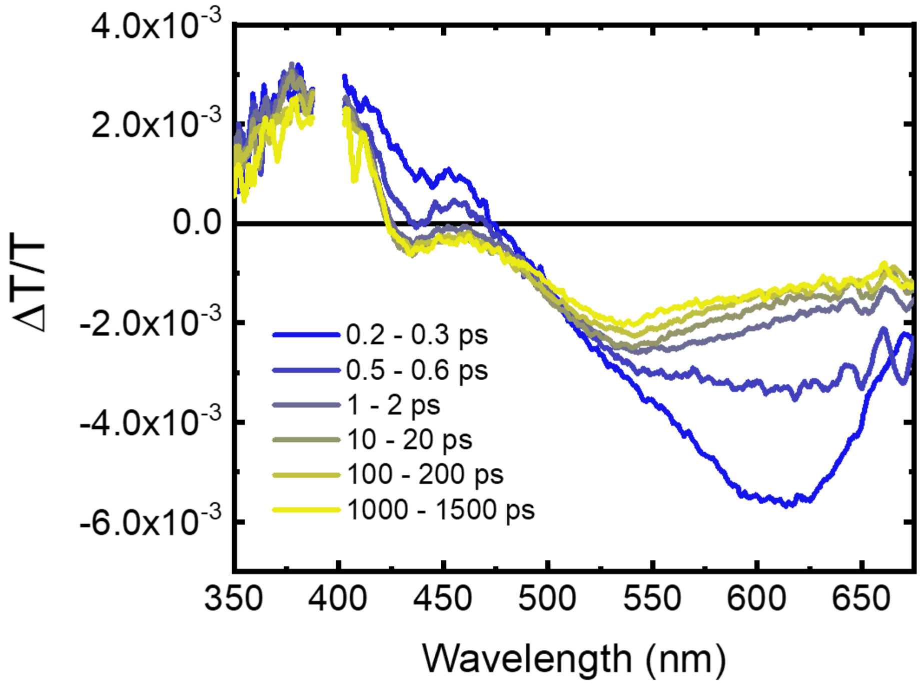

Figure 5.16*: The short-time TA spectra of the 4:1 TFB:TXO-TPA blend film: λ_{ex} = 400 nm, fluence = 44.2 µJ cm^{-2}. Initially, the spectrum closely resembles that of neat TFB, with a singlet PIA at 620 nm, SE at 450 nm and GSB between 350 – 430 nm. The PIA at 620 nm and the SE band disappear within 1 ps and a new PIA at 535 nm is formed. We attribute this to the electron transfer from TFB to TXO-TPA, with the peak at 535 nm assigned to the hole remaining on TFB after the transfer. After 5 ps, there no more spectral evolution, indicating that the electron transfer is complete.*

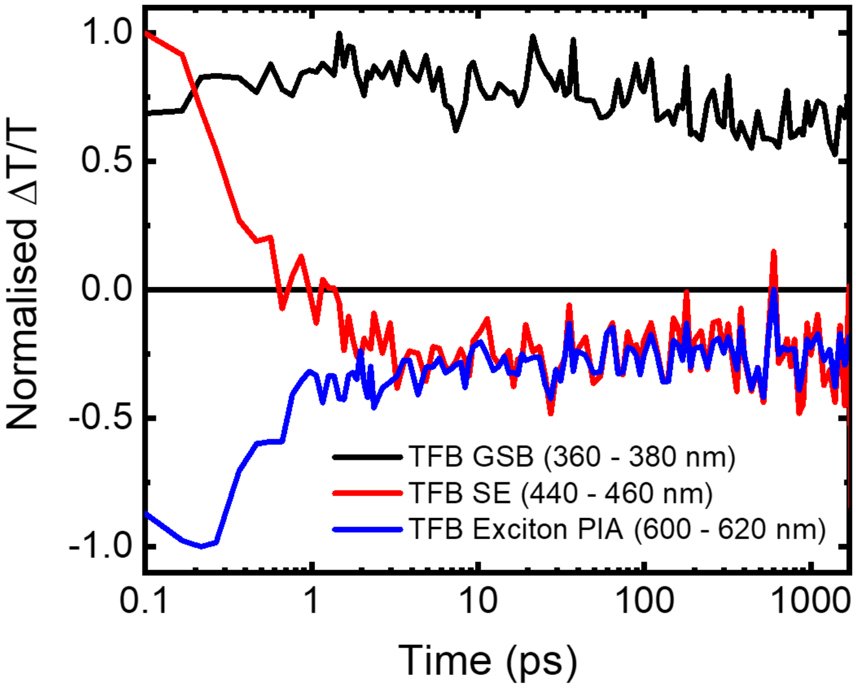

Figure 5.17*: The short-time TA kinetics of the 4:1 TFB:TXO-TPA blend film: λ_{ex} = 400 nm, fluence = 44.2 µJ cm^{-2}. The region associated with the TFB singlet exciton PIA falls rapidly in the first ps, with a corresponding loss of the TFB SE. During this time, the TFB GSB is constant, reflecting that no population is lost.*

5.6.5 Selective Excitation of TXO-TPA in the NPD:TXO-TPA Blend

After confirming that the electron transfer process from TFB to TXO-TPA occurs, we shall now examine the reverse hole transfer process. As with the NPD:TXO-TPA blend, we excite the TFB:TXO-TPA 1:1 blend at 490 nm, below the band gap of TFB with a fluence of 95 µJ cm^{-2}. The TA spectra and kinetics for this measurement are displayed in Figures 5.18 and 5.19. There are no features present in the TA spectrum at the earliest times (100 fs) that can be attributed to the exciton on TXO-TPA. Indeed, the new PIA peaked at 535 nm already possesses an intensity of 80% of the maximum intensity by the 100 fs time resolution of our experiment, indicating the ultrafast timescales of the charge transfer process. The PIA continues to grow in slightly up to 10 ps before slowly decaying away, potentially due to the diffusion of excitons in the neat TXO-TPA domains to the interface. The location of the PIA closely matches the one seen in the TFB:TXO-TPA 4:1 blend when excited at 400 nm, indicating that species formed when TXO-TPA is excited is the same as the one formed by the electron transfer from TFB to TXO-TPA. Thus, this provides conformation that the hole transfer process does indeed occur from TXO-TPA, indicating the possibility that photocurrent can be generated by acceptor absorption too.

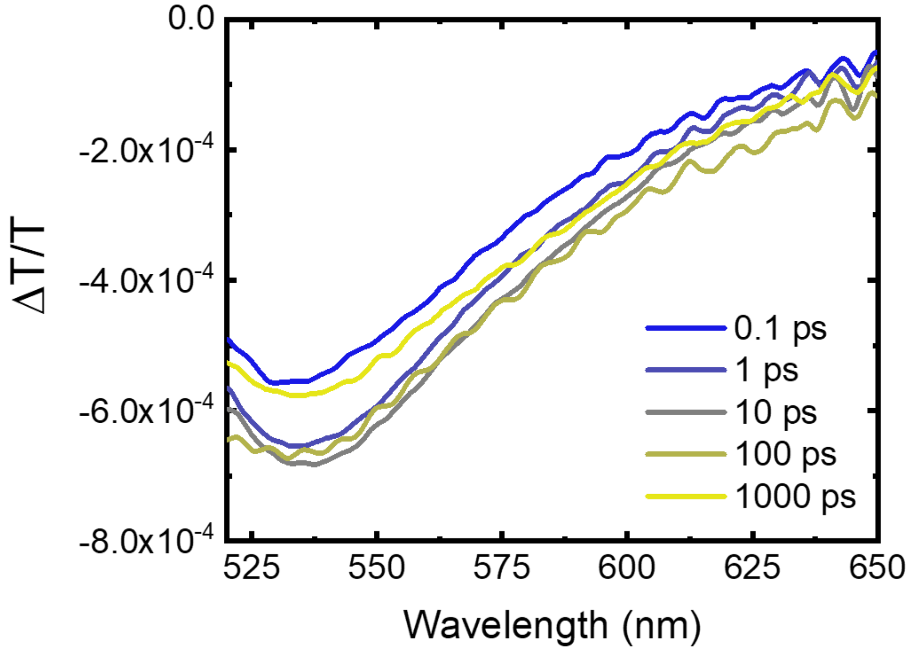

***Figure 5.18**: The short-time TA spectra of the 1:1 TFB:TXO-TPA blend film: λ_{ex} = 490 nm, fluence = 95 µJ cm^{-2}. At the earliest times, there is no obvious PIA belonging to the TXO-TPA singlet exciton present. Rather, there is a new PIA with a peak at 535 nm present from the earliest times resolvable. This PIA does not significantly change in shape over the timescales of the measurement, but does increase slightly in intensity up to 10 ps, indicating the timescales of the hole transfer process.*

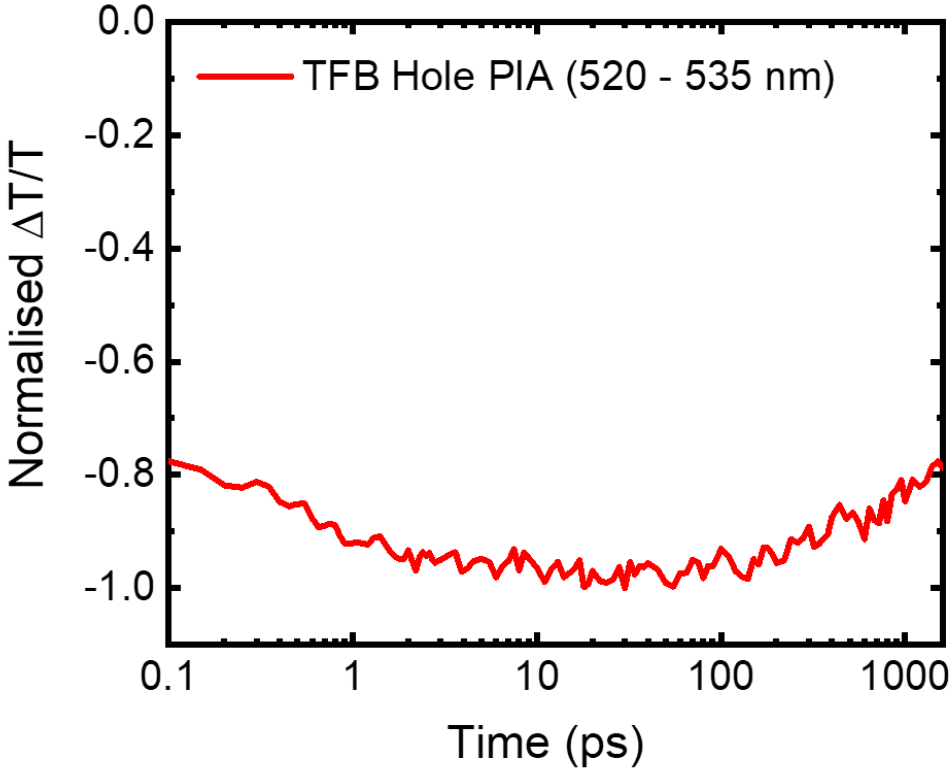

***Figure 5.19**: The short-time TA kinetics of the 1:1 TFB:TXO-TPA blend film: λ_{ex} = 490 nm, fluence = 95 µJ cm^{-2}. The TFB hole PIA is formed initially within the time resolution of our experiment, with a slight increase in intensity up to 10 ps as additional charge transfer occurs. After this time, there is a slight decrease in intensity of the PIA as recombination begins to occur.*

5.6.6 Assignment of the TFB Hole Absorption

In order to confirm our assignment of the PIA at 525 nm as belonging to the hole located on TFB after the charge transfer process, we follow the same tactic employed for the blend with NPD. Thus, we have blended TFB with the electron acceptor [6,6]-Phenyl-C61-butyric acid methyl ester (PC$_{60}$BM) in order to elicit the electron transfer from TFB to PCBM, leaving behind a hole on TFB. This 1:1 blend of TFB: PC$_{60}$BM was excited at 400 nm with a fluence of 35.3 µJ cm^{-2}, yielding the TA spectra seen in Figure 5.20. A strong PIA is formed with a peak at 535 nm, closely matching that seen in the TFB:TXO-TPA blend. Given that a hole is expected to be left behind on TFB after the electron transfer in this blend and the similarities with the TFB:TXO-TPA blend, this PIA can be confidently assigned to the hole on TFB.

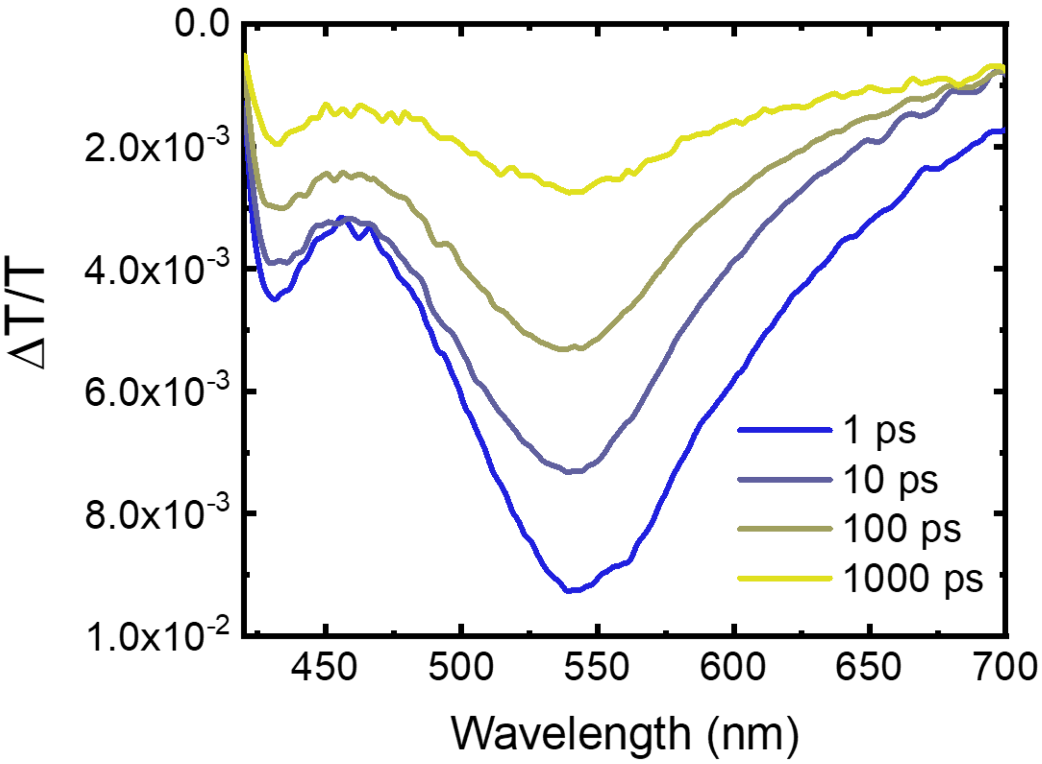

***Figure 5.20**: The short-time TA spectra of the 1:1 TFB:PC_{60}BM 1:1 blend film: λ_{ex} = 400 nm, fluence = 35.3 μJ cm^{-2}. After the expected electron transfer from TFB to PC_{60}BM due to the large LUMO-LUMO offset, a new PIA is formed that doesn't resemble the TFB exciton. The PIA has a sharp peak at 535 nm and closely resembles that seen in the TFB:TXO-TPA blend after charge transfer occurs. Thus, it is assigned to the absorption of the hole located on TFB.*

5.7 Long-Time Transient Absorption of the Blends

5.7.1 Long-Time Transient Absorption of the NPD:TXO-TPA blend

Having now confirmed that both electron transfer from NPD to TXO-TPA and the reverse hole transfer from TXO-TPA to NPD are both possible, we now turn to explore the charge recombination dynamics. For this, we begin by utilising long-time TA to track the decay of the hole PIA located on NPD. For this measurement, we excited with a pump pulse centred at 355 nm, which led to the simultaneous excitation of both TXO-TPA and NPD. Whilst this may result in the generation of charges by both hole transfer from TXO-TPA and electron transfer from the NPD or TFB, we expect both mechanisms to result in the formation of the same CT state (and ultimately free charges), with the electron localised on the TXO-TPA and hole on NPD.[126]

The NPD:TXO-TPA 1:1 blend was excited with a pump wavelength of 355 nm and a fluence of 19.3 μJ cm^{-2}, yielding the TA kinetics shown in Figure 5.21. For this measurement, the NOPA probe was optimised for a narrowband region around the hole PIA to maximise the signal to noise, and as such broadband spectral information is not available. In order to ensure we are in a linear regime with respect to fluence, we have also performed a fluence series, with higher fluences of 62.9 μJ cm^{-2} and 588 μJ cm^{-2} used (Figure 5.22). Reassuringly, when the kinetics are normalised to the fluence used, the kinetics from the two lowest fluences overlay perfectly, with non-linear behaviour only observed in the very high fluence measurement. Therefore, the kinetics of the lowest fluence measurement are expected to give an accurate representation of the recombination dynamics of the blend.

The kinetics of the decay of the 515 – 525 nm region associated with the hole on NPD have a very interesting dynamic. Instead of the typical power-law governed non-geminate recombination of dissociated charges associated with OPV blends,[127] the decay of the NPD hole PIA has rather biphasic behaviour. The decay kinetic possess both an initial "prompt" and longer-time "delayed" decay, characteristic of TADF. These are associated with the initial decay of singlet excited states via fluorescence or non-radiative processes and the delayed decay arising from successive cycles of ISC and rISC through triplet states followed by delayed fluorescence.[70,110,128,129] In this blend, the TADF-type kinetics likely result from the ISC and rISC processes between intermolecular ^{1}CT and ^{3}CT states, as has previously been observed in exciplexes formed between electron donors and acceptors.[130–132] The decay profile is consequently well-fitted with a simple bi-exponential decay, yielding time constants of 7.7 ns and 4.2 μs for the prompt and delayed components, respectively. The long delayed lifetime of the charges formed is quite promising, as it suggests that through the formation of ^{3}CTs in the blend, either via ISC from the ^{1}CT or from non-geminate processes, recombination back to the spin-singlet ground state is supressed as the process is spin-forbidden. This may prove to be quite a beneficial property, as in the absence of any local triplet decay pathways, the ^{3}CT states formed via bimolecular recombination will have a substantial amount of time to re-dissociate before recombining, allowing for the recycling of carriers that may otherwise be lost.

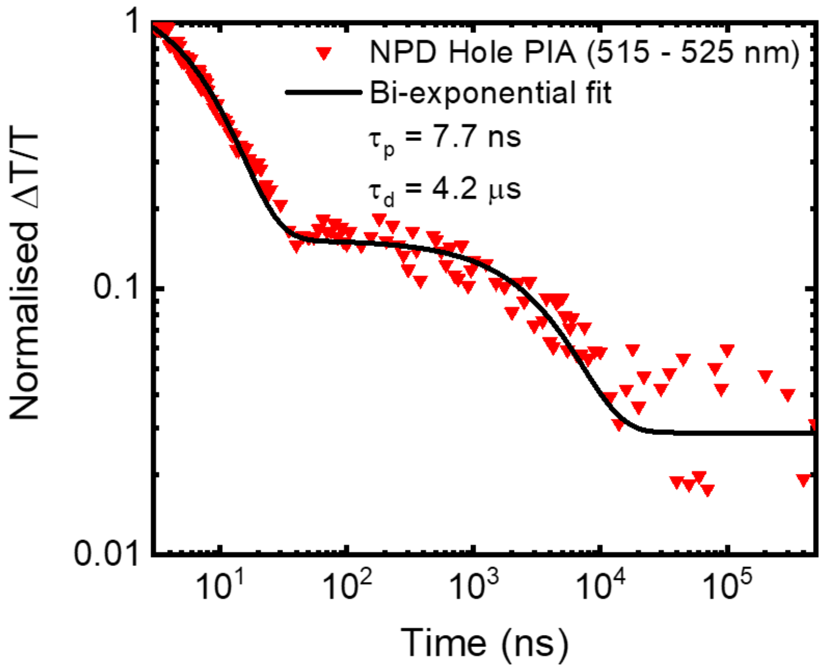

***Figure 5.21**: The long-time TA kinetics of the 1:1 NPD:TXO-TPA blend film: λ_{ex} = 355 nm, fluence = 19.3 μJ cm^{-2}. The NPD hole PIA decays with a biphasic decay that is well fitted by a bi-exponential decay function, yielding lifetimes of 7.7 ns and 4.2 μs for the prompt and delayed components. Such a decay is typical of systems exhibiting TADF, where there is an initial prompt decay of singlet states via fluorescence, ISC or non-radiative decay, with the triplet states formed via ISC undergoing successive cycles of ISC and rISC before ultimately decaying.*

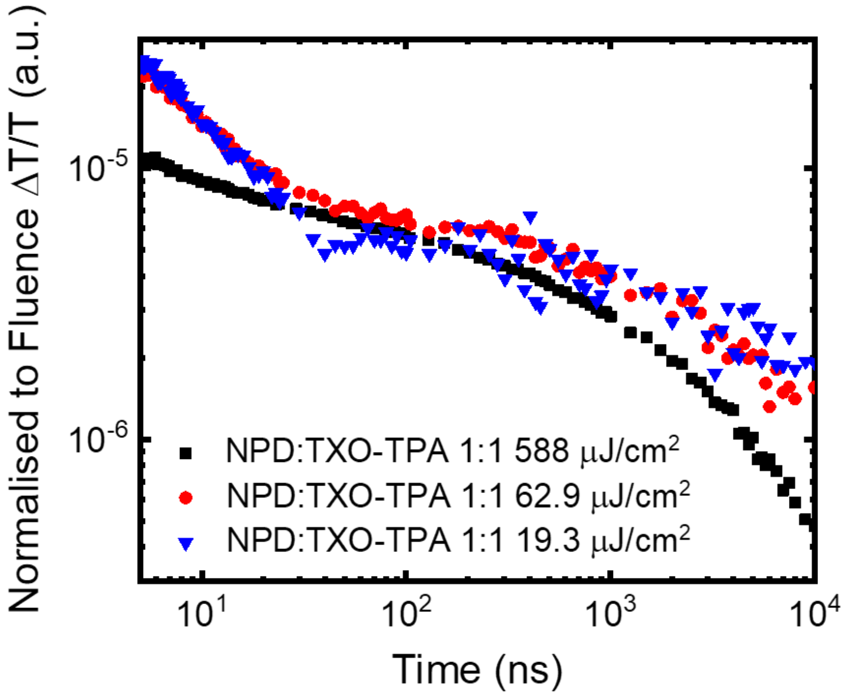

***Figure 5.22**: The long-time TA kinetics of the 1:1 NPD:TXO-TPA blend film: λ_{ex} = 355 nm, fluences = 19.3, 62.9 and 588 μJ cm^{-2}. The kinetics of the lowest fluence measurements overlay perfectly, indicating that we are in a regime free from non-linear recombination effects.*

5.7.2 Long-Time Transient Absorption of the TFB:TXO-TPA blend

We shall now examine the TFB:TXO-TPA 1:1 blend in the same way as the NPD blend before it. The film was excited with a wavelength of 355 nm and a fluence of 6.1 μJ cm^{-2}, giving the TA kinetics taken from the TFB hole PIA (525 – 540 nm) shown in Figures 5.23. We have also performed a fluence series on the blend, with higher fluences of 32.5 μJ cm^{-2} and 345 μJ cm^{-2} used (Figure 5.24). The kinetics of the two lowest fluence measurements, normalised to the fluence, overlay very well, indicating our lowest fluence measurement is performed in a regime free from non-linear recombination effects. As with the NPD:TXO-TPA blend, the kinetics are again well fitted by a bi-exponential function, indicating similar dynamics are at play in these systems with respect to the formation and decay of the ^{1}CT/^{3}CT. The prompt decay is longer in TFB:TXO-TPA though, with a time constant of 27.7 ns, whilst the delayed decay is shorter at 2.2 μs.

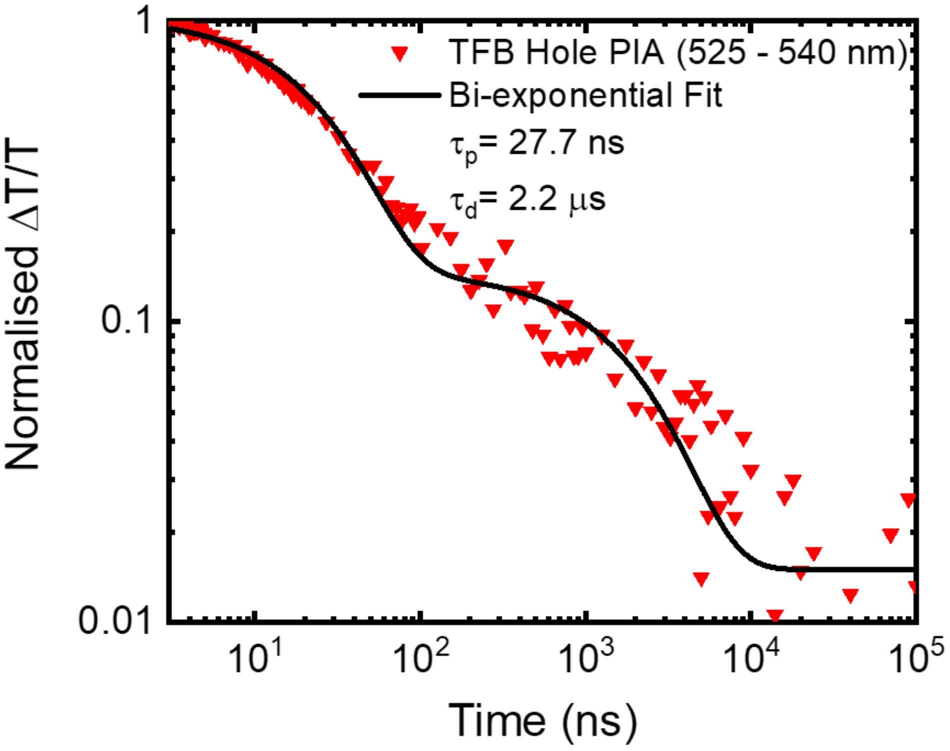

Figure 5.23*: The long-time TA kinetics of the 1:1 TFB:TXO-TPA blend film: λ_{ex} = 355 nm, fluence = 6.1 μJ cm^{-2}. The TFB hole PIA decays with a biphasic decay that is well fitted by a bi-exponential decay function, yielding lifetimes of 27.7 ns and 2.2 μs for the prompt and delayed components. Such a decay is typical of systems exhibiting TADF, where there is an initial prompt decay of singlet states via fluorescence, ISC or non-radiative decay, with the triplet states formed via ISC undergoing successive cycles of ISC and rISC before ultimately decaying.*

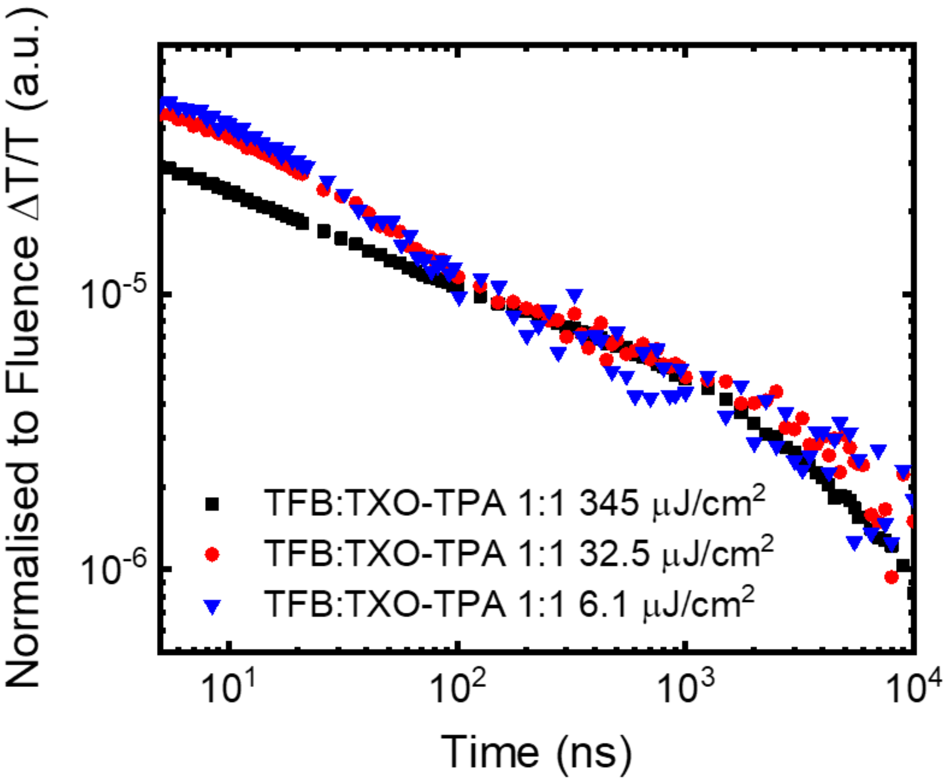

***Figure 5.24**: The long-time TA kinetics of the 1:1 TFB:TXO-TPA blend film: λ_{ex} = 355 nm, fluences = 6.1, 32.5 and 345 µJ cm^{-2}. The kinetics of the lowest fluence measurements overlay perfectly, indicating that we are in a regime free from non-linear recombination effects.*

5.8 Transient Photoluminescence of the Blends

5.8.1 Transient Photoluminescence of the NPD:TXO-TPA Blend

In order to further explore the recombination pathways of the blends, we turn to trPL measurements to explore whether the relatively high PLQE results from the enhanced radiative decay of CT recombination, afforded by the absence of low energy local triplet quenching pathways. We begin with the NPD:TXO-TPA 1:1 blend, where the sample is excited at 400 nm with a fluence of 15.3 µJ cm^{-2}. The resulting transient PL spectra and kinetics are plotted in Figures 5.25 and 5.26. The PL decay kinetics indicate a substantial amount of PL is emitted from the blend over the timescales of charge recombination. This is very exciting, as it suggests despite charge transfer and potentially charge separation occurring, a substantial portion of the decay occurs via radiative pathways over these timescales. This provides good evidence of a lack of non-radiative recombination pathways for the CT states, which we attribute to the absence of a low energy molecular triplet state to which ^{3}CTs can transfer. Therefore, any ^{3}CT states formed will likely either undergo rISC to the ^{1}CT, where radiative emission is spin-allowed, or re-dissociate into charges (which may eventually again recombine, this time to form the emissive ^{1}CT directly). To further emphasise this point, we have integrated the PL kinetics taken a 660 nm over the timescales of the experiment (Figure 5.27) to obtain the fraction of the total PL emitted with respect to time. Whilst the majority of the emission comes directly from the ^{1}CTs formed via charge transfer on early timescales (<100 ns), a substantial portion of the emission (~25%) originates from longer timescales (>100 ns,) by which we expect the initially formed ^{1}CTs to have decayed, leaving behind only the non-emissive ^{3}CTs. This confirms that the enhanced radiative properties of the NPD:TXO-TPA blend originates from the lack of non-radiative pathways for the ^{3}CT.

Fitting the trPL decays with a simple bi-exponential function isn't possible, as the kinetics are a little more complex. However, the timescales do appear to be broadly similar to the TA measurements. For example, there is a slight decrease in the emission decay rate at about 100 ns in the trPL, consistent with the switch over from the prompt to delayed regime in the TA. At around 1 μs, the "delayed" decay phase begins: this is also consistent with the increase NPD hole population decay in the TA at this time, associated with the rISC of ^{3}CTs back to ^{1}CTs.

One final curiosity is the red-shift between the prompt component (spectrum taken at 10 ns) and the delayed component (spectrum taken at 1 μs). This suggests that something is happening to the CT states over the timescales taken for rISC. Previous work be Deotare *et al.* has suggested that long-lived CT states in organic D/A systems have the ability to move diffusively around the BHJ, where they eventually access low-energy sites in the density of states.[133] This has the effect of red-shifting the emission over ns to μs timescales, consisting with our observations in the NPD:TXO-TPA blend. Therefore, we attribute the emission red-shift in the NPD:TXO-TPA blend to this process.

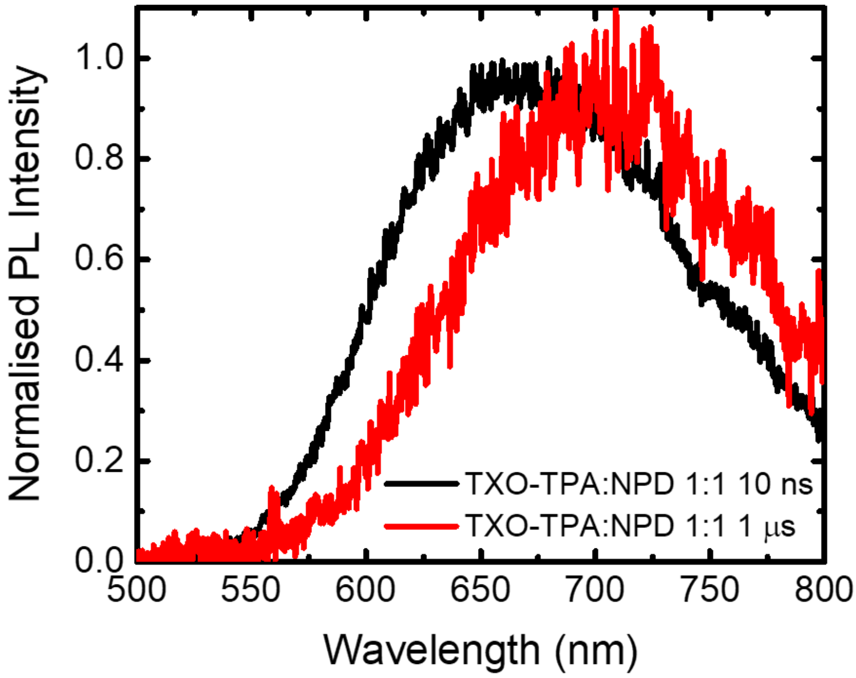

Figure 5.25*: The emission spectra taken from the trPL measurement of the 1:1 NPD:TXO-TPA blend film: λ_{ex} = 400 nm, fluence = 15.3 μJ cm^{-2}. There is a red-shift in the emission spectrum with time, as can be seen by a large change in emission maxima from 660 nm to 700 nm between 10 ns and 1 μs. We assign this red-shift to the diffusion of the long-lived CT states to lower energy sites in the BHJ.*

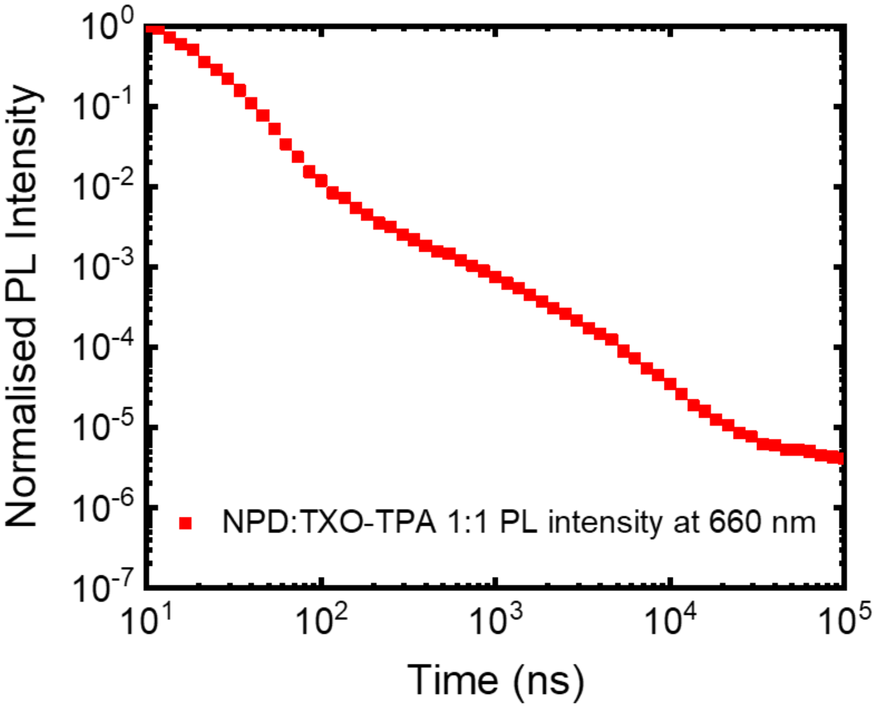

Figure 5.26*: The kinetics of the PL decay at 660 nm, taken from the trPL measurement of the 1:1 NPD:TXO-TPA blend film: λ_{ex} = 400 nm, fluence = 15.3 μJ cm^{-2}. There is a substantial amount of long-lived emission in the blend, occurring at timescales beyond the ^{1}CT decay, indicating that the ^{3}CT must be able to undergo rISC back to the ^{1}CT, or re-dissociate into free charges.*

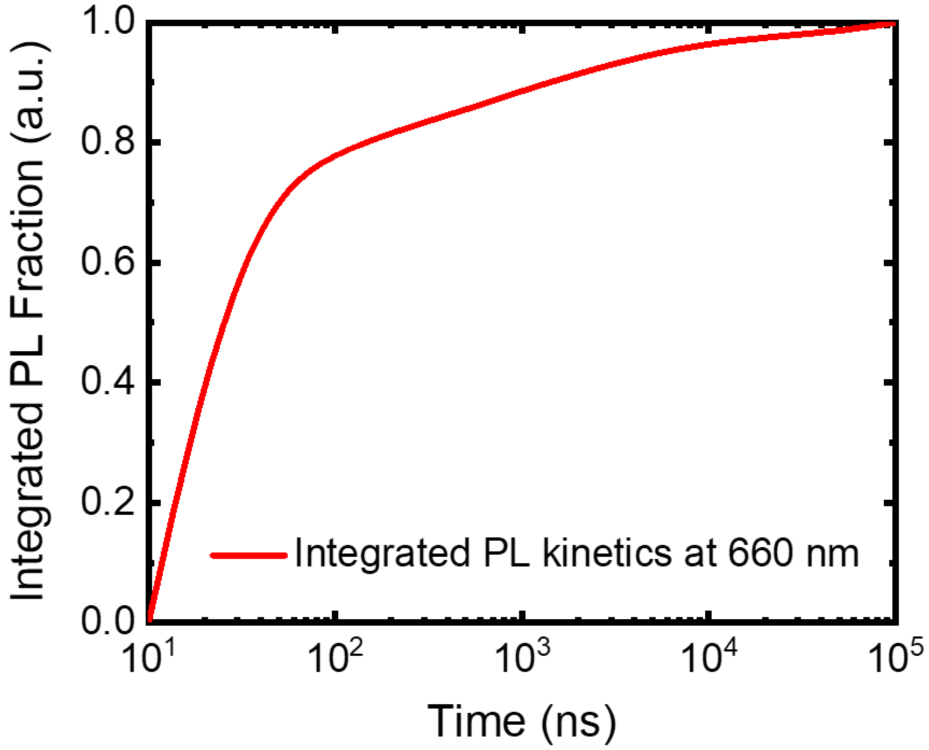

***Figure 5.27**: The integrated PL decay kinetics at 660 nm, taken from the trPL measurement of the 1:1 NPD:TXO-TPA blend film: λ_{ex} = 400 nm, fluence = 15.3 μJ cm^{-2}. To further clarify the point that there is a substantial amount of emission from the blend on timescales beyond the ^{1}CT lifetime, approximately 25% of the emission occurs over timescales of >100 ns. By this time, none of the original population of optically-generated ^{1}CTs remain, meaning any emission must occur from ^{3}CTs that rISC back to the ^{1}CT, or ^{3}CTs that re-dissociate into charges that may eventually recombine to the ^{1}CT.*

5.8.2 Transient Photoluminescence of the TFB:TXO-TPA Blend

We now perform the same trPL experiments and analysis on the 1:1 TFB:TXO-TPA blend, with an excitation wavelength of 400 nm and a fluence of 15.3 μJ cm^{-2}. The PL spectra at 10 ns and 1 μs are shown in Figure 5.27, with the corresponding trPL decay and integrated kinetics in Figures 5.28 and 5.29. As has been the case with previous measurements, we observe very similar behaviour between the TFB:TXO-TPA blend and its NPD counterpart, likely due to the energetic similarities between the materials. In the emission spectra taken at different time points, we observe the same red-shift in PL between prompt and delayed timescales, again attributed to the migration of the long-lived CT states to lower energy sites in the BHJ.

In the trPL kinetics, there appears to be less evidence of the biphasic decay than in the NPD:TXO-TPA blend, consistent with the TA. However, the integrated PL fraction at

650 nm again shows that a significant proportion of the emission occurs at timescales longer than the ^{1}CTs lives for (>100 ns). The proportion is slightly lower than for NPD:TXO-TPA, with approximately 20% of the emission occurring over long timescales. This is consistent with the lower PLQE of the TFB:TXO-TPA blend, suggesting that a smaller proportion of the ^{3}CTs are able to either rISC back to the ^{1}CT or re-dissociate and eventually form the ^{1}CT via recombination.

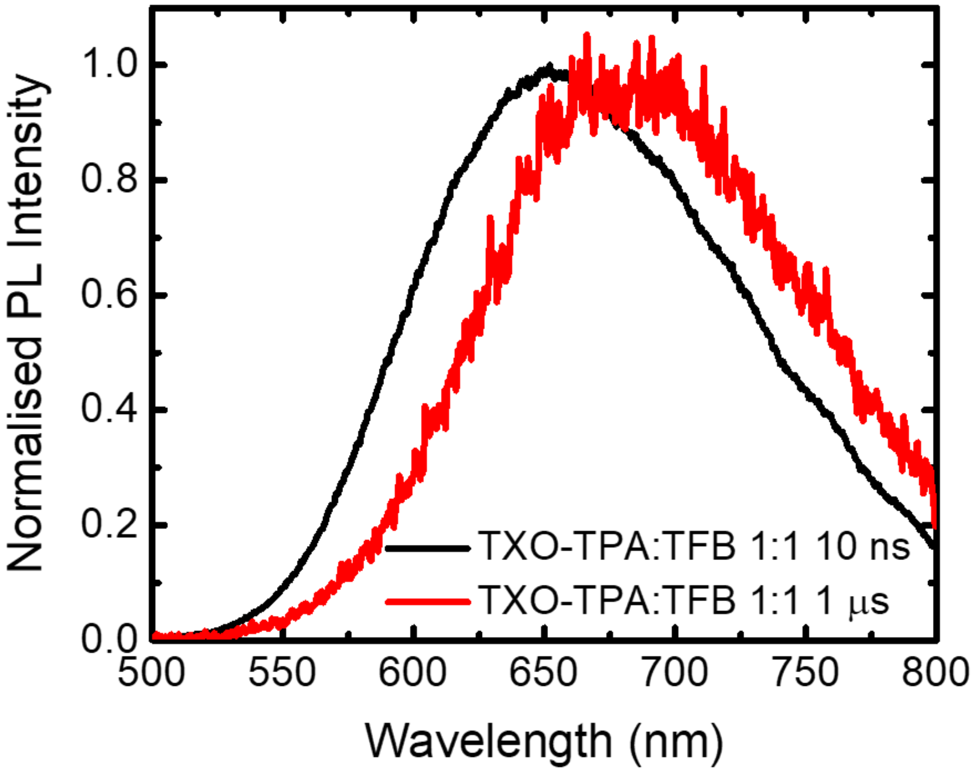

Figure 5.28*: The emission spectra taken from the trPL measurement of the 1:1 TFB:TXO-TPA blend film: λ_{ex} = 400 nm, fluence = 15.3 μJ cm^{-2}. There is a red-shift in the emission spectrum with time, as can be seen by a large change in emission maxima from 650 nm to 680 nm between 10 ns and 1 μs. We assign this red-shift to the diffusion of the long-lived CT states to lower energy sites in the BHJ.*

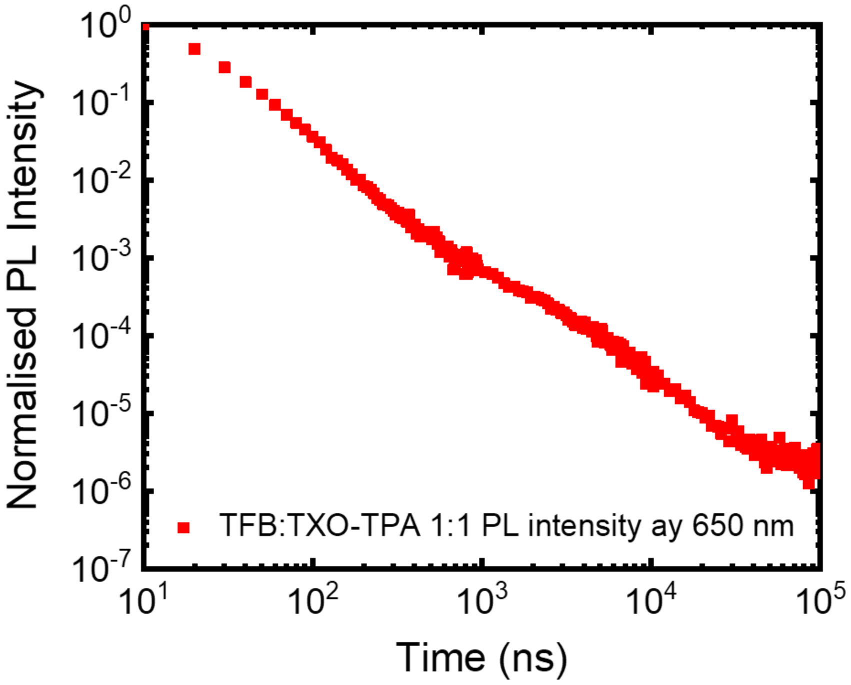

***Figure 5.29**: The kinetics of the PL decay at 650 nm, taken from the trPL measurement of the 1:1 TFB:TXO-TPA blend film: λ_{ex} = 400 nm, fluence = 15.3 μJ cm^{-2}. There is a substantial amount of long-lived emission in the blend, occurring at timescales beyond the ^{1}CT decay, indicating that the ^{3}CT must be able to undergo rISC back to the ^{1}CT, or re-dissociate into free charges.*

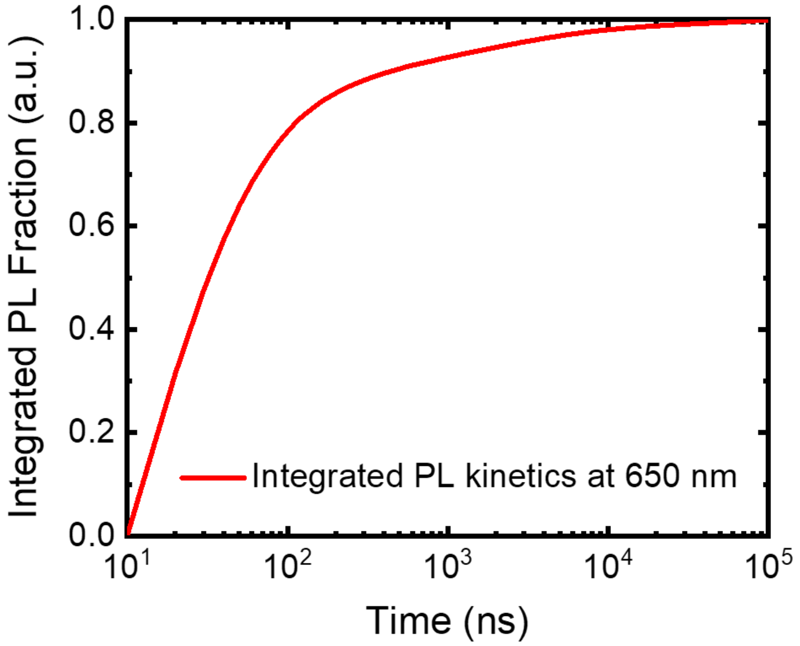

***Figure 5.30**: The integrated PL decay kinetics at 660 nm, taken from the trPL measurement of the 1:1 TFB:TXO-TPA blend film: λ_{ex} = 400 nm, fluence = 15.3 μJ cm^{-2}. To further clarify the point that there is a substantial amount of emission from the blend on timescales beyond the ^{1}CT lifetime, approximately 25% of the emission occurs over timescales of >100 ns. By this time, none of the original population of optically-generated ^{1}CTs remain, meaning any emission must occur from ^{3}CTs that rISC back to the ^{1}CT, or ^{3}CTs that re-dissociate into charges that may eventually recombine to the ^{1}CT.*

5.9 OPV Devices Fabricated From the TXO-TPA Blends

In order to evaluate the effectiveness of our strategy of removing low-lying local triplet states below the ^{3}CT on reducing the non-radiative losses, we have fabricated OPV devices from the NPD:TXO-TPA and TFB:TXO-TPA 1:1 blends. It was not possible to fabricate working devices from the TFB:TXO-TPA blend due to a poor form morphology, with a rough surface and many pinholes in the active layer. Therefore, we shall focus solely on the NPD:TXO-TPA blend. The devices used in this study were fabricated and tested by Qinying Gu. Both conventional and inverted architecture devices were fabricated, with the inverted device structures giving the best performance. The structure of the optimised devices was: ITO/ZnO (30 nm)/NPD:TXO-TPA 1:1 (70 nm)/MoO_3 (10 nm)/Ag (100 nm). In Figure 5:31, the J-V curve of the device is shown, with the key performance metrics included in Table 5.2. Whilst it is initially apparent that the device performance is poor with a PCE of 0.02%, there are some positive metrics: mainly the very high V_{OC} of 1.40 V. However, the J_{SC} and FF are low, at 0.053 mA cm^{-2} and 0.28, respectively. We attribute the low FF to the unequal charge carrier mobility, with the hole mobility of NPD likely much greater than the electron mobility of TXO-TPA.[134]

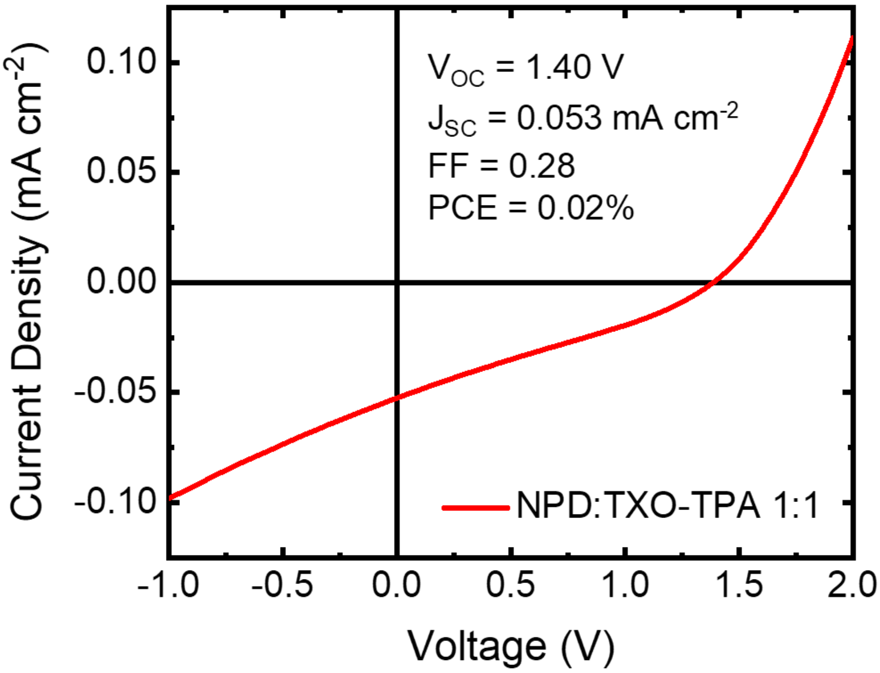

***Figure 5.31**: The current density-voltage curves of the champion NPD:TXO-TPA 1:1 inverted device, measured under an AM1.5G solar spectrum. The PCE was 0.02%. The device structure was ITO / ZnO (30 nm) / NPD:TXO-TPA 1:1 (70 nm) / MoO_3 (10 nm) / Ag (100 nm). Device fabricated and tested by Qinying Gu.*

Blend	V_{OC} (V)	J_{SC} (mA cm^{-2})	FF	PCE (%)
NPD:TXO-TPA	1.40	0.053	0.28	0.02

***Table 5.2**: The key performance metrics of the NPD:TXO-TPA 1:1 device, measured under an AM1.5G solar spectrum.*

The low J_{SC} can be explained by the EQE_{PV} response of the device in Figure 5.32, where there is only significant photocurrent generation in the UV region (<400 nm). A maximum EQE_{PV} of 7% is reported at a wavelength of 375 nm, which is the limit of our EQE_{PV} setup. The integrated EQE_{PV} gives a predicted J_{SC} of 0.11 mA cm^{-2}, not entirely consistent with the measured J_{SC}. However, it is possible that the error inherent to the measurement becomes significant due to the low photocurrent generation of the device, resulting in the discrepancy. Of interest is the presence of photocurrent generation at wavelengths below the NPD absorption onset (>425 nm), indicating that photocurrent generation from excitons generated on TXO-TPA is indeed possible, despite the very low driving energy for this process.

Due to the weak light absorption of the blend, especially in the visible region, we have also calculated the IQE_{PV} as it takes into account photocurrent generation by only those photons absorbed in the active layer, not the total number of incident photons. Therefore, this metric will give us a better idea of the photocurrent generation efficiency of the device. Here, we use the method proposed by Burkhard *et al.*,[135] which uses a transfer matrix formalism to calculate the interferences of coherent reflected and transmitted waves at each interface in the device. This allows us to then determine the electric field intensity of the different wavelengths of light throughout the whole device stack. For this calculation, the real and imaginary index of refraction, n and k, for the electrodes and interlayers in the stack can be obtained from the literature.[136,137] For the active layer, the approximation $n = 2$ can be used without inducing significant error and k can be calculated from the following relation:[135]

$$k = \frac{\lambda\alpha}{4\pi} \tag{5.1}$$

Where λ is the wavelength of light and α is the absorption coefficient, which can be determined from the steady-state absorption spectrum by:

$$\alpha = \frac{(OD)\ln(10)}{x} \tag{5.2}$$

Where OD is the optical density of the film and x is the film thickness. Using this information, we can determine the fraction of incident light absorbed in the active layer and therefore the $\mathrm{IQE_{PV}}$.

The resulting calculated $\mathrm{IQE_{PV}}$ response, also displayed in Figure 5.32, is a nearly flat line with a maximum $\mathrm{IQE_{PV}}$ of 13%. An important point is that whist the $\mathrm{IQE_{PV}}$ is typically calculated using the total fraction of light reflected from the device (equation 2.88), here we have chosen to calculate it using only the fraction of light absorbed by the active layer. This is done as the interlayers, such as ZnO, absorb strongly at the same wavelengths as the active layer. This parasitic absorption could distort the apparent performance of the device, giving $\mathrm{IQE_{PV}}$ values that substantially underestimate the ability of the active layer to generate photocurrent. Interestingly, we can see in long-time TA of this blend (Figure 5.21) that the

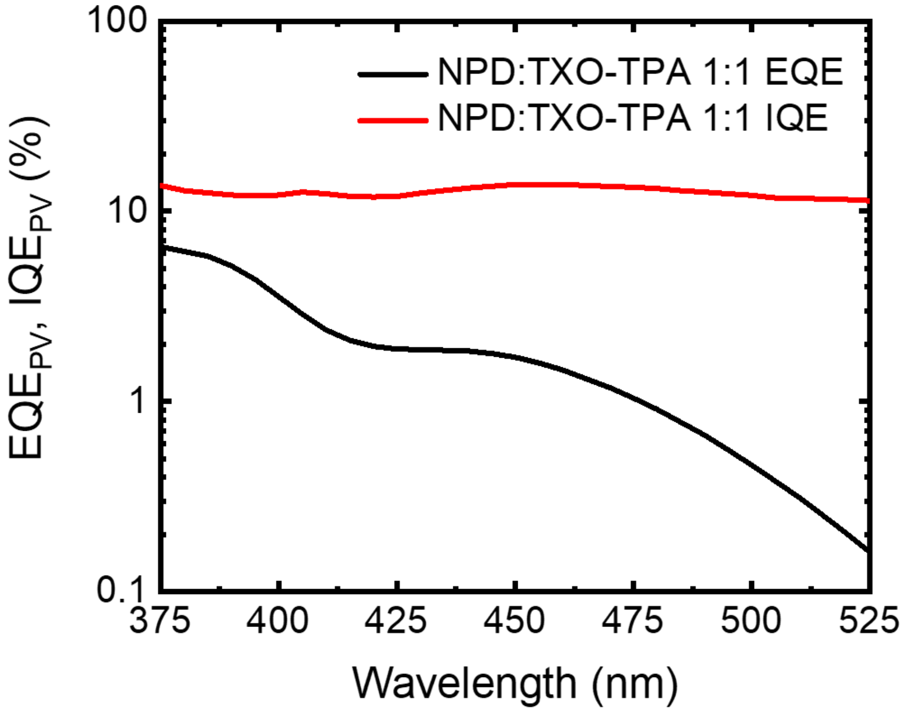

***Figure 5.32**: The $\mathrm{EQE_{PV}}$ and $\mathrm{IQE_{PV}}$ response curves of the champion NPD:TXO-TPA 1:1 devices. The $\mathrm{EQE_{PV}}$ max is 7% at 375 nm, whilst the $\mathrm{IQE_{PV}}$ response is fairly flat, with a maximum of 13%. The flat $\mathrm{IQE_{PV}}$ response suggests photocurrent generation by both NPD and TXO-TPA is equally efficient, despite a very small energetic offset for the hole transfer from TXO-TPA to NPD. Device fabricated and tested by Qinying Gu.*

population of holes on NPD remaining on the timescales of charge extraction (100 ns – 1 μs) is roughly equal to the IQE_{PV}.[138] This implies that perhaps one factor limiting the device performance is the decay rate of the ^1CT, with a large proportion (80 – 90%) of charges decaying before extraction. The shape of the IQE_{PV} curve tells us that photocurrent generation is equally efficient from both NPD and TXO-TPA, indicating that the small HOMO-HOMO offset seems to provide no additional barrier to CT state formation and ultimately charge photogeneration. We attribute the ability to separate excitons on TXO-TPA with a small offset to the rapid formation of a strong ICT state in TXO-TPA after optical excitation, which provides a built-in charge separation in the molecule. We propose that this pre-separation of charges on TXO-TPA prior to the charge transfer process reduces the coulombic attraction between the electron and hole, therefore decreasing the energy required to overcome the coulombic binding energy. Indeed, it is even possible that the ICT may dissociate spontaneously into free charges, further facilitating photocurrent generation. This is in-line with previous observations in D/A-type organic small molecules used in OPV applications.[139]

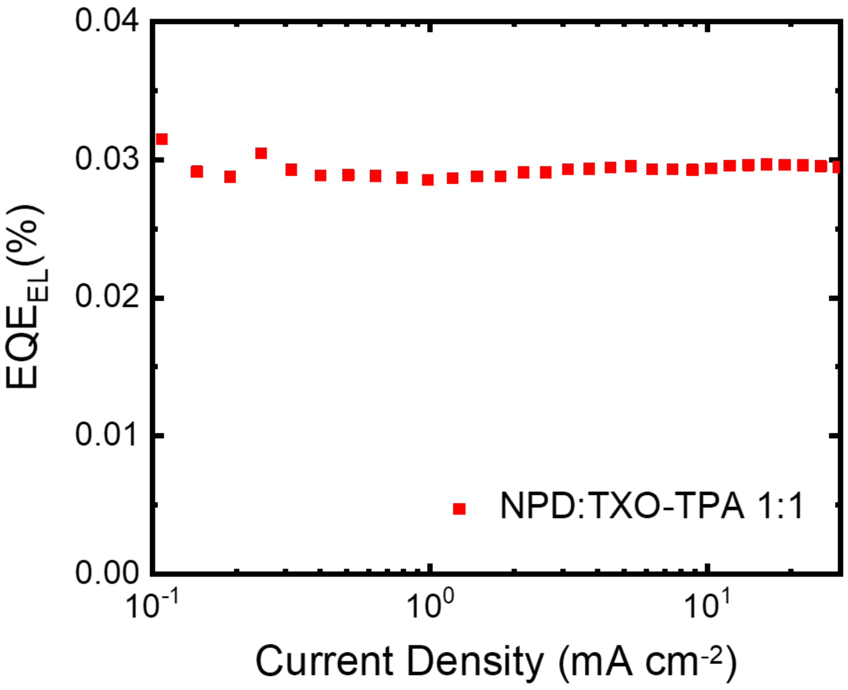

***Figure 5.33**: The plot of current vs EQE_{EL} of the champion NPD:TXO-TPA 1:1 device. The maximum EQE_{EL} of 0.03% is reached across a wide range of current densities. Device fabricated and tested by Qinying Gu.*

Finally, we examine the emissive properties of the NPD:TXO-TPA 1:1 device to determine whether the radiative efficiency of the blend has been improved compared to OPV systems with energetically-accessible triplets. The EQE_{EL} of the device is given in Figure 5.33. Excitingly, we report a very high EQE_{EL} max of 0.03%, flat across a wide range of current densities. This corresponds to an extremely low non-radiative voltage loss of 234 meV, as calculated from equation 2.93. Such a result indicates that designing an OPV blend where there is an absence of molecular triplet states below the ^{3}CT is indeed a promising tactic for reducing non-radiative voltage loss and confirms the viability of our approach.

5.10 Conclusions

In summary, we have demonstrated in our model study the feasibility of an OPV device utilising a low ΔE_{ST} TADF electron acceptor material. Through ultrafast TA measurements, we show the ability to separate excitons generated on TXO-TPA when blended with materials with suitable energetics, which is a prerequisite to successful OPV device operation.[140] Further to this, we then establish the long lived nature of these new species, with the hole localised on the electron donor and the electron on the TADF acceptor. A long carrier lifetime is extremely important to ensure that the free electrons and holes live long enough to reach their respective electrodes.[36] These processes are summarised in Figure 5.34. In our system, the carrier lifetime was enhanced by the formation of ^{3}CTs, either through direct ISC from the ^{1}CT or through bimolecular recombination, which are spin protected against decay to the ground state.[113] This is in contrast to more typical polymer-donor OPV systems, where ^{3}CT formation ultimately results in the loss of carriers through local triplet formation and constitutes a major energy loss pathway.[141] We credit the relatively high PLQE and EQE_{EL} of our blends to the removal of this non-radiative pathway. Maximising the EQE_{EL} is key to creating an “ideal” solar cell and this result brings OPV closer to its inorganic counterparts, which have efficiencies approaching the Shockley-Queisser limit.[142] Through PL measurements, we determine the main radiative pathway to be from exciplex emission from the ^{1}CT, confirmed by the characteristic red shifted emission from that of the pure donor material.[143–145] Finally, we verify that photocurrent can be extracted from an TADF acceptor OPV device with a low energy loss, highlighting its potential as a new class of donor material for OPV applications.

These findings could potentially have a significant impact on design rules for donor materials used in OPV, leading to the development of a new class of low ΔE_{ST} acceptor materials to reduce non-radiative losses and to maximise PCE. The TXO-TPA acceptor that we use in this study was optimised for OLED applications and consequently has many non-ideal properties for use in OPV. These include a low oscillator strength in the visible (>400 nm) region, a relatively wide band gap of 2.18 eV and a poor electron mobility that all hindered device performance. Consequently, efforts should centre on improving these parameters in order to realise the full potential of a low ΔE_{ST} donor OPV device, with a particular focus on creating materials that balance the ΔE_{ST} and oscillator strength. Such materials would ideally possess a relatively small ΔE_{ST} (100–200 meV) to ensure that the molecular triplet state is higher in energy than the ^{3}CT,[112] whilst retaining significant oscillator strength for the ICT transition to enhance light absorption and photocurrent generation.[111] If these criteria can be met, then a device based off a low ΔE_{ST} donor could lead to record OPV efficiencies and push the field closer towards the Shockley-Queisser limit.

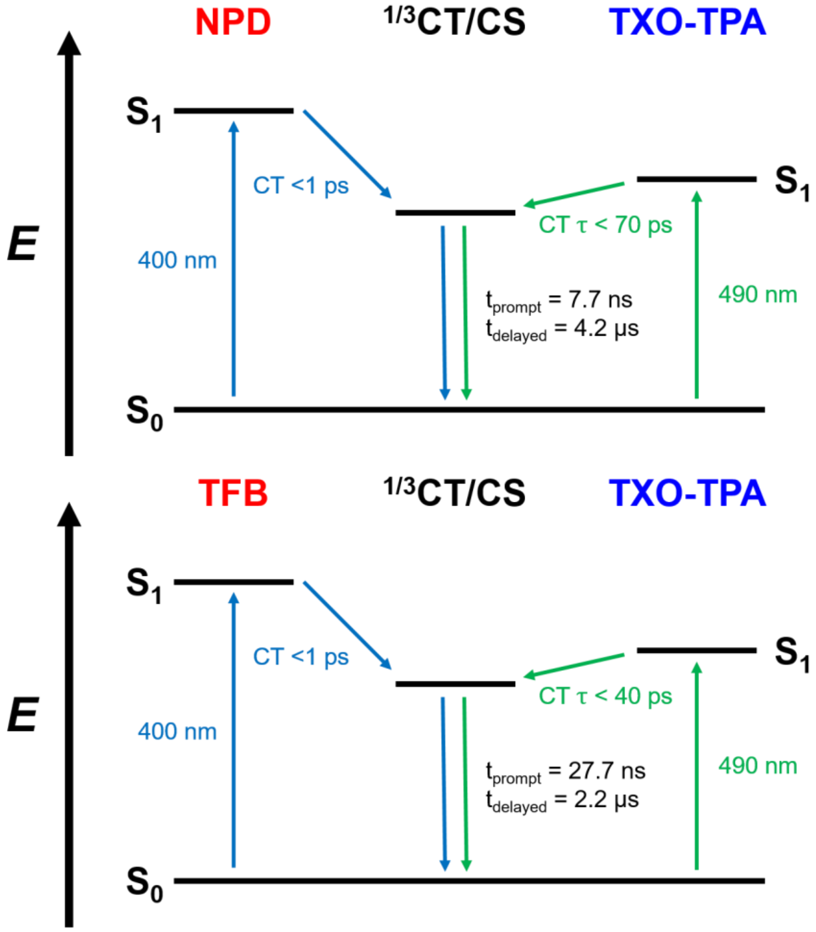

***Figure 5.34**: Schematics summarizing the photophysical processes occurring in the NPD:TXO-TPA and TFB:TXO-TPA blends, as determined from the TA experiments.*

6 A Red-Absorbing Low Exchange Energy Material for OPV and OLED Applications

6.1 Motivation

As we have determined in the previous chapter, utilising a low exchange energy acceptor has proven to be a viable strategy to reduce the non-radiative voltage loss in an OPV device. However, due to the non-ideal properties of the TADF material TXO-TPA used, including weak visible light absorption and likely low electron mobility, the OPV device performance was poor. Therefore, we shall now seek to build on this initial work by employing materials with more suitable optical and electronic properties. For this purpose, we have identified a novel class of materials, known broadly as curcuminoids, which may possess these prerequisite attributes. Firstly, they have demonstrated the ability to form efficient NIR-emitting OLEDs with $\mathrm{EQE_{EL}}$'s of up to 10%, utilising TADF to convert non-emissive triplets back into singlets.[146] The presence of efficient rISC implies a small exchange energy is present, important for our application. Secondly, they also possess strong light absorption in the visible spectral region up to 700 nm. This has led to their successful use as donor materials in OPVs with fullerene acceptors, with some derivatives achieving PCEs of $>4\%$.[147] Given their exciting properties, curcuminoids have great potential for use as low exchange energy acceptors for OPV when paired with a suitable wider-gap electron donor. In addition to investigating the use of curcuminoid derivatives as electron acceptors for OPV, we will also undertake a detailed spectroscopic analysis of the photophysics of the pure curcuminoid material in its use as a TADF emitter in OLEDs and as an electron donor in a blend with a fullerene acceptor. We believe these additional studies are of great interest, given the novelty of these materials and lack of prior spectroscopic investigations.

6.2 Materials

The curcuminoid derivative employed as the low exchange energy acceptor, known herein simply as "curcuminoid" was synthesised by Dandan Yao and used as provided. The electron donors poly(9,9-dioctylfluorene-*alt*-bithiopene) (F8T2) and TFB and the electron acceptor

$PC_{60}BM$ were purchased from Sigma Aldrich, whilst the electron donors 4,4',4''-Tris[(3-methylphenyl)phenylamino]triphenylamine (m-MTDATA) and NPD and the wide band-gap host 3,3'-Di(9*H*-carbazol-9-yl)-1,1'-biphenyl (mCBP) were acquired from Lumtec. The structures of the materials used in this study are shown in Figure 6.1. In addition, the energetic of these materials are displayed in Table 6.1, including the energy of the lowest local triplet state where appropriate. The blue/green absorbing electron donor F8T2 was chosen for pairing with the curcuminoid due to its complementary absorption spectrum and the possibility of creating an OPV blend with a very low energy loss. The very small HOMO-HOMO offset between the D and A is nominally given as 0 eV due to the close alignment of the HOMOs,[148] but is likely not completely accurate due to the difficulties in obtaining accurate and consistent HOMO level energies from CV.[117] However, it is probable that the energetic offset is minimal, allowing for the possibility of hole transfer from the curcuminoid with very little energy loss, consistent with the previous observations in the NPD:TXO-TPA and TFB:TXO-TPA blends. Whilst the triplet energy of F8T2 has not been reported, given the empirical rule for organic polymers where $\Delta E_{ST} = 0.6 - 0.7$ eV,[108] one may expect the triplet of F8T2 to lie at around 1.7 – 1.8 eV. This is consistent with observations of F8T2:$PC_{60}BM$ blends, where triplets are formed on $PC_{60}BM$ in preference to F8T2. Given the triplet energy of the fullerene is around ~1.5 eV,[61] this implies the triplet of F8T2 >1.5 eV as they do not form,[149] in-line with the expected values. As the CT energy of an F8T2:curcuminoid blend is likely similar to that of the neat curcuminoid due to the small energetic offset, this would place the triplet of F8T2 at an equal of higher energy to the ^{3}CT, a prerequisite for the successful implementation of our strategy to remove the triplet loss pathway. The triplet energy of the curcuminoid has not previously been reported, however given its propensity for mediating the rISC of the triplet state back to the singlet, any molecular triplets formed on this component are not likely to represent a significant loss pathway. Additionally, the electron donors m-MTDATA, NPD and TFB are employed to provide alternatives to F8T2 with larger HOMO-HOMO offsets to ensure that efficient hole transfer from the curcuminoid can occur. Due to the wider band gaps of these materials, their triplet exciton energies all lie well above the energy of any CT state formed between them and the curcuminoid,[113,150,151] negating the possibility of any molecular triplet formation on the electron donor.

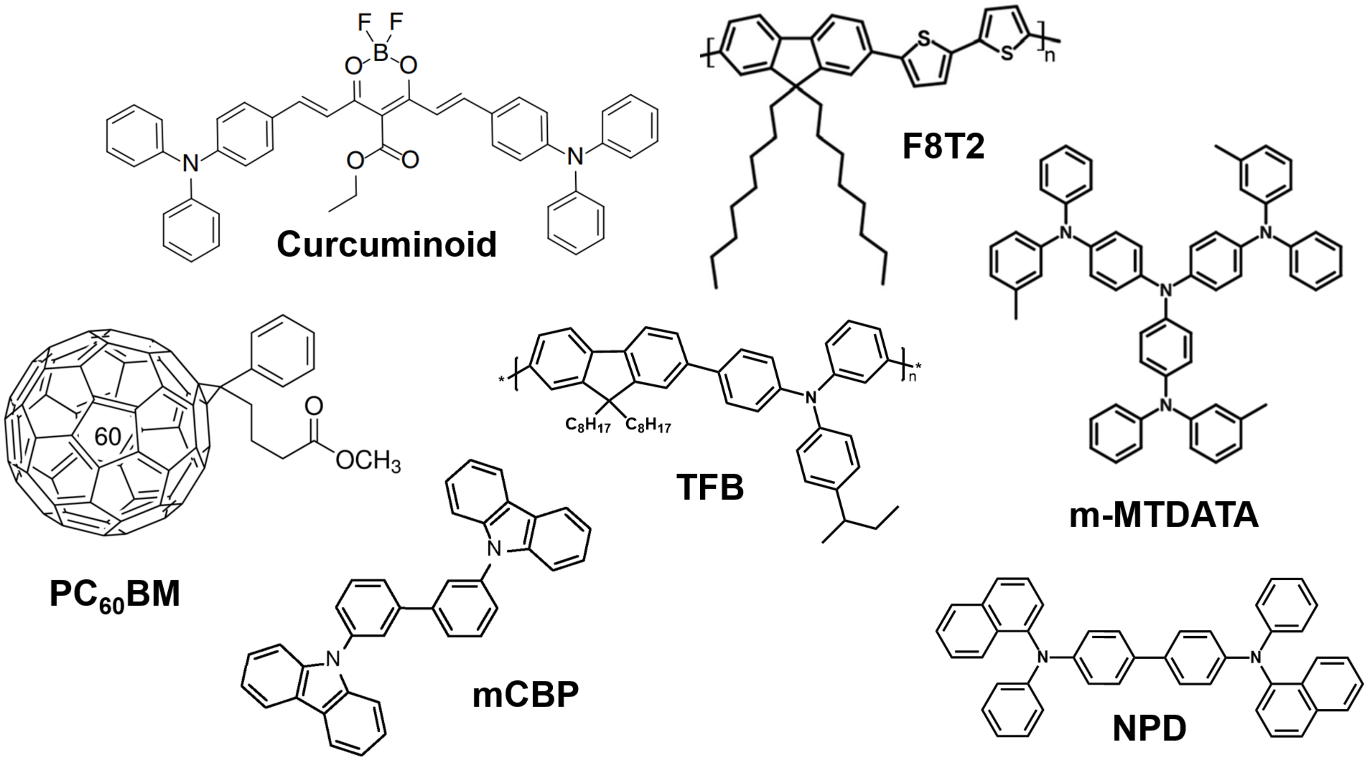

***Figure 6.1**: The chemical structures of the materials used in this study: the TADF material curcuminoid, the electron donors F8T2, m-MTDATA, NPD and TFB, the electron acceptor $PC_{60}BM$ and the wide band-gap host material mCBP.*

Material	HOMO (eV)	E_g (eV)	HOMO + E_g (eV)	HOMO-HOMO offset (eV)	"LUMO-LUMO" offset (eV)	T_1 energy (eV)
Curcuminoid	-5.50	1.70	-3.80	-	-	1.5
F8T2	-5.50	2.40	-3.10	0	0.7	~1.7 – 1.8*
m-MTDATA	-5.10	3.10	-2.00	0.4	1.8	2.7
NPD	-5.19	3.00	-2.19	0.31	1.61	2.3
TFB	-5.16	2.90	-2.26	0.34	1.54	2.2
$PC_{60}BM$	-6.30	2.30	-4.00	0.8	0.2	1.5
mCBP	-6.00	3.60	-2.40	-	-	2.8

***Table 6.1**: The energetics and optical properties of the materials under study in this section, including the energetic offsets with the curcuminoid and triplet energies, where appropriate.*

** Triplet energy of F8T2 estimated from the empirical rule that $\Delta E_{ST} = 0.6 – 0.7$ eV in organic conjugated polymers.*

6.3 Photophysics of the Curcuminoid

6.3.1 Steady-State Absorption and Photoluminescence of the Curcuminoid

We begin our work on the curcuminoid by examining the properties of the neat material in order to develop our understanding of this novel class of materials. Firstly, we examine the steady-state absorption spectrum of a neat film of the curcuminoid, spun at 3000 rpm from a 5 mg/mL solution in chloroform to give a film thickness of 90 nm (Figure 6.2). The primary feature is a broad absorption band spanning most of the visible region from 450 – 700 nm, assigned to the ICT transition between the triphenylamine donor and the borondifluoride acceptor.[146] Of interest is the absorption strength of the ICT band, which appears to have a much greater intensity than is typical of TADF ICT-type emitters. This suggests a greater overlap of the initial and final orbitals involved in the electronic transition (equation 2.38) that imparts a higher oscillator strength, which also results in a larger exchange energy (equation 2.38) and a $\Delta E_{ST} = 200$ meV. At first observation, such properties appear incompatible with a relatively efficient NIR TADF emitter ($EQE_{EL} = 10\%$)[146] and we shall address this point later in this section.

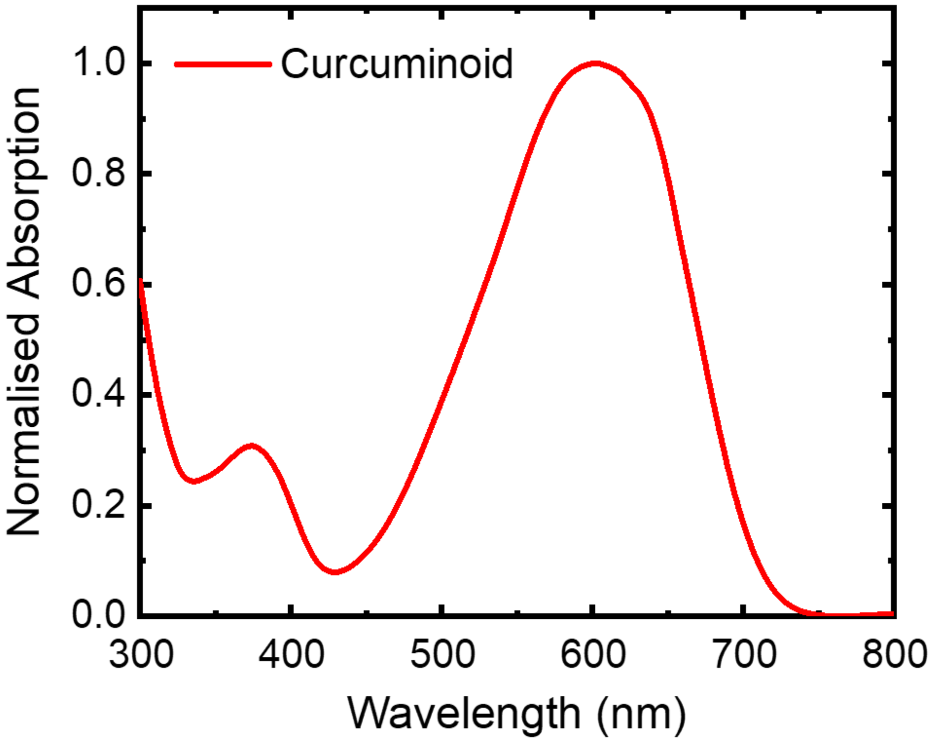

***Figure 6.2**: The normalised absorption spectrum of a neat film of the curcuminoid.*

Turning next to the PL of the curcuminoid, we have diluted the material at a 6 wt % ratio in the wide band gap, high triplet energy (2.8 eV) host mCBP to obtain the best emissive performance.[152] The need for dilution of the emitter is in line with previous work where the PLQE of the neat material was very low (3.5%),[146] likely due to concentration quenching effects.[120] With this dilution, we obtained a maximum PLQE of 52%, similar to earlier reports.[146] The PL spectrum of the curcuminoid:mCBP 6:94 film is shown in Figure 6.3. The PL maxima is at about 730 nm, confirming the use of this material as a NIR emitter.

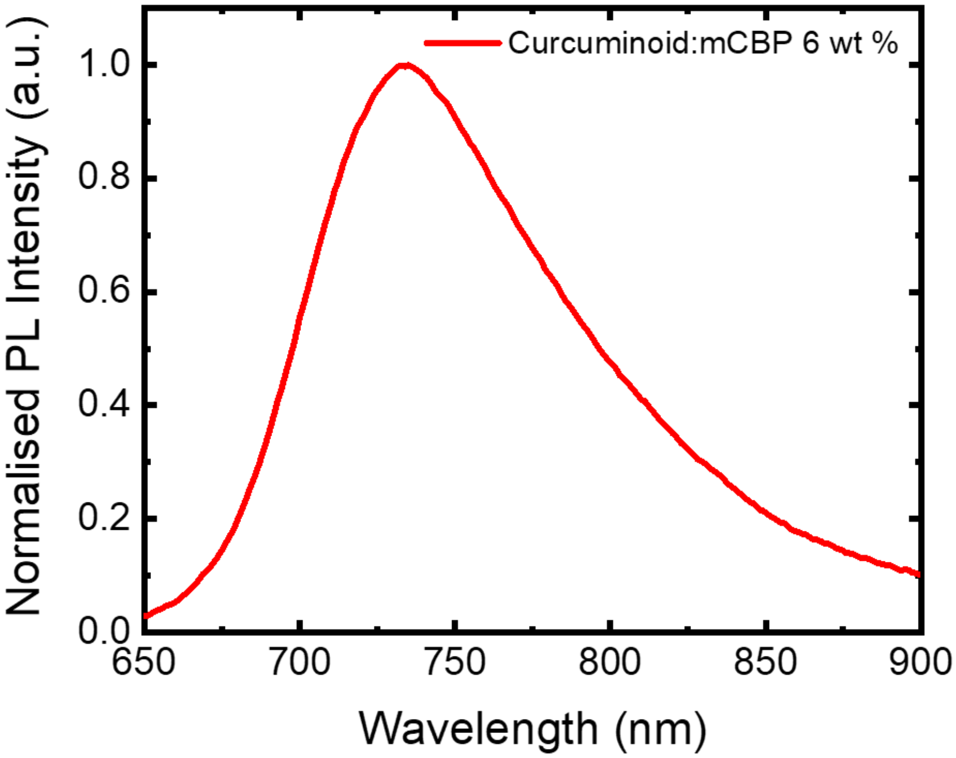

***Figure 6.3**: The normalised PL spectra of a curcuminoid:mCBP 6:94, excited at a wavelength of λ_{ex} = 520 nm. A PLQE of 52% was obtained for this doped film, largely consistent with previous reports on the curcuminoid.*

6.3.2 Short-Time Transient Absorption of the Neat Curcuminoid

Having explored the basic steady-state properties of the curcuminoid, we now turn to the transient measurements, starting first with TA. The TA spectrum and kinetics of a neat film of the curcuminoid, pumped at 610 nm with a fluence of 7 μJ cm^{-2}, are shown in Figures 6.4 and 6.5. Present at the earliest times are three features: the curcuminoid GSB, peaked at 630 nm; the SE band between 700 – 900 nm and a weak PIA band at 1000 nm. Given the maximum of the SE at this time, the PIA can be attributed to the singlet exciton on the curcuminoid.

As time progresses, there is a red-shifting and rapid loss of the SE band, with a much smaller decrease in the intensity of the GSB that is particularly apparent in the kinetics. Over the timescales of SE loss, the PIA band in the IR appears to broaden, with a contribution at higher energies around 950 nm that appears to increase in-tandem with the SE loss. Finally, by 1 ns, the SE has been completely quenched and a weaker, red-shifted GSB remains with a weak PIA band centred at 950 nm. The fact that the loss of the SE is much more rapid than the GSB is interesting, as if the loss of SE was solely due to the radiative/non-radiative decay of singlet states back to the ground state, one would expect the GSB and SE to decay in-step. As this is not the case, it implies that a conversion of the singlet population to another, non-emissive state must be occurring. Because of this, most obvious conclusion is that the loss of singlets is as a result of the relatively rapid ISC to the triplet state, supported by the formation of a new PIA band, which is therefore assigned to the triplet state.

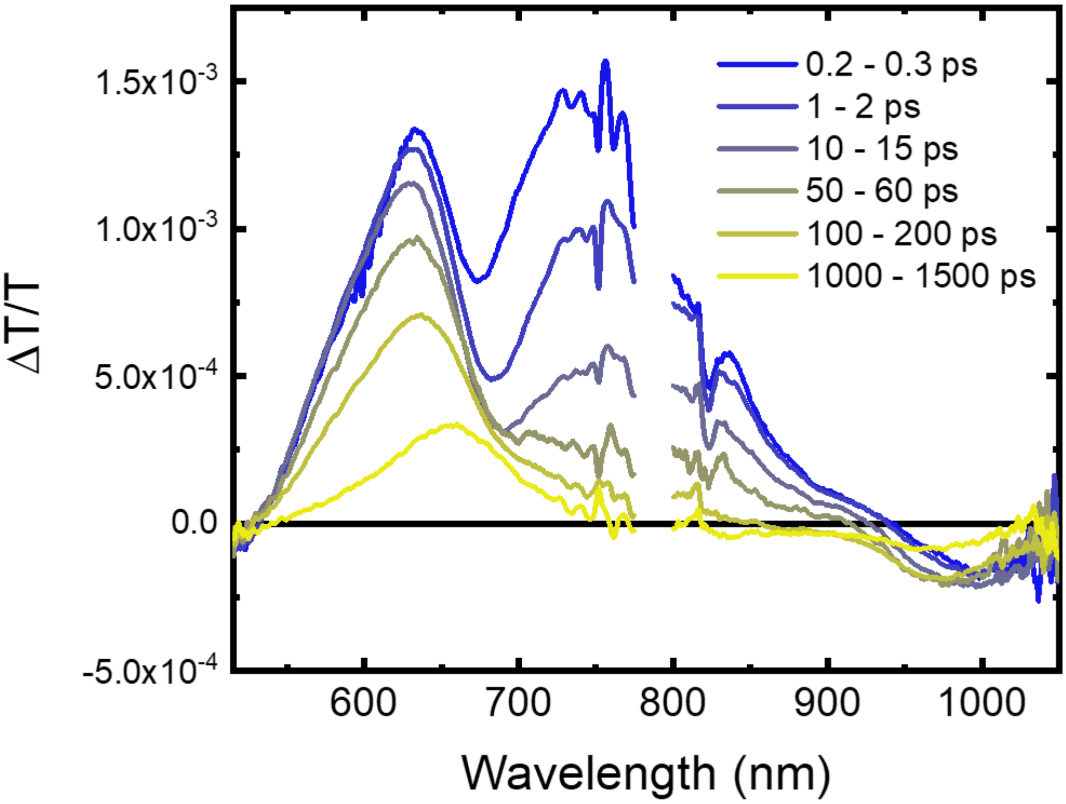

***Figure 6.4**: The short-time TA spectra of a neat film of the curcuminoid: λ_{ex} = 610 nm, fluence = 7 μJ cm^{-2}. Initially present in the 550 – 675 nm region is the GSB, a broad SE band is in the 700 – 900 nm region and a weak PIA is peaked at 1000 nm, attributed to the singlet exciton. As time progresses, the SE band decays more rapidly than the GSB, until it is no longer visible by 1 ns. Left behind is a weaker, red-shifted GSB and a new, slightly higher energy PIA band at 950 nm, likely resulting from triplet excitons formed by relatively rapid ISC.*

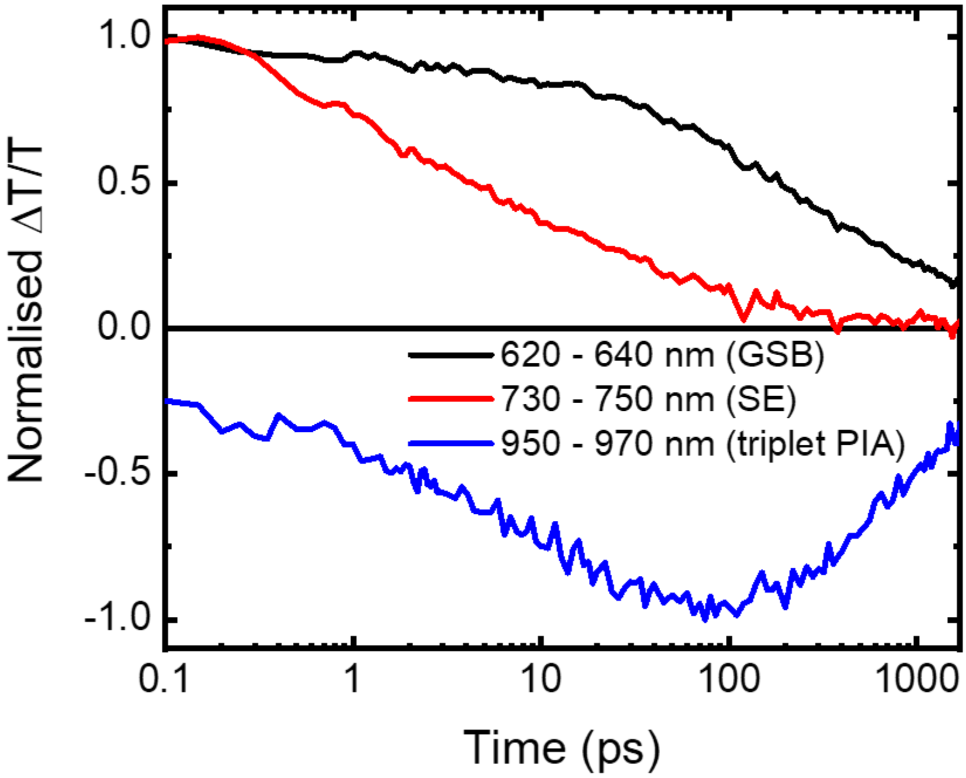

Figure 6.5*: The short-time TA kinetics of a neat film of the curcuminoid: λ_{ex} = 610 nm, fluence = 7 μJ cm^{-2}. The kinetic traces of the regions associated with the GSB, SE and triplet exciton PIA clearly show the processes occurring in the neat curcuminoid film. The difference in the decay rate of the GSB and SE is obvious, providing strong evidence that the loss of emissive singlet excitons cannot only be due to radiative or non-radiative recombination to the ground state. Therefore, a conversion to a non-emissive state, most likely triplets, must be occurring in competition with singlet decay to ground. The rise in the region associated with the new PIA forming appears to occur over the same timescales as the loss of the SE, suggesting that it is associated with a new species being formed from the singlet.*

6.3.3 Short Time Transient Absorption of the Curcuminoid Doped Into mCBP

Next, we turn to the curcuminoid doped into mCBP at 6 wt %, a very similar film to those that gave the best EQE$_{EL}$ the previously reported OLEDs of 10%.[146] The films were spin coated at 4000 rpm from a chloroform solution with a total concentration of 20 mg/mL. For the TA measurements, an excitation wavelength of 610 nm and a fluence of 21.4 μJ cm^{-2}, with the resulting TA spectra and kinetics displayed in Figures 6.6 and 6.7. In the TA spectra, a broad positive feature is seen initially, covering the entire spectral range between 600 – 900 nm. This is assigned to a mixture of the GSB and SE, with the peaks merged into one due to the smaller

Stokes-shift of the diluted film compared to the neat film. In comparison to the neat film, the decay of the GSB and SE regions proceed at similar speeds, indicating perhaps a reduction in ISC rate. By 1 ns though, the SE region (>700 nm) has completely decayed, leaving behind a weak GSB peaked at 640 nm. This likely represents the small amount of singlets that undergo ISC to the triplet state and are no longer directly emissive. In the region probed, there is no obvious PIAs belonging to the singlet or triplet present.

The fact that only a very small amount of triplets are ultimately formed after optical excitation is likely related to the surprisingly strong absorption of the ICT band. As the oscillator strength of the absorptive ICT transition is relatively high, this also results in a strong emission from this state. Therefore, the rate of the emission of the singlet is likely to be much larger than ISC, meaning most singlets decay radiatively in preference to ISC. This is unusual amongst TADFs, where often a very large proportion of the excited states undergo ISC due to the strongly decoupled HOMO and LUMO wavefunctions imparting a very slow rate of radiative decay to the singlet, often comparable to or slower than the rate of ISC.[153]

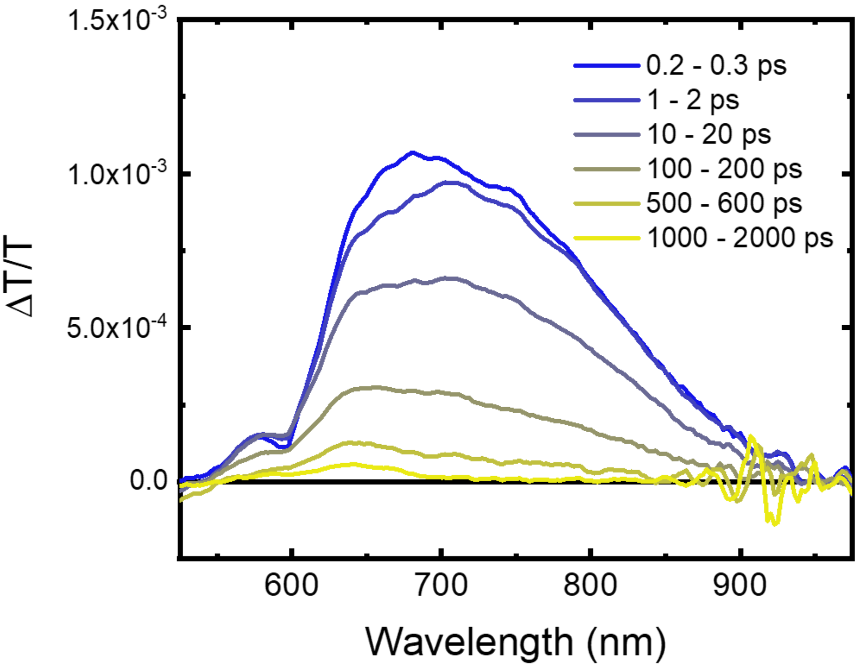

***Figure 6.6**: The short-time TA spectra of the curcuminoid doped in mCBP at 6 wt %: λ_{ex} = 610 nm, fluence = 21.4 μJ cm^{-2}. Initially present is a very broad positive feature, spanning 600 – 900 nm. This is assigned to a mixture of the curcuminoid GSB and SE. The SE region (>700 nm) appears to decay a little more quickly than the GSB region (600 – 700 nm), though the difference isn't as great as in the neat film. This suggests that ISC is not as fast in the doped film. After 1 ns, the SE region has decayed to zero, but a weak GSB of the curcuminoid remains. This represents the remaining excited state population that has undergone ISC to the triplet state.*

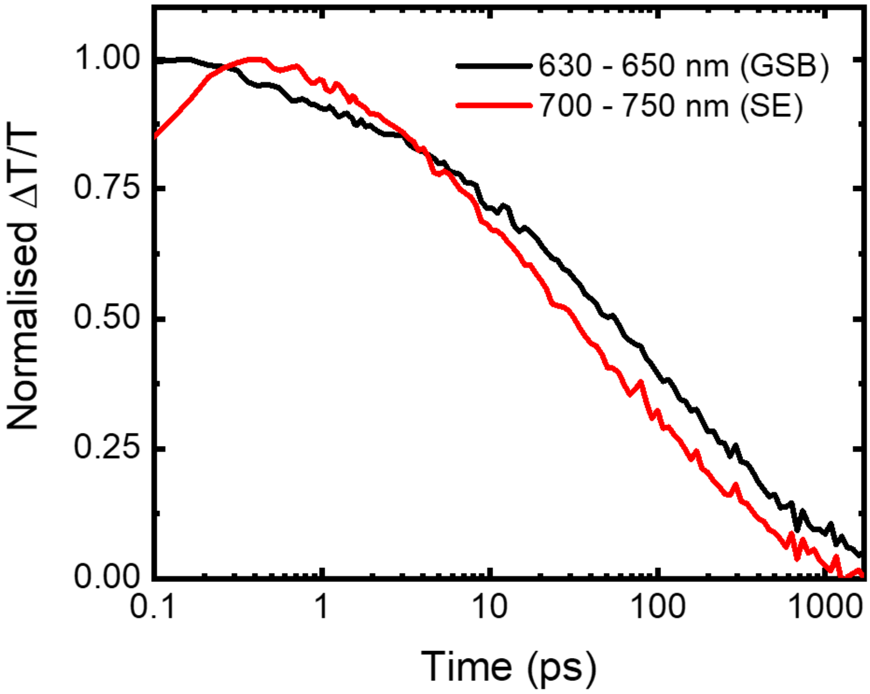

Figure 6.7*: The short-time TA kinetics of the curcuminoid doped in mCBP at 6 wt %: λ_{ex} = 610 nm, fluence = 21.4 μJ cm^{-2}. The GSB kinetic tracks the higher energy edge of the braod positive feature, whilst the SE kinetic is taken from the region associated with the PL maximum of the curcuminoid:mCBP film. The SE falls a little quicker than the GSB, though the difference is not as dramatic as in the neat film. This is attributed to a decreased rate of ISC in the doped film. After 1 ns, the SE has disappeared, leaving behind only a weak GSB, coming from the small amount of singlets that have undergone ISC to the triplet state.*

6.3.4 Long-Time Transient Absorption of the Curcuminoid Doped Into mCBP

To explore the fate of the small amount of triplets generated from optical excitation in the curcuminoid:mCBP blend, we turn to long-time techniques, including TA and trPL. Beginning with the TA, we have excited the same 6 wt % film at 532 nm with a fluence of 53 μJ cm^{-2}. The generated TA spectrum and kinetics are plotted in Figures 6.8 and 6.9. Within the first couple of ns, which is likely somewhat limited by the time resolution of the experiment, we observe the same very broad positive feature as the short time TA, previously attributed to a mixture of the GSB and SE. This lower energy side of the band rapidly decays, leaving behind a feature reminiscent of the curcuminoid GSB at 650 nm. Additionally, due to the extended range of the probe, we can now observe a PIA band out past 1000 nm. Though very weak over these timescales, it is still present after the singlet has fully decayed. Therefore, the long-lived part at least may be assigned to the PIA of the triplet on the curcuminoid. Tracking the kinetics of all these features, we see a sharp drop in the intensity of all within the first few ns, with the SE region going to zero. For the GSB and PIA bands, a plateau is reached by around 10 ns, where little extra decay occurs. This plateau is very long lived: the kinetic of the PIA can be well fitted by a bi-exponential decay with time constants of 1.7 ns for the prompt component (likely instrument-response limited) and 126 μs for the delayed component. Such a slow time constant for what is presumably the rISC process is very unusual amongst TADFs, where time constants on the order of 1 – 10's μs are more common.[154,155] This is well explained by the relatively large oscillator strength, which is facilitated by the relatively large overlap of the HOMO and LUMO wavefunctions in the curcuminoid.[146] This also results in the ΔE_{ST} being somewhat larger than is typical in TADFs at 200 meV, causing the rate of rISC to be slowed.

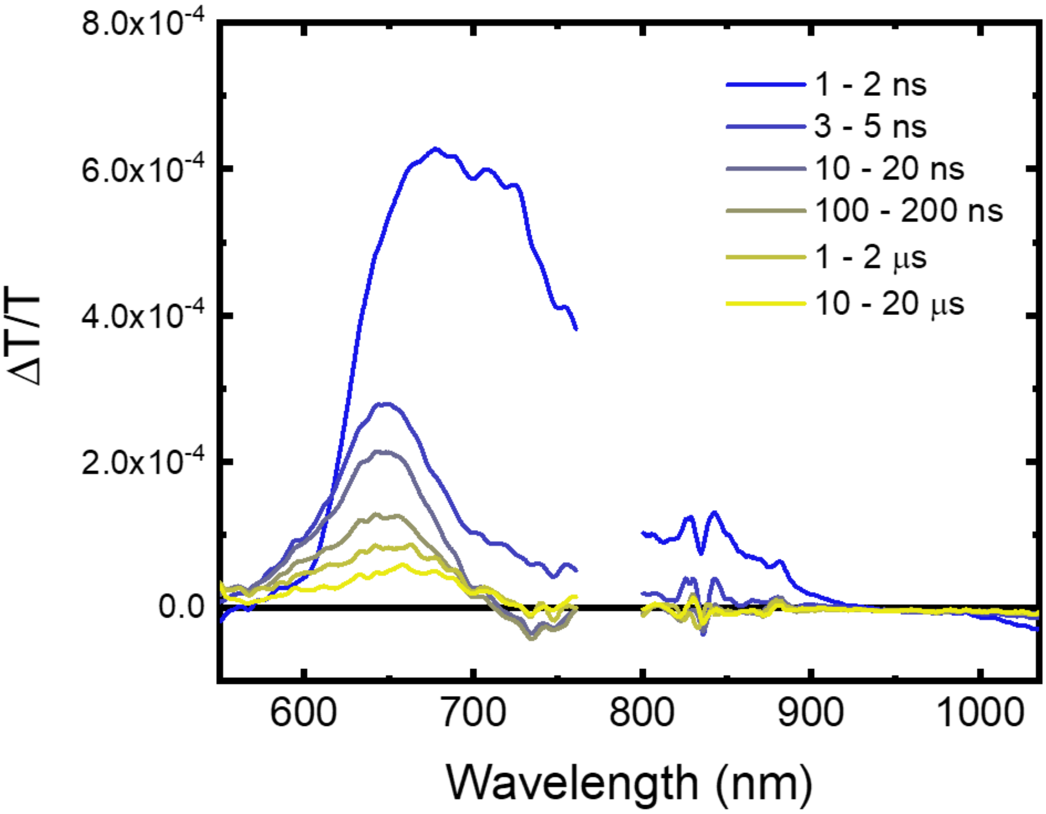

***Figure 6.8**: The long-time TA spectra of the curcuminoid doped in mCBP at 6 wt %: λ_{ex} = 532 nm, fluence = 53 μJ cm^{-2}. Initially present is a very broad positive feature, spanning 600 – 900 nm and in good agreement with the short-time TA. This is assigned to a mixture of the curcuminoid GSB and SE. The SE region (>700 nm) has fully decayed after a few ns, leaving behind a long-lived GSB peaked at 650 nm. Also now visible thanks to the extended probe range is a PIA band out past 1000 nm. Though very weak, it is still present on timescales after the singlet has decayed, so it is assigned to the triplet of the curcuminoid.*

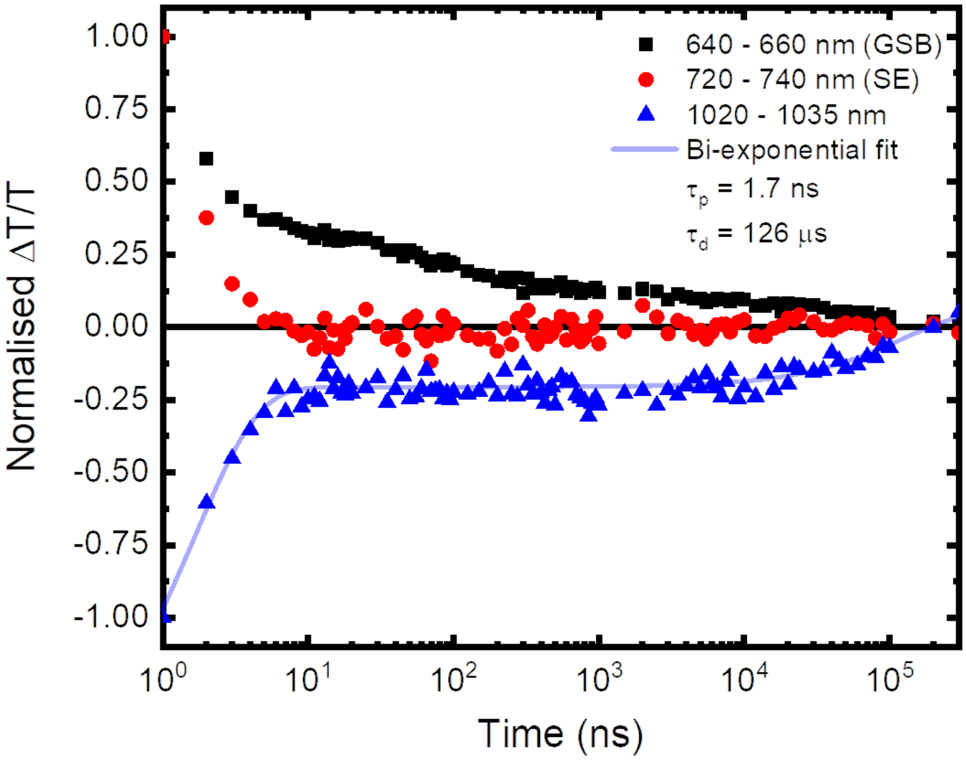

***Figure 6.9**: The long-time TA kinetics of the curcuminoid doped in mCBP at 6 wt %: λ_{ex} = 532 nm, fluence = 53 μJ cm^{-2}. The kinetics from all regions (GSB, SE and the PIA) possess a very rapid initial decay, likely instrument response limited. After this, the SE disappears, indicating that no more singlet states are present in the film. The GSB and PIA in the NIR then plateau for a long period of time, before very slowly decaying. A fit to the PIA associated with the triplet reveals a delayed lifetime of 126 μs, most likely giving the timescale for rISC in the curcuminoid.*

6.3.5 Transient Photoluminescence of the Curcuminoid Doped Into mCBP

To complete our picture of the long-time behaviour of the curcuminoid:mCBP 6:94 film, we have performed trPL. For consistency with the TA measurements, the sample was also excited at 532 nm with a fluence of 15.3 μJ cm^{-2}. The resulting normalised trPL spectra and kinetics are shown in Figures 6.10 and 6.11. The emission spectrum for both the prompt (2 ns) and delayed (10 μs) components overlay perfectly, indicating that they both result from radiative decay via the singlet state, as would be expected in a TADF material.[70] This clarifies that even though the ΔE_{ST} may be somewhat larger than is classically expected for TADF (due to the high oscillator strength), rISC back to the singlet is still able to occur. This is confirmed by the trPL kinetics, taken from the peak of the emission at 720 – 740 nm. Though the delayed component of the emission is weak, due to the majority of photo-generated excited states decaying to ground before undergoing ISC, it is nonetheless present. This is clarified by integrating the PL kinetics, as shown in Figure 6.12: approximately 90% of the emission occurs from the singlet state within the first 10 ns.

However, it is important to note is that under OLED operating conditions, excited states are created via the electrical injection of charges, not photoexcitation. As previously discussed, this leads to the formation of triplet to singlets in a roughly 3:1 ratio, as governed by spin statistics.[13] Therefore, the ability to rISC to the emissive singlet state from the triplet is critical for efficient device operation. The EQE_{EL} =10% of the best performing OLEDs fabricated from this material (at the time of publication a record for a NIR emitting TADF), including the very strong efficiency roll-off at high current densities,[146] can be readily explained from our optical investigations. We find that rISC proceeds extremely slowly in this material, owing to the increased HOMO-LUMO overlap and larger ΔE_{ST}. At lower current densities, where there are few charges in the emissive layer, the slow rISC does not have a hugely detrimental impact on device operation. This is because even though triplet excitons formed live a long time, there are relatively few other triplets or charges in close proximity that they can annihilate with. As such, emission can proceed relatively efficiently, aided by the very rapid singlet radiative decay which ensures that when rISC finally occurs emission from the singlet is very efficient. However, at higher current densities, the build-up of triplet states in the emissive layer leads to significant loss processes involving the triplets annihilating with other triplets or charge species that are present in a much greater concentration than before.[156] Consequently, the EQE_{EL} rapidly drops off with increasing current densities, limiting the usefulness of the device under higher current density conditions (>100 mA cm^{-2}) more akin to those expected for commercial operation.

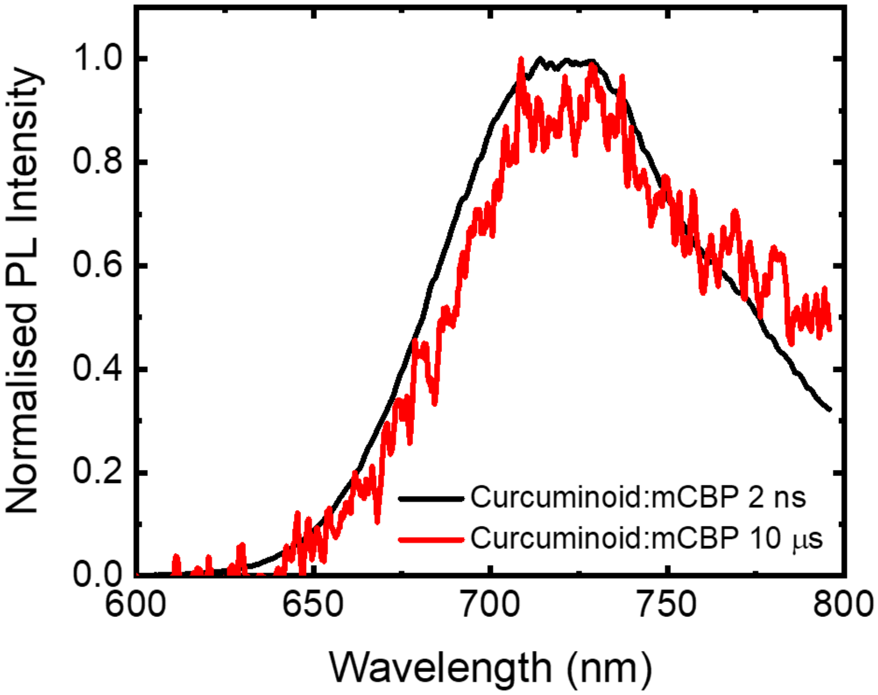

***Figure 6.10**: The emission spectra taken from the trPL measurement of the curcuminoid:mCBP 6:94 film: λ_{ex} = 532 nm, fluence = 15.3 μJ cm^{-2}. The prompt (2 ns) and delayed (10 μs) emission components overlap perfectly, indicating that the delayed emission results from rISC from the triplets back to the singlet state, as would be expected for a TADF emitter. This confirms that rISC is indeed possible in the curcuminoid, despite the predicted relatively large ΔE_{ST}.*

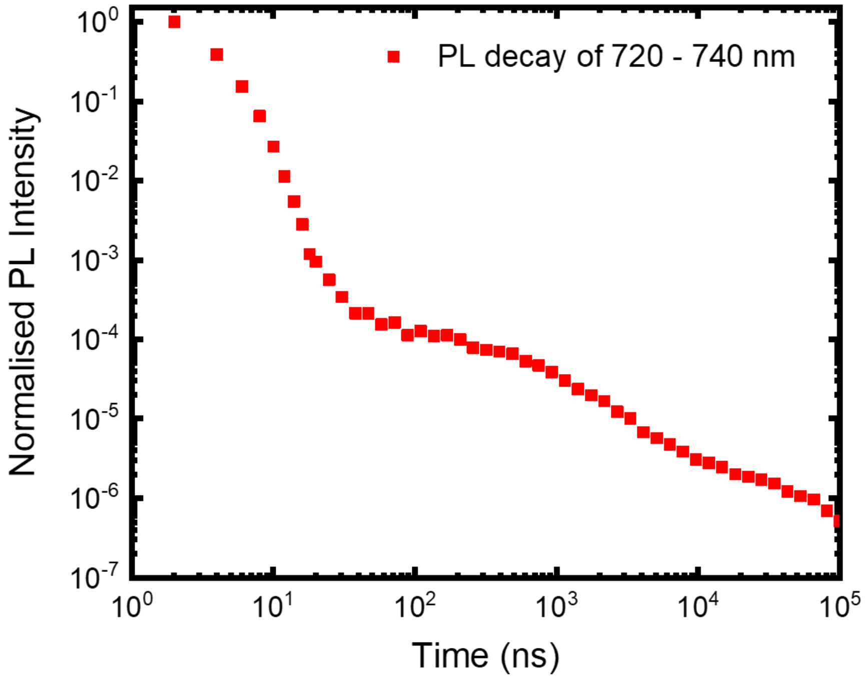

***Figure 6.11**: The integrated PL decay kinetics between 720 - 740 nm, taken from the trPL measurement of the curcuminoid:mCBP 6:94 film: λ_{ex} = 532 nm, fluence = 15.3 μJ cm^{-2}. There is evidence for some weak delayed PL, though the majority of the emission occurs within the first 10 ns, consistent with previous observations in the TA.*

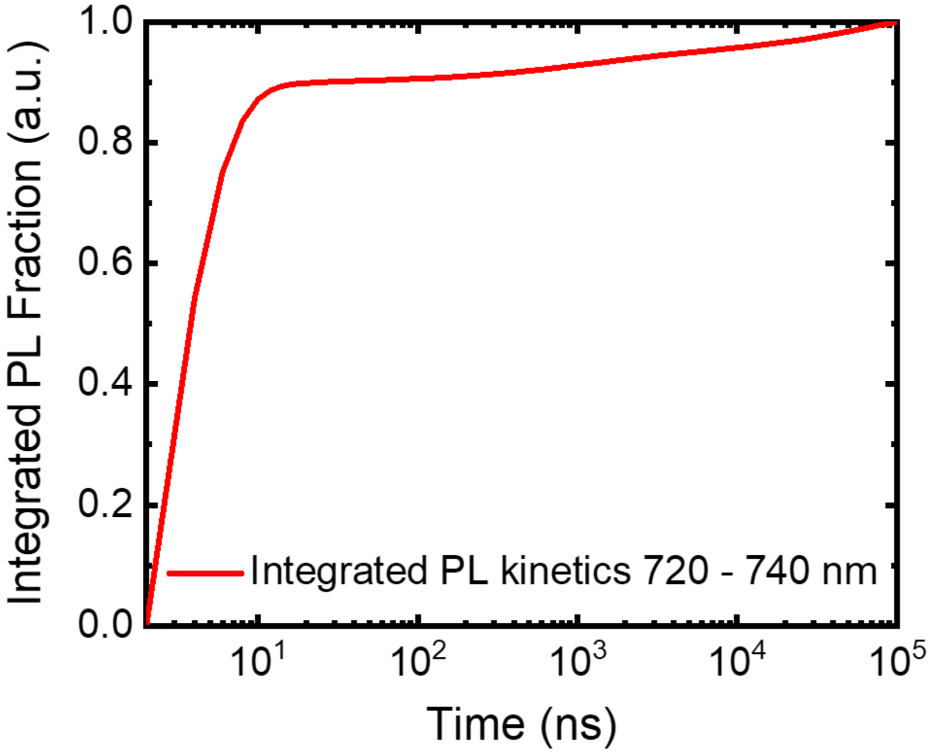

***Figure 6.12**: The integrated PL decay kinetics between 720 – 740 nm, taken from the trPL measurement of the curcuminoid:mCBP 6:94 film: λ_{ex} = 532 nm, fluence = 15.3 μJ cm^{-2}. From this, it is apparent that approximately 90% of the total emission occurs within the first 10 ns. This is consistent with the previous TA measurements, where the majority of the excited state population decays by this time.*

6.4 Organic Solar Cells Based on the Curcuminoid:PC$_{60}$BM Blend

6.4.1 OPV Device Performance of the Curcuminoid:PC$_{60}$BM Blend

Having now thoroughly investigated the photophysics of the curcuminoid material and related these findings back to the observed OLED device performance, we now begin our study of the photovoltaic application of the curcuminoid. Given that good performance has previously been reported in blends of curcuminoid derivatives with the electron acceptor PC$_{60}$BM,[147] we shall begin by studying this blend. In-line with previous reports where the best device performance was obtained for blends with roughly a 1:1 ratio,[147] conventional architecture devices with a 1:1 weight ratio of curcuminoid:PC$_{60}$BM were fabricated by Patrick Conaghan. The device stack was: ITO / PEDOT:PSS / curcuminoid:PC$_{60}$BM 1:1 / Ca / Al. The active layer was spun from a chloroform solution with a total concentration of 20 mg/mL. The devices were tested under an AM1.5G solar spectrum and the resulting J-V curves are shown in Figure 6.13. A reasonable PCE of 2.1% was achieved, with a respectable V_{OC} of 1.1 V, a J_{SC} of 6.1 mA cm^{-2} and a low FF of 0.33, summarised in Table 6.2. Whilst the performance of other curcuminoid derivatives was higher, we still consider this a representative system to explore the photophysics of the curcuminoid acting in an electron donor role.

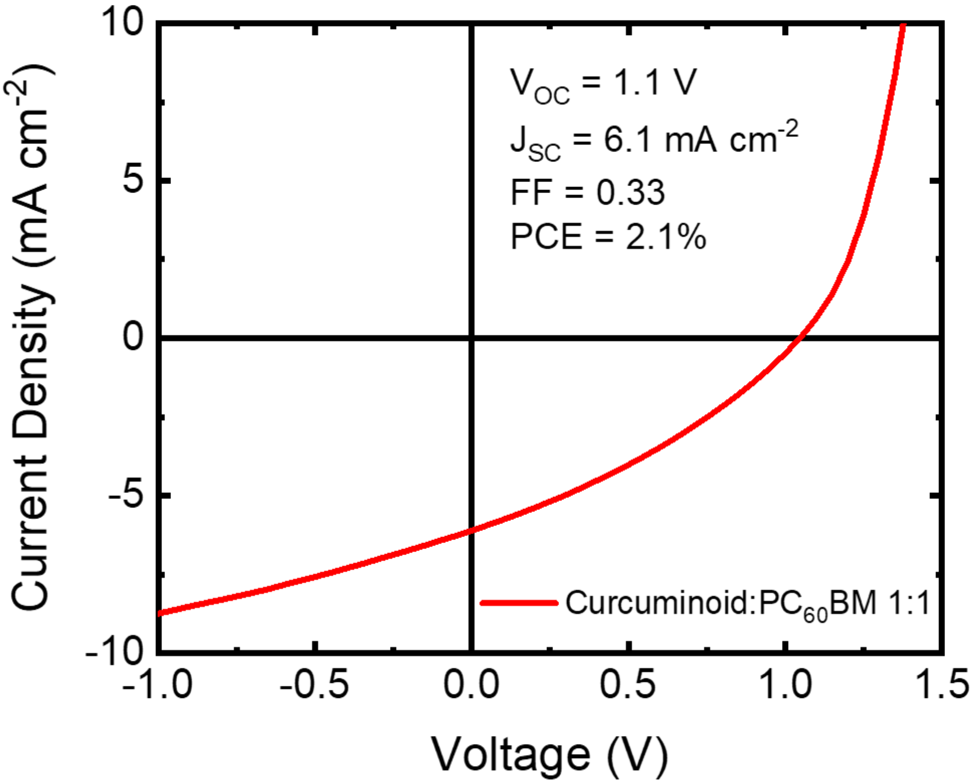

***Figure 6.13**: The current density-voltage curves of the champion curcuminoid:PC$_{60}$BM 1:1 conventional device, measured under an AM1.5G solar spectrum. The PCE was 2.1%. The device structure was ITO / PEDOT:PSS / curcuminoid:PC$_{60}$BM / Ca / Al. The device was fabricated and tested by Patrick Conaghan.*

Blend	V_{OC} (V)	J_{SC} (mA cm^{-2})	FF	PCE (%)
Curcuminoid:PC$_{60}$BM 1:1	1.10	6.1	0.33	2.1

***Table 6.2**: The key performance metrics of the curcuminoid:PC$_{60}$BM 1:1 device, measured under an AM1.5G solar spectrum.*

6.4.2 Short-Time Transient Absorption of the Curcuminoid:PC$_{60}$BM Blend

Continuing our work exploring the curcuminoid in an electron donor role, we turn to TA to examine the photophysics leading to charge generation. Here, we have performed experiments on a film fabricated the same way as the active layer in the previously discussed OPV devices. The 1:1 curcuminoid:PC$_{60}$BM film was excited with a pump wavelength of 610 nm and a fluence of 3.6 μJ cm^{-2}. From this measurement, the TA spectra and kinetics are shown in Figures 6.14 and 6.15. At the earliest times of 100 fs, the curcuminoid GSB is clearly visible, though the SE band between 700 – 900 nm that was prominent in the neat material is rather diminished. On timescales of $<$1 ps, a sharp PIA band at 680 nm rapidly forms, continuing to grow in up to around 100 ps. Given the reasonable OPV performance, charge generation must be happening relatively efficiently and so this new feature is assigned to the hole left behind on the curcuminoid after the electron transfer process. We therefore attribute the diminished SE signal to the rapid charge transfer that occurs in the blend, in line with reports on other fullerene acceptor OPV systems.[98,157,158]

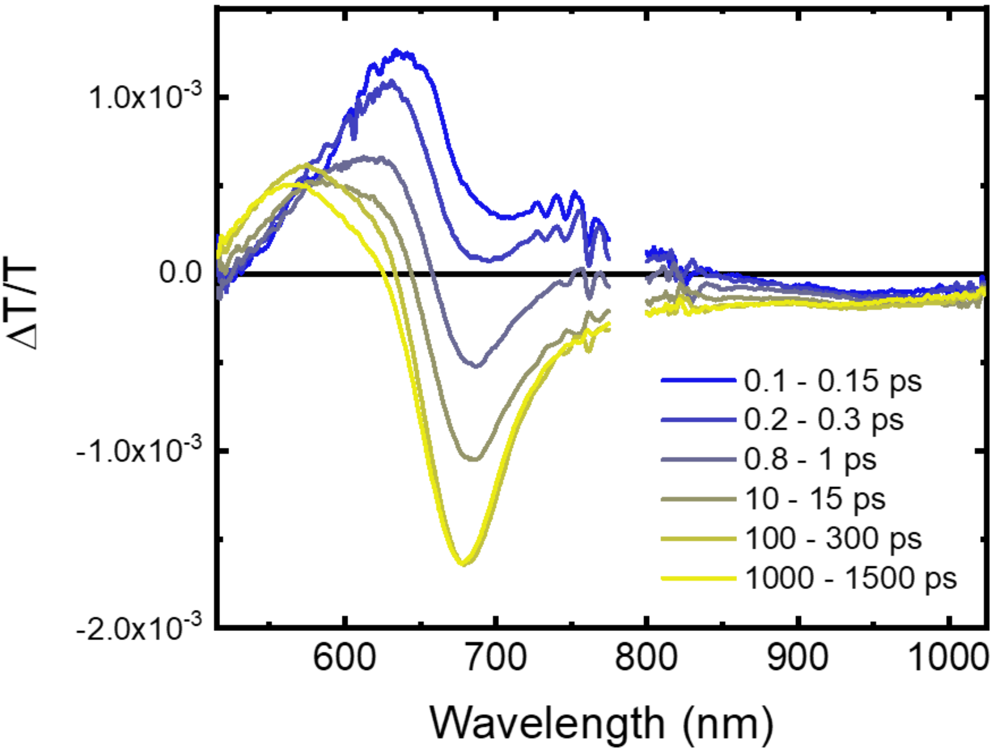

Figure 6.14*: The short-time TA spectra of the curcuminoid:PC$_{60}$BM 1:1 blend: λ_{ex} = 610 nm, fluence = 3.6 μJ cm^{-2}. The curcuminoid GSB is immediately visible after excitation at around 630 nm. However, in contrast to the neat material, the SE band between 700 – 900 nm is much weaker. The SE rapidly disappears and a new PIA band at 680 nm forms in-step. This is attributed the electron transfer process, quenching the singlet excitons and their SE, whilst forming a new PIA that is assigned to the hole left behind on the curcuminoid.*

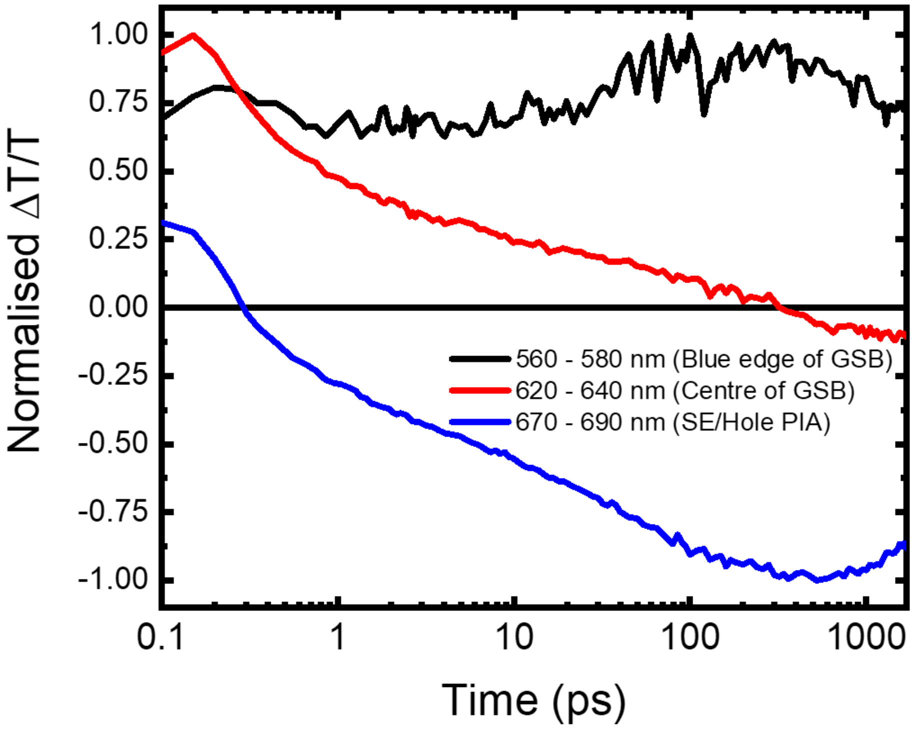

***Figure 6.15**: The short-time TA kinetics of the curcuminoid:$PC_{60}BM$ 1:1 blend: λ_{ex} = 610 nm, fluence = 3.6 μJ cm^{-2}. The kinetics are relatively difficult to interpret due to the overlapping curcuminoid GSB, SE and hole PIAs. However, the blue line, representing the probe region initially associated with the SE band and finally the hole PIA clearly shows the conversion process. This region is first positive, before rapidly becoming negative within the first few hundred fs, signalling the start of charge transfer. The intensity of the hole PIA band increases more slowly up to a few hundred ps, indicating the timescales by which charge transfer is completed.*

Given the convoluted nature of the curcuminoid GSB, SE and hole PIA features, we turn to GA in order to separate them. The extracted GA spectra and kinetics are shown in Figures 6.16 and 6.17, giving a clearer picture of the charge transfer process. We have extracted an initial species that very closely resembles the curcuminoid GSB from the neat material and a weak SE band, consistent with the initial species being made up of spectral signatures related to the curcuminoid singlet exciton. The final species formed contains the sharp PIA we have assigned to the curcuminoid hole PIA, as well as a positive feature that matches closely the curcuminoid absorption profile and is as such attributed to the GSB overlapping with the hole PIA. In the initial species kinetics, there is a rapid loss of singlet exciton-like characteristics <1 ps, before a slower decay. This biphasic behaviour likely results from the initial, rapid dissociation of excitons formed near the interface with $PC_{60}BM$, before the slower diffusion of excitons formed in the bulk to the interface, where they are then dissociated over later times.[152]

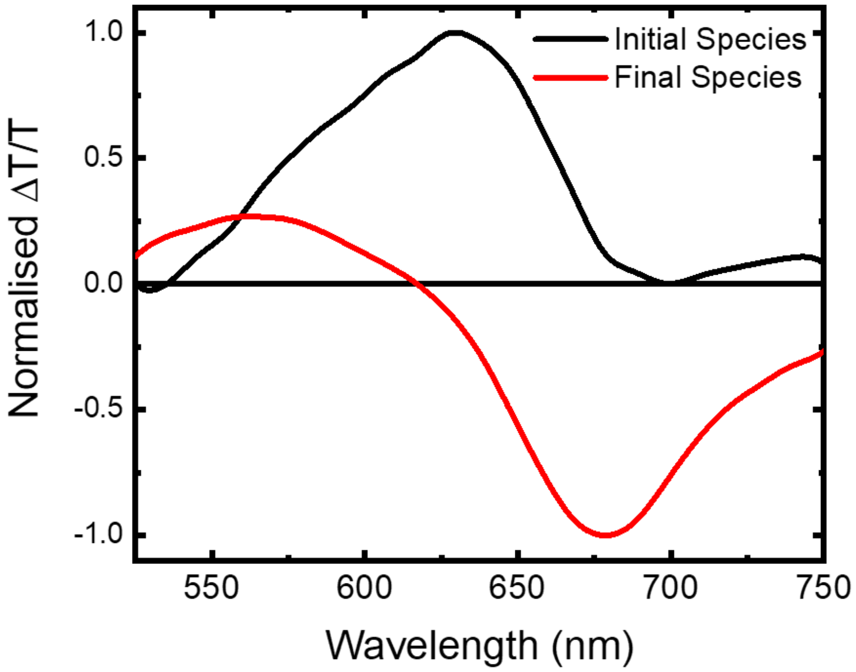

Figure 6.16: *The GA extracted spectral features from the TA on the curcuminoid:PC$_{60}$BM 1:1 blend film, taken from Figure 6.14. The black spectrum is present initially and closely resembles features associated with the curcuminoid singlet exciton, including a weak SE band out towards 750 nm. As time progresses, a new species is formed, containing the curcuminoid GSB and a sharp PIA at 680 nm. This new feature is associated with the hole on the curcuminoid after electron transfer to PC$_{60}$BM.*

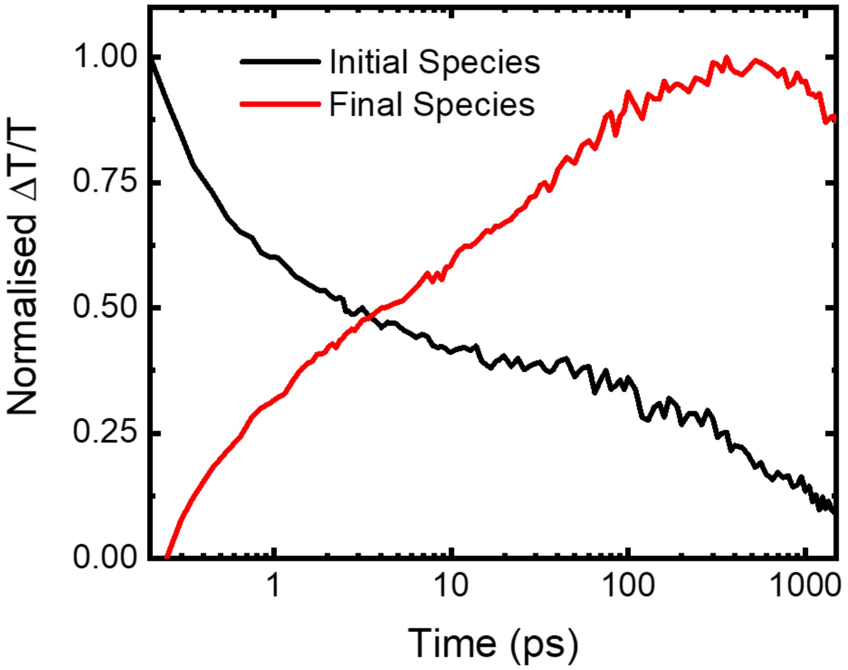

Figure 6.17: *The corresponding kinetics of the GA extracted spectral from the TA on the curcuminoid:PC$_{60}$BM 1:1 blend film, taken from Figure 6.14. The electron transfer process, causing the decay of the initial species, appears to have a biphasic nature. The initial (<1 ps) component is assigned to the dissociation of excitons generated on curcuminoid molecules near the interface with PC$_{60}$BM. The slower decay over longer times is attributed to the dissociation of excitons formed in the bulk to the interface prior to charge transfer.*

6.4.3 Long-Time Transient Absorption of the Curcuminoid:PC$_{60}$BM Blend

To complete our study on the photophysics of the curcuminoid:PC$_{60}$BM blend, we have measured the long-time TA. The same film was excited at 532 nm with a fluence of 7.1 μJ cm^{-2}, giving the TA spectra and kinetics in Figures 6.18 and 6.19. As expected, the TA spectrum at 3 ns closely resembles that from the longest time points of the short-time TA, with a GSB between 525 – 650 nm and the sharp PIA at 680 nm. The slight increase in probe range on the NIR side reveals more clearly an additional PIA band that extends out past 1100 nm. Kinetic slices from the GSB, hole PIA and NIR PIA regions show that all species decay in-step, with few species remaining by 100 μs. The fact that than NIR PIA band matches closely the other features indicates it is most likely an additional absorption of one of the charge states present in the blend. The long lifetime of the charge PIAs formed is consistent with the ability to extract significant photocurrent from the OPV device fabricated from the same materials, explaining the reasonable performance obtained. Finally, we note a slight blue-shift of the hole PIA over long (>1 μs) times towards 660 nm. An explanation for this is not immediately apparent, but may be rationalised by the tendency of charges localising in low-energy sites in the density of states present in the BHJ.[94]

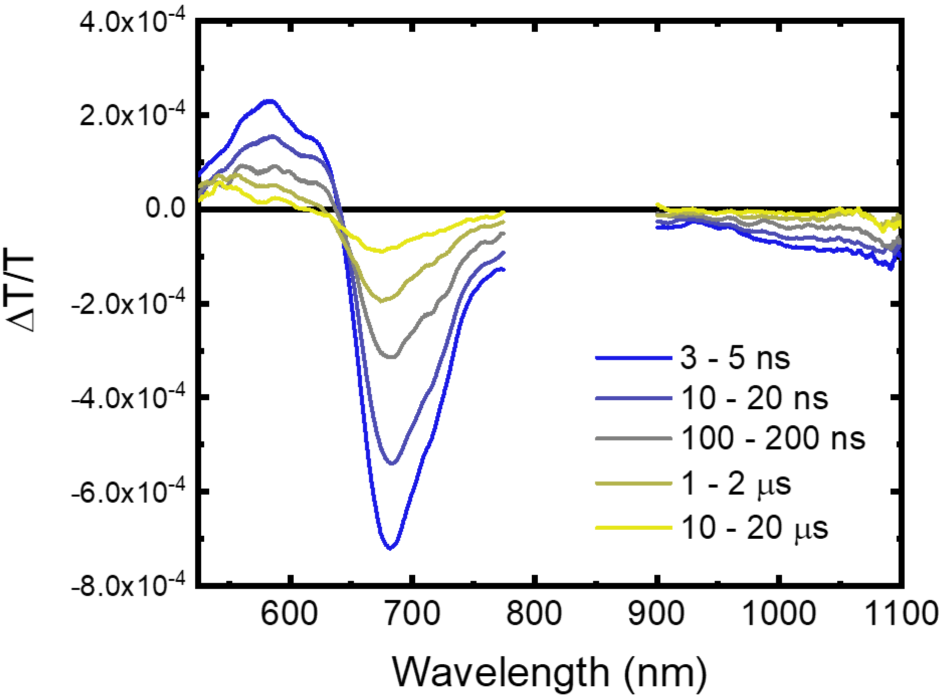

***Figure 6.18**: The long-time TA spectra of the curcuminoid:PC$_{60}$BM 1:1 blend: λ_{ex} = 532 nm, fluence = 7.1 μJ cm^{-2}. Consistent with the short-time data, the curcuminoid GSB and hole PIA are visible, as well as a more clearly resolved PIA in the NIR out towards 1100 nm. All features decay in-step, with a slight blue-shift of the hole PIA over longer times (>1 μs), tentatively attributed the localisation of charges in low-energy sites in the BHJ.*

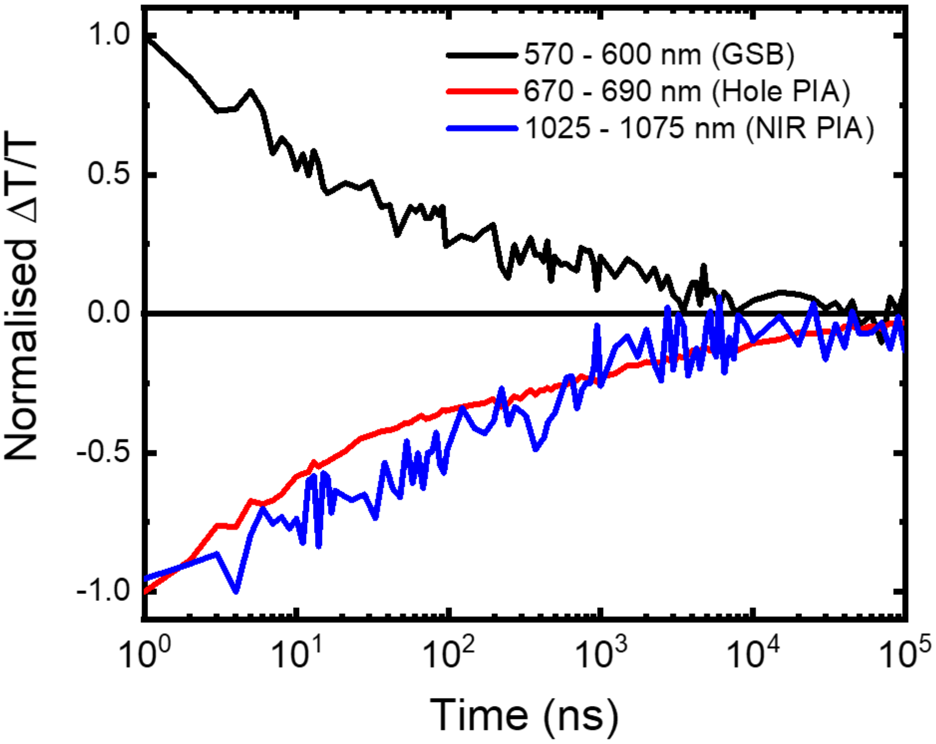

***Figure 6.19**: The long-time TA kinetics of the curcuminoid:PC$_{60}$BM 1:1 blend: λ_{ex} = 532 nm, fluence = 7.1 μJ cm^{-2}. All species present in the film decay largely in-step, likely via bimolecular recombination processes. The lifetime of the species is quite long, leaving sufficient time for charge extraction to occur in a device before recombination can occur, contributing to the reasonable OPV device performance seen.*

6.5 Organic Solar Cells Based on the F8T2:Curcuminoid Blend

6.5.1 Steady-State Absorption of F8T2 and its Blend with the Curcuminoid

The first blend employing the curcuminoid as the acceptor that we choose to investigate is perhaps the one that shows the most promise: F8T2:curcuminoind. As previously discussed, the energy level alignment and complementary absorption of F8T2 and the curcuminoid allow it to absorb light strongly across the whole visible spectrum (400 – 700 nm), as well potentially generate charges with a very low energy loss due to the close alignment of the HOMO levels. Figure 6.20 shows the absorption spectrum of neat films of the curcuminoid and F8T2. As before, the curcuminoid film was spun at 3000 rpm from a 5 mg/mL solution in chloroform, whilst the F8T2 film was spin cast at 3000 rpm from a 10 mg/mL chlorobenzene solution. Additionally, a 1:1 blend ratio by weight film of F8T2:curcuminoid was deposited in the same way as the equivalent OPV device, the performance of which will be discussed later. For this film, a 20 mg/mL solution in chloroform was deposited onto the substrate with a spin speed of 4000 rpm, with the resulting absorption spectrum shown in Figure 6.21. The absorption spectra of the neat films and the blends serves to emphasise the effectiveness of this material combination absorbing light over the whole visible spectrum, a prerequisite for efficient OPV device performance.

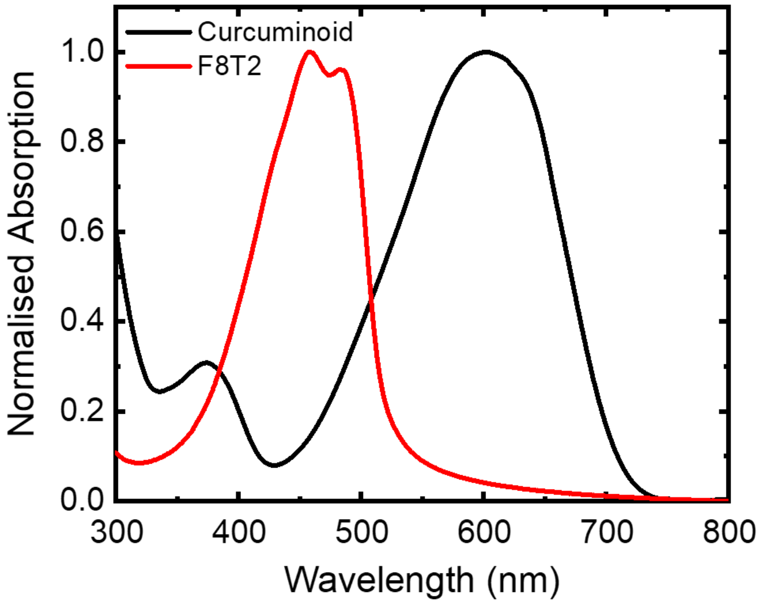

***Figure 6.20**: The normalised absorption spectra of neat films of the curcuminoid and F8T2. Note the complementary absorption spectra, allowing for the strong absorption of all photons in the visible region (400 – 700 nm).*

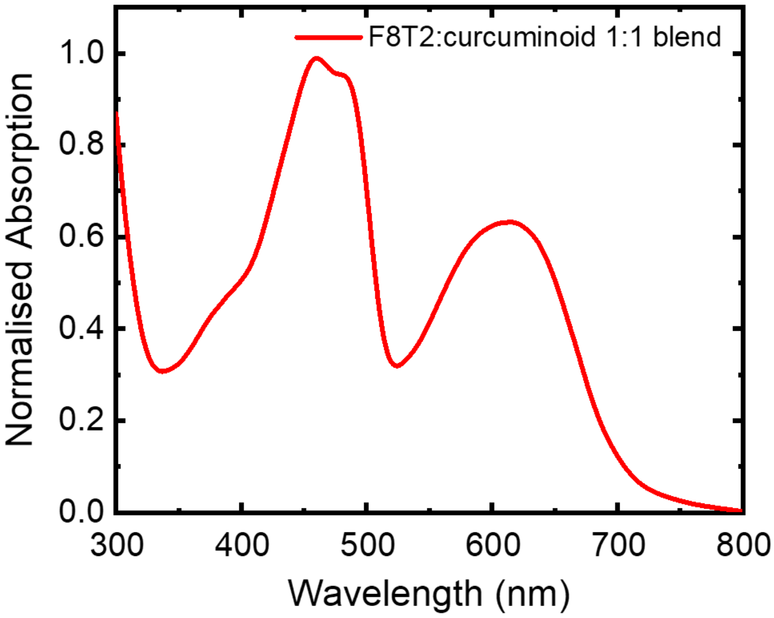

***Figure 6.21**: The normalised absorption spectrum of the 1:1 F8T2:curcuminoid blend film, fabricated in the same way as the OPV device.*

6.5.2 OPV Device Performance of the F8T2:Curcuminoid Blend

Conventional structure OPV devices using the F8T2:curcuminoid blend were then fabricated by Patrick Conaghan. The device stack consisted of: ITO / PEDOT:PSS / F8T2:curcuminoid 1:1 / Ca / Al, with the active layer spin-coated as previously described. The devices were then tested under an AM1.5G solar spectrum and the J-V characteristics were recorded. The resulting J-V data is shown in Figure 6.22, where the device performance is surprisingly poor. The impressive V_{OC} of 1.2 V (optical band gap = 1.7 eV) was counterbalanced by a low J_{SC} of 0.33 mA cm^{-2} and a poor FF of 0.26, leading to an overall PCE of 0.1%. This device data is summarised in Table 6.3. Given the disappointing nature of the device performance, we decided to perform further studies on the blend in order to deduce the reasons for the poor performance, hoping to learn lessons that could be applied to future attempts to make efficient OPV devices.

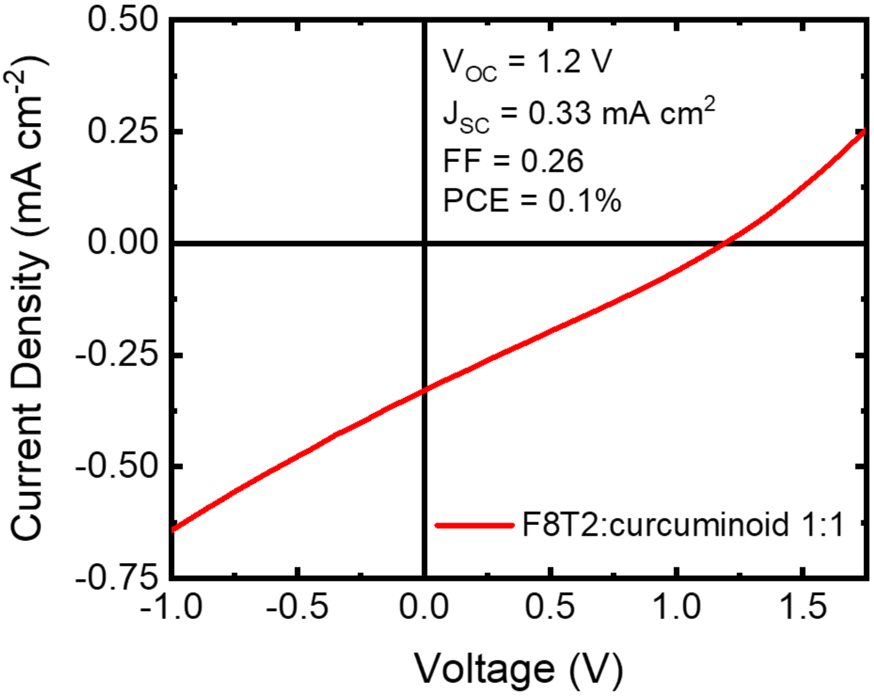

***Figure 6.22**: The current density-voltage curves of the champion F8T2:curcuminoid 1:1 conventional architecture device, measured under an AM1.5G solar spectrum. The PCE was 0.1%. The device structure was ITO / PEDOT:PSS / F8T2:curcuminoid / Ca / Al. Devices fabricated and tested by Patrick Conaghan.*

Blend	V_{OC} (V)	J_{SC} (mA cm^{-2})	FF	PCE (%)
F8T2:curcuminoid 1:1	1.20	0.33	0.26	0.1

***Table 6.3**: The key performance metrics of the F8T2:curcuminoid 1:1 device, measured under an AM1.5G solar spectrum.*

6.5.3 Short-Time Transient Absorption of Neat F8T2

In order to study the processes occurring in the blend after photon absorption, we once again turn to TA. Before we can study the F8T2:curcuminoid blend, we must first understand the photophysical processes occurring in neat F8T2. Therefore, TA was performed on an F8T2 film fabricated in the same way as for the steady-state absorption measurements. In this experiment, the film was excited using a 400 nm pulse and a fluence of 1.6 μJ cm^{-2}, giving the TA spectra and kinetics in Figures 6.23 and 6.24. There are two features that dominate the TA spectrum plot: an SE band with a vibronic progression that closely matches those in the reported steady-state PL of this material[159] and a strong PIA peaked at 975 nm. Given that the PIA is present immediately after excitation, we assign this to the PIA of the singlet exciton. The SE band and the singlet PIA both decay together over timescales towards one ns, where a broad PIA, spanning the range from 650 – 900 nm remains. Given the loss of features associated with the singlet exciton, we attribute this new PIA to triplets formed via ISC.

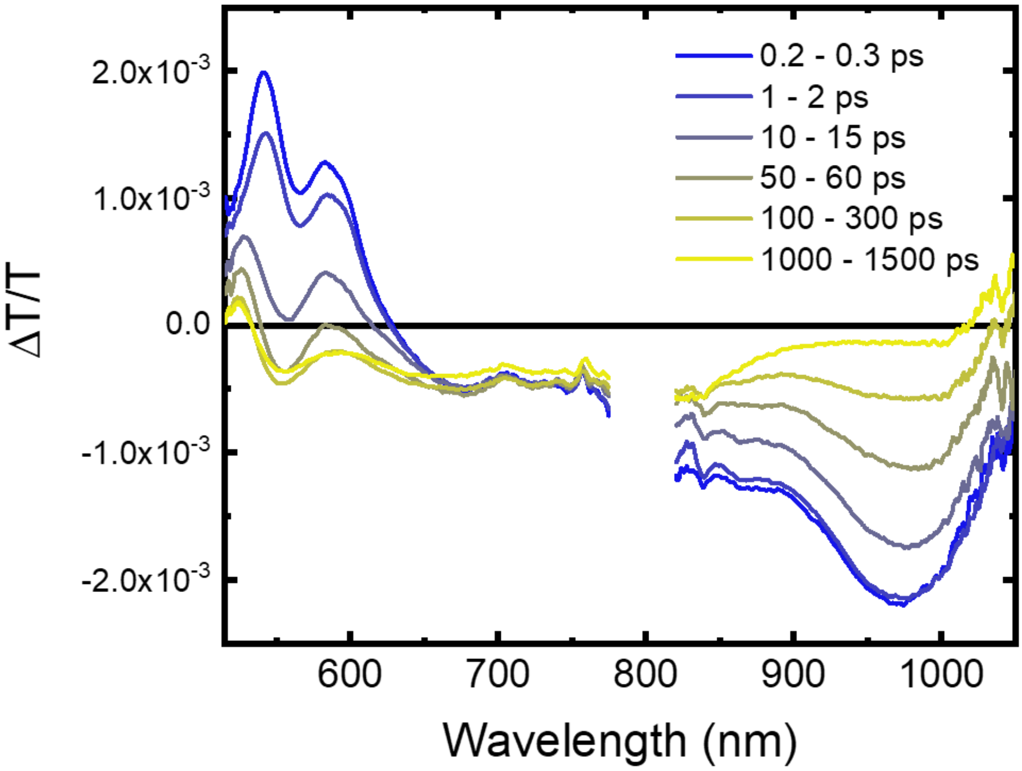

***Figure 6.23**: The short-time TA spectra of a film of neat F8T2: λ_{ex} = 400 nm, fluence = 1.6 μJ cm^{-2}. The positive feature between 525 – 625 nm with a clear vibronic progression is assigned to the F8T2 SE, whilst the strong PIA in the NIR at 975 nm formed immediately after excitation results from the singlet PIA. By 1 ns, both the SE and singlet PIA have decayed, leaving behind a broad PIA between 650 – 900 nm that likely results from the triplet formed via ISC.*

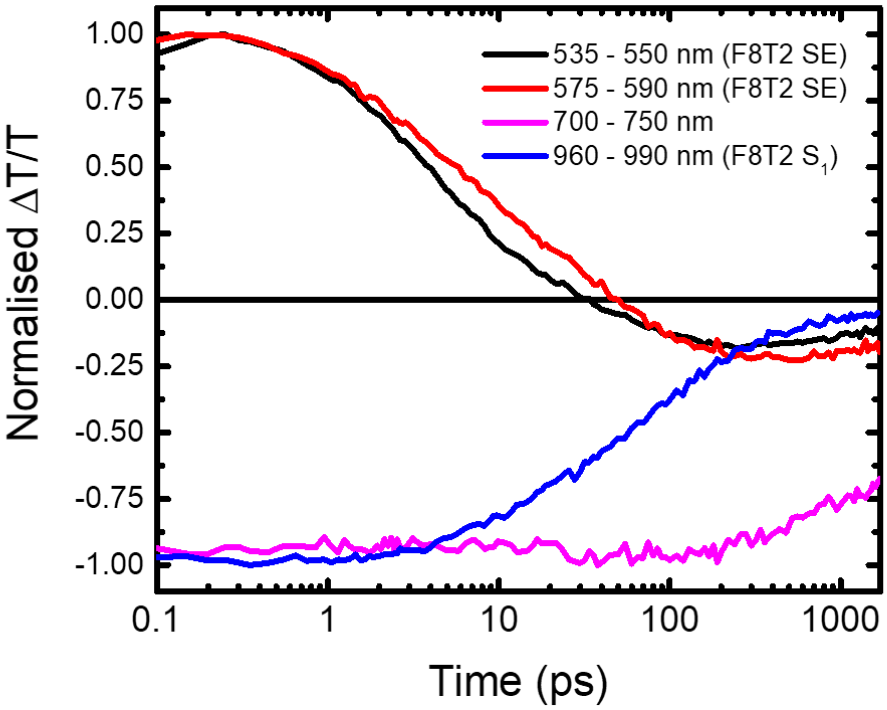

***Figure 6.24**: The short-time TA kinetics of a film of neat F8T2: λ_{ex} = 400 nm, fluence = 1.6 μJ cm^{-2}. Both vibronic peaks of the SE decay very closely, also in-step with the singlet exciton PIA, with evolution mostly complete by 1 ns. During this time, there is little change in the intensity of the region associated with the triplet exciton forming (700 – 750 nm) and this feature dominates the spectrum by 1 ns.*

6.5.4 Short-Time Transient Absorption of the F8T2:Curcuminoid Blend

Now that we are aware of the TA features of both the neat curcuminoid and F8T2 films, we can finally examine the TA of the blend. We begin by exciting the curcuminoid selectively at 610 nm, below the band gap on F8T2, allowing us to track only excitons generated on the curcuminoid. For this measurement, we use a fluence of 7 μJ cm^{-2}, and the resulting TA spectra and kinetics are displayed in Figures 6.25 and 6.26. The TA spectra and kinetics obtained bear a close resemblance to that of the pure curcuminoid (Figures 6.4 and 6.5), making determination if any charge transfer occurs difficult. Perhaps the most reliable way to investigate this process is to examine the kinetics of the SE band, as if charge transfer is occurring, we would expect this to be quenched more rapidly than in the neat film. We have plotted the kinetics from the SE in both films together in Figure 6.27 to aid our comparison. We can see that the SE of the blend decays a little more quickly, with the sign of the signal eventually going negative by about 30 ps, indicating the formation of a new PIA band in this region. Given that we expect some charge transfer to be occurring in this blend due to the small photocurrent extracted, we assign this new PIA band between 700 – 800 nm as belonging to the hole residing on F8T2, in line with previous reports.[160] However, as the charge transfer appears to be relatively slow, we expect that it may compete with triplet formation on the curcuminoid. Indeed, there is a new PIA band forming around 950 – 970 nm in the blend, which matches that seen in the neat material. The kinetics in this region also match closely, with the growth of this PIA peaking at about 100 ps in both cases (Figure 6.27). Even though we have seen that triplets can rISC back to the singlet state in the curcuminoid, this process is extremely slow with a time constant on the order of 126 μs. Given the expected relatively large ΔE_{ST} for a TADF material and minimal HOMO-HOMO offset for hole transfer in the blend, it is not clear if the triplet state is too low in energy to undergo charge transfer, though the fact that the triplet behaves similarly in the blend to the neat film suggests it does not dissociate in the blend. If this is indeed the case, then the very long-lived triplet states will build up in the film, where they can undergo triplet-charge annihilation processes that can significantly reduce the device performance.[54,55] In fact, the relatively rapid decay of this PIA after 100 ps hints that this processes may be already occurring at relatively early times.

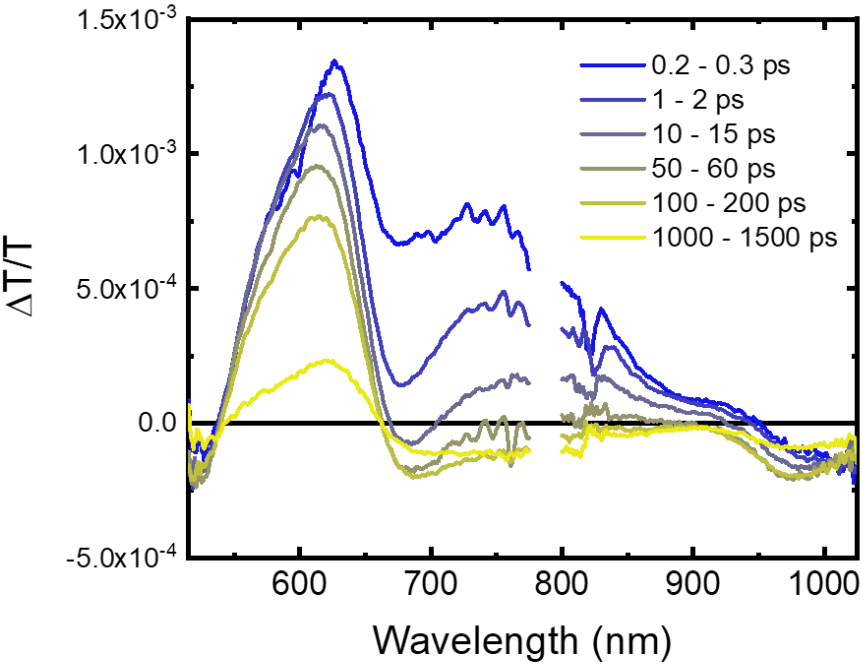

***Figure 6.25**: The short-time TA spectra of a 1:1 blend film of F8T2:curcuminoid: λ_{ex} = 610 nm, fluence = 7 μJ cm^{-2}. The excitation wavelength is below the band gap of F8T2, allowing us to track only those excitons generated on the curcuminoid. The spectrum bears a close resemblance to that of the neat curcuminoid. However, the SE band appears to decay more quickly in the blend than the neat material, also forming a weak PIA band between 700 – 800 nm. This interconversion is therefore assigned to the hole transfer process occurring. A band around 950 – 970 nm also forms, similar to the neat film. This PIA is attributed to triplets forming on the curcuminoid, as they do in the neat material.*

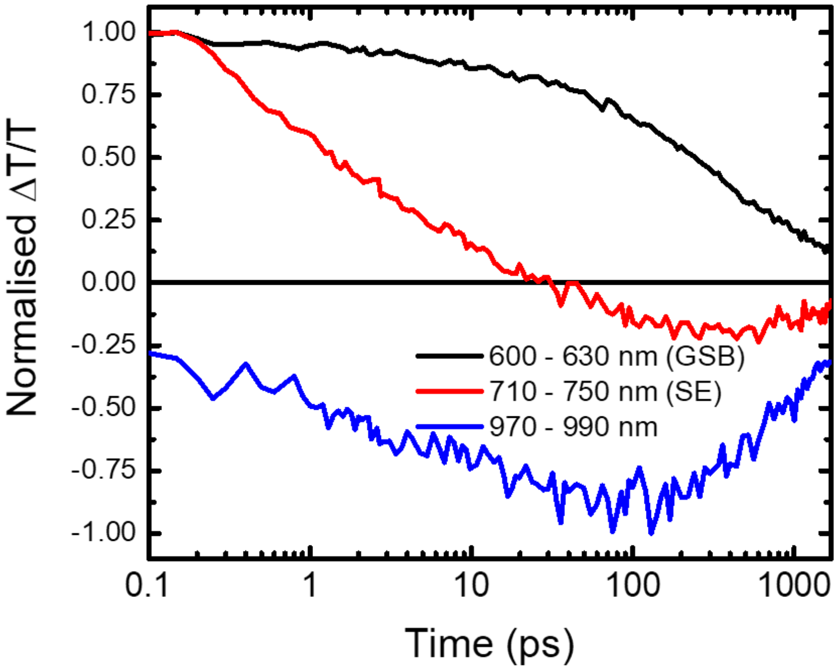

Figure 6.26: *The short-time TA kinetics of a 1:1 blend film of F8T2:curcuminoid:* λ_{ex} *= 610 nm, fluence = 7 μJ cm*$^{-2}$*. The kinetics of the GSB and triplet region (970 – 990 nm) closely mirror that of the neat curcuminoid film. However, the SE region decays more quickly than in the neat film and the signal in this region even becomes negative by around 30 ps, implying that a charge transfer process is occurring.*

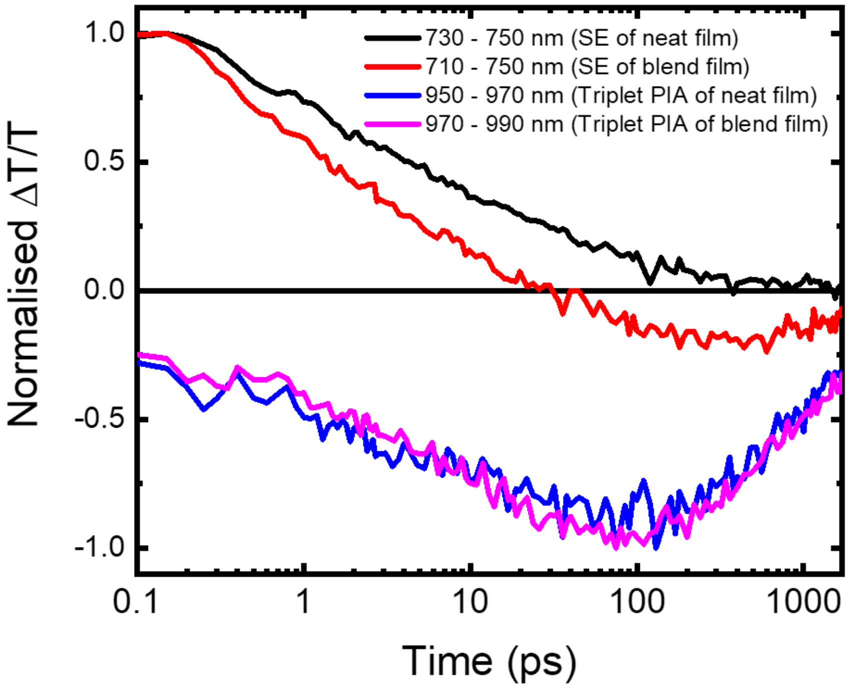

Figure 6.27: *The short-time TA kinetics of both the neat curcuminoid and 1:1 blend film of F8T2:curcuminoid overlaid. The region associated with the SE in the blend film decays slightly more quickly than in the neat film, implying the hole transfer process is occurring. However, the region associated with the triplet PIA on the curcuminoid evolves identically in both films. This implies that ISC is competitive with charge transfer in the blend film, limiting the effectiveness of the blend to efficiently generate charges.*

Having now understood the processes occurring from excitons generated on the curcuminoid, we can now explore the fate of excitons created on the electron donor F8T2. Whilst the wider band gap of F8T2 means it cannot be selectively excited, we can choose a pump wavelength where it is the primary absorber. Therefore, we excite the same film with a 490 nm pulse and a fluence of 3.4 μJ cm^{-2} in order to predominantly excite F8T2. The resulting TA spectrum and kinetics are shown in Figures 6.28 and 6.29. There is significant early-time (<1 ps) evolution when exciting F8T2, that may appear somewhat complex to understand at first glance. However, looking at the initial spectrum at 100 fs, we see features larger reminiscent of the singlet exciton on F8T2: a positive feature with two peaks at 550 nm and 580 nm resembles clearly the SE of F8T2, with the PIA at 975 nm obviously belonging to the singlet exciton on F8T2. There is also an additional positive band at around 630 nm, resulting from the small amount of excitons generated directly on the curcuminoid. The F8T2 SE and singlet PIAs decay very rapidly within the first 600 fs, leaving behind a strong GSB at around 620 nm that is reminiscent of the curcuminoid. Additionally, there is a small positive band at around 750 nm, a region associated with the curcuminoid SE. The curcuminoid SE is then rapidly quenched again over the following few ps, eventually forming the final spectrum seen at 1 ns. This consists of the curcuminoid GSB between 550 – 650 nm, the F8T2 hole PIA between 700 – 800 nm and another PIA band around 950 nm. This final spectrum matches almost perfectly with that seen when selectively exciting the curcuminoid in Figure 6.25.

Examining the data step-by-step, we can build up a clear picture of the photophysics occurring. Looking at the spectral evolution in the first ps, we see the loss of the F8T2 SE and singlet PIA, with the formation of the curcuminoid GSB and SE bands. The creation of SE on the curcuminoid in particular provides a very strong clue as to what is occurring. As emissive singlet excitons must be being created on the curcuminoid, ultrafast FRET from F8T2 to the curcuminoid can be decisively said to occur. This is not unexpected given the very strong overlap of the F8T2 emission spectrum and the curcuminoid absorption.[159] After excitons are created on the curcuminoid, the spectra evolves very closely to that seen in Figure 6.25, ultimately resulting in the same final spectra by 1 ns. Given that effectively all of the charge transfer occurs via the curcuminoid, if this process is not particularly efficient and competes with triplet formation, as expected from our analysis of the TA when exciting at 610 nm, then we can explain why the device performance of this once promising blend is poor.

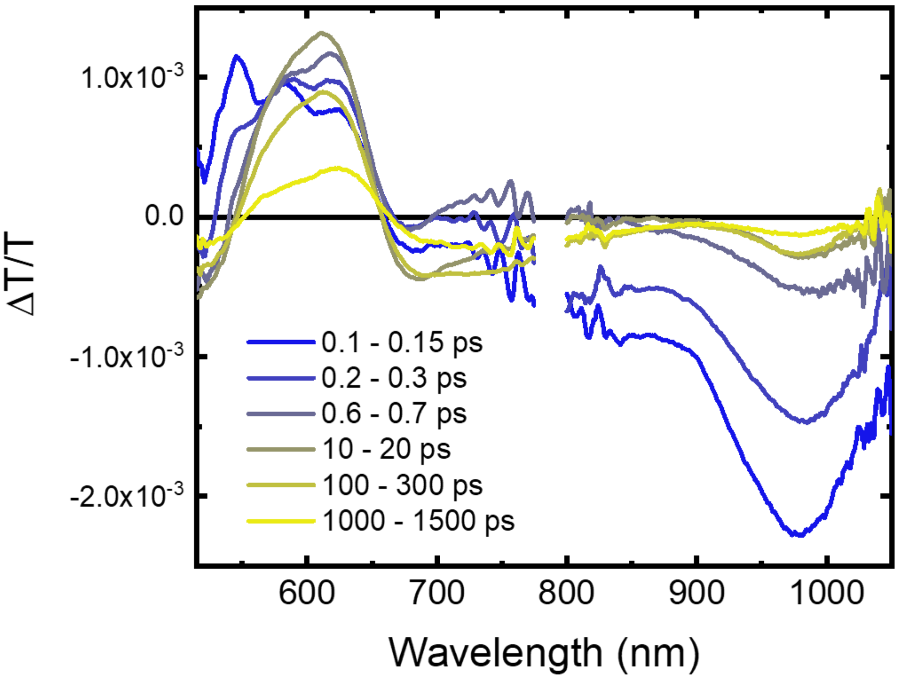

***Figure 6.28**: The short-time TA spectra of a 1:1 blend film of F8T2:curcuminoid: λ_{ex} = 490 nm, fluence = 3.4 μJ cm^{-2}. The SE and singlet PIAs of F8T2 decay very rapidly, forming the GSB and SE bands associated with the curcuminoid. The presence of the SE band in particular suggests that presence of singlet excitons on the curcuminoid, which must be formed by ultrafast FRET from F8T2. After the singlets have been formed on the curcuminoid, the spectral evolution proceeds in a similar manner to when the curcuminoid was selectively excited at 610 nm.*

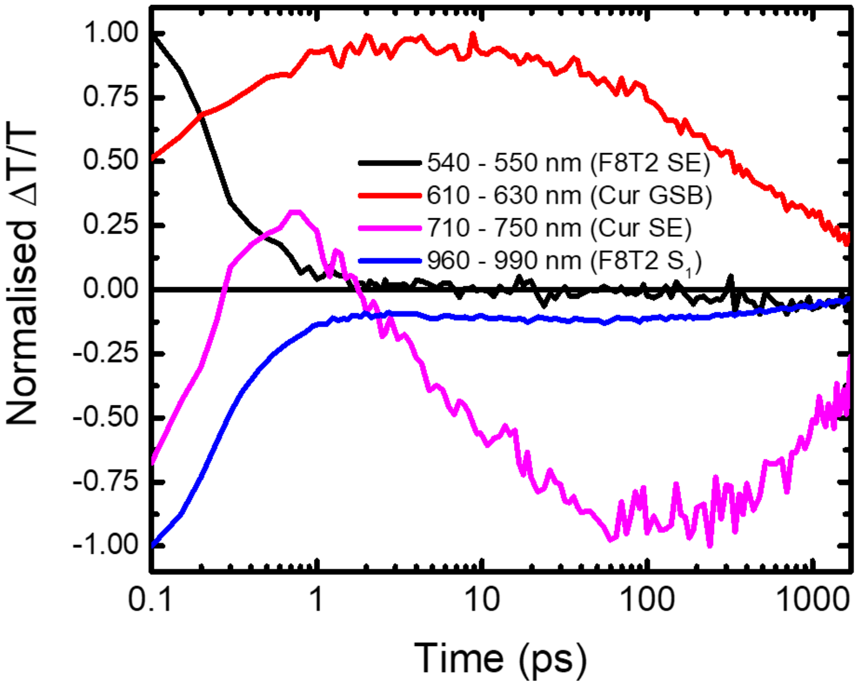

***Figure 6.29**: The short-time TA kinetics of a 1:1 blend film of F8T2:curcuminoid: λ_{ex} = 490 nm, fluence = 3.4 μJ cm^{-2}. The simultaneously rapid loss of the F8T2 SE and singlet PIAs, with the concurrent rise of the curcuminoid GSB and SE bands can be clearly seen in the kinetics of the relevant regions.*

6.6 Organic Solar Cells Based On Other Donor:Curcuminoid Blends

After the poor performance of the F8T2:curcuminoid blend, we have decided to pair the curcuminoid with a variety of other wider band gap materials that can act as electron donors in an OPV device. For these devices, electron materials were chosen to have a larger HOMO-HOMO offset with the curcuminoid in the hope that the hole transfer would now be fast enough to out-compete any curcuminoid triplet formation. The materials chosen are m-MTDATA, which has previously been employed as an electron donor in OPV devices that have shown moderate performance,[161] and NPD and TFB, used before in the work with TXO-TPA. The devices were fabricated by Patrick Conaghan and had the following conventional architecture device stack: ITO / PEDOT:PSS / donor:curcuminoid 1:1 / Ca / Al. A 1:1 weight ratio of the donor to curcuminoid was used for all devices and the active layer was spun from a 20 mg/mL chloroform solution at spin speeds of 4000 rpm for the m-MTDATA and NPD blends, with 7000 rpm used for the TFB blends. As before, all devices were tested under an AM1.5G solar spectrum, with the measured J-V characteristics shown in Figure 6.30, summarised in Table 6.4. From the J-V curves, it is apparent that the performance of all devices was poor, with all PCEs under 0.1%. Given the low performance of the curcuminoid when used as the electron acceptor in all devices, including with F8T2 previously, the logical conclusion is that is it not well suited for use in this role. The reason for this is not immediately forthcoming, but may be related to a possible low electron mobility of the curcuminoid, which stops the hole from escaping the CT state formed after charge transfer.[47] Other potential reasons include an unfavourable BHJ morphology that is not conductive to charge extraction,[162] or the formation of long-lived triplet excitons on the curcuminoid that can annihilate with charges.[54,55] Given the reasonable performance of the curcuminoid when acting as the electron donor in tandem with fullerene acceptors, it seems future work involving curcuminoids in OPV devices would be wise to focus on employing them as the electron donor component only.

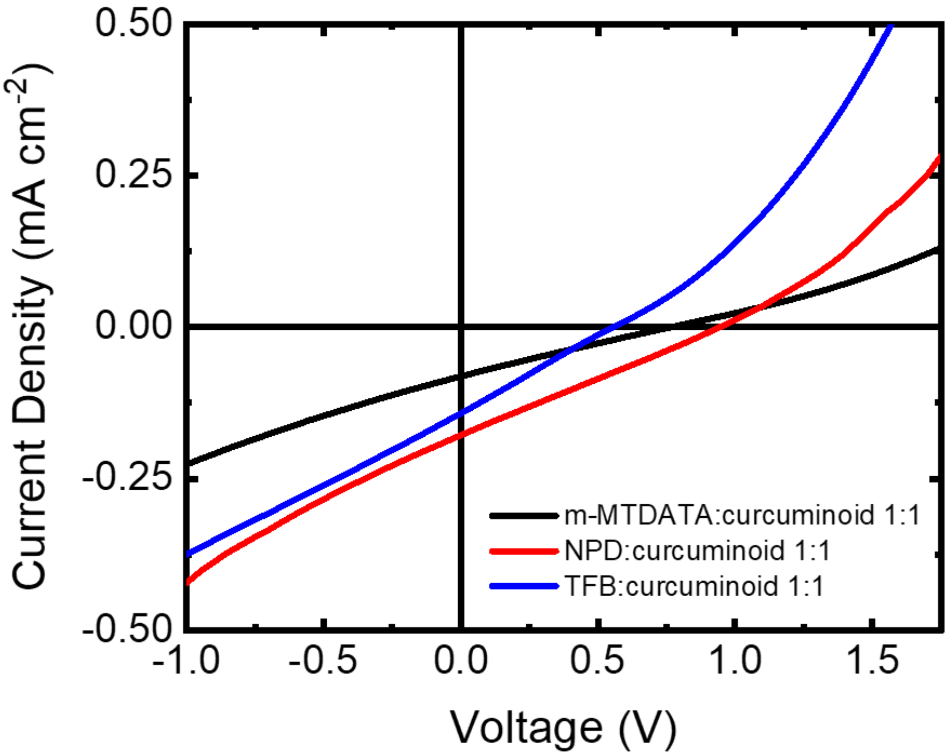

***Figure 6.30**: The current density-voltage curves of the champion m-MTDATA, NPD and TFB:curcuminoid 1:1 conventional architecture devices, measured under an AM1.5G solar spectrum. The PCE of all devices was under 0.1%. The device structure was ITO / PEDOT:PSS / donor:curcuminoid / Ca / Al. Devices fabricated and tested by Patrick Conaghan.*

Blend	V_{OC} (V)	J_{SC} (mA cm^{-2})	FF	PCE (%)
m-MTDATA:curcuminoid 1:1	0.75	0.08	0.24	0.01
NPD:curcuminoid 1:1	0.94	0.18	0.25	0.04
TFB:curcuminoid 1:1	0.55	0.14	0.25	0.02

***Table 6.4**: The key performance metrics of the donor:curcuminoid 1:1 device, measured under an AM1.5G solar spectrum.*

6.7 Conclusions

To summarise, we have investigated one member of a novel class of materials, know broadly as "curcuminoids". These materials have shown great promise in both OPV and OLED applications, demonstrating PCEs >4% and EQE_{EL}s of 10%,[146,147] but little was known about their photophysics or mechanisms of operation. Additionally, in line with our earlier work examining the use of low exchange energy materials in OPV electron acceptor roles to minimise non-radiative voltage loss, we attempted to utilise the curcuminoid as the acceptor with a range of wider band gap donor materials.

Through time-resolved spectroscopic measurements on the neat curcuminoid and films where it is diluted in a wide band gap host, we have discovered evidence that explains the OLED performance of this material. We found that due to its high oscillator strength, and a larger ΔE_{ST} than is typical for TADF emitters, the rate of radiative decay of the singlet state dominates over ISC. However, for species that do make it into the triplet manifold, rISC is very slow, with a time constant of 126 µs. At higher injection current densities in an OLED device, this would lead to a build-up of triplet states in the emissive layer, explaining the severe efficiency roll-off observed in OLEDs fabricated using the curcuminoid as the emissive material.[146]

In OPV applications where the curcuminoid is utilised as the electron donor with a fullerene acceptor, we confirm the reasonable performance of this class of materials with a moderate PCE of 2.1%. Through TA studies of the blend, we find that electron transfer from the curcuminoid to the fullerene proceeds rapidly and that the resulting charge species are long lived enough for extraction in an OPV device.[138] However, the spectroscopic measurements do not give any clue to the reasons for the low FF, which is by far the weakest performance metric of the device. Previous work has suggested that this may be due to unbalanced charge mobilities,[147] which can lead to space charge limited photocurrents and increased recombination.[163]

Finally, we attempted to employ the curcuminoid as the electron acceptor material, paired with a wide band gap donor that had a local triplet energy higher than the CT state. When blended with the polymer F8T2, poor device performance was observed, with a PCE of

0.1%. Though TA, we determined that excitons created on F8T2 underwent extremely rapid, sub-600 fs FRET to the curcuminoid. Therefore, the majority of charge transfer in the blend occurred from excitons on the curcuminoid. Here, we saw some evidence for a slow hole transfer process occurring, likely as a result of the isoenergetic HOMO levels in the blend. However, it appeared that hole transfer was slow enough that ISC was somewhat competitive, leading to the formation of triplet excitons on the curcuminoid. From previous work on the application of the curcuminoid in OLEDs, we know that these triplet excitons are extremely long-lived, meaning that they will build-up in the BHJ and annihilate with charges that are formed.[54,55] The photophysical processes occurring in both the blends of F8T2 and $PC_{60}BM$ with the curcuminoid are summarised in Figure 6.31. We also attempted to fabricate OPV devices by blending the curcuminoid with other wide band gap electron donors, this time with a larger HOMO-HOMO offset to increase the rate of the hole transfer. Nonetheless, device performance was still extremely poor, with all PCEs <0.1%. From this, we can conclude that the curcuminoid appears not to be suitable for use as the electron acceptor in OPV blends. We consider the most likely explanation for this to be that the electron mobility of the curcuminoid is low, which inhibits CT state dissociation and charge collection.[47]

Despite the setback, we still believe the curcuminoid family holds promise for low energy loss OPV applications. From our work, we have determined that the curcuminoid must be employed as the electron donor material to have any hope of making a reasonable device. Therefore, the design of wider band gap NFAs, preferably with a small exchange energy presents an interesting avenue for future investigations. If an NFA with a triplet energy above that of the CT state formed between it and the curcuminoid could be found, then we predict that good device performance with supressed triplet formation and a low energy loss could be realised. Searching the existing literature on NFAs, we consider the rhodanine class of acceptors to be prime candidates, given their relatively wide band gaps and A-D-A-type structures. This bequeaths them strong ICT character in their singlet excited state, a prerequisite for a low exchange energy.[164]

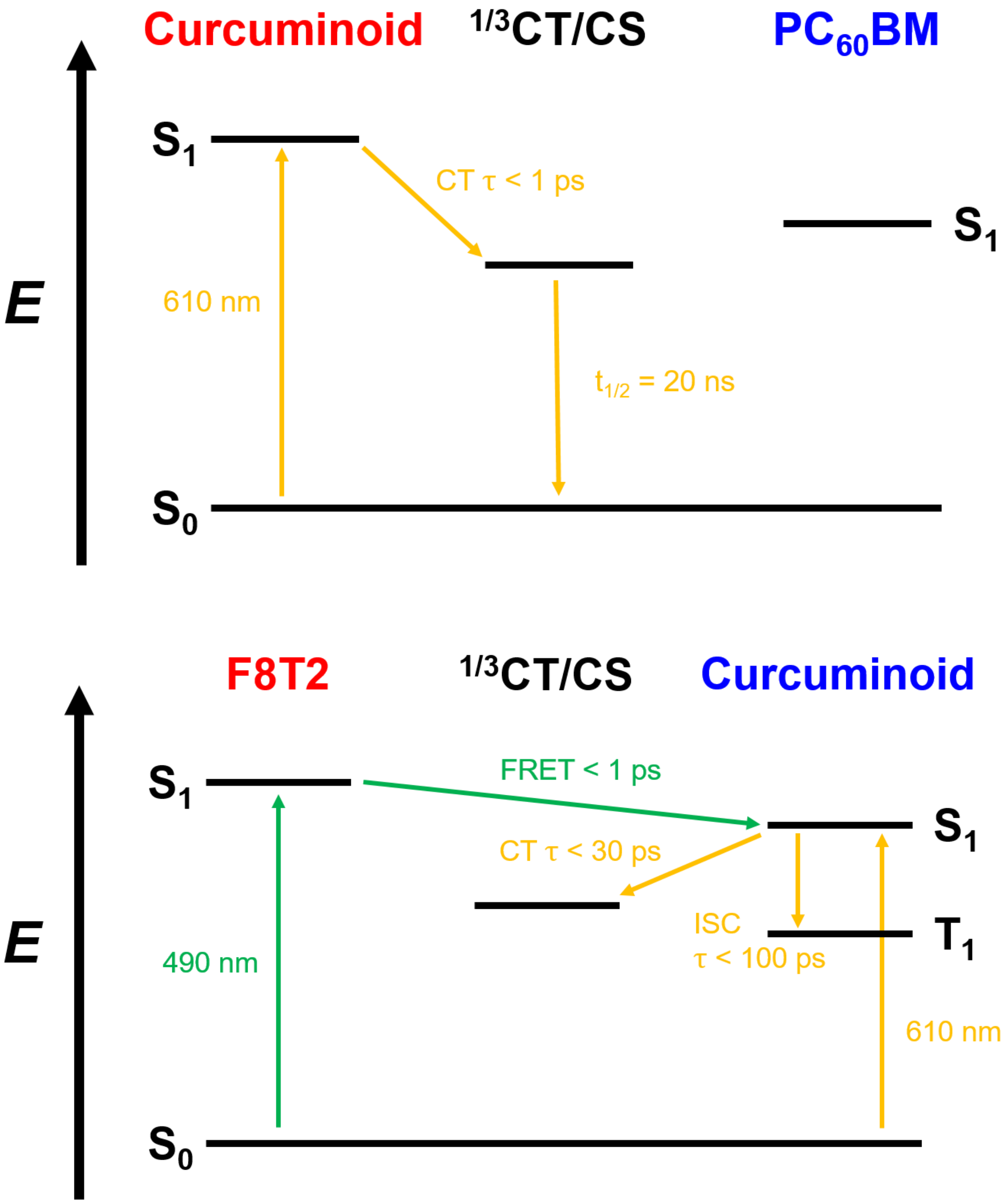

Figure 6.31: *Schematics summarizing the photophysical processes occurring in the Curcuminoid:PC$_{60}$BM and F8T2:Curcuminoid blends, as determined from the TA experiments.*

7 Summary and Future Outlook

In summary, this thesis provides a blueprint on how to reduce the non-radiative voltage loss that plagues OPV devices by targeting triplet excitons formed though recombination processes. Though the investigation of multiple system and wide range of organic materials, we have carried out systematic studies into factors that can inhibit triplet formation in organic solar cells. The strategies employed consist of both the kinetic and thermodynamic suppression of this process, which we note can be equally successful and therefore are both valid avenues for future investigation.

In Chapter 4, we examined two closely-related NFA-based organic solar cells that demonstrated a particularly low total energy loss. Here, we determined through electroluminescence measurements that supressed non-radiative recombination was largely responsible for this impressive metric. Upon learning this, we embarked on a detailed spectroscopic study of the two blends to uncover the reasons for the enhanced radiative efficiency of the blends. From this work, we concluded that the formation of triplet excitons localised on either the donor or acceptor was not appreciably occurring in either blend. Therefore, we concluded that turning off triplet exciton formation was the primary contributor to the exceptionally low non-radiative recombination losses, especially in the P2:A2 blend.

With this in mind, we developed the hypothesis that if re-dissociation of the CT state was substantially faster than the back electron transfer from the ^{3}CT that formed the local triplet, then triplet formation would be inhibited. To test this, we performed some preliminary calculations on the blends, modelling the back electron transfer from ^{3}CT to the local triplet state using Marcus theory. Noting that three variables control the rate of the electron transfer: reorganisation energy, the driving energy for the electron transfer and electronic coupling, we decided to investigate the role that they played in the back electron transfer rate. As the reorganisation energy in organic systems is fairly constant, we fixed this at a representative value and observed the effect of varying driving energy and electronic coupling on the rate. From this analysis, we concluded that energy difference between the ^{3}CT and the local triplet would have to be unrealistically large to significantly slow the rate of the back electron transfer.

Therefore, with this knowledge and the known energetics of our systems, we determined that the electronic coupling between the states may be the parameter that controls whether local triplet states are formed from the ^{3}CT. However, the actual magnitude of the electronic coupling, as well as the reorganisation energy and diving energy for the back electron transfer in the systems has not yet been investigated. Therefore, in order to confirm our hypothesis that reduced electronic coupling is the primary factor for suppressing triplet formation, a more detailed computational study of the material to investigate the electronic coupling is needed. In addition to this, accurate measurements to determine the reorganisation energy and the energies of the local triplet and CT states would also be extremely beneficial to our analysis.

This work suggests that significant attention should be given to the magnitude of the electronic coupling between the D and A in order to ensure triplets do not form in NFA devices. One key way to control this parameter is through the interfacial molecular orientation: it has been determined that molecules with the donor molecules face-on to the acceptor have an increased electronic coupling and reduced non-radiative voltage losses.[165] Therefore, strategies to design molecules that preferably adopt this orientation are likely to be fruitful in in ensuring that triplet formation remains unfavourable.

In Chapter 5, we investigated model OPV system consisting of a wider band gap, high triplet energy electron donor (NPD, TFB) paired with a lower band gap, small exchange energy acceptor (TXO-TPA). The aim of this work was to construct a system where there were no local triplet states lower in energy than the ^{3}CT, so that it would be thermodynamically impossible for them to form. With this, we hoped to observe an enhanced efficiency of radiative recombination and consequently reduced energy loss, in-line with the removal of a significant non-radiative recombination pathway. Through optical spectroscopic studies, we determined that both electron and hole transfer occurred efficiently, resulting in the creation of charge carriers. These charge carriers were very long lived and showed a significant proportion of their emission originating over the timescales associated with charge recombination processes. Consequently, the radiative efficiencies of the blends were very high by the standards of organic solar cells, comparable to that of neat films of the TADF acceptor material TXO-TPA. All of this evidenced the effectiveness of making the local triplet states energetically inaccessible in minimising the non-radiative losses in organic solar cells. However, device performance was poor, with low photocurrents and fill factors, though the V_{OC} was impressively high. We attributed the low performance to the low mobility of electrons on the acceptor, the UV-centric absorption of the materials and the decay of ^{1}CT states on timescales faster than charge extraction.

Building on the work from the previous chapter, in Chapter 6 we obtained a low exchange energy TADF material with a relatively narrow band gap and strong visible light absorption over the visible range. Belonging to the novel class of materials broadly known as "curcuminoids", they have shown great promise in both OLED and OPV applications, with an EQE_{EL} of 10% and a PCE of >4% when blended with a fullerene acceptor. Noting the lack of spectroscopic investigations into these materials, we decided to explore the photophysics of both the neat material and its blend with a fullerene acceptor first, before utilising it as a low exchange energy acceptor. Through this, we determined that the extremely slow rISC was the limiting factor of OLED performance at higher current densities, explaining in the severe efficiency roll off observed.

Turning to OPV applications, we paired the curcuminoid with the wider band gap electron donor F8T2. With this blend, we aimed to create a device where not only local triplet formation was impossible, but in contrast to previous efforts in Chapter 5, also absorbed light strongly over the entire visible region. Unfortunately, device performance was poor, which was ascribed to two factors: triplet formation on the curcuminoid component via direct ISC from the singlet that competed with charge transfer and the poor electron mobility of the curcuminoid, which hindered the ability to extract photo-generated charges. We attempted to remedy these shortcomings by employing electron donors with a larger HOMO-HOMO offset with the curcuminoid in the hope that hole transfer would outcompete ISC. However, device performance was even worse, suggesting that the curcuminoid is not suitable for use as the electron accepting component. Despite this, we still hold hope that the curcuminoids can be used to fabricate organic solar cells with suppressed triplet formation. With this in mind, future work should include retuning the curcuminoid to the electron donor role, where it has already demonstrated good performance. Here, it should be paired with a wider band gap electron acceptor with a relatively strong ICT character. If the exchange energy of the acceptor can be reduced, then it will ease the restrictive requirements for a wider band gap acceptor (>2 eV) with a deep LUMO (~4 eV), that also has a local triplet energy of above the CT state energy. Provided that such an acceptor can be found, we envisage that excellent performance from a curcuminoid donor OPV with a low non-radiative energy loss can be achieved.

Despite the poor device performance seen in the devices that were engineered to have no energetically accessible local triplet states, we still consider this work a promising proof-of-concept for this strategy. Indeed, it would be worthwhile to spend time searching for additional pairs of D and A molecules that fulfil this design criteria in the hope that they offer better device performance than previously seen. Additionally, efforts to synthesise molecules specifically for this purpose may prove to be the most effective approach. For this, a narrow-gap NFA with a small exchange energy, possibly based upon the structures of other efficient NFAs, would be a primary target. This could be achieved by using steric hindrance around the bond linking the D and A moieties to induce twisting out of plane, a tactic already widely employed in TADF materials to reduce the exchange energy.[70,72,76] If the exchange energy could be reduced enough to make the triplet on the NFA no longer energetically accessible, whilst still allowing for reasonable light absorption, then such a material could substantially reduce non-radiative voltage losses and maintain good photovoltaic performance.

List of Publications

Gillett A.J., Ko S.J., Lee J., Karki A., Bazan G.C., Nguyen T.Q. and Friend R.H. (2019) Suppressed local triplet formation is key to minimising voltage loss in organic solar cells. *In preparation.*

Gillett A.J., Evans E.W., Gu Q., Menke S.M., Conaghan P.J., Chen Y.S., Greenfield J.L., Sadhanala A. and Friend R.H. (2019) Spontaneous dissociation and recombination of organic excitons with charge transfer character leads to efficient spin-mixing. *In preparation.*

Shivanna R., Bourelle S.A., Senanayak S.P., Gillett A.J., Friend R.H. and Deschler F. (2019) Exciton spin dynamics and their dependence on monovalent cation dipole moment in layered 2D metal-halide perovskites. *Under review in Nature Communications (January 2019).*

Montanaro S., Gillett A.J., Feldmann S., Evans E.W., Friend R.H. and Wright I.A. (2019) Red-shifted delayed fluorescence at the expense of photoluminescence quantum efficiency-an intramolecular charge-transfer molecule based on a benzodithiophene-4,8-dione acceptor. *Physical Chemistry Chemical Physics*, 2019, 21, 10580 – 10586.

Thomas T.H., Harkin D.J., Gillett A.J., Lemaur V., Nikolka M., Sadhanala A., Richter J.M, Armitage J., Chen H., MuCulloch I., Menke S.M., Oliver Y., Beljonne D. and Sirringhaus H. (2019) Short contacts between chains enhancing luminescence quantum yields and carrier mobilities in conjugated polymers. *Nature Communications*, 2019, 10, 2614.

Xin A., Evans E.W., Dong S., Gillett A.J., Guo H., Chen Y., Hele T.J.H., Friend R.H. and Li F. Efficient radical-based light-emitting diodes with doublet emission. *Nature*, 2018, 563, 536–540.

Booker E.P., Thomas T.H., Quarti C., Stanton M.R., Dashwood C.D., Gillett A.J., Richter J.M., Pearson A.J., Davis N.J.K.L., Sirringhaus H., Price M.B., Greenham N.C., Beljonne B., Dutton S.E. and Deschler F. (2017) Formation of long-lived colour centers for broadband visible light emission in low-dimensional layered perovskites. *Journal of the American Chemical Society*, 2017, 139, 18632–18639.

References

1 J. H. Burroughes, D. D. C. Bradley, A. R. Brown, R. N. Marks, K. Mackay, R. H. Friend, P. L. Burns and A. B. Holmes, *Nature*, 1990, 347, 539–541.

2 C. J. Brabec, *Sol. Energy Mater. Sol. Cells*, 2004, 83, 273–292.

3 R. H. Friend, R. W. Gymer, A. B. Holmes, J. H. Burroughes, R. N. Marks, C. Taliani, D. D. C. Bradley, D. A. Dos Santos, J. L. Brédas, M. Lögdlund and W. R. Salaneck, *Nature*, 1999, 397, 121–128.

4 B. Crone, A. Dodabalapur, Y. Lin, R. Filas, Z. Bao, A. LaDuca, R. Sarpeshkar, H. Katz and W. Li, *Nature*, 2000, 403, 521–523.

5 W. Shockley and H. J. Queisser, *J. Appl. Phys.*, 1961, 32, 510–519.

6 S. Rühle, *Sol. Energy*, 2016, 130, 139–147.

7 M. Yamaguchi, T. Takamoto, K. Araki and N. Ekins-Daukes, *Sol. Energy*, 2005, 79, 78–85.

8 J. Zhao, A. Wang and M. A. Green, *Prog. Photovoltaics Res. Appl.*, 1999, 7, 471–474.

9 J. Yuan, Y. Zhang, L. Zhou, G. Zhang, H.-L. Yip, T.-K. Lau, X. Lu, C. Zhu, H. Peng, P. A. Johnson, M. Leclerc, Y. Cao, J. Ulanski, Y. Li and Y. Zou, *Joule*, 2019, 3, 1–12.

10 L. Meng, Y. Zhang, X. Wan, C. Li, X. Zhang, Y. Wang, X. Ke, Z. Xiao, L. Ding, R. Xia, H.-L. Yip, Y. Cao and Y. Chen, *Science (80-.).*, 2018, 2612, 1094–1098.

11 M. Hösel, R. R. Søndergaard, M. Jørgensen and F. C. Krebs, *Energy Technol.*, 2013, 1, 102–107.

12 G. Chen, H. Sasabe, Z. Wang, X.-F. Wang, Z. Hong, Y. Yang and J. Kido, *Adv. Mater.*, 2012, 24, 2768–2773.

13 A. Rao, P. C. Y. Chow, S. Gélinas, C. W. Schlenker, C.-Z. Li, H.-L. Yip, A. K.-Y. Jen, D. S. Ginger and R. H. Friend, *Nature*, 2013, 500, 435–439.

14 P. Atkins and J. De Paula, *Atkins' Physical Chemistry*, Oxford University Press,

2009.

15 N. J. Turro, V. Ramamurthy and J. C. Scaiano, *Principles of Molecular Photochemistry: an Introduction*, University Science Books, 2009.

16 A. Köhler and H. Bässler, *Electronic Processes in Organic Semiconductors*, WILEY-VCH Verlag, 2015.

17 Y. S. Lee and M. Kertesz, *J. Chem. Phys.*, 1988, 88, 2609–2617.

18 M. Pope and C. E. Swenberg, *Electronic Processes in Organic Crystals and Polymers*, 1999.

19 A. Miyata, A. Mitioglu, P. Plochocka, O. Portugall, J. T.-W. Wang, S. D. Stranks, H. J. Snaith and R. J. Nicholas, *Nat. Phys.*, 2015, 11, 582–587.

20 R. Hull, in *Properties of Crystalline Silicon*, 2002.

21 T. M. Clarke and J. R. Durrant, *Chem. Rev.*, 2010, 110, 6736–6767.

22 J. Frenkel, *Phys. Rev.*, 1931, 37, 17–44.

23 T. Chen, L. Zheng, J. Yuan, Z. An, R. Chen, Y. Tao, H. Li, X. Xie and W. Huang, *Sci. Rep.*, 2015, 5, 10923.

24 A. Endo, M. Ogasawara, A. Takahashi, D. Yokoyama, Y. Kato and C. Adachi, *Adv. Mater.*, 2009, 21, 4802–4806.

25 S. Nepurek and J. Sworakowski, *J. Appl. Phys.*, 1980, 51, 2098.

26 W. Siebrand, *J. Chem. Phys.*, 1967, 47, 2411–2422.

27 T. Forster, *Naturwissenschaften*, 1946, 33, 166–175.

28 D. L. Dexter, *J. Chem. Phys.*, 1953, 21, 836–850.

29 R. A. Marcus and N. Sutin, *Biochim. Biophys. Acta - Rev. Bioenerg.*, 1985, 811, 265–322.

30 D. C. Coffey, B. W. Larson, A. W. Hains, J. B. Whitaker, N. Kopidakis, O. V. Boltalina, S. H. Strauss and G. Rumbles, *J. Phys. Chem. C*, 2012, 116, 8916–8923.

31 A. J. Ward, A. Ruseckas, M. M. Kareem, B. Ebenhoch, L. A. Serrano, M. Al-Eid, B.

Fitzpatrick, V. M. Rotello, G. Cooke and I. D. W. Samuel, *Adv. Mater.*, 2015, 27, 2496–2500.

32 S. Zhang, Y. Qin, J. Zhu and J. Hou, *Adv. Mater.*, 2018, 30, 1–7.

33 M. Knupfer, *Appl. Phys. A Mater. Sci. Process.*, 2003, 77, 623–626.

34 P. Peumans and S. R. Forrest, *Chem. Phys. Lett.*, 2004, 398, 27–31.

35 J. Nelson, *Curr. Opin. Solid State Mater. Sci.*, 2002, 6, 87–95.

36 G. Li, R. Zhu and Y. Yang, *Nat. Photonics*, 2012, 6, 153–161.

37 B. P. Lyons, N. Clarke and C. Groves, *Energy Environ. Sci.*, 2012, 5, 7657.

38 R. R. Lunt, N. C. Giebink, A. A. Belak, J. B. Benziger and S. R. Forrest, *J. Appl. Phys.*, 2009, 105, 053711.

39 G. Dennler, M. Scharber and C. Brabec, *Adv. Mater.*, 2009.

40 C. L. Braun, *J. Chem. Phys.*, 1984, 80, 4157–4161.

41 S. Gélinas, T. S. Van Der Poll, G. C. Bazan and R. H. Friend, *Science (80-.).*, 2014, 343, 512.

42 S. M. Menke, A. Cheminal, P. Conaghan, N. A. Ran, N. C. Greehnam, G. C. Bazan, T.-Q. Nguyen, A. Rao and R. H. Friend, *Nat. Commun.*, 2018, 9, 277.

43 K. Kawashima, Y. Tamai, H. Ohkita, I. Osaka and K. Takimiya, *Nat. Commun.*, 2015, 6, 10085.

44 J. Liu, S. Chen, D. Qian, B. Gautam, G. Yang, J. Zhao, J. Bergqvist, F. Zhang, W. Ma, H. Ade, O. Inganäs, K. Gundogdu, F. Gao and H. Yan, *Nat. Energy*, 2016, 1, 16089.

45 S. N. Hood and I. Kassal, *J. Phys. Chem. Lett.*, 2016, 7, 4495–4500.

46 Y. Puttisong, Y. Xia, X. Chen, F. Gao, I. A. Buyanova, O. Inganäs and W. M. Chen, *J. Phys. Chem. C*, 2018, 122, 12640–12646.

47 A. K. K. Kyaw, D. H. Wang, C. Luo, Y. Cao, T. Q. Nguyen, G. C. Bazan and A. J. Heeger, *Adv. Energy Mater.*, 2014, 4, 1–9.

48 S. M. Menke, N. A. Ran, G. C. Bazan and R. H. Friend, *Joule*, 2018, 2, 25–35.

49 J. Lee, S.-J. Ko, M. Seifrid, H. Lee, C. McDowell, B. R. Luginbuhl, A. Karki, K. Cho, T.-Q. Nguyen and G. C. Bazan, *Adv. Energy Mater.*, 2018, 8, 1801209.

50 J. Lee, S.-J. Ko, M. Seifrid, H. Lee, B. R. Luginbuhl, A. Karki, M. Ford, K. Rosenthal, K. Cho, T.-Q. Nguyen and G. C. Bazan, *Adv. Energy Mater.*, 2018, 8, 1801212.

51 D. Bi, W. Tress, M. I. Dar, P. Gao, J. Luo, C. Renevier, K. Schenk, A. Abate, F. Giordano, J.-P. Correa Baena, J.-D. Decoppet, S. M. Zakeeruddin, M. K. Nazeeruddin, M. Grätzel and A. Hagfeldt, *Sci. Adv.*, 2016, 2, e1501170.

52 U. Rau, U. W. Paetzold and T. Kirchartz, *Phys. Rev. B*, 2014, 90, 035211.

53 A. Nitzan, S. Mukamel and J. Jortner, *J. Chem. Phys.*, 1975, 63, 200–207.

54 P. C. Y. Chow, S. Gélinas, A. Rao and R. H. Friend, *J. Am. Chem. Soc.*, 2014, 136, 3424–3429.

55 I. A. Howard, J. M. Hodgkiss, X. Zhang, K. R. Kirov, H. A. Bronstein, C. K. Williams, R. H. Friend, S. Westenhoff and N. C. Greenham, *J. Am. Chem. Soc.*, 2010, 132, 328–335.

56 S. D. Dimitrov, S. Wheeler, D. Niedzialek, B. C. Schroeder, H. Utzat, J. M. Frost, J. Yao, A. Gillett, P. S. Tuladhar, I. McCulloch, J. Nelson and J. R. Durrant, *Nat. Commun.*, 2015, 6, 6501.

57 J. Benduhn, F. Piersimoni, G. Londi, A. Kirch, J. Widmer, C. Koerner, D. Beljonne, D. Neher, D. Spoltore and K. Vandewal, *Adv. Energy Mater.*, 2018, 8, 1800451.

58 H. Zhang, H. Yao, J. Hou, J. Zhu, J. Zhang, W. Li, R. Yu, B. Gao, S. Zhang and J. Hou, *Adv. Mater.*, 2018, 30, 1800613.

59 Z. Xiao, X. Jia and L. Ding, *Sci. Bull.*, 2017, 62, 1562–1564.

60 Y. Cui, H. Yao, L. Hong, T. Zhang, Y. Xu, K. Xian, B. Gao, J. Qin, J. Zhang, Z. Wei and J. Hou, *Adv. Mater.*, 2019, 1808356, 1808356.

61 C. W. Schlenker, K. S. Chen, H. L. Yip, C. Z. Li, L. R. Bradshaw, S. T. Ochsenbein,

F. Ding, X. S. Li, D. R. Gamelin, A. K. Y. Jen and D. S. Ginger, *J. Am. Chem. Soc.*, 2012, 134, 19661–19668.

62 N. Thejo Kalyani and S. J. Dhoble, *Renew. Sustain. Energy Rev.*, 2012, 16, 2696–2723.

63 E. S. Hellerich, J. J. Intemann, M. Cai, R. Liu, M. D. Ewan, B. C. Tlach, M. Jeffries-EL, R. Shinar and J. Shinar, *J. Mater. Chem. C*, 2013, 1, 5191.

64 B. Geffroy, P. le Roy and C. Prat, *Polym. Int.*, 2006, 55, 572–582.

65 N. C. Greenham, R. H. Friend and D. D. C. Bradley, *Adv. Mater.*, 1994, 6, 491–494.

66 J. Kido and Y. Iizumi, *Appl. Phys. Lett.*, 1998, 73, 2721–2723.

67 C. Adachi, M. A. Baldo, M. E. Thompson and S. R. Forrest, *J. Appl. Phys.*, 2001, 90, 5048–5051.

68 D. Y. Kondakov, *J. Appl. Phys.*, 2007, 102, 114504.

69 N. A. Kukhta, T. Matulaitis, D. Volyniuk, K. Ivaniuk, P. Turyk, P. Stakhira, J. V. Grazulevicius and A. P. Monkman, *J. Phys. Chem. Lett.*, 2017, 8, 6199–6205.

70 H. Uoyama, K. Goushi, K. Shizu, H. Nomura and C. Adachi, *Nature*, 2012, 492, 234–238.

71 S. K. Lower and M. A. El-Sayed, *Chem. Rev.*, 1966, 66, 199–241.

72 M. K. Etherington, J. Gibson, H. F. Higginbotham, T. J. Penfold and A. P. Monkman, *Nat. Commun.*, 2016, 7, 13680.

73 B. T. Lim, S. Okajima, A. K. Chandra and E. C. Lim, *Chem. Phys. Lett.*, 1981, 79, 22–27.

74 F. B. Dias, K. N. Bourdakos, V. Jankus, K. C. Moss, K. T. Kamtekar, V. Bhalla, J. Santos, M. R. Bryce and A. P. Monkman, *Adv. Mater.*, 2013, 25, 3707–3714.

75 J. Gibson, A. P. Monkman and T. J. Penfold, *ChemPhysChem*, 2016, 17, 2956–2961.

76 Y. Olivier, B. Yurash, L. Muccioli, G. D'Avino, O. Mikhnenko, J. C. Sancho-García, C. Adachi, T.-Q. Nguyen and D. Beljonne, *Phys. Rev. Mater.*, 2017, 1, 075602.

77 W. B. Jackson, N. M. Amer, A. C. Boccara and D. Fournier, *Appl. Opt.*, 1981, 20, 1333.

78 J. C. De Mello, H. F. Wittmann and R. H. Friend, *Adv. Mater.*, 1997, 9, 230–232.

79 C. Manzoni, D. Polli and G. Cerullo, *Rev. Sci. Instrum.*, 2006, 77, 023103.

80 D. Brida, S. Bonora, C. Manzoni, M. Marangoni, P. Villoresi, S. De Silvestri and G. Cerullo, *Opt. Express*, 2009, 17, 12510.

81 A. P. Kalyanomy Deb, *IEEE Trans. Evol. Comput.*, 2001, 6, 182–197.

82 M. A. Green, K. Emery, Y. Hishikawa, W. Warta, E. D. Dunlop, D. H. Levi and A. W. Y. Ho-Baillie, *Prog. Photovoltaics Res. Appl.*, 2017, 25, 3–13.

83 Y. Zhang, H. Yao, S. Zhang, Y. Qin, J. Zhang, L. Yang, W. Li, Z. Wei, F. Gao and J. Hou, *Sci. China Chem.*, 2018, 61, 1328–1337.

84 N. J. Jeon, H. Na, E. H. Jung, T. Y. Yang, Y. G. Lee, G. Kim, H. W. Shin, S. Il Seok, J. Lee and J. Seo, *Nat. Energy*, 2018, 3, 682–689.

85 W. Zhao, S. Li, H. Yao, S. Zhang, Y. Zhang, B. Yang and J. Hou, *J. Am. Chem. Soc.*, 2017, 139, 7148–7151.

86 A. Polman, M. Knight, E. C. Garnett, B. Ehrler and W. C. Sinke, *Science (80-.).*, 2016, 352, aad4424–aad4424.

87 D. Luo, W. Yang, Z. Wang, A. Sadhanala and Q. Hu, *Science (80-.).*, 2018, 1446, 1442–1446.

88 K. Vandewal, K. Tvingstedt, A. Gadisa, O. Inganäs and J. V. Manca, *Nat. Mater.*, 2009, 8, 904–909.

89 S. De Wolf, J. Holovsky, S. J. Moon, P. Löper, B. Niesen, M. Ledinsky, F. J. Haug, J. H. Yum and C. Ballif, *J. Phys. Chem. Lett.*, 2014, 5, 1035–1039.

90 N. Chandrasekaran, E. Gann, N. Jain, A. Kumar, S. Gopinathan, A. Sadhanala, R. H. Friend, A. Kumar, C. R. McNeill and D. Kabra, *ACS Appl. Mater. Interfaces*, 2016, 8, 20243–20250.

91 M. B. Upama, M. Wright, B. Puthen-Veettil, N. K. Elumalai, M. A. Mahmud, D.

Wang, K. H. Chan, C. Xu, F. Haque and A. Uddin, *RSC Adv.*, 2016, 8, 20243–20250.

92 P. B. Deotare, W. Chang, E. Hontz, D. N. Congreve, L. Shi, P. D. Reusswig, B. Modtland, M. E. Bahlke, C. K. Lee, A. P. Willard, V. Bulovic, T. Van Voorhis and M. A. Baldo, *Nat. Mater.*, 2015, 14, 1130–1134.

93 K. Vandewal, J. Benduhn and V. C. Nikolis, *Sustain. Energy Fuels*, 2018, 2, 538–544.

94 D. Qian, Z. Zheng, H. Yao, W. Tress, T. R. Hopper, S. Chen, S. Li, J. Liu, S. Chen, J. Zhang, X. K. Liu, B. Gao, L. Ouyang, Y. Jin, G. Pozina, I. A. Buyanova, W. M. Chen, O. Inganäs, V. Coropceanu, J. L. Bredas, H. Yan, J. Hou, F. Zhang, A. A. Bakulin and F. Gao, *Nat. Mater.*, 2018, 17, 703–709.

95 S. Ullbrich, J. Benduhn, X. Jia, V. C. Nikolis, K. Tvingstedt, F. Piersimoni, S. Roland, Y. Liu, J. Wu, A. Fischer, D. Neher, S. Reineke, D. Spoltore and K. Vandewal, *Nat. Mater.*, 2019, 18, 459–464.

96 M. E. Ziffer, S. B. Jo, H. Zhong, L. Ye, H. Liu, F. Lin, J. Zhang, X. Li, H. W. Ade, A. K. Y. Jen and D. S. Ginger, *J. Am. Chem. Soc.*, 2018, 140, 9996–10008.

97 Y. Tamai, Y. Fan, V. O. Kim, K. Ziabrev, A. Rao, S. Barlow, S. R. Marder, R. H. Friend and S. M. Menke, *ACS Nano*, 2017, 11, 12473–12481.

98 S. Gélinas, A. Rao, A. Kumar, S. L. Smith, A. W. Chin, J. Clark, T. S. van der Poll, G. C. Bazan and R. H. Friend, *Science (80-.).*, 2014, 343, 512–517.

99 Y. Liu, L. Zuo, X. Shi, A. K. Y. Jen and D. S. Ginger, *ACS Energy Lett.*, 2018, 3, 2396–2403.

100 K. Meng, Q. Ding, S. Wang and Q. Gong, *Chem. Phys. Lett.*, 2011, 515, 155–158.

101 S. M. Falke, C. A. Rozzi, D. Brida, M. Maiuri, M. Amato, E. Sommer, A. Rubio, G. Cerullo, E. Molinari and C. Lienau, *Science (80-.).*, 2014, 344, 1001–1005.

102 D. W. Gehrig, I. A. Howard and F. Laquai, *J. Phys. Chem. C*, 2015, 119, 13509–13515.

103 Y. Yi, V. Coropceanu and J. L. Brédas, *J. Mater. Chem.*, 2011, 21, 1479–1486.

104 Y. W. Soon, H. Cho, J. Low, H. Bronstein, I. McCulloch and J. R. Durrant, *Chem.*

Commun., 2013, 49, 1291–1293.

105 P. C. Y. Chow, S. Gélinas, A. Rao and R. H. Friend, *J. Am. Chem. Soc.*, 2014, 136, 3424–3429.

106 H. Kraus, M. C. Heiber, S. Väth, J. Kern, C. Deibel, A. Sperlich and V. Dyakonov, *Sci. Rep.*, 2016, 6, 1–8.

107 S. L. Smith and A. W. Chin, *Phys. Chem. Chem. Phys.*, 2014, 16, 20305–20309.

108 A. P. Monkman, H. D. Burrows, L. J. Hartwell, L. E. Horsburgh, I. Hamblett and S. Navaratnam, *Phys. Rev. Lett.*, 2001, 86, 1358–1361.

109 P. L. Santos, J. S. Ward, P. Data, A. S. Batsanov, M. R. Bryce, F. B. Dias and A. P. Monkman, *J. Mater. Chem. C*, 2016, 4, 3815–3824.

110 T.-A. Lin, T. Chatterjee, W.-L. Tsai, W.-K. Lee, M.-J. Wu, M. Jiao, K.-C. Pan, C.-L. Yi, C.-L. Chung, K.-T. Wong and C.-C. Wu, *Adv. Mater.*, 2016, 28, 6976–6983.

111 B. Milián-Medina and J. Gierschner, *Org. Electron. physics, Mater. Appl.*, 2012, 13, 985–991.

112 D. Veldman, S. C. J. Meskers and R. A. J. Janssen, *Adv. Funct. Mater.*, 2009, 19, 1939–1948.

113 W. Chang, D. N. Congreve, E. Hontz, M. E. Bahlke, D. P. McMahon, S. Reineke, T. C. Wu, V. Bulović, T. Van Voorhis and M. A. Baldo, *Nat. Commun.*, 2015, 6, 6415.

114 H. Wang, L. Xie, Q. Peng, L. Meng, Y. Wang, Y. Yi and P. Wang, *Adv. Mater.*, 2014, 26, 5198–204.

115 S. A. Choulis, V.-E. Choong, M. K. Mathai and F. So, *Appl. Phys. Lett.*, 2005, 87, 113503.

116 K. Goushi, R. Kwong, J. J. Brown, H. Sasabe and C. Adachi, *J. Appl. Phys.*, 2004, 95, 7798–7802.

117 J.-L. Bredas, *Mater. Horiz.*, 2014, 1, 17–19.

118 W. L. Li, Z. Q. Gao, Z. Y. Hong, C. S. Lee and S. T. Lee, *Synth. Met.*, 2000, 111, 53–56.

119 J. Clark, R. Archer, T. Redding, C. Foden, J. Tant, Y. Geerts, R. H. Friend and C. Silva, *J. Appl. Phys.*, 2008, 103, 124510.

120 S. Forget, S. Chenais, D. Tondelier, B. Geffroy, I. Gozhyk, M. Lebental and E. Ishow, *J. Appl. Phys.*, 2010, 108, 064509.

121 D. Mühlbacher, M. Scharber, M. Morana, Z. Zhu, D. Waller, R. Gaudiana and C. Brabec, *Adv. Mater.*, 2006, 18, 2884–2889.

122 J. S. Ward, R. S. Nobuyasu, M. A. Fox, A. S. Batsanov, J. Santos, F. B. Dias and M. R. Bryce, *J. Org. Chem.*, 2018, 83, 14431–14442.

123 M. Okazaki, Y. Takeda, P. Data, P. Pander, H. Higginbotham, A. P. Monkman and S. Minakata, *Chem. Sci.*, 2017, 8, 2677–2686.

124 G. Cerullo, G. Lanzani, M. Zavelani-Rossi and S. De Silvestri, *Phys. Rev. B*, 2001, 63, 241104.

125 D. M. Guldi and M. Prato, *Acc. Chem. Res.*, 2000, 33, 695–703.

126 A. A. Bakulin, S. D. Dimitrov, A. Rao, P. C. Y. Chow, C. B. Nielsen, B. C. Schroeder, I. McCulloch, H. J. Bakker, J. R. Durrant and R. H. Friend, *J. Phys. Chem. Lett.*, 2013, 4, 209–215.

127 Y. W. Soon, T. M. Clarke, W. Zhang, T. Agostinelli, J. Kirkpatrick, C. Dyer-Smith, I. Mcculloch, J. Nelson and J. R. Durrant, *Chem. Sci.*, 2011, 2, 1111–1120.

128 Q. Zhang, J. Li, K. Shizu, S. Huang, S. Hirata, H. Miyazaki and C. Adachi, *J. Am. Chem. Soc.*, 2012, 134, 14706–14709.

129 H. Tanaka, K. Shizu, H. Miyazaki and C. Adachi, *Chem. Commun.*, 2012, 48, 11392.

130 T. Zhang, B. Zhao, B. Chu, W. Li, Z. Su, X. Yan, C. Liu, H. Wu, F. Jin and Y. Gao, *Org. Electron. physics, Mater. Appl.*, 2015, 25, 6–11.

131 D. Chen, Z. Wang, D. Wang, Y. C. Wu, C. C. Lo, A. Lien, Y. Cao and S. J. Su, *Org. Electron. physics, Mater. Appl.*, 2015, 25, 79–84.

132 K. Goushi, K. Yoshida, K. Sato and C. Adachi, *Nat. Photonics*, 2012, 6, 253–258.

133 P. B. Deotare, W. Chang, E. Hontz, D. N. Congreve, L. Shi, P. D. Reusswig, B.

Modtland, M. E. Bahlke, C. K. Lee, A. P. Willard, V. Bulovic, T. Van Voorhis and M. A. Baldo, *Nat. Mater.*, 2015, 14, 1130–1134.

134 S. Naka, H. Okada, H. Onnagawa, Y. Yamaguchi and T. Tsutsui, *Synth. Met.*, 2000, 111, 331–333.

135 G. F. Burkhard, E. T. Hoke and M. D. McGehee, *Adv. Mater.*, 2010, 22, 3293–3297.

136 H. Yoshikawa and S. Adachi, *Jpn. J. Appl. Phys.*, 1997, 36, 6237–6243.

137 E. A. Taft and H. R. Philipp, *Phys. Rev.*, 1961, 121, 1100–1103.

138 A. Kumar, G. Lakhwani, E. Elmalem, W. T. S. Huck, A. Rao, N. C. Greenham and R. H. Friend, *Energy Environ. Sci.*, 2014, 7, 2227.

139 O. V. Kozlov, Y. N. Luponosov, A. N. Solodukhin, B. Flament, Y. Olivier, R. Lazzaroni, J. Cornil, S. A. Ponomarenko and M. S. Pshenichnikov, *Adv. Opt. Mater.*, 2017, 5, 1700024.

140 N. Sariciftci, L. Smilowitz, A. J. Heeger and F. Wudl, *Science (80-.).*, 1992, 258, 1474–1476.

141 A. Rao, P. C. Y. Chow, S. Gélinas, C. W. Schlenker, C. Li, H. Yip, A. K.-Y. Jen, D. S. Ginger and R. H. Friend, *Nature*, 2013, 500, 435–439.

142 W. Shockley and H. J. Queisser, *J. Appl. Phys.*, 1961, 32, 510–519.

143 S. J. He, D. K. Wang, N. Jiang, J. S. Tse and Z. H. Lu, *Adv. Mater.*, 2016, 28, 649–654.

144 S. A. Jenekhe and J. A. Osaheni, *Science (80-.).*, 1994, 265, 765–768.

145 T. Granlund, L. a. a. Pettersson, M. R. Anderson and O. Inganäs, *J. Appl. Phys.*, 1997, 81, 8097.

146 D. H. Kim, A. D'Aléo, X. K. Chen, A. D. S. Sandanayaka, D. Yao, L. Zhao, T. Komino, E. Zaborova, G. Canard, Y. Tsuchiya, E. Choi, J. W. Wu, F. Fages, J. L. Brédas, J. C. Ribierre and C. Adachi, *Nat. Photonics*, 2018, 12, 98–104.

147 F. Archet, D. Yao, S. Chambon, M. Abbas, A. D'Aléo, G. Canard, M. Ponce-Vargas, E. Zaborova, B. Le Guennic, G. Wantz and F. Fages, *ACS Energy Lett.*, 2017, 2,

1303–1307.

148 J. H. Huang, C. Y. Yang, Z. Y. Ho, D. Kekuda, M. C. Wu, F. C. Chien, P. Chen, C. W. Chu and K. C. Ho, *Org. Electron. physics, Mater. Appl.*, 2009, 10, 27–33.

149 J. J. Benson-Smith, H. Ohkita, S. Cook, J. R. Durrant, D. D. C. Bradley and J. Nelson, *Dalt. Trans.*, 2009, 0, 10000–10005.

150 K. Goushi, R. Kwong, J. J. Brown, H. Sasabe and C. Adachi, *J. Appl. Phys.*, 2004, 95, 7798–7802.

151 S. A. Choulis, V. Choong, M. K. Mathai, F. So, S. A. Choulis, V. Choong, M. K. Mathai and F. So, *Appl. Phys. Lett.*, 2016, 113503, 2003–2006.

152 S. A. Bagnich, A. Rudnick, P. Schroegel, P. Strohriegl and A. Kohler, *Philos. Trans. R. Soc. A Math. Phys. Eng. Sci.*, 2015, 373, 20140446–20140446.

153 L. Yu, Z. Wu, G. Xie, C. Zhong, Z. Zhu, H. Cong, D. Ma and C. Yang, *Chem. Commun.*, 2016, 52, 11012–11015.

154 T. Hosokai, H. Matsuzaki, H. Nakanotani, K. Tokumaru, T. Tsutsui, A. Furube, K. Nasu, H. Nomura, M. Yahiro and C. Adachi, *Sci. Adv.*, 2017, 3, e1603282.

155 F. B. Dias, J. Santos, D. R. Graves, P. Data, R. S. Nobuyasu, M. A. Fox, A. S. Batsanov, T. Palmeira, M. N. Berberan-Santos, M. R. Bryce and A. P. Monkman, *Adv. Sci.*, 2016, 3, 1–10.

156 H. van Eersel, P. A. Bobbert, R. A. J. Janssen and R. Coehoorn, *J. Appl. Phys.*, 2016, 119, 163102.

157 S. M. Falke, C. A. Rozzi, D. Brida, M. Maiuri, M. Amato, E. Sommer, A. De Sio, A. Rubio, G. Cerullo, E. Molinari and C. Lienau, *Science (80-.).*, 2014, 344, 1001–1005.

158 A. E. Jailaubekov, A. P. Willard, J. R. Tritsch, W. L. Chan, N. Sai, R. Gearba, L. G. Kaake, K. J. Williams, K. Leung, P. J. Rossky and X. Y. Zhu, *Nat. Mater.*, 2013, 12, 66–73.

159 P. L. Santos, L. A. Cury, F. B. Dias and A. P. Monkman, *J. Lumin.*, 2016, 172, 118–123.

160 K. Yonezawa, M. Ito, H. Kamioka, T. Yasuda, L. Han and Y. Moritomo, *Adv. Opt. Technol.*, 2012, 2012, 1–10.

161 W. Chang, D. N. Congreve, E. Hontz, M. E. Bahlke, D. P. McMahon, S. Reineke, T. C. Wu, V. Bulović, T. Van Voorhis and M. a Baldo, *Nat. Commun.*, 2015, 6, 6415.

162 F. Liu, Y. Gu, J. W. Jung, W. H. Jo and T. P. Russell, *J. Polym. Sci. Part B Polym. Phys.*, 2012, 50, 1018–1044.

163 L. Murphy, W. Hong, H. Aziz and Y. Li, *Sol. Energy Mater. Sol. Cells*, 2013, 114, 71–81.

164 S. Holliday, R. S. Ashraf, C. B. Nielsen, M. Kirkus, J. A. Rohr, C. H. Tan, E. Collado-Fregoso, A. C. Knall, J. R. Durrant, J. Nelson and I. McCulloch, *J. Am. Chem. Soc.*, 2015, 137, 898–904.

165 N. A. Ran, S. Roland, J. A. Love, V. Savikhin, C. J. Takacs, Y.-T. Fu, H. Li, V. Coropceanu, X. Liu, J.-L. Brédas, G. C. Bazan, M. F. Toney, Di. Neher and T.-Q. Nguyen, *Nat. Commun.*, 2017, 8, 79.